



**HAL**  
open science

# Constitutive behaviour modelling of short fibre reinforced composites under dynamic loading

Mariem Nciri

► **To cite this version:**

Mariem Nciri. Constitutive behaviour modelling of short fibre reinforced composites under dynamic loading. Mechanics of materials [physics.class-ph]. Université de Valenciennes et du Hainaut-Cambresis; École nationale d'ingénieurs de Tunis (Tunisie), 2017. English. NNT : 2017VALE0016 . tel-01635545

**HAL Id: tel-01635545**

**<https://theses.hal.science/tel-01635545>**

Submitted on 15 Nov 2017

**HAL** is a multi-disciplinary open access archive for the deposit and dissemination of scientific research documents, whether they are published or not. The documents may come from teaching and research institutions in France or abroad, or from public or private research centers.

L'archive ouverte pluridisciplinaire **HAL**, est destinée au dépôt et à la diffusion de documents scientifiques de niveau recherche, publiés ou non, émanant des établissements d'enseignement et de recherche français ou étrangers, des laboratoires publics ou privés.

## Thèse de doctorat

### Pour obtenir le grade de Docteur de l'Université de **VALENCIENNES ET DU HAINAUT-CAMBRÉSIS**

Discipline, spécialité selon la liste des spécialités pour lesquelles l'Ecole Doctorale est accréditée :

#### MÉCANIQUE

Présentée et soutenue par **Mariem NCIRI**

Le **11/05/2017**, à Valenciennes

#### École doctorale :

Sciences Pour l'Ingénieur (SPI), Lille Nord-de-France

#### Équipe de recherche, Laboratoire :

Laboratoire d'Automatique, de Mécanique et d'Informatique Industrielles et Humaines (LAMIH)

### **Modélisation du Comportement des Composites à Fibres Courtes Non-Alignées en Dynamique**

#### Rapporteurs :

- BERNASCONI, Andrea. Professeur, Politecnico di Milano
- AMMAR, Amine. Professeur, Arts et Métiers ParisTech, ENSAM Angers

#### Examineurs :

- DOGHRI, Issam. Professeur, Université Catholique de Louvain (**Président du jury**)
- HADDAR, Nader. Maître de Conférences, École Nationale d'Ingénieurs de Sfax
- NOTTA-CUVIER, Délphine. Maître de Conférences, Université de Valenciennes
- CHAARI, Fahmi. Maître de Conférences, Université de Valenciennes

#### Invité :

- MAALEJ, Yamen. Maître de Conférences, École Nationale d'Ingénieurs de Tunis

#### Directeurs de thèse :

- LAURO, Franck. Professeur, Université de Valenciennes
- ZOUARI, Bassem. Professeur, École Nationale d'Ingénieurs de Sfax



# THESE

Présentée à  
**L'École Nationale d'Ingénieurs de Sfax**  
En vue de l'obtention du

## DOCTORAT

Dans la discipline *Mécanique*

Par  
**Mariem NCIRI**

### **Modélisation du Comportement des Composites à Fibres Courtes Non-Alignées en Dynamique**

Soutenu le 11/05/2017 devant le jury composé de :

<b>M. BERNASCONI, Andrea. Professeur, Politecnico di Milano</b>	Rapporteur
<b>M. AMMAR, Amine. Professeur, Arts et Métiers ParisTech ENSAM Angers</b>	Rapporteur
<b>M. DOGHRI, Issam. Professeur, Université Catholique de Louvain</b>	Examineur
<b>M. HADDAR, Nader. Maître de Conférences, École Nationale d'Ingénieurs de Sfax</b>	Examineur
<b>Mme. NOTTA-CUVIER, Déléphine. Maître de Conférences, Université de Valenciennes</b>	Examineur
<b>M. CHAARI, Fahmi. Maître de Conférences, Université de Valenciennes</b>	Examineur
<b>M. MAALEJ, Yamen. Maître de Conférences, École Nationale d'Ingénieurs de Tunis</b>	Invité
<b>M. LAURO, Franck. Professeur, Université de Valenciennes</b>	Directeur de thèse
<b>M. ZOUARI, Bassem. Professeur, École Nationale d'Ingénieurs de Sfax</b>	Directeur de thèse

---

# *Acknowledgements*

---

First of all, I express my deepest feelings of gratitude to my supervisors Franck Lauro and Bassem Zouari for their trust on my abilities and for these three years of support and guidance.

My sincere thanks go to Delphine Notta-Cuvier for the scientific supervision conducted with boundless enthusiasm, the unvaluable advices and availability, and for all what I have learnt thanks to her. Thanks to her help this work is seeing the daylight.

My thanks go as well to Fahmi Chaari for his significant help, especially with processing X-ray tomography, and his priceless advices and the interesting discussions we have had.

I extend my thanks to Yamen Maalej for his trust and encouragements all along these three years. My thanks go as well to Rémi Delille, Grégory Haugou, Frédéric Robache and Denis Lesueur for their unvaluable help in the realisation of the experimental work.

I am also grateful to Catherine Foucard, Sabine Guilain and Isabelle Oliveira for their availability and help with administrative formalities.

I have also a thought for all those I met and shared time with during this thesis, especially Sylvain Treutenare, Ludovic Dufour, Rim Chtourou, Anthony Bracq and Van Tu Doan.

I owe my thanks to the members of the jury for having honoured me and accepting to assess my work.

Last but not least, I am very grateful to all my family and my friends, for their continuous support, and to Mehdi for his incredible patience and support through these intense years.





---

# *Abbreviations and notations*

---

## **Acronyms/Abbreviations**

SFRC	Short Fibre Reinforced Composite
SFRT	Short Fibre Reinforced Thermoplastic
PP	Polypropylene
$\mu$ -CT	Micro-Computed Tomography
IFD	Injection Flow Direction
VE	Viscoelastic
VP	Viscoplastic
E-VP	Elasto-Viscoplastic
VE-VP	Viscoelastic-Viscoplastic
DMA	Dynamic Mechanical Analysis
MFR	Melt Flow Rate
DIC	Digital Image Correlation

## **Operators**

$x_i$	component $i$ of a vector $x$
$x_{ij}$	component $ij$ of a second-order tensor $x$
$x_{ijkl}$	component $ijkl$ of a fourth-order tensor $x$
$x^T$	Transpose of tensor $x$
$\dot{x}$	Material time derivative of $x$
$\langle \cdot \rangle$	Macauley bracket
$\delta_{ij}$	Kronecker symbol
:	Double contraction of tensors
$\frac{\partial x}{\partial a}$	Partial derivative of $x$ with respect to $a$
$\delta_{ij}$	Kronecker symbol

## Variables and parameters

### Matrix viscoelasticity

$\sigma_M$	Cauchy stress tensor of the matrix material
$\sigma_{M,dev}$	Deviatoric part of the matrix stress tensor
$\sigma_{M,H}$	Dilatational part of the matrix stress tensor
$\varepsilon$	Total strain tensor
$\varepsilon^{ve}$	Viscoelastic part of the strain tensor
$\varepsilon_{dev}^{ve}$	Deviatoric part of the viscoelastic strain tensor
$\varepsilon_H^{ve}$	Dilatational part of the viscoelastic strain tensor
$\rho_M$	Density of the matrix material
$\phi_M$	Helmholtz free energy of the matrix material
$\phi_M^{ve}$	Viscoelastic part of the Helmholtz free energy
$R^{ve}$	Fourth-order relaxation tensor
$E_\infty$	Long-term elastic modulus
$E_i$	$i^{th}$ time dependent modulus
$G$	Shear relaxation function
$K$	Bulk relaxation function
$G_\infty$	Long-term shear modulus
$K_\infty$	Long-term bulk modulus
$G_i$	$i^{th}$ shear relaxation modulus
$K_i$	$i^{th}$ bulk relaxation modulus
$\tau_i^d$	$i^{th}$ deviatoric relaxation time
$\mu_i^d$	$i^{th}$ deviatoric viscous coefficient
$\tau_i^v$	$i^{th}$ volumetric relaxation time
$\mu_i^v$	$i^{th}$ volumetric viscous coefficient

**Matrix viscoplasticity**

$\psi_M^{vp}$	Viscoplastic potential of dissipation
$\varepsilon^{vp}$	Viscoplastic part of the strain tensor
$n$	Viscoplastic flow direction tensor
$\lambda$	Viscoplastic multiplier
$\kappa$	Hardening variable/cumulative viscoplastic strain
$I_1$	First invariant of the matrix Cauchy stress tensor
$I_2$	Second invariant of the matrix Cauchy stress tensor
$f$	Raghava yield surface
$F^{vp}$	Dynamic yield surface
$\sigma^{vp}$	Viscous overstress function
$\mu$	Hydrostatic pressure dependency parameter
$\sigma_{comp}$	Yield surface in compression
$\sigma_t$	Yield surface in tension
$H$	Hardening thermodynamic force/function
$a^+$	Volume variation parameter under positive pressure
$a^-$	Volume variation parameter under negative pressure
$m$	Strain rate sensitivity parameter
$\dot{\kappa}_0$	Viscosity parameter

## Fibre/Composite parameters

$\bar{d}^i$	Fibre orientation vector of the $i^{th}$ fibre medium
$A^i$	Orientation matrix of the $i^{th}$ fibre medium
$v_F^i$	Volume fraction of the $i^{th}$ fibre medium
$v_F$	Total volume fraction of fibres
$v_M$	Matrix volume fraction
$\sigma_F^{0,i}$	1D fibre axial stress
$\sigma_F^i$	Stress tensor of the $i^{th}$ fibre medium
$\sigma_c$	Composite stress tensor
$F_F^i$	Tensor of deformation gradient of the $i^{th}$ fibre medium
$F$	Total deformation gradient tensor
$C$	Right Cauchy-Green tensors of the composite
$C_F^i$	Right Cauchy-Green tensors of the $i^{th}$ fibre medium
$\varepsilon_F^{0,i}$	1D Hencky strain of the fibres
$\tau$	Interfacial Shear Strength
$L^i$	Fibres length in the $i^{th}$ medium
$r^i$	Fibre radius in the $i^{th}$ medium
$E_F^i$	Elasticity modulus in the $i^{th}$ fibre medium
$N_{fam}$	Number of fibre media
$\rho$	Density of the composite material
$\rho_F^i$	Density of the $i^{th}$ fibre medium
$\phi_F^i$	Helmholtz free energy of the $i^{th}$ fibre medium

**Ductile damage parameters**

D	Damage scalar variable
$\tilde{\sigma}_M$	Effective Cauchy stress tensor of the matrix material
$\mathcal{D}$	Fourth-order damage tensor
$\mathcal{D}'$	Derivative of the damage tensor
$\mathcal{D}^\alpha$	Intermediate fourth-order damage tensor
$\mathcal{M}^\alpha$	Inverse of the intermediate fourth-order damage tensor
Y	Damage thermodynamic force
$Y_{dev}$	Deviatoric part of the damage thermodynamic force
$Y_H$	Hydrostatic part of the damage thermodynamic force
$\psi_M^D$	Damage dissipation potential
S	Damage parameter

**Interfacial debonding and failure parameters**

$\varepsilon_{th}$	Threshold strain value of debonding initiation
$L^{\alpha D}$	Microfailure length over the partially debonded fibre for fibre medium $\alpha$
$\delta^{\alpha}$	length on which load transmission is prevented for fibre medium $\alpha$
$v_v^{nucl}$	Volume fraction of nucleated voids
$v_v^{crit}$	Critical volume fraction of nucleated voids



---

# *Contents*

---

<b>Acknowledgements</b>	<b>1</b>
<b>Abbreviations and notations</b>	<b>3</b>
<b>Table of Contents</b>	<b>9</b>
<b>List of Tables</b>	<b>11</b>
<b>List of Figures</b>	<b>13</b>
<b>1 General Introduction</b>	<b>1</b>
<b>2 State of art of short fibre reinforced composites behaviour and modelling</b>	<b>7</b>
2.1 Generalities about short-fibre reinforced thermoplastics . . . . .	7
2.1.1 Microstructure of short fibre reinforced composites . . . . .	8
2.1.2 Techniques of orientation measurement . . . . .	10
2.2 Behaviour of thermoplastic matrices . . . . .	11
2.3 Behaviour of short fibre reinforced composites . . . . .	13
2.4 Modelling of short fibre reinforced composites . . . . .	14
2.5 Conclusion . . . . .	19
<b>3 Constitutive model for short-fibre reinforced composites</b>	<b>21</b>
3.1 Presentation of the approach for SFRC modelling . . . . .	22
3.2 Constitutive laws of SFRC behaviour model . . . . .	23
3.2.1 Viscoelastic-viscoplastic behaviour model of thermoplastic matrix . . . . .	23
3.2.2 Modelling of fibres mechanical response . . . . .	36
3.2.3 Modelling of composite mechanical response . . . . .	38
3.3 Conclusion . . . . .	40



<b>4</b>	<b>Experimental procedure for the parameters identification and validation of the model</b>	<b>43</b>
4.1	Characterisation of the implemented behaviour model . . . . .	43
4.1.1	PP matrix VE-VP behaviour model . . . . .	44
4.1.2	Extension of the modelling to PP matrix reinforced with short glass fibres	61
4.1.3	Validation of the composite model for tensile tests at different loading direction and strain-rate . . . . .	82
4.2	Conclusion . . . . .	88
<b>5</b>	<b>Damage and fracture modelling</b>	<b>91</b>
5.1	State of art of damage characterisation and modelling for SFRC . . . . .	91
5.2	Modelling of matrix ductile damage . . . . .	93
5.2.1	Anisotropic damage model for the matrix material . . . . .	93
5.2.2	Thermodynamic formulation of damage evolution laws . . . . .	96
5.2.3	Characterisation and validation of the matrix damage model . . . . .	98
5.3	Fibre-Matrix interfacial damage . . . . .	107
5.4	Validation of the damage model . . . . .	114
5.5	Fracture modelling . . . . .	117
5.5.1	Damage development based criteria . . . . .	117
5.5.2	Tensile tests with notched specimens . . . . .	119
5.5.3	Identification and verification of the fracture criteria . . . . .	121
5.6	Conclusion . . . . .	130
	<b>Conclusion</b>	<b>133</b>
5.7	General conclusion . . . . .	133
5.8	Future works . . . . .	135
	<b>Bibliography</b>	<b>137</b>
<b>A</b>	<b>Identification of the parameter <math>C^{nucl}</math></b>	<b>145</b>
	<b>Abstract</b>	<b>147</b>
	<b>Résumé</b>	<b>149</b>

---

# *List of Tables*

---

3.1 Return-mapping algorithm for the computation of VE-VP thermoplastic matrix behaviour . . . . .	35
3.2 Material parameters of the matrix and composite constitutive laws . . . . .	41
4.1 DMA cycles . . . . .	45
4.2 Identified linear viscoelastic parameters of the PP matrix material . . . . .	49
4.3 DIC acquisition rate . . . . .	51
4.4 Standard deviation of DIC strains (for an axial displacement of 4.5 mm at 1 mm/min)	52
4.5 Viscoplastic parameters of PP matrix material . . . . .	60
4.6 Supplier specifications of the composites materials . . . . .	61
4.7 Fibre average orientation with respect to specimen axis over the specimen central volume for the different $\theta$ specimens of PPGF30 . . . . .	78
4.8 Angle-Volume fraction data at $0^\circ$ for PP-30GF (PP30-0-1) and PP-40GF (PP40-0-1)	82
5.1 Values of critical axial strain for different distributions of fibre orientation of $0^\circ$ -specimens . . . . .	126
5.2 Total void computed at a composite axial strain of 0.05 for different angles of fibre orientation . . . . .	128



---

# *List of Figures*

---

1.1 Stiffness of various materials with respect to their densities . . . . .	2
1.2 Polypropylene matrix reinforced with 40% of short glass fibres under uniaxial tension test at a constant strain rate. In the figure $\sigma_f$ represents the failure stress [1]. . .	3
2.1 Example of a microstructure: Polyamide 6.6 matrix reinforced with short glass fibres [8] . . . . .	9
2.2 Melt flow profile of short fibre reinforced polymer within mould cavity during filling.	10
2.3 Stress-strain diagrams for PP with 40 wt.% glass fibres at different strain rates [52]	15
3.1 Raghava yield surface for different values of the hydrostatic pressure dependency parameter, $\eta$ . . . . .	29
3.2 Viscoplastic dissipation potential for different values of $a^+$ and $a^-$ . . . . .	30
3.3 Schematic representation of the computation of composite stress tensor . . . . .	39
4.1 Geometry of DMA specimen . . . . .	45
4.2 An example of a stress response to an applied sinusoidal strain for frequencies equal to 0.05, 0.1, 0.25, 0.5 and 1 Hz . . . . .	46
4.3 Storage (a) and loss (b) moduli versus angular pulsation for PP matrix . . . . .	47
4.4 Comparison of measured and identified loss and storage moduli over a wide range of angular pulsation, $\omega$ . . . . .	49
4.5 Geometry of tensile specimens (dimensions in mm) . . . . .	50
4.6 Definition of ROI and ZOI for the strain field measurement using DIC technique . .	51
4.7 Influence of the facet size on the computation of “Axial strain” in a critical zone during a rigid body motion test . . . . .	52
4.8 DIC strains computed during the test of PP at 1 mm/min . . . . .	53
4.9 Quasi-static and dynamic tensile behaviour of PP, as measured by DIC . . . . .	54
4.10 Compression test set-up . . . . .	55
4.11 Compression behaviour of PP at two different strain rates . . . . .	56
4.12 Evolution of the viscoplastic Poisson ratio versus true axial strain . . . . .	57

4.13	Experimentally obtained behaviour surface with the $SE\dot{E}$ method . . . . .	58
4.14	Behaviour laws obtained with the $SE\dot{E}$ method . . . . .	59
4.15	Tensile and compression behaviour of PP for the identification of the parameter of hydrostatic pressure dependency (at $1 \text{ mm}\cdot\text{min}^{-1}$ ) . . . . .	59
4.16	Comparison between modelled and experimental tensile behaviour of PP at different loading rates (Continuous lines = Experimental data, Dashed lines = Numerical data) with scattering bars . . . . .	61
4.17	Orientation of tensile specimens in injection-moulded plates . . . . .	62
4.18	Scanned volume and definition of angles $\theta$ and $\psi$ . . . . .	63
4.19	Reconstructed 3D microstructure of PP-30GF by micro-computed tomography . . . . .	63
4.20	Treatment of 2D grey-scaled images obtained from $\mu$ -CT scan of a PP-30GF specimen . . . . .	64
4.21	Example of directionality histogram obtained for a PP-30GF specimen cut at $0^\circ$ with respect to the IFD . . . . .	64
4.22	Variation of the fibre orientation through the specimen thickness (Skin-Shell-Core structure) . . . . .	65
4.23	Comparison of results obtained with a “step” of 1 and 10 from a PP-30GF specimen at an angle $\theta = 0^\circ$ for the selection of the 2D grey-scaled images through the thickness . . . . .	66
4.24	Comparison of scan results at different locations over the specimen ROI . . . . .	67
4.25	Fibre orientation of specimens cut at different locations and $0^\circ$ with respect to IFD for PP-30GF . . . . .	68
4.26	Fibre orientation of specimens cut at angles equal to $20^\circ$ , $45^\circ$ , $60^\circ$ and $90^\circ$ with respect to IFD for PP-30GF . . . . .	69
4.27	Fibre orientation histograms of specimens cut at angles equal to $0^\circ$ , $20^\circ$ , $45^\circ$ , $60^\circ$ and $90^\circ$ with respect to IFD for PP-40GF . . . . .	70
4.28	Fibre distribution of orientation of specimens cut at angles equal to $0^\circ$ , $20^\circ$ , $45^\circ$ , $60^\circ$ and $90^\circ$ with respect to IFD for PP-30GF . . . . .	72
4.29	Fibre distribution of orientation of specimens cut at angles equal to $0^\circ$ , $20^\circ$ , $45^\circ$ , $60^\circ$ and $90^\circ$ with respect to IFD for PP-40GF . . . . .	73
4.30	Tensile specimens for optical extensometry measurement . . . . .	75
4.31	Tensile tests at different strain rates and loading angles for PP-30GF . . . . .	76
4.32	Tensile tests at different strain rates and loading angles for PP-40GF . . . . .	77

<i>List of Figures</i>	15
4.33 Observation of anisotropic behaviour by considering different loading directions from quasi-static tensile tests (at $1 \text{ mm}\cdot\text{min}^{-1}$ ) for PP (dashed line) and the composite materials (PP-30GF and PP-40GF) . . . . .	78
4.34 Tensile behaviour of $0^\circ$ - specimens (at $1 \text{ mm}\cdot\text{min}^{-1}$ ) with different average values of $\psi$ . . . . .	79
4.35 Apparent rigidity of PP-30GF and PP-40GF at different strain rates . . . . .	79
4.36 Average axial stress at break of PP-30GF and PP-40GF at different strain rates . . . .	80
4.37 Comparison of experimental and numerically simulated tensile behaviour of specimens PP30-0-1 ( $\tau = 23 \text{ MPa}$ ) and PP40-0-1 ( $\tau = 26.5 \text{ MPa}$ ) . . . . .	81
4.38 Representation of the layered structure of the fibre orientation for the computation of the tensile response of a PP30-0 specimen (at $1 \text{ mm}\cdot\text{min}^{-1}$ ) . . . . .	83
4.39 Results of simulated tensile test with layered distributions of fibre orientation of a PP30-0 specimen at $1 \text{ mm}\cdot\text{min}^{-1}$ . . . . .	84
4.40 Comparison of experimental and numerical data for tests of $0^\circ$ specimens of PP-30GF	85
4.41 Comparison of experimental and numerical data for tests of $20^\circ$ specimens of PP-30GF	85
4.42 Comparison of experimental and numerical data for tests of $45^\circ$ specimens of PP-30GF	85
4.43 Comparison of experimental and numerical data for tests of $60^\circ$ specimens of PP-30GF	86
4.44 Comparison of experimental and numerical data for tests of $90^\circ$ specimens of PP-30GF	86
4.45 Comparison of experimental and numerical data for tests of $0^\circ$ specimens of PP-40GF	87
4.46 Comparison of experimental and numerical data for tests of $20^\circ$ specimens of PP-40GF	87
4.47 Comparison of experimental and numerical data for tests of $45^\circ$ specimens of PP-40GF	87
4.48 Comparison of experimental and numerical data for tests of $60^\circ$ specimens of PP-40GF	88
4.49 Comparison of experimental and numerical data for tests of $90^\circ$ specimens of PP-40GF	88
5.1 Definition of the damaged and effective configurations in Continuum Damage Mechanics . . . . .	94
5.2 Damage anisotropy of the reinforced matrix material . . . . .	95
5.3 Influence of parameter S on the evolution of the damage variable D ( $1 \text{ mm}\cdot\text{min}^{-1}$ ) .	100
5.4 Influence of parameter S on the damaged matrix response at tension ( $1 \text{ mm}\cdot\text{min}^{-1}$ )	100
5.5 Damage variable determination from cyclic tests using the stiffness-loss method [38]	101
5.6 Cartography corresponding to an engineering strain of 0.087 and determination of the ROI of homogeneous strain . . . . .	101
5.7 Stress-true strain response for cyclic uniaxial tensile test on PP . . . . .	102
5.8 Damage evolution law calculated using the stiffness-loss method . . . . .	103

5.9 Identification of the parameter S . . . . .	105
5.10 Influence of damage on computation of PP matrix tensile behaviour, for a wide range of strain rate . . . . .	106
5.11 Anisotropy of the matrix damage for the PP-30GF composite (data computed using distributions of fibre orientation of specimens PP30-0-4 and PP30-90-4) . . . . .	107
5.12 A schematic representation of failure scenario in SFRC subjected to an axial loading (in the direction of the fibre axis) . . . . .	108
5.13 Effect of fibre/matrix debonding on load transmission . . . . .	109
5.14 Influence of parameter b on the fibre length unavailable for load transmission (a fixed at 0.2) . . . . .	112
5.15 Influence of parameter a on the fibre length unavailable for load transmission (b fixed at 2) . . . . .	112
5.16 Influence of parameter a on the fibre axial stress (b fixed at 2) . . . . .	113
5.17 Influence of parameter a on the composite PP-GF30 axial stress (b fixed at 2), in the case of specimen PP30-0-1 tested at $1 \text{ mm} \cdot \text{min}^{-1}$ . . . . .	113
5.18 Comparison of experimental and numerical results for the identified parameters a and b (specimen PP30-0-1 tested at $1 \text{ mm} \cdot \text{min}^{-1}$ ) . . . . .	114
5.19 Implementation scheme . . . . .	115
5.20 Verification of the model with the implemented matrix and interfacial damage models by comparison with experimental results in the case of PP-30GF . . . . .	116
5.21 Fibre debonding in a fracture surface of PP-30GF tested at $1 \text{ mm} \cdot \text{min}^{-1}$ (visualised by MEB) . . . . .	118
5.22 Evolution of cumulated void volume fraction with different distributions of fibre orientation resulting from different cutting angles $\theta$ . . . . .	119
5.23 Notched specimen geometry and definition of the ROI . . . . .	120
5.24 Influence of the facet size on the measured axial strain at the step 150 (corresponding to an engineering strain of 0.04) . . . . .	121
5.25 Cartography of axial strains at the pre-failure step (last step) for $0^\circ$ -specimens with a facet size of $31 \times 31 \text{ pix}^2$ . . . . .	122
5.26 Local strain measurement at the pre-failure step of the specimen PP30-0-4 . . . . .	122
5.27 Influence of the mesh size on the strain localisation at the notch zone . . . . .	123
5.28 simulated zone of failure initiation . . . . .	124

<i>List of Figures</i>	17
5.29 Identification of the critical cumulated void fraction with results obtained for the specimen PP30-0-4 . . . . .	124
5.30 Evolution of the cumulated void (a) with different distributions of fibre orientation obtained from specimens cut at $\theta = 0^\circ$ (b) . . . . .	125
5.31 Failure criteria at $0^\circ$ with respect to IFD (dashed vertical lines correspond to the experimental minimum (PP30-0-5) and maximum (PP30-0-6) failure strains obtained with notched specimens . . . . .	126
5.32 Cartography of axial strains at the pre-failure step (last step) for $90^\circ$ -specimens with a facet size of $31 \times 31 \text{ pix}^2$ . . . . .	127
5.33 Identification of the failure strain with notched specimen PP30-90-4 . . . . .	129
5.34 Failure criteria at $90^\circ$ with respect to IFD (dashed vertical lines correspond to the experimental minimum (PP30-90-3) and maximum (PP30-90-5) failure strains obtained with notched specimens . . . . .	130
5.35 Cumulated void evolution for theoretical composites with aligned fibres ( $0^\circ$ and $90^\circ$ )	130
5.36 Fracture surface of PP-30GF tested at (a) $1 \text{ mm.min}^{-1}$ and (b) $1000 \text{ mm.min}^{-1}$ obtained by SEM obserbations. . . . .	136
A.1 Total volume variation and strain volume variation fraction of the composite material (PP-30GF) . . . . .	146
A.2 Comparison between experimental and computed void volume fraction with the identified value of $C^{nucl}$ (with data corresponding to the notch specimen PP30-0-4) . . . . .	146





## *General Introduction*

---

Composite materials are known as new generation of strong-stiff and lightweight materials. Yet this kind of material has existed in nature for thousands of years now, like wood, bamboo and bones, long before the modern engineering community thought of developing the first composite material. In general a composite is made from two or more distinct materials with significantly different physical and/or chemical properties, which produce a material with properties different from those of the individual components. The first phase of composite material is called matrix and its main role is to transfer load to reinforcing agents. Polymeric matrices are under concern in this work. Scientists developed the first polymers, a result of the polymerisation process of monomers, at the beginning of the 20<sup>th</sup> century. Examples of synthetic polymeric structures, amongst others, include nylon, polyethylene, polyster, and epoxy. According to their thermomechanical properties, two categories of polymeric matrices can be found: Thermoset (e.g. epoxies) and thermoplastic (e.g. nylon, polypropylene, high density polyethylene, polycarbonate) polymers. The primary physical difference is that thermoplastics, with linear and branched chains, can be remelted back into a liquid form, whereas thermoset plastics, with crosslinked chains, will always remain in a permanent solid state. Given the relatively “weak” properties of polymeric materials, reinforcement is needed to create a stiff material. Therefore, a second phase is introduced as reinforcing agent like particles, nanotubes, nanoparticles or fibres (continuous, long or short). A relation between density and Young’s modulus for various materials can be seen in Figure 1.1, where the high mechanical properties of reinforcement (fibres, particles), compared to those of polymeric ones, are highlighted.

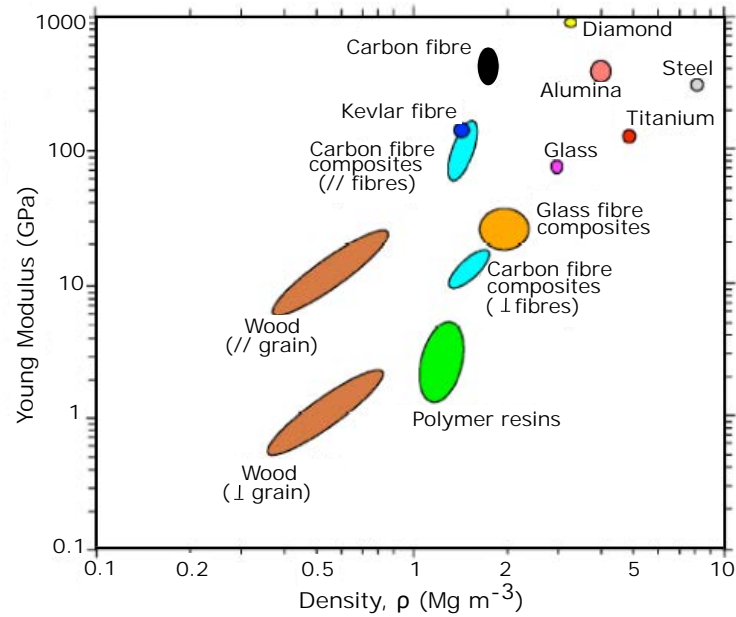


Figure 1.1: Stiffness of various materials with respect to their densities

With fibre reinforcement, it is well established that stiffness, strength and, for many polymers, toughness are improved. The dimensional stability, creep resistance, ageing and weathering properties, crucial in some applications, can also be improved. The increase in stiffness and failure stress of a Polypropylene matrix reinforced by 40% in volume fraction of short glass fibres and loaded in main fibre direction is highlighted in Figure 1.2.

Two categories of reinforcing fibres can be distinguished: continuous (or long) and short fibres. The fibre reinforced composites with the highest mechanical properties are those with continuous fibre reinforcement. However, such materials cannot be adapted easily to mass production and are generally confined to products in which the property benefits outweigh the cost penalty. Short fibre reinforced composites (SFRC) can offer a unique combination of properties with interestingly superior mechanical properties over the parent polymers. Among other advantages, short-fibre reinforced composites are interesting from an industrial point of view for their relatively low cost and easy manufacturing process as they can be processed in a manner similar to polymeric materials. In the case of thermoplastics, conventional fabrication techniques, such as extrusion compounding and injection moulding, are available, allowing mass production of components with quite intricate shapes.

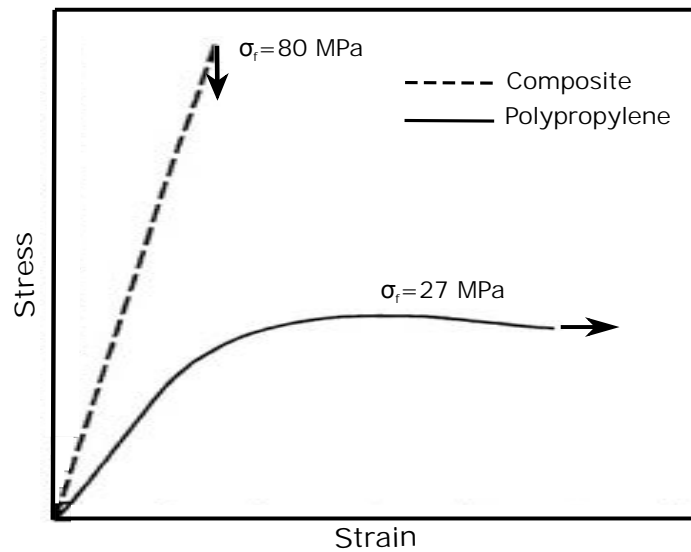


Figure 1.2: Polypropylene matrix reinforced with 40% of short glass fibres under uniaxial tension test at a constant strain rate. In the figure  $\sigma_f$  represents the failure stress [1].

In this context, short fibre reinforced composites are finding ever-increasing interest in engineering applications, such as automotive industry (e.g. for the manufacturing of instrument panels of vehicles).

The kind of composite material to be further discussed in this manuscript is a thermoplastic matrix reinforced with short glass fibres. The properties of SFRC are partly induced by the composition (fibre volume fraction) and partly by the processing, giving a wide range of property combinations to which both designer and manufacturer should be alert. By adding suitable fibres and by controlling factors such as the aspect ratio, the dispersion, the fibres orientation and the fibre-matrix adhesion, significant improvements in property can be achieved.

The extensive use of these composites needs, however, a thorough theoretical knowledge of their properties and their interactions with process and/or loading conditions the material will have to withstand. This becomes more crucial under extreme loading conditions (e.g. crash or impact loading) with the material behaviour complexity (e.g. polymeric matrices viscosity). In that context, characterisation of short fibre composite materials, prediction of effective mechanical properties and micromechanical analytical modelling under various loading conditions are a field of study for researchers. For instance, when targeted structures are subjected to high speed loading application, robust theoretical approach that can take strain-rate sensitivity into account, in addition to other specificities (like reinforcement complexity and damage phenomena) are needed for a reliable prediction of the materials behaviour.

Taking all the aforementioned into consideration, the ultimate objective of this thesis work is to present an efficient approach for the numerical modelling of short fibre composite in the framework of dynamic loading. Major guidelines for this work is that most important interdependent phenomena, for instance, viscosity, complex anisotropy, failure mechanisms, are to be fully addressed in a unified modelling. The proposed approach is at an intermediate scale between complex homogenisation approaches and often inaccurate purely phenomenological descriptions. The current approach is based on the additive decomposition of the composite thermodynamic potential. The composite is thus seen as the assembly of a matrix medium and several media of embedded fibres. The deformation gradient, applied to the composite as a whole, and its multiplicative decomposition implicitly link the media. A main asset of this approach is its adaptability to all kinds of reinforcement characteristics (orientation and geometrical properties) and matrix behaviour while keeping the implementation relatively easy. The matrix behaviour is modelled as strain rate dependent using a coupled Viscoelastic (VE)-Viscoplastic (VP) scheme. Complex distributions of fibre orientation are considered, leading to an accurate representation of the actual reinforcement orientations. Thus, the coupled influence of strain rate and anisotropy of SFRC behaviour can be modelled. An experimental campaign is conducted in order to identify the material parameters used in the model. According to experimental observations, damage mechanisms, mainly matrix ductile damage and fibre-matrix decohesion occur during the material loading. These phenomenon are introduced in the constitutive model which is implemented in an explicit finite element code. The accuracy of the developed model is evaluated by comparison with experimental tests at various loading configurations and for a wide range of strain rates.

In order to fulfill the aforementioned objectives the work is structured according to the following major lines: A part is dedicated to the proposition of a modelling approach with the development and implementation of constitutive laws for short fibre reinforced thermoplastic material subjected to dynamic loadings. A second part is about the experimental investigations conducted in order to identify the material parameters, to microscopically characterise the fibres distribution of orientation and to characterise the composite behaviour under different loading configurations. A Final part is devoted to the modelling of failure mechanisms in SFRC as a progression of damage phenomena leading to composite's ultimate failure.

## Outlines of the report

The manuscript is structured around the most important issues to deal with when modelling and characterizing the composite behaviour until its ultimate failure. It is organized as follows:

- *Chapter 2* introduces general aspects related to the material under investigation and provides a background for the mechanical characterisation of short fibre composite thermoplastics. Most important contributions for the modelling of short fibre reinforced composites are reviewed throughout this chapter. Different approaches that have been developed will be presented and a bigger attention to the fundamental approaches on micromechanical modelling will be paid. Finally the chapter highlights the motivations of the modelling choices presented in this work.
- *Chapter 3* deals with the developed constitutive model. Firstly, the thermodynamic basis of the approach is presented. Then the different constitutive laws associated to the matrix, the fibres and the short-fibre-reinforced composite are presented for non damaged material.
- *Chapter 4* deals with the experimental procedure for the identification of the involved material parameters and the characterisation of the composite material behaviour. Tests and procedure for identification of matrix material parameters are first described. The composite microstructure is then analysed, in particular thanks to the characterisation of complex distributions of fibre orientation by micro-computed tomography. Finally the proposed constitutive model is validated by comparison between the simulation results and the experimental data.
- *Chapter 5* is devoted to the modelling of damage mechanisms and ultimate failure of short fibre reinforced composites. Damage modelling is performed by associating an anisotropic ductile damage model to the matrix material and an interfacial damage model to fibre-matrix interface. Identification of the involved parameters is based on experimental tests realised on a SFRC. Finally, a fracture criteria is defined as a threshold of the predicted damage amount that a SFRC can withstand.
- Finally *Chapter 6* gives a conclusion of this work. The manuscript ends with perspectives for further study and some possibilities of improvements of the current work.



# *State of art of short fibre reinforced composites behaviour and modelling*

---

Short fibre reinforced composite materials (SFRC) are attractive for many industrial applications thanks to interesting mechanical and physical properties. Their superior mechanical properties in combination with low manufacturing cost are the main reasons behind their wide use and study. A wide range of investigations have been done in order to assess the potential and limitations of such materials in different loadings or environmental conditions, for numerous combinations of matrix and reinforcement materials. It was widely reported that main factors governing the physical and mechanical behaviour of SFRC are the properties of the individual constituents, fibre volume fraction, fibre orientation and length distributions and fibre-matrix interface strength.

The present chapter provides a background for general aspects and mechanical characterisation of short fibre composite materials. Through this chapter different experimental investigations and numerical approaches that have been developed by numerous researchers through the years will be presented. The chapter begins by discussing the main aspects and manufacturing processes with the major factors affecting the behaviour of short fibre composite. It continues by addressing the major results about the characterisation of the material's behaviour and then the fundamental numerical methods and theoretical approaches on micromechanical analytical modelling.

## **2.1 Generalities about short-fibre reinforced thermoplastics**

The significant improvements induced by adding fibres to thermoplastics in mechanical (stiffness, strength, toughness, resistance to creep, dimensional stability) and thermal (maximum service temperature) properties can be obtained without sacrificing the mouldability of the materials for SFRC. Conventional extrusion compounding and injection moulding machines designed for



unfilled thermoplastics, allowing rapid production of components with complex shapes, can then be used for SFRC [2]. In fact, common commercial grades of fibre reinforced thermoplastics can be processed at temperature, pressure, injection rate and cycle duration similar to those used to process unfilled thermoplastics. There are, however, differences between processing of fibre reinforced materials and unfilled thermoplastics that must be heeded. For instance, the fibre length degradation, which affects fibre aspect ratio, depends on tools and operating conditions [3].

Most influencing process parameters are flow speed and temperature and mould geometry [4, 5]. Other crucial properties of SFRC, such as fibres' distribution of orientation, are strongly dependent on manufacturing process. In addition, as reported for instance by Milewski [6] and Fu et al [7], increasing the volume fraction of fibres increases the probability of fibre to fibre interaction and then has a direct consequence on the fibre length, aspect ratio and orientation. In the following of this section, attention is paid to morphological aspects of SFRC and then to the fibre orientation as main source of anisotropy in the material.

### 2.1.1 Microstructure of short fibre reinforced composites

The macroscopic behaviour of short fibre reinforced composites is directly dependent on its constituents properties (i.e. fibres and matrix material properties), fibre/matrix interfacial properties and the reinforcement configuration. Among microstructural characteristics of SFRC the reinforcement configuration and properties are of great importance (i.e. fibre volume fraction, fibre orientation and length distributions, interfacial properties,...). The fibre volume fraction is usually fairly controlled, though local variations of fibre density (i.e. significantly higher and lower fibre content than the average value) may occur. There are, however, very few reports of measurements of this in the literature. In contrast, short fibre orientation is difficult to control (see Figure 2.3) and constitutes a process-dependent property that greatly influences the overall properties of the composite material.

Tool geometry and processing conditions are beyond process parameters to be manipulated specifically to control the fibre orientation distribution in the product. Attempts to control distributions of fibre orientation have been proposed by developing models for the dependence of fibre orientation distribution on processing conditions [9, 10]. A study was performed by Goettler [11] on fibre orientation during injection flow in order to optimise the composite directional strength and stiffness using a kinematic model. Akay and Barkley [12] have treated process parameters, fibre orientation distribution and mechanical properties as inter-related variables for injection-moulded short-glass fibre-reinforced polypropylene. They have shown that an increase in melt and mould

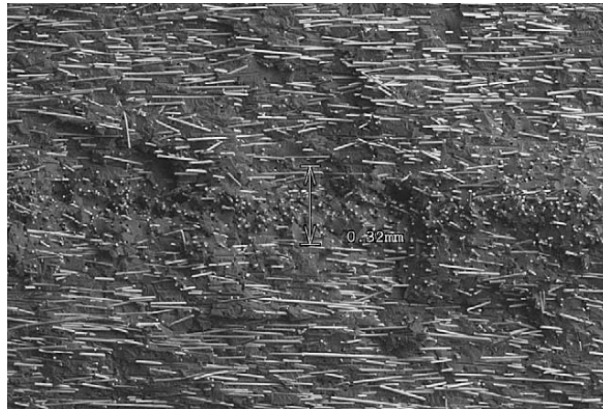


Figure 2.1: Example of a microstructure: Polyamide 6.6 matrix reinforced with short glass fibres [8]

temperature and injection speed cause a significant decrease in short fibre alignment along the injection flow direction. In their study they also investigated the gradual change in the preferential fibre alignment in the mouldings. In fact, an injection moulded short fibre composite tends to have a stratified morphology in which the most prominent feature is the variation of fibre orientation distribution through the thickness. This layered structure is mainly induced by differential solidification, shearing and melt-flow or fountain-flow patterns effect (including divergence, convergence and shape of the flow fronts). A schematic representation of the fountain flow process is given in Figure 2.2. Interactions with neighbouring fibres and/or with mould wall are also reported to be of significant influence on the fibre alignment during melt-flow process. Base on microscopic observation, it has been reported that injection moulded samples exhibit a skin/shell/core/shell/skin organisation through thickness with different fibre orientation [12, 13].

The fibres in the shell regions are predominantly aligned along the flow direction due to high shearing near the mould wall surface. The core region consists, however, on predominantly transverse fibre alignment, owing to low shearing and high extensional flow. Finally, the fibres in skin regions, i.e. in areas adjacent to the walls of the mould cavity, adopt random orientation because they are rapidly freed in contact with comparatively cold walls during the fountain flow process [14, 15].

A study on the layered structure of short fibre reinforced polymers was recently presented by Thi [13], where it is found that layer proportions, i.e. layers relative thickness, are globally dependent on the process parameters (e.g. mould geometry, matrix material viscosity, injection speed, fibre

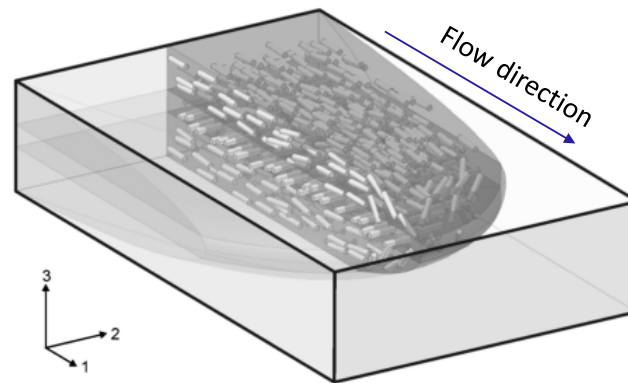


Figure 2.2: Melt flow profile of short fibre reinforced polymer within mould cavity during filling.

content and aspect ratio,...). According to the work presented by Akay and Barkley [12], fibre orientation within injection moulded SFRC has a direct effect on tensile properties of the composite. They examined the evolution of the elastic moduli and ultimate tensile strength values and found that they are reduced when increasing the core relative thickness.

Given the complexity of SFRC microstructure and its crucial effect on the mechanical behaviour, a number of researchers have been interested in developing accurate techniques for measuring the fibre orientation in injection-molded parts formed from short-fibre composite.

### 2.1.2 Techniques of orientation measurement

Measuring fibre orientations started first by acquiring data either from polished sections by reflective microscopy or from microtomed samples by transmission optical microscopy or contact microradiography. Experimental results in this category are reported in [4, 16, 17, 18].

Fischer and Eyerer [19], Bay and Tucker [20], Zhu et al [21] and Hine et al [22] measured short-fibre orientations by examining polished cross-sections by optical reflective microscopy. In these works, they considered the ellipse-shaped intersection of a fibre with a plane to calculate the misalignment angle of the fibres axis. Later, Zak [23] proposed a three-dimensional measurement of distribution of fibre orientation by combining data from two consecutive closely spaced cross-sections of a specimen. This method was presented as an unbiased distribution data for the near-zero misalignment angles and a solution to the orientation duality problem. Eberhardt and Clarke [24] and Clarke et al [25, 26] presented automated techniques of the use of confocal laser scanning microscopy for the measurement of 3D distributions of orientation which enables semi-

transparent materials to be optically sectioned for a given distance from the sample's surface. Compared to conventional optical and electron microscopies, acoustic, and scanning tunneling microscopies, x-ray microtomography offers unique imaging capabilities, for instance the possibility of three-dimensional scanning. A comparison between optical and tomographic methods is performed by Bernasconi et al [27]. The system consists of a high-resolution imaging x-ray detector and high-speed tomographic image reconstruction procedures together with a collimated monochromatic area-filling x-ray beam. Tomography scanning technique is based on mathematical analysis that consists on the reconstruction of a function from values of its line integrals [28]. Transmission tomography implements the needed mathematics to create non-destructive cross-sectional images of the internal structure of a sample from measurement and analysis of penetrating radiation directed through the sample in multiple coplanar rays [29]. Shen et al [30] used micro-CT to observe and measure the fibre orientation in a 5 wt% short-glass-fibre-reinforced phenolic foam. They reconstructed the 3D fibre distribution of the foam from the obtained micro-CT images, and then they imported this 3D quantitative information into the software program Auto-CAD and used it to analyze the spatial length and orientation of the individual fibres. A global characterisation of fibre orientation distribution by micro-CT was proposed by Nguyen Thi et al [31] for high fibre content.

In this work, x-ray microtomography will be used for the characterisation of the reinforcement configuration in a short-glass-fibre-reinforced polypropylene at microscopic scale.

## 2.2 Behaviour of thermoplastic matrices

In this thesis work, composites under study are polymer reinforced composites. General aspects about polymeric behaviour and, more precisely, thermoplastic polymers are reviewed in the following paragraphs.

Polymer materials result of the polymerisation of small size organic molecules, called monomers. The structure of the formed macromolecules differs and give rise to different architectures. Two main types can be distinguished according to these architectures; thermoset and thermoplastic polymers. Attention will be paid here to thermoplastics as widely used polymers in the case of short fibre reinforced polymers. The molecular structure of thermoplastic polymers is either crystalline (organized, in which the chains are aligned), amorphous (not organised, e.g. Polystyrene (PS) and Polycarbonate (PC)) or semi-crystalline, where the two structures coexist and the corresponding polymer is characterised by a degree of crystallinity (e.g. Polyethylene (PE) and Polypropylene

(PP)) [32].

Many studies have been dedicated to the characterisation of thermoplastic behaviour when subjected to a wide range of loading conditions. The rate dependency is one of the main features of semi-crystalline thermoplastics that becomes more crucial when dealing with high speed applications, in particular. Zhang and Moore [33] have shown the significant increase in the response of High Density Polyethylene (HDPE) as the strain rate hardening is varied.

For the global behaviour of thermoplastic polymers usually a distinction is made between the linear elastic and/or linear viscoelastic regime at small strains, the nonlinear viscoelastic response at moderate strains and the viscoplastic behaviour at rather large strains. The modeling of the mechanical response of these polymers can be a difficult task because the numerical model representing material's behaviour must account for all of these deformation regimes. In the literature, these polymer materials are usually described and modelled as viscoelastic (VE), elasto-viscoplastic (EVP) or viscoelastic-viscoplastic (VE-VP). The difference between these classes of behaviour can be illustrated by a uniaxial tension test which comprises a monotonic loading phase followed by unloading to zero stress. In the case of viscoelasticity, the response is rate dependent in both phases, which implies that the stress-strain slope (Young's modulus) increases with increasing strain rate. Upon unloading to zero stress, the material retrieves its initial zero stress state, not instantly, after a sufficient waiting time. A complete description of viscoelastic behaviour is given by Christensen [34], Findley [35] and Salençon [36]. An elasto-viscoplastic polymer will behave differently during the same uniaxial loading/unloading test. Below an initial yield stress, the response is rate-independent linear elastic. Beyond it the stress-strain response is both nonlinear and rate-dependent, with the stress increasing with the strain rate. After unloading to zero stress, there remains an irreversible strain which decreases but does not disappear even after a long time. For a description of EVP models, one can refer to Perzyna [37] and Lemaitre and Chaboche [38]. A thermoplastic polymer can also behave as a combination of these two types of behaviour. In fact, when the response is rate dependent below and above the yield stress, the overall behaviour is classified as viscoelastic-viscoplastic. This combination has got a physical explanation in the case of semi-crystalline thermoplastics. Indeed, several micromechanical observations tend to show that crystalline lamellae and amorphous chains are assembled in series and obey VE and VP behaviour, respectively [39]. Chaboche [40] considered this case to develop a combined constitutive model for polymeric materials. A more thorough study of viscoelastic-viscoplastic behaviour modelling will be further addressed in the manuscript. In addition to rate dependency, thermoplastics can show a strong dependency to temperature, as demonstrated by Karger-Kocsis and Friedrech [41]. The

later property is however not in the scope of this work.

Other features can characterise the behaviour of thermoplastics when subjected to a wide range of loading conditions. For instance they can exhibit non isochoric plastic flow and pressure dependent behaviour. Non-isochoric plastic flow of polymers has been studied by various authors. The volumetric strain of polyethylene terephthalate (PET) and high-impact polystyrene (HIPS) has been measured by G'Sell [42] using a video-controlled testing where the longitudinal and transverse strains are measured by tracking markers positioned on the specimens. In the same way, the volume strain measurement for polypropylene (PP) material was quantified by G'Sell et al [43] and Jerabek et al [44]. From the obtained results, authors concluded that the plastic deformation should not be considered as an isochoric process. The effect of hydrostatic pressure on the behaviour and for instance on the yield stress of polymers has been widely studied as well (e.g., Wang and Pan [45]; Khan and Farrokh [46]). It was reported that this is caused by the structure of the polymer chains in thermoplastic polymers. Under a load, a specific energy is needed to move a chain segment or side chain. The flexibility of chains requires a certain free volume, which is smaller at higher hydrostatic pressures. Thereby, the inner molecular forces have a stronger effect. Thus, the molecular flexibility is restricted and is affected by the applied hydrostatic pressure. Sauer and Pae [47] have highlighted the particular dependency to hydrostatic pressure in semi-crystalline polypropylene.

As stated in introduction, polymeric materials often serves as the binder in composite materials when reinforced by stiff inclusions (particles, fibres (long or short), platelets, etc...). In this case, the complexity of their behaviour is enhanced by the presence of fillers with complex properties, in terms of geometry, orientation. The following section highlights the main aspects in the behaviour of reinforced polymers and precisely in the case of short fibre reinforced thermoplastics.

### **2.3 Behaviour of short fibre reinforced composites**

The mechanical behaviour of short fibre reinforced composites can be complex because of the complexity of the polymeric matrix behaviour and of the reinforcement characteristics, for instance in terms of distribution of orientation and length. Experimental investigations exist in the literature for the characterisation of short fibre reinforced composites. An extended study on mechanical and thermal properties of short fibre composite materials has been presented by Thomason [48]. The author investigates the influence of fibre length and volume fraction of a composite consisting of short glass fibres embedded in a polypropylene matrix. Results show that

stiffness increases almost linearly with respect to fibre concentration up to a volume fraction of 60%. A similar dependency between fibre length and stiffness was observed. Composites with higher fibre content show lower stiffness which may be due to fibre packing and out-of-plane orientation tendency. Moreover, when applications with severe loading conditions, such as crash or impact, are targeted, it is crucial to characterise the dependency of the material to strain rate. As thermoplastic polymers, such as polypropylene (PP) exhibit a viscoelastic and/or viscoplastic behaviour, i.e. sensitive to strain rate, the mechanical behaviour of composite material is likely to be directly impacted by this property of matrix material. This strain rate sensitivity is reported by Mouhmid et al. for a short-glass-fibre reinforced PA6,6 [49], Reis et al. for a short-glass-fibre reinforced polyurethane [50] and Schofig et al. [51] for glass-fibre-reinforced polypropylene and polybutene-1. In the same way Fitoussi et al. proved the sensitivity of a glass-fibre-reinforced ethylene-propylene copolymer to strain rate by tensile tests performed in the injection flow direction of the composite [52] (Figure 2.3). In such materials, where the complexity of matrix behaviour can be added to that of the reinforcement properties, the strain rate sensitivity has to be associated to the anisotropy induced by the fibres. Therefore, the coupled effect of strain rate dependency and fibre orientation has to be characterised in the case of SFRC. There is however a lack of data concerning this issue. A work is presented by Krivachy et al [53] on the characterisation of the mechanical behaviour of short fibre thermoplastic (Crastin: Polybutylene-terephthalat and Acrylnitril/Styrol/Acrylester with 20 weight % short-glass fibres) under compression, shear and tension loadings at different velocities. Results show that the material appeared to be strongly anisotropic and strain rate dependent, with additional influence of hydrostatic pressure on plasticity and failure behaviour. The study was however limited to an orthotropic assimilation of the material and no coupled effect of anisotropy and strain rate sensitivity was directly studied. Finally, the behaviour of short fibre reinforced composites can be considerably affected by different coexisting damage phenomena. It is reported in literature that the most important are fibre-matrix interfacial debonding and matrix anisotropic ductile damage [54, 55]. A more particular attention is paid to the development of damage phenomena within a short fibre reinforced composite in the chapter 4 of this report.

## 2.4 Modelling of short fibre reinforced composites

Computation of macroscopic stress-strain relationship of SFRC is treated in the literature mainly on the basis of micro-mechanical approaches. For these approaches, the macroscopic response of



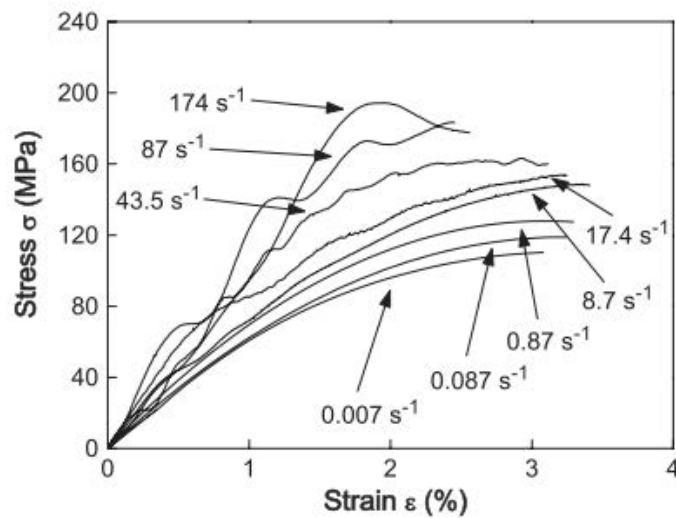


Figure 2.3: Stress-strain diagrams for PP with 40 wt.% glass fibres at different strain rates [52]

the heterogeneous material depends on the properties of its constituents as well as on their spatial distribution, i.e., the microstructure configuration. Among them one may cite: direct finite element (FE) analysis on representative cells of the microstructure [56], mean-field homogenization (MFH) techniques and the asymptotic or mathematical theory of homogenization [57, 58].

The mechanical behaviour modelling of a short fibre composite was first addressed by the implementation of micromechanical models. Innovative works were released first in 1889 by Voigt and in 1929 by Reuss. Both models were reference works since the earlier developed models were mainly based on the Voigt and Reuss models, known later as the Rule of Mixtures (RoM) and the Inverse Rule of Mixtures (IRoM), respectively. A modification of the Rule of Mixture was later proposed in the pioneering work by Cox in 1952 [59] based on stress distribution along a fibre using the shear lag model. It consisted on modifying the Rule of Mixture by introducing a fibre length factor. The shear lag model uses microstructural parameters such as fibre length and fibre to fibre distance in order to calculate macroscopic effective properties.

Later, the problem of multi-phases materials started to be differently and more thoroughly addressed. The concept of phase concentration tensor of stress and strain was first introduced by Hill [60, 61]. In his work, Hill treated the calculation of macroscopic elastic properties by taking into account the relative concentration and geometry of inclusions. Inclusions are assumed to be aligned ellipses and to have the same elastic properties as that of short fibres. The method is based on the solution of



the auxiliary elastic problem involving a uniformly loaded infinite mass containing an ellipsoidal inhomogeneity.

This concept was originally proposed by Eshelby in 1957 by analysing the heterogeneities of stress and strain fields caused by an ellipsoidal inclusion embedded in an infinite matrix. The analysis is based on a four steps virtual experiment, where the infinite matrix is subjected to a far field strain. The strain and stress perturbations induced by the presence of the inclusion are treated by an elastic accommodation between the inclusion and its surroundings [62].

The common process of homogenization methods can be summarized in two steps. Firstly, a local problem of a single inclusion has to be solved in order to obtain the local response and secondly a process of averaging of the local behaviour to obtain the global response takes place. The assumption of non-interaction between inhomogeneities is considered to be valid in case of low volume fraction of reinforcement. However, industrial applications of short fibre composites generally demands relatively high fibre volume fraction, as a consequence this assumption is rarely respected. Therefore, different theories have been developed to take into account such interactions in the stress/strain fields. One of the most used homogenisation schemes is the model proposed by Mori and Tanaka [63]. Similarly, The dilute diffusion model and the self-consistent model have been developed, respectively, for the cases of low and high concentration of fillers. The direct use of the homogenization methods was limited to linear elastic composites. Its extension to different and more complex types of behaviour was first dealt with in the case of linear viscoelastic composites. It consisted on applying the homogenisation schemes to an equivalent linear isothermal elastic representation of the viscoelastic behaviour, but in Laplace-Carson space. Using the correspondance principle, constitutive equations are recast in a linear elastic form into the Laplace domain [64, 65]. After homogenisation in the Laplace space, the effective properties are found by the inverse transform. The case of non-linear behaviour was more complicated when dealing with homogenizations schemes. Some formulations were proposed to tackle the problem of inelastic composites by linearizing the constitutive laws and retrieving a linear elastic-like representation of the model. Two of the most used linearization methods are secant [66, 67] and incremental methods [68].

In the same way elasto-viscoplastic behaviour was dealt with. Masson and Zaoui [69] and Pierard and Doghri [70] used the correspondance principle to model linearised elasto-viscoplastic composites. Ju [71] and Doghri [72] worked on the linearization of time-discretized constitutive equations. Later, the affine [73, 74, 75, 76] and the incrementally affine formulations [77] where the proposal leads to thermo-elastic-like relations in the Laplace-Carson (L-C) and the time do-

mains, respectively, have been proposed.

The case of viscoelastic-viscoplastic composites is more complicated and there are few available models. Indeed, compared to viscoelastic or elasto-(visco) plastic behaviour modelling, the modelling of viscoelastic-viscoplastic (VE-VP) short-fibre reinforced composites has received little attention up to now and even less in case of relatively complex microstructure. A micromechanical model was proposed by Kim and Muliana [78] for predicting a VE-VP response of particle reinforced composites. The studied composite consists of linear elastic spherical particles dispersed in a homogeneous VE-VP matrix. The proposed model is actually an extension of a previously proposed micromechanical model by Muliana and Kim [78] for nonlinear VE composites. It assumes a composite microstructure with randomly distributed particles, idealized by periodically distributed cubic particles in a matrix medium. A unit-cell micromodel is then generated with this microstructure. The cells and subcells homogenization method is developed in terms of the average strains and stresses in the subcells. Good results were obtained with this model for low volume fractions of particles, i.e. when interactions between particles can be neglected. Aboudi [79] proposed a micromechanical model for multiphase materials in which matrix and reinforcements phases can both behave as a VE-VP material. The model is based on an asymptotic homogenization technique of composite materials with a periodic microstructure. The response of the developed model depends highly on the complexity of composite's microstructure.

All the aforementioned models are micromechanical models. The common base of the presented theoretical work in micromechanical aspects is the idealisation of the materials morphology, based on assumptions like equal distances between fibres, the uniform length and orientation, etc. Yet, a closer examination of material's morphology can give rise to a more realistic representation of the microstructure of the composite taking into account various geometric parameters and allows to develop more accurate material behaviour laws which can be evaluated through a computational approach.

Works dealing with numerical models for short fibre composites considering microstructures or micromechanical properties have been proposed in the literature. Hine [80] has proposed finite element model for the prediction of elastic properties of composites with aligned short fibres of uniform length. Representations of the microstructure are realised by geometric periodicity. Pan [81] also studied the effect of random fibre orientation on the macroscopic effective stiffness properties of composite. Through the paper, the author underlines the difficulty of creating models that represent the geometry at micro-level for high volume fraction. A method of generating three dimensional, random fibrous realisations is presented which is based on the Random Sequential

Absorption (RSA) algorithm. Fibres were simulated as sphere-cylinders, which are cylinders with a hemisphere attached to both ends. LRSM is a method proposed by Ianita and Weitsmann [82] and is a windowing approach able to rapidly evaluate a large number of fibre arrangements for in-plane orientation. Calculations of effective properties are based on the classical laminate theory. The method has the ability to measure the statistical inhomogeneity in the material by information derived from local region. Berger et al [83] investigates the elastic constants of short fibre composite materials using a three dimensional RVE. Fibres were simulated as cylinders for the case of random orientation and aligned fibres. The periodic microstructure was created using the RSA method. The author discusses the limitation of the fibre volume fraction with this method.

As it was explained by Kari et al. [84] the main advantage of analysing SFRC using numerical models is the ability to approach, to a satisfactory degree, the real micro-structure of the material. The author evaluates the effective mechanical properties of a randomly distributed short fibre composite, for relatively high fibre volume fraction (40%).

Although various contributions have been proposed to model short fibre reinforced composites, there are still remarkable efforts to do in order to attain a satisfying accuracy and efficiency of modelling. In fact, handling simultaneously the two most important features about the composite behaviour, i.e. complex microstructure and behaviour laws is still a field of study. Numerical models can be limited by the heterogeneity of the reinforcement and its properties and specially by the time consuming computation. Moreover, in addition to limitations dealing with constituents' behaviour laws, homogenization methods, based on inclusion-type problems can become very difficult to handle in the case of reinforcement with non-aligned short fibres. To overcome this difficulty, Doghri and Tinel [85] have developed a double step homogenisation procedure. In a first step, a two-phase "pseudo-grain" constituted of the matrix material reinforced with identical and aligned fibres is homogenised. The second step then consists in the homogenisation of all pseudo-grains to compute mechanical properties at the representative elementary volume scale, taking all orientations of the fibres into account.

All these contributions show that the difficulty of implementing homogenisation based models for SFRC increases significantly as the behaviour of constituents and fibres orientation distribution become more complex. The main drawback of this approach is its numerical cost related to the inversion of the Laplace transform. Alternative approaches need then to be developed in order to present a unified model, where the materials complexity can be efficiently taken into account.

## 2.5 Conclusion

In this chapter, most important mechanical and microstructural properties of short-fibre reinforced thermoplastics are presented with a highlight on short fibre orientation. The most important existing results about the polymeric materials, and more precisely thermoplastics, and mechanical behaviour of short fibre reinforced composites are presented. This literature survey concerns, in a second part, the main theoretical models developed through the years. Micromechanical models provide a useful tool for the prediction of material mechanical behaviour. There is, however, a lack of contributions where an accurate representation of the microstructure is represented while the complexity of the materials behaviour is taken into account. Indeed, the complexity of the composite microstructure, constituents behaviour, and interactions between them, are main features to be addressed for an efficient modelling of the material behaviour. Considering the case of extreme loading, when additional phenomena can intervene (i.e. damage mechanisms), and the high cost of the available approaches in terms of computation time, it can be concluded that effort is still needed for an efficient and complete modelling that goes beyond the limits of the existing models. The presented literature survey is also an indicator that a more simple and holistic approach can be proposed as an alternative to the computation time costly available approaches. It is therefore very interesting to consider models of composite behaviour at an intermediate scale between very complex homogenisation approaches and often inaccurate purely phenomenological descriptions. Consequently, in this thesis, an alternative modelling based on the additive decomposition of the composite thermodynamic potential is considered. The composite is seen as the assembly of a matrix medium and several media of embedded fibres. The deformation gradient, applied to the composite as a whole, and its multiplicative decomposition implicitly link the media. Nedjar [87] used this approach for viscoelastic materials, assuming that fibres carry load only in tension. Klinkel et al. [88] showed it can be theoretically applied to non-linear elasto-plastic behaviour for the matrix and the fibres but without a practical application of their implementations in the analysis of a short-fibre-reinforced material's behaviour. More recently, Notta-Cuvier et al. [86] used this approach to deal with rate-independent elastoplastic SFRC behaviour. A main asset of this approach is its adaptability to all kinds of reinforcement characteristics (orientation and geometrical properties) and matrix behaviour while keeping the implementation relatively easy. The present work treats the modelling of SFRC's behaviour when subjected to severe loading conditions, in particular at high strain rates. To this end, the matrix behaviour is modelled using a coupled VE-VP scheme. Complex distributions of fibre orientation are considered, leading to an

accurate representation of the actual reinforcement orientations so that the coupled influence of strain rate and anisotropy of SFRC behaviour can be modelled.

## *Constitutive model for short-fibre reinforced composites*

---

It is reported from the existing contributions, described in chapter 2, that mechanical behaviour modelling of short-fibre reinforced composites (SFRC) becomes very difficult when dealing with complex behaviour of the constituents (e.g. non-linear time-rate dependent behaviour) and/or complex reinforcement configuration (e.g. complex fibre orientation). To the author's knowledge, no direct or practical application is presented today for the modelling of fibre reinforced strain rate dependent matrix with distributions of fibre orientation. Given the issues raised in previously reported works, it can be very interesting to consider models of composite behaviour at an intermediate scale between generally limited and inaccurate phenomenological descriptions and complex homogenization approaches. Following this line, we focus in this work on an alternative approach originally proposed by Nedjar [87] and Klinkel et al. [88] that consists in assimilating the composite to an assembly of a matrix medium with several media of embedded fibres. One of main assets of this approach is its adaptability to all kinds of behaviour of matrix and fibre media while keeping a relative simplicity of implementation. Recently, this approach has been used by Notta-Cuvier et al. [54, 86] for the modelling of non-linear pressure dependent and damageable behaviour of SFRC. In the current work, we consider the later approach to address the modelling of SFRC behaviour when subjected to severe loading conditions, and more precisely, at high strain rates (e.g. cases of crash, impact...). Moreover, the division of the short fibres into several families having their own mechanical and geometrical properties and orientation allows easy consideration of all types of reinforcement characteristics, including distributed or random orientations. In order to reproduce the strain rate dependency of the matrix material, a coupled viscoelastic-viscoplastic (VE-VP) model is implemented in the framework of non-associated viscoplasticity. The case of distributed orientations is considered for the reinforcing fibres with load transmission at fibre/matrix interface described by an adapted shear-lag model

[89].

This chapter presents, in a first part, the developed constitutive laws for matrix, fibres, load transfer and composite mechanical response. The implementation of those laws in an explicit temporal integration scheme and its validation are subsequently presented.

### 3.1 Presentation of the approach for SFRC modelling

In the current modelling, the composite is seen as the assembly of a matrix medium and several media of embedded fibres. The deformation gradient, applied to the composite as a whole, and its additive decomposition implicitly link the media, combined with the assumption of thermodynamic potentials (elastic, plastic, viscoelastic..., as relevant) proper to each constituent. The reinforced composite material is formed of short fibres assumed to be uniformly dispersed in a thermoplastic matrix. Fibres with the same orientation, geometrical characteristics and mechanical behaviour are grouped into a same family. Each fibre family - or medium - is therefore characterised by its own orientation vector, expressed in a global coordinate system, i.e. linked to the matrix, and volume fraction, computed according to actual fibre distribution of orientations and geometrical characteristics. It can be noted that in the present work, all fibres will be assumed to have the same geometrical characteristics but distributions of fibre length could be considered, for instance. A fundamental assumption is that fibres carry load only in their direction of orientation. Each medium of fibres is therefore assumed to behave as one-dimensional and the deformation gradient tensor applied to a given fibre family is the projection of the global deformation gradient tensor, which is applied to the composite, along fibre orientation. It is worth noticing that the distribution of the short fibres into several families allows to model all types of fibres orientation, including distributed and random orientations, in a simple way. The fibres' behaviour is assumed to remain linear elastic. Indeed, it is very likely that the composite fails before the stress applied to the fibres reaches their initial yield stress, because of ductile damage of matrix material and/or fibres debonding, for example. So, extending the implementation to irreversible fibre strain seems irrelevant. The strain-rate dependency of the SFRC is introduced through a coupled viscoelastic-viscoplastic constitutive model associated to the matrix material response. The mechanical behaviour of each medium is solved separately before composite's behaviour is established using an additive decomposition of the specific free energy potential, as described in the next sections.

## 3.2 Constitutive laws of SFRC behaviour model

### 3.2.1 Viscoelastic-viscoplastic behaviour model of thermoplastic matrix

One of the challenges when modelling SFRC is to introduce an accurate modelling of the constitutive behaviour of the polymeric matrix, for instance thermoplastic matrix, that takes all behaviour specificities (e.g. dependency to strain-rate and temperature, non-isochoric hardening, ductile damage) into account. The mechanical response of a thermoplastic polymer strongly depends on the loading conditions, especially if it is likely to be subjected to extreme operating ones (e.g. high loading speed). In the two last decades, many constitutive models, following physical and phenomenological approaches, have been developed for the behaviour modelling of polymers. The viscoelastic and viscoplastic behaviour of thermoplastics have been modelled using multi-scale approaches, as presented in [90, 91, 92]. In these models, representative volume elements are considered as aggregates of two-phase composite inclusions. Each inclusion consists on a stack of parallel crystalline lamellae in the amorphous phase. The physically-based theories are attractive in the modelling of polymers macroscopic behaviour as it takes the micro-structural phenomena into account. However, the identification of the associated material parameters is complex and cannot be done by simple experimental tests (e.g., tension or compression tests ...). In the case of phenomenologically-based approaches, viscoelastic-viscoplastic rheological models have been proposed based on the connection of Newton, Hooke and Slider elements. Khan et al. [93] have proposed a phenomenological model to describe the time and temperature dependency of thermoplastics. However, in these models an important number of parameters are required to obtain good predictions. Another formalism, coming within the framework of continuum mechanics, considers that the physical discontinuities at the micro-structural level are globally described, i.e. at the scale of a homogenised bulk element of the material. Chaboche [94] has discussed the ability of classic thermodynamics of irreversible processes to describe the behaviour of polymers and proposed a viscoelastic model based on an extension of the “Generalised Standard Material” concept. Some authors have modelled the behaviour of polymeric materials as nonlinear viscoelastic, for instance, by using a combination of linear and/or nonlinear dashpots and springs [93, 95, 96]. Strain-rate dependency of thermoplastics have also been described by Elasto-Viscoplastic (E-VP) constitutive models as presented by Regrain et al. [97], Drozdov et al. [98] and Balieu et al. [99]. More recently, elasto-viscoplastic constitutive models based on viscous overstress (VBO) and derived from the unified state variable theory for metallic materials have been extended to polymer modelling by Krempl and Khan [100], Khan and Yeakle [101] and Colak [102]. Finally, for a more reliable



and complete modelling of the strain rate dependency in both parts of the behaviour, i.e. elastic and inelastic, coupled viscoelastic-viscoplastic (VE-VP) laws have been proposed by Ayoub et al [103], Khan and Zhang [104] and Miled et al [105].

This part of the work is devoted to the modelling of strain rate dependency of SFRC by introducing a coupled viscoelastic-viscoplastic law for the matrix behaviour prediction. The VE-VP model of the homogeneous thermoplastic polymer is written under small strain hypothesis and isothermal conditions. The model is developed within the formalism of the thermodynamics of irreversible processes based on the works proposed by Christensen [34] and Christensen and Naghdi [106]. It is worth mentioning that the undamaged state of the matrix material is considered in this part, i.e. damage development is not taken into account at this level of the modelling.

### 3.2.1.1 Thermodynamic formulation

A coupled viscoelastic-viscoplastic model is introduced here in the framework of thermodynamics of irreversible processes for the description of thermodynamic matrix behaviour. A non-associated viscoplasticity formulation is used where a pressure dependent yield surface is introduced. The theory of Generalised Standard Materials, where constitutive equations derive from two different potentials, is adopted. As presented by Lemaitre and Chaboche [38], the first potential designates the material free energy and the second one its dissipation function. The formulation is restricted to small strain and isothermal conditions.

Based on the first and second laws of thermodynamics, the Clausius-Duhem inequality postulates that the change in entropy is positive or null [34] and leads, when assuming isothermal conditions, to the inequality:

$$\sigma_M : \dot{\varepsilon} - \rho_M \dot{\phi}_M \geq 0 \quad (3.1)$$

$\rho_M$  is the density of the matrix material and  $\dot{\phi}_M$  is the time derivative of its Helmholtz free energy.  $\sigma_M$  and  $\dot{\varepsilon}$  are, respectively, the matrix Cauchy stress tensor and time derivative of the strain tensor. Under isothermal conditions, the total strain,  $\varepsilon$ , is the observable state variable. Irreversible phenomena are described by the internal state variables, as defined later.

The derivation of the state laws is based on the decomposition of the total strain into two parts: a viscoelastic (VE) strain,  $\varepsilon^{ve}$ , and a viscoplastic (VP) one,  $\varepsilon^{vp}$ , [99, 107, 108] so that:

$$\varepsilon = \varepsilon^{ve} + \varepsilon^{vp} \quad (3.2)$$

It is worth noting that this decomposition is valid in the framework of small deformation only, which is consistent with the composite behaviour modelling. Indeed, although unreinforced polymeric matrix can exhibit high level of deformation, strain at break of short-fibre reinforced matrix generally does not exceed a few percent (as subsequently highlighted in the experimental investigation). Based on this split, it is assumed that the Helmholtz free energy can be decomposed into a VE part,  $\phi_M^{ve}$ , and a VP part,  $\phi_M^{vp}$ , representing stored energies due to, respectively, the viscoelastic response and the material hardening [105, 38, 109]. Then:

$$\phi_M = \phi_M^{ve} + \phi_M^{vp} \quad (3.3)$$

A representation of the VE part of the free energy is given by Christensen and Naghdi [106] in terms of linear and quadratic functionals of temperature and strain tensor components for linear VE solids. Using their results in the case of isothermal conditions, an expression of  $\phi_M^{ve}$  as a functional of  $\varepsilon_{ij}^{ve}$  is given by:

$$\rho_M \phi_M^{ve} = \frac{1}{2} \int_{-\infty}^t \int_{-\infty}^t F_{ijkl}(t - \tau, t - \zeta) \frac{\partial \varepsilon_{ij}^{ve}(\tau)}{\partial \tau} \frac{\partial \varepsilon_{kl}^{ve}(\zeta)}{\partial \zeta} d\tau d\zeta \quad (3.4)$$

where the Einstein summation convention is used. According to Christensen and Naghdi [106], the integrating function,  $F$ , verifies the following symmetry properties:

$$\begin{cases} F_{ijkl}(\zeta, \tau) = F_{ijkl}(\tau, \zeta) \\ F_{ijkl}(\zeta, \tau) = F_{jikl}(\zeta, \tau) = F_{ijlk}(\zeta, \tau) \end{cases} \quad (3.5)$$

and the following property:

$$F_{ijkl}(\tau, \zeta) = R_{ijkl}^{ve}(\tau + \zeta) \quad (3.6)$$

with  $R^{ve}$  the fourth-order relaxation tensor of the matrix material. Given these properties, the VE free energy can be expressed as follows:

$$\rho_M \phi_M^{ve} = \frac{1}{2} \int_{-\infty}^t \int_{-\infty}^t R_{ijkl}^{ve}(2t - \tau - \zeta) \frac{\partial \varepsilon_{ij}^{ve}(\tau)}{\partial \tau} \frac{\partial \varepsilon_{kl}^{ve}(\zeta)}{\partial \zeta} d\tau d\zeta \quad (3.7)$$

For the calculation of the free energy time derivative, the integral in Equation (3.7) is first rewritten as follows:

$$\rho_M \phi_M^{ve} = \int_{-\infty}^t \int_{-\infty}^t C(t, \tau, \zeta) d\tau d\zeta \quad (3.8)$$

where the function  $C$  is assumed to verify the differentiability and continuity conditions, so that the time derivative of the VE free energy can be expressed as:

$$\rho_M \dot{\phi}_M^{ve} = \int_{-\infty}^t \int_{-\infty}^t \frac{\partial C(t, \tau, \zeta)}{\partial t} d\tau d\zeta + \int_{-\infty}^t C(t, \tau, t) d\tau + \int_{-\infty}^t C(t, t, \zeta) d\zeta \quad (3.9)$$

Given the later expression,  $\rho_M \dot{\phi}_M^{ve}$  (3.7) is written as follows:

$$\begin{aligned} \rho_M \dot{\phi}_M^{ve} = & \left( \int_{-\infty}^t R_{ijkl}^{ve}(t - \zeta) \frac{\partial \varepsilon_{kl}^{ve}(\zeta)}{\partial \zeta} d\zeta \right) \dot{\varepsilon}_{ij}^{ve} + \\ & \frac{1}{2} \int_{-\infty}^t \int_{-\infty}^t \frac{\partial R_{ijkl}^{ve}}{\partial t} (2t - \tau - \zeta) \frac{\partial \varepsilon_{ij}^{ve}(\zeta)}{\partial \zeta} \frac{\partial \varepsilon_{kl}^{ve}(\tau)}{\partial \tau} d\tau d\zeta \end{aligned} \quad (3.10)$$

The expression of the VP part,  $\phi_M^{vp}$ , of the Helmholtz free energy (3.3) and its time derivative are expressed, according to Lemaitre and Chaboche [38], as:

$$\begin{aligned} \rho_M \phi_M^{vp}(\kappa(t)) &= \int_{-\infty}^{\kappa(t)} H(\zeta) d\zeta \\ \rho_M \dot{\phi}_M^{vp} &= H \dot{\kappa} \end{aligned} \quad (3.11)$$

where  $H$  and  $\kappa$  are the hardening thermodynamic force and its associated variable, respectively. Given the expressions (3.10) and (3.11), the time derivative of the total free energy becomes:

$$\begin{aligned} \rho_M \dot{\phi}_M = & \left( \int_{-\infty}^t R^{ve}(t - \zeta) : \frac{\partial \varepsilon^{ve}(\zeta)}{\partial \zeta} d\zeta \right) : \dot{\varepsilon}^{ve} + \\ & \frac{1}{2} \int_{-\infty}^t \int_{-\infty}^t \frac{\partial \varepsilon^{ve}(\tau)}{\partial \tau} : \frac{\partial R^{ve}}{\partial t} (2t - \tau - \zeta) : \frac{\partial \varepsilon^{ve}(\zeta)}{\partial \zeta} d\tau d\zeta + H \dot{\kappa} \end{aligned} \quad (3.12)$$

The Clausius-Duhem inequality is then expressed as follows:

$$\begin{aligned} & \left( \sigma_M - \int_{-\infty}^t R^{ve}(t - \tau) : \frac{\partial \varepsilon^{ve}(\tau)}{\partial \tau} d\tau \right) : \dot{\varepsilon}^{ve} + \sigma_M : \dot{\varepsilon}^{vp} \\ & - \frac{1}{2} \int_{-\infty}^t \int_{-\infty}^t \frac{\partial \varepsilon^{ve}(\zeta)}{\partial \zeta} : \frac{\partial R^{ve}}{\partial t} (2t - \tau - \zeta) : \frac{\partial \varepsilon^{ve}(\tau)}{\partial \tau} d\tau d\zeta - H \dot{\kappa} \geq 0 \end{aligned} \quad (3.13)$$

The dissipation inequality (3.13) has to be verified for any transformation, in particular for any value of the time derivative of viscoelastic strain. This implies that:

$$\sigma_M - \int_{-\infty}^t R^{ve}(t - \tau) : \frac{\partial \varepsilon^{ve}(\tau)}{\partial \tau} d\tau = 0 \quad (3.14)$$

and

$$\sigma_M : \dot{\varepsilon}^{vp} - \frac{1}{2} \int_{-\infty}^t \int_{-\infty}^t \frac{\partial \varepsilon^{ve}(\zeta)}{\partial \zeta} : \frac{\partial R^{ve}}{\partial t} (2t - \tau - \zeta) : \frac{\partial \varepsilon^{ve}(\tau)}{\partial \tau} d\tau d\zeta - H\dot{\kappa} \geq 0 \quad (3.15)$$

In addition, VE part of the dissipation term (3.15) have to be positive or null, so that:

$$-\frac{1}{2} \int_{-\infty}^t \int_{-\infty}^t \frac{\partial \varepsilon^{ve}(\zeta)}{\partial \zeta} : \frac{\partial R^{ve}}{\partial t} (2t - \tau - \zeta) : \frac{\partial \varepsilon^{ve}(\tau)}{\partial \tau} d\tau d\zeta \geq 0 \quad (3.16)$$

The state law verified by the matrix Cauchy stress tensor,  $\sigma_M$ , is finally given by:

$$\sigma_M = \int_0^t R^{ve}(t - \tau) : \frac{\partial \varepsilon^{ve}(\tau)}{\partial \tau} d\tau \quad (3.17)$$

### 3.2.1.2 Linear viscoelasticity

The viscoelastic fourth-order relaxation tensor of the matrix material is expressed based on the phenomenological Generalised Maxwell model. In that case, the unidimensional relaxation modulus modelled by an N-elements Generalised maxwell model is expressed in terms of Prony series as follows:

$$E(t) = E_\infty + \sum_{i=1}^N E_i(t) \quad (3.18)$$

where  $E_\infty$  is the long-term elastic modulus and the  $E_i, i \in \{1, \dots, N\}$ , are the time dependent moduli. Within this formalism, the fourth-order relaxation tensor of the matrix material is expressed as follows:

$$R^{ve}(t) = 2G(t)I^{dev} + 3K(t)I^{vol} \quad (3.19)$$

where  $I^{vol}$  and  $I^{dev}$  are volumetric and deviatoric operators defined by:  $I^{vol} = \frac{1}{3}I \otimes I$  and  $I^{dev} = I - I^{vol}$ , with  $I$  and  $I$  are respectively the second and the fourth order identity tensors.  $G(t)$  and  $K(t)$  are, respectively, shear and bulk relaxation functions and are expressed as:

$$\begin{cases} G(t) = G_\infty + \sum_{i=1}^N G_i \exp\left(-\frac{t}{\tau_i^d}\right) \\ K(t) = K_\infty + \sum_{i=1}^N K_i \exp\left(-\frac{t}{\tau_i^v}\right) \end{cases} \quad (3.20)$$

$\tau_i^d, \tau_i^v, G_i$  and  $K_i, i \in \{1, \dots, N\}$ , are respectively the deviatoric and volumetric relaxation times and their corresponding shear and bulk moduli.  $G_\infty$  and  $K_\infty$  are respectively the long-term shear and bulk moduli. According to Ohkami and Ichikawa [110], the deviatoric and volumetric relaxation

times are expressed as follows:

$$\tau_i^d = \frac{\eta_i^d}{G_i}, \quad \tau_i^v = \frac{\eta_i^v}{K_i} \quad \forall i \in \{1, \dots, N\} \quad (3.21)$$

where  $\eta_i^d$  and  $\eta_i^v$  are the deviatoric and volumetric viscous coefficients.

The VE strain tensor  $\varepsilon^{ve}(t)$  is divided, in the same way, into deviatoric,  $\varepsilon_{dev}^{ve}(t)$ , and dilatational,  $\varepsilon_H^{ve}(t)$ , parts:

$$\varepsilon^{ve}(t) = \varepsilon_{dev}^{ve}(t) + \varepsilon_H^{ve}(t) I \quad (3.22)$$

Consistently, and based on developments described by Miled et al. [105], a deviatoric,  $\sigma_{M,dev}(t)$ , and a dilatational,  $\sigma_{M,H}(t)$ , parts of the stress tensor are defined by:

$$\begin{cases} \sigma_{M,dev}(t) = \sigma_{M\infty,dev}(t) + \sum_{i=1}^N \sigma_{M_i,dev}(t) \\ \sigma_{M,H}(t) = \sigma_{M\infty,H}(t) + \sum_{i=1}^N \sigma_{M_i,H}(t) \end{cases} \quad (3.23)$$

where

$$\begin{cases} \sigma_{M\infty,dev}(t) = 2G_\infty \varepsilon_{dev}^{ve}(t) \\ \sigma_{M\infty,H}(t) = 3K_\infty \varepsilon_H^{ve}(t) \end{cases} \quad (3.24)$$

$$\begin{cases} \sigma_{M_i,dev}(t) = 2G_i \int_{-\infty}^t \exp\left(\frac{\zeta-t}{\tau_i^d}\right) \frac{\partial \varepsilon_{dev}^{ve}(\zeta)}{\partial \zeta} d\zeta \\ \sigma_{M_i,H}(t) = 3K_i \int_{-\infty}^t \exp\left(\frac{\zeta-t}{\tau_i^v}\right) \frac{\partial \varepsilon_H^{ve}(\zeta)}{\partial \zeta} d\zeta \end{cases} \quad (3.25)$$

### 3.2.1.3 Non-associated viscoplasticity

In addition to linear viscoelastic behaviour, matrix material can show a non-linear plastic behaviour, possibly strain-rate dependent, i.e. viscoplastic (VP). The thermoplastic matrix behaviour is also pressure sensitive, i.e. sensitive to the nature of loading (e.g., tension, compression...) and non-isochoric in the plastic domain. Consequently, the framework of non-associated viscoplasticity is considered in this work, following Perzyna model [37]. The pressure dependency of the viscoplastic flow is introduced by Raghava yield surface [111]. Viscoplastic flow occurs as soon as the first invariant,  $I_1$  (Eq. 3.26a), and the second invariant,  $I_2$  (Eq. 3.26b), of the matrix Cauchy stress tensor reach a critical combination given by the yield surface expression (Eq. 3.27).

$$I_1 = tr(\sigma_M(t)) = tr(\sigma_{M,H}(t)) \quad (3.26a)$$

$$I_2 = \frac{1}{2} \boldsymbol{\sigma}_{M,dev}(t) : \boldsymbol{\sigma}_{M,dev}(t) \quad (3.26b)$$

$$f(I_1, I_2, R) = \frac{(\eta - 1)I_1 + \sqrt{(\eta - 1)^2 I_1^2 + 12\eta I_2}}{2\eta} - \sigma_t - H(\kappa) \geq 0 \quad (3.27)$$

In previous expression, the hydrostatic pressure dependency parameter,  $\eta$ , is defined by the ratio between the quasi-static initial yield stresses in compression,  $\sigma_{comp}$ , and in tension,  $\sigma_t$ , so that  $\eta = \sigma_{comp}/\sigma_t$ . A representation of the Raghava yield surface in the  $\sqrt{3I_2} - I_1$  plane, for different values of the hydrostatic pressure parameter  $\eta$ , is given in Figure 3.1. It can be seen that for a value of  $\eta$  set to 1, the Raghava yield surface becomes the pressure independent von Mises yield surface.

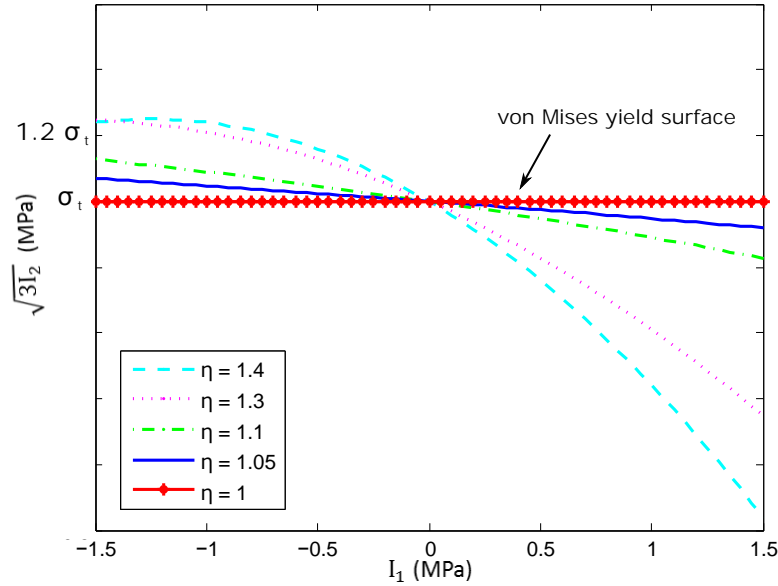


Figure 3.1: Raghava yield surface for different values of the hydrostatic pressure dependency parameter,  $\eta$

In expression 3.27,  $H(\kappa)$  is the isotropic hardening function that must be identified in tension for the considered polymeric material. It is important to note that all types of hardening laws can be considered in the present behaviour model. For the applications considered in this work, hardening law given by Eq. (3.28) will be considered.

$$H(\kappa) = h_1 \exp(h_2 \kappa^2) (1 - \exp(-h_3 \kappa)) \quad (3.28)$$

where  $h_1$ ,  $h_2$  and  $h_3$  are material parameters and  $\kappa$ , defined as the hardening variable, can be

assimilated to the cumulated viscoplastic strain (Eq 3.29) in the case of undamaged material.

$$\kappa = \int_t \sqrt{\frac{2}{3} \dot{\epsilon}^{vp} : \dot{\epsilon}^{vp}} dt \quad (3.29)$$

with  $\dot{\epsilon}^{vp}$  the viscoplastic strain rate tensor. The non-symmetric and non-isochoric plastic flow of the polymeric matrix is modelled by a hyperbolic viscoplastic dissipation potential [99], defined by:

$$\psi_M^{vp}(I_1, I_2) = \sqrt{3I_2 + \frac{1}{3} \left( a^+ \langle I_1 \rangle^2 + a^- \langle -I_1 \rangle^2 \right)} \quad (3.30)$$

where the symbol  $\langle \cdot \rangle$  is the Macauley braket defined by  $\langle x \rangle = \frac{(x + |x|)}{2}$ , for any scalar  $x$ .  $a^+$  and  $a^-$  are volume variation parameters under positive and negative hydrostatic pressure, respectively. The viscoplastic dissipation potential is presented in terms of  $I_1$  in Figure 3.2, for different values of parameters  $a^+$  and  $a^-$ .

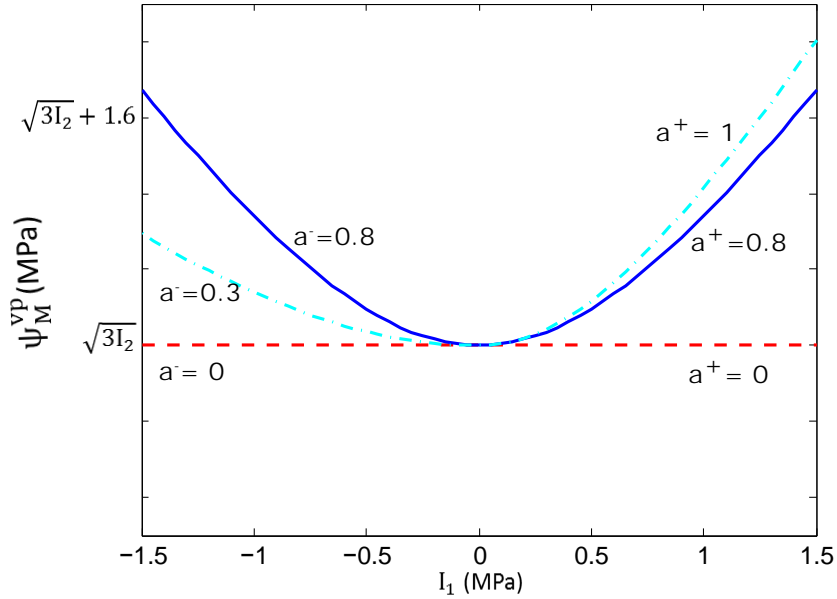


Figure 3.2: Viscoplastic dissipation potential for different values of  $a^+$  and  $a^-$

In the framework of non-associated viscoplasticity,  $\dot{\epsilon}^{vp}$  is derived from the viscoplastic potential of dissipation,  $\psi_M^{vp}$ , and expressed by the normality rule in terms of the viscoplastic multiplier rate,  $\dot{\lambda}$ , as follows:

$$\dot{\epsilon}^{vp} = \dot{\lambda} \frac{\partial \psi_M^{vp}}{\partial \sigma_M} = \dot{\lambda} n \quad (3.31)$$

where  $n$  is the viscoplastic flow direction tensor. Given the expression of  $\psi_M^{vp}$ , (3.30), the expres-

sion of the viscoplastic strain rate tensor becomes:

$$\dot{\boldsymbol{\varepsilon}}^{vp} = \dot{\lambda} \frac{\frac{3}{2} \boldsymbol{\sigma}_{M,dev} + \frac{1}{9} (a^+ \langle I_1 \rangle + a^- \langle -I_1 \rangle) \mathbf{I}}{3I_2 + \frac{1}{27} (a^+ \langle I_1 \rangle^2 + a^- \langle -I_1 \rangle^2)} \quad (3.32)$$

The viscoplastic multiplier rate,  $\dot{\lambda}$ , is calculated here using the approach of overstress based viscoplasticity. According to the latter theory, the static yield surface,  $f$  (Eq. 3.27), is extended to a dynamic yield surface,  $F^{vp}$ , defined as follows [37]:

$$F^{vp}(I_1, I_2, H, \dot{\kappa}) = \frac{(\eta - 1)I_1 + \sqrt{(\eta - 1)^2 I_1^2 + 12\eta I_2}}{2\eta} - (\sigma_t + H(\kappa)) - \sigma^{vp} \quad (3.33)$$

where  $\sigma^{vp}$  is the viscous overstress. As postulated in Perzyna's model [37], this overstress is defined as follows:

$$\sigma^{vp} = (\sigma_t + H(\kappa)) \left( \frac{\dot{\kappa}}{\dot{\kappa}_0} \right)^m \quad (3.34)$$

where  $m$  and  $\dot{\kappa}_0$  are the strain rate sensitivity and viscosity parameters, respectively.  $\dot{\kappa}$  is the equivalent viscoplastic strain-rate, defined by:

$$\dot{\kappa} = \sqrt{\frac{2}{3} \dot{\boldsymbol{\varepsilon}}^{vp} : \dot{\boldsymbol{\varepsilon}}^{vp}} = \dot{\lambda} \sqrt{\frac{2}{3} \mathbf{n} : \mathbf{n}} \quad (3.35)$$

The standard Kuhn-Tucker loading/unloading conditions are then applied to the dynamic yield surface (i.e.,  $F^{vp} \leq 0$ ,  $\dot{\lambda} \geq 0$ ,  $\dot{\lambda} F^{vp} = 0$ ) for the determination of the viscoplastic multiplier. It can be noted that both static and dynamic yield surfaces are updated all along the implementation. As a consequence, during unloading overstress does not systematically vanish and stress state can remain in the viscoplastic domain (i.e. stress state above the static yield surface, on updated dynamic surface). The rate form of the viscoplastic multiplier is obtained by substituting its expression into the dynamic yield surface and is as follows:

$$\dot{\lambda} = \begin{cases} 0 & , \text{ if } f < 0, \\ \frac{\dot{\kappa}_0}{\sqrt{\frac{2}{3} \mathbf{n} : \mathbf{n}}} \left( \frac{(\eta - 1)I_1 + \sqrt{(\eta - 1)^2 I_1^2 + 12\eta I_2}}{2\eta (\sigma_t + H(\kappa))} \right)^{\frac{1}{m}} & , \text{ if } f \geq 0 \end{cases} \quad (3.36)$$



Finally, the viscoplastic strain rate tensor is given by:

$$\dot{\boldsymbol{\varepsilon}}^{vp} = \begin{cases} 0 & , \text{if } f < 0, \\ \frac{\dot{\kappa}_0}{\sqrt{\frac{2}{3}} \mathbf{n} : \mathbf{n}} \left( \frac{(\eta - 1)I_1 + \sqrt{(\eta - 1)^2 I_1^2 + 12\eta I_2}}{2\eta (\sigma_t + H(\kappa))} \right)^{\frac{1}{m}} \mathbf{n} & , \text{if } f \geq 0 \end{cases} \quad (3.37)$$

In the constitutive model, the dynamic yield surface takes place only if the static yield function is positive or null ( $f \geq 0$ ). When the current stress lies in the viscoelastic domain ( $f < 0$ ), the viscoplastic strain rate tensor  $\dot{\boldsymbol{\varepsilon}}^{vp}$  vanish. The viscoplastic deformation takes place only when the condition  $f \geq 0$  is satisfied.

### 3.2.1.4 Summary of the matrix constitutive model (algorithm)

In this section, the incremental formulation of the stress update is presented. A viscoelastic predictor/viscoplastic corrector scheme is used in order to integrate the constitutive laws of behaviour model. This schema is an extension of classical return-mapping algorithms implemented in the framework of elastoplasticity [112]. More precisely, the aim of the algorithm detailed hereafter is to compute values of variables at a given time  $t_{n+1}$ , knowing their values at  $t_n$  (current step) and the total strain increment,  $\Delta\boldsymbol{\varepsilon}$ , between  $t_n$  and  $t_{n+1}$ . During the trial prediction, the strain increment is assumed to be entirely viscoelastic, i.e.  $\Delta\boldsymbol{\varepsilon} = \Delta\boldsymbol{\varepsilon}^{ve}$  and  $\Delta\boldsymbol{\varepsilon}^{vp} = 0$ . As a consequence, viscoplastic and cumulative viscoplastic strains in the trial step remain at the value computed at increment  $n$ . Trial deviatoric and hydrostatic stresses at  $t = t_{n+1}$  are therefore given by:

$$\boldsymbol{\sigma}_{M_{\infty},dev}^{tr}(t_{n+1}) = 2G_{\infty}\boldsymbol{\varepsilon}_{dev}^{ve}(t_{n+1}) \quad (3.38)$$

$$\boldsymbol{\sigma}_{M_{\infty},H}^{tr}(t_{n+1}) = 3K_{\infty}\boldsymbol{\varepsilon}_H^{ve}(t_{n+1}) \quad (3.39)$$

$$\boldsymbol{\sigma}_{M_i,dev}^{tr}(t_{n+1}) = \exp\left(-\frac{\Delta t}{\tau_i^d}\right) \boldsymbol{\sigma}_{M_i,dev}(t_n) + 2G_i \int_{t_n}^{t_{n+1}} \exp\left(\frac{\zeta - t_{n+1}}{\tau_i^d}\right) \frac{\partial \boldsymbol{\varepsilon}_{dev}^{ve}(\zeta)}{\partial \zeta} d\zeta \quad (3.40)$$

$$\boldsymbol{\sigma}_{M_i,H}^{tr}(t_{n+1}) = \exp\left(-\frac{\Delta t}{\tau_i^v}\right) \boldsymbol{\sigma}_{M_i,H}(t_n) + 3K_i \int_{t_n}^{t_{n+1}} \exp\left(\frac{\zeta - t_{n+1}}{\tau_i^v}\right) \frac{\partial \boldsymbol{\varepsilon}_H^{ve}(\zeta)}{\partial \zeta} d\zeta \quad (3.41)$$

In order to compute the integrals in equations (3.40) and (3.41) over  $[t_n, t_{n+1}]$ , the VE strain rate is assumed to be constant over this time interval. Using the approximation  $\Delta\boldsymbol{\varepsilon}^{ve} = \dot{\boldsymbol{\varepsilon}}^{ve}(t_{n+1})\Delta t$ , it

leads to:

$$\sigma_{M_i,dev}^{tr}(t_{n+1}) = \exp\left(-\frac{\Delta t}{\tau_i^d}\right) \sigma_{M_i,dev}(t_n) + 2G_i \left[1 - \exp\left(-\frac{\Delta t}{\tau_i^d}\right)\right] \frac{\tau_i^d}{\Delta t} \Delta \varepsilon_{dev}^{ve} \quad (3.42)$$

$$\sigma_{M_i,H}^{tr}(t_{n+1}) = \exp\left(-\frac{\Delta t}{\tau_i^v}\right) \sigma_{M_i,H}(t_n) + 3K_i \left[1 - \exp\left(-\frac{\Delta t}{\tau_i^v}\right)\right] \frac{\tau_i^v}{\Delta t} \Delta \varepsilon_H^{ve} \quad (3.43)$$

Then, recalling expression (3.23), updated trial stress can be computed as follows:

$$\sigma_{M,dev}^{tr}(t_{n+1}) = \sigma_{M_{\infty},dev}^{tr}(t_{n+1}) + \sum_{i=1}^N 2\bar{G}_{M_i} \Delta \varepsilon_{dev}^{ve} + \exp\left(-\frac{\Delta t}{\tau_i^d}\right) \sigma_{M_i,dev}(t_n) \quad (3.44)$$

$$\sigma_{M,H}^{tr}(t_{n+1}) = \sigma_{M_{\infty},H}^{tr}(t_{n+1}) + \sum_{i=1}^N 3\bar{K}_{M_i} \Delta \varepsilon_H^{ve} + \exp\left(-\frac{\Delta t}{\tau_i^v}\right) \sigma_{M_i,H}(t_n) \quad (3.45)$$

where

$$\bar{G}_i = G_i \left[1 - \exp\left(-\frac{\Delta t}{\tau_i^d}\right)\right] \frac{\tau_i^d}{\Delta t} \quad (3.46)$$

and

$$\bar{K}_i = K_i \left[1 - \exp\left(-\frac{\Delta t}{\tau_i^v}\right)\right] \frac{\tau_i^v}{\Delta t} \quad (3.47)$$

The computed trial stress tensor can then be recast as follows:

$$\sigma_M^{tr}(t_{n+1}) = \sigma_{M,dev}^{tr}(t_{n+1}) + \sigma_{M,H}^{tr}(t_{n+1}) I \quad (3.48)$$

Once the trial Cauchy stress tensor is known, the corresponding trial yield surface can be expressed:

$$f^{tr}(I_1^{tr}, I_2^{tr}, \kappa_n) = \frac{(\eta - 1)I_1^{tr} + \sqrt{(\eta - 1)^2 I_1^{tr2} + 12\eta I_2^{tr}}}{2\eta} - \sigma_t - H(\kappa_n) \quad (3.49)$$

The trial first and second stress invariants are determined in terms of the trial stress tensor, i.e.  $I_1^{tr} = I_1(\sigma_M^{tr}(t_{n+1}))$  and  $I_2^{tr} = I_2(\sigma_M^{tr}(t_{n+1}))$ . In case of purely viscoelastic deformation (i.e.  $f^{tr} < 0$ ), quantities computed at the trial step are solutions of the problem at increment  $n + 1$ . In particular,  $\sigma_{M,n+1} = \sigma_M^{tr}$ ,  $\varepsilon_{n+1}^{ve} = \varepsilon^{ve,tr}$  and  $\kappa_{n+1} = \kappa^{tr} = \kappa_n$ . Otherwise the deformation is viscoelastic-viscoplastic and a viscoplastic corrector schema is needed to compute matrix behaviour. In particular, the actual strain increment tensor must be split into a viscoelastic and a viscoplastic part, i.e.  $\Delta \varepsilon = \Delta \varepsilon^{ve} + \Delta \varepsilon^{vp}$ . Then, considering that  $\Delta \varepsilon^{vp} = \Delta \lambda \mathbf{n}_{n+1}$ , with  $\mathbf{n}_{n+1}$  the viscoplastic flow direction tensor, expressed in terms of stress invariants,  $I_1^{n+1} = I_1^{tr}$  and  $I_2^{n+1} = I_2^{tr}$  (Eq. 3.50), the

incremental form of the plastic multiplier  $\Delta\lambda$  is given by Eq. (3.51).

$$\mathbf{n}_{n+1} = \frac{\frac{3}{2}\sigma_{M,n+1} + \frac{1}{9}(a^+ \langle I_1^{n+1} \rangle + a^- \langle -I_1^{n+1} \rangle)I}{\sqrt{3I_2^{n+1} + \frac{1}{27}(a^+ \langle I_1^{n+1} \rangle^2 + a^- \langle -I_1^{n+1} \rangle^2)}} \quad (3.50)$$

$$\Delta\lambda = \frac{\Delta t \dot{\kappa}_0}{\sqrt{\frac{2}{3}\mathbf{n}_{n+1} : \mathbf{n}_{n+1}}} \left\langle \frac{\boldsymbol{\sigma}_{n+1}^{vp}}{\boldsymbol{\sigma}_t + H(\kappa_n)} \right\rangle^{\frac{1}{m}} \quad (3.51)$$

where

$$\boldsymbol{\sigma}_{n+1}^{vp} = \frac{(\eta - 1)I_1^{n+1} + \sqrt{(\eta - 1)^2 I_1^{n+1^2} + 12\eta I_2^{n+1}}}{2\eta} - \boldsymbol{\sigma}_t - H(\kappa_n) \quad (3.52)$$

An updated cumulative viscoplastic strain,  $\kappa_{n+1}$ , is obtained from  $\kappa_n$  following  $\kappa_{n+1} = \kappa_n + \Delta\kappa$  with the cumulative viscoplastic strain increment  $\Delta\kappa$  expressed as follows:

$$\Delta\kappa = \sqrt{\frac{2}{3}\mathbf{n}_{n+1} : \mathbf{n}_{n+1}}\Delta\lambda \quad (3.53)$$

Finally, all state variables are updated and stored for the next time step. The complete algorithm for the viscoelastic-viscoplastic matrix constitutive model is summarised in Table 3.1.

Table 3.1: Return-mapping algorithm for the computation of VE-VP thermoplastic matrix behaviour

---

Input: VE and VP parameters

(i) Trial (visco)elastic strain increment split into a deviatoric part and a hydrostatic part:

$$\Delta \boldsymbol{\varepsilon}^{ve} = \Delta \boldsymbol{\varepsilon}_{dev}^{ve} + \Delta \boldsymbol{\varepsilon}_H^{ve} \quad (3.22)$$

(ii) Computation of the matrix Cauchy stress tensor components,  $\boldsymbol{\sigma}_{M_i,dev}^{tr}(t_{n+1})$  and  $\boldsymbol{\sigma}_{M_i,H}^{tr}(t_{n+1})$ , corresponding to the trial (visco)elastic strain increment:

$$\boldsymbol{\sigma}_{M_i,dev}^{tr}(t_{n+1}) = \exp\left(-\frac{\Delta t}{\tau_i^d}\right) \boldsymbol{\sigma}_{M_i,dev}(t_n) + 2\bar{G}_i \Delta \boldsymbol{\varepsilon}_{dev}^{ve}, \quad (3.23)$$

$$\boldsymbol{\sigma}_{M_i,H}^{tr}(t_{n+1}) = \exp\left(-\frac{\Delta t}{\tau_i^v}\right) \boldsymbol{\sigma}_{M_i,H}(t_n) + 3\bar{K}_i \Delta \boldsymbol{\varepsilon}_H^{ve}, \quad (3.23)$$

$$\boldsymbol{\sigma}_M^{tr}(t_{n+1}) = \sum_{i=1}^N \boldsymbol{\sigma}_{M_i,dev}^{tr}(t_{n+1}) + \boldsymbol{\sigma}_{M_i,H}^{tr}(t_{n+1}) I$$

$$I_1^{tr} = \text{tr}(\boldsymbol{\sigma}_M^{tr}), \quad I_2^{tr} = \frac{1}{2} \sum_{i=1}^N \boldsymbol{\sigma}_{M_i,dev}^{tr} : \sum_{i=1}^N \boldsymbol{\sigma}_{M_i,dev}^{tr} \quad (3.26)$$

(iii) Assess (visco)plastic flow:

$$\text{if } f_{n+1}^{tr}(I_1^{tr}, I_2^{tr}, \boldsymbol{\kappa}_n) \leq 0 \text{ then } (\cdot)_{n+1} = (\cdot)^{tr} \quad (3.27)$$

else

(iv) Viscoplastic strain increment-viscoplastic stress return:

$$\boldsymbol{\sigma}_{n+1}^{vp} = \frac{(\eta - 1)I_1^{n+1} + \sqrt{(\eta - 1)^2 I_1^{n+1^2} + 12\eta I_2^{n+1}}}{2\eta} - \boldsymbol{\sigma}_t - H(\boldsymbol{\kappa}_n) \quad (3.34)$$

$$\mathbf{n}_{n+1} = \frac{\frac{3}{2}\boldsymbol{\sigma}_{M,dev}^{n+1} + \frac{1}{9}(a^+ \langle I_1^{n+1} \rangle + a^- \langle -I_1^{n+1} \rangle) I}{\sqrt{3I_2^{n+1} + \frac{1}{27}(a^+ \langle I_1^{n+1} \rangle^2 + a^- \langle -I_1^{n+1} \rangle^2)}} \quad (3.31)$$

$$\Delta \lambda = \frac{\Delta t \dot{\boldsymbol{\kappa}}_0}{\sqrt{\frac{2}{3} \mathbf{n}_{n+1} : \mathbf{n}_{n+1}}} \left\langle \frac{\boldsymbol{\sigma}_{n+1}^{vp}}{\boldsymbol{\sigma}_t + H(\boldsymbol{\kappa}_n)} \right\rangle^{\frac{1}{m}} \quad (3.36)$$

$$\Delta \boldsymbol{\varepsilon}^{vp} = \Delta \lambda \mathbf{n}_{n+1} \quad (3.37), \quad \Delta \boldsymbol{\kappa} = \sqrt{\frac{2}{3} \mathbf{n}_{n+1} : \mathbf{n}_{n+1}} \Delta \lambda \quad (3.35)$$

(v) update stresses:

$$\boldsymbol{\sigma}_{M_i,dev}(t_{n+1}) = \exp\left(-\frac{\Delta t}{\tau_i^d}\right) \boldsymbol{\sigma}_{M_i,dev}(t_n) + 2G_i \left[1 - \exp\left(-\frac{\Delta t}{\tau_i^d}\right)\right] \frac{\tau_i^d}{\Delta t} (\Delta \boldsymbol{\varepsilon}_{dev}^{ve} - \Delta \boldsymbol{\varepsilon}_{dev}^{vp})$$

$$\boldsymbol{\sigma}_{M_i,H}(t_{n+1}) = \exp\left(-\frac{\Delta t}{\tau_i^v}\right) \boldsymbol{\sigma}_{M_i,H}(t_n) + 3K_i \left[1 - \exp\left(-\frac{\Delta t}{\tau_i^v}\right)\right] \frac{\tau_i^v}{\Delta t} (\Delta \boldsymbol{\varepsilon}_H^{ve} - \Delta \boldsymbol{\varepsilon}_H^{vp})$$

(vi) store  $\boldsymbol{\varepsilon}_{n+1}^{ve}$ ,  $\boldsymbol{\kappa}_{n+1}$

Output: Matrix stress tensor,  $\boldsymbol{\sigma}_M$

---

### 3.2.2 Modelling of fibres mechanical response

In SFRC, the load applied to the polymeric matrix is transferred to embedded fibres through the interface. Due to relatively high aspect ratio of fibres (i.e. length divided by diameter), generally higher than 15 [113]), each fibre family is assumed to carry load only in its axis direction, i.e. behaves unidimensionnaly. As a consequence, fibres are assumed to deform longitudinally while keeping a constant diameter, i.e. deformation is assumed to remain negligible in transverse directions. Moreover, as already stated in section (3.1), it is assumed that fibre behaviour remains linear elastic. The presence of fibres with variable characteristics in the composite material is modelled by the coexistence of  $N_{fam}$  families. Each family  $i$  ( $i \in \{1, \dots, N_{fam}\}$ ) is characterized by its elastic properties (Young modulus  $E_F^i$ ), its orientation vector,  $\vec{a}^i$ , and therefore orientation matrix,  $A^i$ , defined by  $A^i = \vec{a}^i \otimes \vec{a}^i$ , i.e.  $A_{kl}^i = a_k^i \otimes a_l^i, \forall k, l$ , and its geometric properties (i.e., diameter and length). It can be noted that no reorientation of fibres upon loading will be considered in this work, i.e.  $\vec{a}^i$  and  $A^i$  remain constant during loading. A volume fraction,  $v_F^i$ , is associated to each family of fibres so that:

$$\sum_{i=1}^{N_{fam}} v_F^i = v_F = 1 - v_M \quad (3.54)$$

$v_F$  and  $v_M$  are respectively the total volume fraction of fibres and matrix in the composite material. The computation of 1D fibre axial stress,  $\sigma_F^{0,i}$  is based on the assumption of a local iso-strain state between the fibres and the matrix, in the fibre axis direction. The tensor of deformation gradient sustained by the fibres,  $F_F^i$ , is defined as the projection of the total deformation gradient tensor,  $F$ , (i.e., applied to the composite material) in the direction of fibres' orientation.

$$F_F^i = FA^i \quad \forall i \in \{1, \dots, N_{fam}\} \quad (3.55)$$

The right Cauchy-Green tensors of the composite,  $C$ , and fibre families,  $C_F^i$ , are defined by Equation (3.56) and are therefore linked by the relation (3.57).

$$C = F^T F \quad \text{and} \quad C_F^i = F_F^{iT} F_F^i \quad \forall i \in \{1, \dots, N_{fam}\} \quad (3.56)$$

$$C_F^i = A^i C A^i \quad \forall i \in \{1, \dots, N_{fam}\} \quad (3.57)$$

By construction, each tensor  $C_F^i$  has a unique eigenvalue different from zero, called  $\lambda_F^i$ , with associated eigenvector  $\vec{a}^i$ .  $\lambda_F^i$  actually stands for the square of the ratio of the fibres current length by initial length. As a consequence, with the small strain assumption, the 1D Hencky strain of the

fibres,  $\varepsilon_F^{0,i}$ , is simply expressed from  $\lambda_F^i$  as follows:

$$\varepsilon_F^{0,i} = \frac{1}{2} \ln(\lambda_F^i) \quad \forall i \in \{i, \dots, N_{fam}\} \quad (3.58)$$

A modified shear lag model is used to compute fibre axial stress,  $\sigma_F^{0,i}$ . This model is based on initial work by Bowyer and Bader [89], expressing the average stress in a fibre as a function of its length,  $L$ , its radius,  $r$ , the interfacial shear strength,  $\tau$ , and the strain state in the composite material,  $\varepsilon$ . This approach has then been extended to cases of complex fibre orientations, as described in details by Notta-Cuvier et al. [86]. According to the latter formulation, if fibre length in family  $i$ ,  $L^i$ , is higher than a specific length,  $L_\varepsilon^i$  (3.59), fibre stress grows from zero at fibre tip and reaches a plateau at a distance  $L_\varepsilon^i$  from fibre tip for a maximum value given by  $E_F^i \varepsilon_F^{0,i}$ ,  $\forall i \in \{i, \dots, N_{fam}\}$ .

$$L_\varepsilon^i = \frac{E_F^i \varepsilon_F^{0,i} r^i}{\tau^i} \quad \forall i \in \{i, \dots, N_{fam}\} \quad (3.59)$$

where  $\varepsilon_F^{0,i}$  is the fibre axial strain whose computation is described before. It is worth noting that below this fibre's length, stress does not reach its maximum value. According to this, the 1D-stress state of each fibre family,  $\sigma_F^{0,i}$ ,  $\forall i$ , can be computed using Eq (3.60). It can be noted that particular cases where fibres have different elastic properties (i.e. different values of  $E_F^i$ ) can be dealt with and that the fibres response under compression is assumed to be the same as under tension (i.e. buckling is neglected) [86].

$$\begin{cases} \sigma_F^{0,i} = \varepsilon_F^{0,i} \left( 1 - \frac{E_F^i r^i}{2L^i \tau^i} \left| \varepsilon_F^{0,i} \right| \right) E_F^i & \text{if } \left| \varepsilon_F^{0,i} \right| \leq \frac{L^i \tau^i}{E_F^i r^i} \\ \sigma_F^{0,i} = \text{sign}(\varepsilon_F^{0,i}) \frac{L^i \tau^i}{2r^i} & \text{otherwise} \end{cases} \quad (3.60)$$

To compute fibre stress tensor in the global coordinate system, "quasi" iso-stress states are assumed between the fibres and the matrix material in transverse and shear directions with respect to fibre axis, in addition to iso-strain state assumption in fibre axis direction. More precisely, fibre stresses in those directions are assumed to be equal to those of a fictitious purely viscoelastic material (with viscoelastic parameters of the matrix material), consistently with the well-known principle of lower bound assumption. The expression of 3D stress tensor of fibre family  $i$ ,  $\sigma_F^i$ , is

therefore expressed in the global coordinate system by:

$$\sigma_F^i = T^i \begin{bmatrix} \sigma_F^{0,i} & \sigma_{M12}^{0,i} & \sigma_{M13}^{0,i} \\ \sigma_{M12}^{0,i} & \sigma_{M22}^{0,i} & \sigma_{M23}^{0,i} \\ \sigma_{M13}^{0,i} & \sigma_{M23}^{0,i} & \sigma_{M33}^{0,i} \end{bmatrix} T^{i-1} \quad \forall i \quad (3.61)$$

where  $T^i$  is the transition matrix from the coordinate system related to the fibre family  $i$  to the global one.  $\sigma_{Mkl}^{0,i}$ ,  $k, l \in \{1, 2, 3\}$ , are stress components of the purely viscoelastic "matrix" material, expressed in the coordinate system of fibre family  $i$ .

### 3.2.3 Modelling of composite mechanical response

Once 3D stress tensors of the matrix material and all fibre families are computed, the stress tensor applied to the composite material can be determined, as a combination of the contribution of all fibre and matrix media [86]. The stress computation of the different constituents is schematically represented in Figure 3.3.

In practice, the state potential of the composite material, here the Helmholtz free energy, is assumed to be additively split into a part specific to the matrix medium and other parts specific to each fibre family (3.62).

$$\rho \phi_c = v_M \rho_M \phi_M + \sum_{i=1}^{N_{fam}} v_F^i \rho_F^i \phi_F^i \quad (3.62)$$

where  $\rho$ ,  $\rho_M$  and  $\rho_F^i$  are the densities of the composite material, the matrix material and the fibre family  $i$ , respectively.  $\phi_M$  and  $\phi_F^i$  are the Helmholtz free energies of the matrix and the fibre family  $i$ , respectively. These state potentials have to verify Clausius-Duhem inequality, simplified here for isothermal transformations:

$$\sigma_c : D - \left[ v_M \rho_M \dot{\phi}_M + \sum_{i=1}^{N_{fam}} v_F^i \rho_F^i \dot{\phi}_F^i \right] \geq 0 \quad (3.63)$$

where  $\sigma_c$  is the composite stress tensor.  $D$  is the rate of deformation tensor, assimilated to  $\dot{\epsilon}$  under the hypothesis of small perturbations.  $\dot{\phi}_M$  and  $\dot{\phi}_F^i$  are the time derivative of the Helmholtz free energies of the matrix and the fibre family  $i$ , respectively.

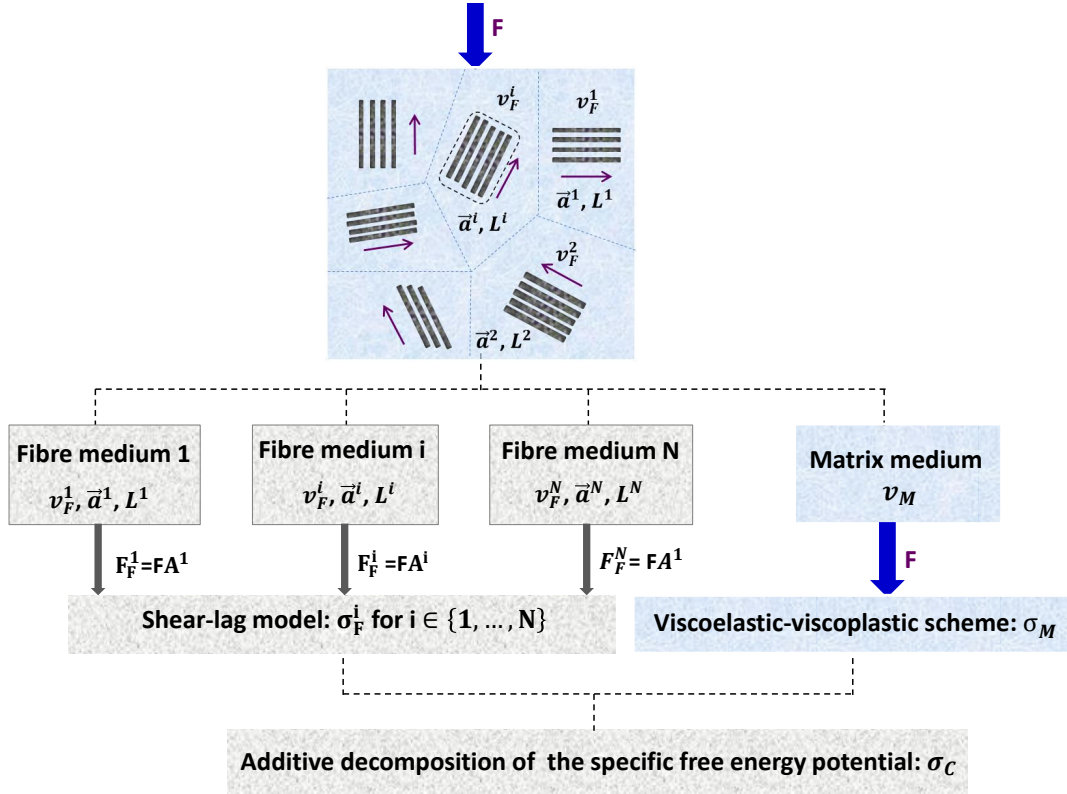


Figure 3.3: Schematic representation of the computation of composite stress tensor

It is important to note that the composite strain tensor,  $\varepsilon$ , is here identical to the matrix strain tensor. The expressions of the total free energy of matrix material and of its time derivative have been established in section (3.2.1.1). It is reminded that:

$$\rho_M \dot{\phi}_M = \frac{1}{2} \int_0^t \int_0^t \frac{\partial \varepsilon^{ve}(\tau)}{\partial \tau} : R^{ve}(2t - \tau - \zeta) : \frac{\partial \varepsilon^{ve}(\zeta)}{\partial \zeta} d\tau d\zeta + \left( \int_0^t R^{ve}(t - \zeta) : \frac{\partial \varepsilon^{ve}(\zeta)}{\partial \zeta} d\zeta \right) : \dot{\varepsilon}^{ve} + \rho_M \dot{\phi}_M^{vp} \quad (3.64)$$

Concerning the fibre media, each potential,  $\phi_F^i$ , is a function of the scalar axial strain,  $\varepsilon_F^{0,i}$  (3.58). Yet for convenience, the fibre Hencky strain tensors expressed in the global coordinate system by  $\varepsilon_{Fkl}^i = T_{k1}^i T_{1l}^{i-1} \varepsilon_F^{0,i}$ ,  $\forall k, l, \forall i$ , are considered, so that  $\frac{d\phi_F^i}{dt} = \frac{\partial \phi_F^i}{\partial \varepsilon_F^i} : \frac{\partial \varepsilon_F^i}{\partial t}$ ,  $\forall i$ . If assuming small displacements, the Hencky strain tensors can be assimilated to the Green-Lagrange strain tensors,  $\mathcal{E}_F^i$ . These are expressed from the right Cauchy-Green tensors by  $\mathcal{E}_F^i = \frac{1}{2} (C_F^i - I)$ ,  $\forall i$ . Relation (3.57) therefore leads to the approximation  $\frac{\partial \varepsilon_F^i}{\partial t} \approx A^i \frac{\partial \varepsilon}{\partial t} A^i$ ,  $\forall i$ . Finally, noting that  $X : (A^i Y A^i) =$



$(A^i X A^i) : Y$ , by construction of matrices  $A^i$ , and for any matrices  $X$  and  $Y$ , these developpements give rise to a factorized expression of Clausius-Duhem inequality (3.65).

$$\begin{aligned} & \left[ \sigma_c - v_M \int_0^t R^{ve}(t-\zeta) : \frac{\partial \varepsilon^{ve}(\zeta)}{\partial \zeta} d\zeta - \sum_{i=1}^{N_{fam}} v_F^i \rho_F^i A^i \frac{\partial \phi_F^i}{\partial \varepsilon_F^i} A^i \right] : \dot{\varepsilon} - \\ & \frac{1}{2} v_M \int_0^t \int_0^t \frac{\partial \varepsilon^{ve}(\tau)}{\partial \tau} : \frac{\partial R^{ve}}{\partial t}(2t-\tau-\zeta) : \frac{\partial \varepsilon^{ve}(\zeta)}{\partial \zeta} d\tau d\zeta + \\ & v_M \int_0^t R^{ve}(t-\zeta) : \frac{\partial \varepsilon^{ve}(\zeta)}{\partial \zeta} d\zeta : \dot{\varepsilon}^{vp} - v_M \rho_M \dot{\phi}_M^{vp} \geq 0 \end{aligned} \quad (3.65)$$

The Clausius-Duhem inequality (3.65) has to be verified for any state of the strain rate tensor,  $\dot{\varepsilon}$ . Then, the system  $(\Omega)$  (3.66) is an admissible solution. Finally, considering the state laws  $\rho_F^i \frac{\partial \phi_F^i}{\partial \varepsilon_F^i} = \sigma_F^i$ ,  $\forall i$ , and the expression of the matrix stress tensor given in Equation (3.17), the stress state of the composite material can be expressed by Equation (3.67):

$$(\Omega) \left\{ \begin{aligned} & \sigma_c = v_M \int_0^t R^{ve}(t-\zeta) : \frac{\partial \varepsilon^{ve}(\zeta)}{\partial \zeta} d\zeta - \sum_{i=1}^{N_{fam}} v_F^i \rho_F^i A^i \frac{\partial \phi_F^i}{\partial \varepsilon_F^i} A^i \\ & - \frac{1}{2} v_M \int_0^t \int_0^t \frac{\partial \varepsilon^{ve}(\tau)}{\partial \tau} : \frac{\partial R^{ve}}{\partial t}(2t-\tau-\zeta) : \frac{\partial \varepsilon^{ve}(\zeta)}{\partial \zeta} d\tau d\zeta + \\ & v_M \int_0^t R^{ve}(t-\zeta) : \frac{\partial \varepsilon^{ve}(\zeta)}{\partial \zeta} d\zeta : \dot{\varepsilon}^{vp} - v_M \rho_M \dot{\phi}_M^{vp} \geq 0 \end{aligned} \right. \quad (3.66)$$

$$\sigma_c = v_M \sigma_M + \sum_{i=1}^{N_{fam}} v_F^i A^i \sigma_F^i A^i \quad (3.67)$$

Through this chapter, a set of parameters, associated to the behaviour laws of matrix and composite behaviour have been introduced (cf Table 3.2). The identification of those parameters lays on several mechanical experiments and microtomographic observations, as described in the next chapter. Experimental tests will also be used in order to validate the implementation of the composite behaviour model.

### 3.3 Conclusion

A behaviour model for SFRC is presented here, based on an original approach that aims to be an efficient alternative to more complex homogenisation procedures. This part of the work deals with the presentation of the developed approach and the constitutive laws associated to the different constituents for the computation of the composite response. The strain rate dependency in the composite behaviour is modelled by a coupled viscoelastic-viscoplastic law associated to the matrix

Table 3.2: Material parameters of the matrix and composite constitutive laws

Parameters		
Matrix parameters	Viscoelasticity	$E_\infty, E_i, \tau_i$ for $i \in (1, \dots, N)$
	Initial yield stress	$\sigma_i$
	Hardening parameters	$h_1, h_2$ and $h_3$
	Viscoplastic parameters	$\dot{\kappa}_0, m$
	Hydrostatic pressure dependency	$\eta$
	Volume variation	$a^+$ and $a^-$
Fibres/Composite parameters	Distribution of orientation	$v_F^i, \vec{a}^i$ for $i \in (1, \dots, N_{fam})$
	Fibre length and radius	$L^i$ and $r^i$ for $i \in (1, \dots, N_{fam})$
	Elastic properties	$E_F^i$ for $i \in (1, \dots, N_{fam})$
	Interfacial Shear Strength	$\tau^i$ for $i \in (1, \dots, N_{fam})$

material. More precisely, a linear viscoelastic is considered and a viscoplastic schema is introduced to reproduce the strain rate influence over the yield/hardening part of the material response. The complex fibre orientations, including distributed and random orientations, are modelled in a simple way, so that actual distributions of fibre orientation can be taken into account. The implementation of the constitutive model is performed in the framework of small deformations in the explicit finite element code ABAQUS as a user-material subroutine (VUMAT), written in FORTRAN77.

The identification of the involved material parameters and the reinforcement properties is the object of the following chapter, where the model validity is verified in the case of short-fibre reinforced composite subjected to a variety of loading conditions.



# *Experimental procedure for the parameters identification and validation of the model*

---

Identification and validation of the developed constitutive model are the object of the current chapter. An identification procedure, based on an experimental investigation, is performed so that all the parameters involved in the current development can be determined. In the first part of this chapter, the characterisation of the matrix material model is targeted. Viscoelasticity is characterised by means of Dynamic Mechanical Analysis (DMA). Then, the hardening and flow parameters (viscoplasticity and pressure dependency parameters) are extracted from monotonic tests realised at different loading conditions (tension and compression) and loading speeds (i.e. different strain rates) using optical extensometry or Digital Image Correlation. The identification of VP parameters is based on the SEÉ method proposed by Lauro et al. [116]. The second part of the chapter deals with the characterisation of the reinforcement properties (geometry and orientation) so that actual properties can be used for the evaluation of the model accuracy. Finally the global behaviour of the short-fibre reinforced composite is characterised by experimental tests carried out at various loading conditions and speeds, so that the anisotropy-strain rate dependency coupled effect can be investigated. Tensile results are used for the validation of the developed model for a wide range of strain rate, by comparison with numerical results. Note that at this stage, failure phenomena (damage and fracture) of SFRC are not addressed.

## **4.1 Characterisation of the implemented behaviour model**

The accuracy of the implemented SFRC constitutive model is now assessed for a polypropylene (PP) reinforced with short glass fibres.

### 4.1.1 PP matrix VE-VP behaviour model

The matrix material under investigation is a Polypropylene (PP-commercial grade Moplen HP500N supplied by Lyon dell Basell). According to the supplier, Moplen HP500N is a homopolymer for injection moulding applications, with a MFR of  $12 \text{ g} \cdot (10\text{min})^{-1}$  and a density of  $0.9 \text{ g} \cdot (\text{cm})^{-3}$ . PP plates, 200 mm-edge squares with a thickness of 2.5 mm, are injection moulded following the process conditions prescribed by the supplier.

#### 4.1.1.1 Identification of material parameters based on DMA and monotonic tests at different strain rate

In order to characterise the viscoelastic-viscoplastic behaviour of the PP matrix, different experiments are carried out at various loading rates. First, Dynamic Mechanical Analysis is performed to identify the viscoelastic parameters. Then, flow parameters, i.e. associated to the hardening and pressure dependent and non-isochoric viscoplastic behaviour, are characterised by means of tensile (realised at different strain rates) and compression tests. Using data acquired from Digital Image Correlation (DIC) for tensile tests, the non-isochoric plastic flow behaviour is first characterised (by the identification of the expansion parameter). The pressure dependency is then identified based on tension/compression results. Finally, the use of DIC method has made possible the determination of the hardening and viscoplastic parameters by means of the SEE method [116].

## Dynamic Mechanical analyses

Small amplitude oscillatory tensile experiments are performed on an electromagnetic tensile machine (INSTRON E3000) with a 3 kN cell force. Tests are performed at room temperature on flat rectangular specimens (Figure 4.1) cut in an injected PP plate. A sinusoidal deformation characterised by an angular frequency,  $\omega$ , is applied to the specimen. The imposed strain is therefore set as follows:

$$\varepsilon(t) = \varepsilon_0 \cos(\omega t) = \varepsilon_0 \Re \{ \exp(i\omega t) \} \quad (4.1)$$

where  $\varepsilon_0$  is the strain amplitude,  $t$  the time and  $\Re \{ \cdot \}$  stands for the real part of any complex number.

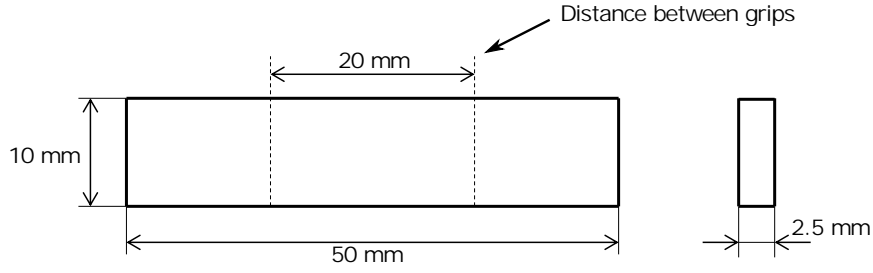


Figure 4.1: Geometry of DMA specimen

The applied frequency is progressively increased from 0.01 Hz to 30 Hz with several loading cycles per frequency (Table 4.1). The strain amplitude,  $\epsilon_0$ , is equal to 0.5% for all cycles and all frequencies. Five specimens are tested for each frequency. In the framework of small deformations,

Table 4.1: DMA cycles

Frequencies (Hz)	number of cycles
0.01	3
0.05	4
0.1	5
0.25	6
0.5	8
1	21
10	201
20	301
30	301

the stress response is sinusoidal as well. As can be seen in Figure 4.2, the stress sinusoidal evolution is with the same pulsation,  $\omega$ , but with a different amplitude,  $\sigma_0$ , and an out-of-phase angle (loss angle),  $\delta$ , compared to applied strain. It takes then the following form:

$$\sigma(t) = \sigma_0 \cos(\omega t + \delta) = \sigma_0 \Re \{ \exp(i(\omega t + \delta(\omega))) \} \quad (4.2)$$

A complex modulus,  $E^*$ , dependent on the loading pulsation, is then defined by the ratio of stress and strain as follows:

$$E^*(\omega) = \frac{\sigma_0}{\epsilon_0} \exp(i\delta(\omega)) \quad (4.3)$$

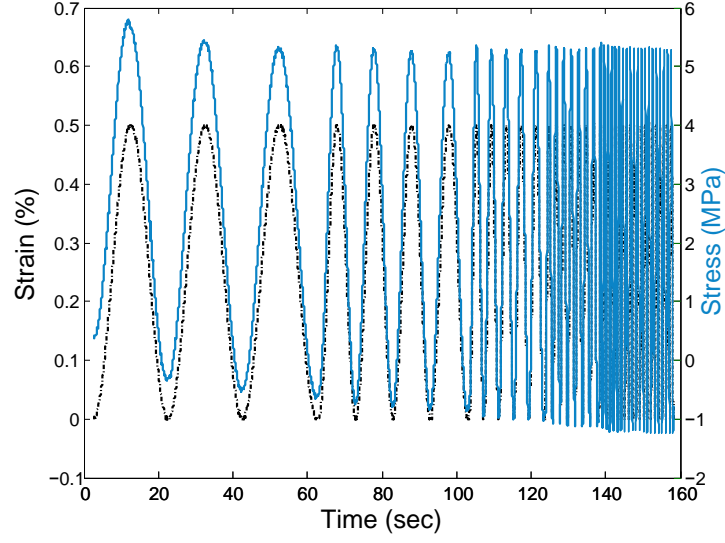


Figure 4.2: An example of a stress response to an applied sinusoidal strain for frequencies equal to 0.05, 0.1, 0.25, 0.5 and 1 Hz

$E^*$  can be split into a real part,  $E' = \Re\{E^*\}$ , called storage modulus, associated to the elastic response and in phase with the applied strain, and an imaginary part,  $E'' = \Im\{E^*\}$ , called loss modulus, associated to the viscous response and  $\frac{\pi}{2}$  out of phase with the applied strain, so that:

$$E^* = E' + iE'' \quad (4.4)$$

where the storage and loss moduli are defined by:

$$E' = \frac{\sigma_0}{\varepsilon_0} \cos(\delta) \quad (4.5)$$

$$E'' = \frac{\sigma_0}{\varepsilon_0} \sin(\delta) \quad (4.6)$$

The loss angle,  $\delta$ , can therefore be expressed from the ratio between the storage and loss moduli as follows:

$$\tan(\delta) = \frac{E''}{E'} \quad (4.7)$$

The measured data are shown in Figure 4.3, where the storage modulus increases with the pulsation, while the loss modulus decreases.

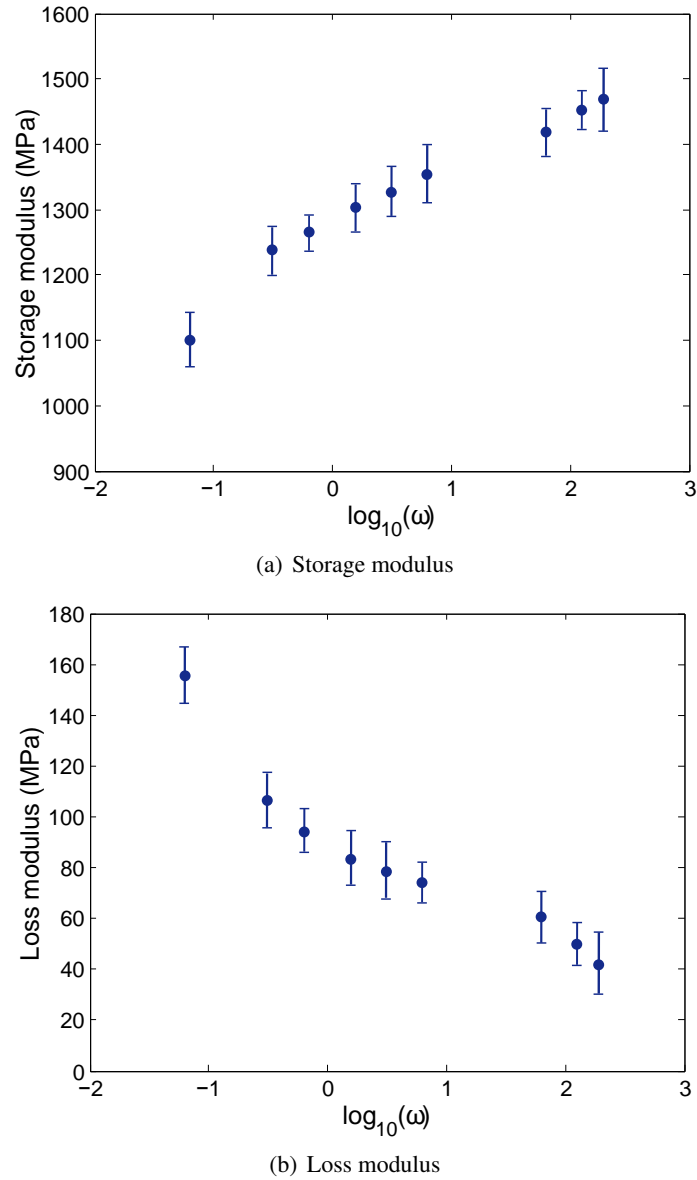


Figure 4.3: Storage (a) and loss (b) moduli versus angular pulsation for PP matrix

The Maxwell parameters (see Section 3.2.1.2) are identified based on results of DMA. Considering the case of uniaxial loading, a one-dimensional form of the hereditary integral expression of the stress-strain relation (Eq. 3.17) can be expressed as follows:

$$\sigma_M(t) = \int_{-\infty}^t E(t-\zeta) \frac{d\varepsilon(\zeta)}{d\zeta} d\zeta \quad (4.8)$$

where  $E(t)$  is the relaxation modulus. Considering that an elastic Hooke element is arranged in



parallel with a finite number  $N$  of Maxwell elements,  $E(t)$  can be expressed as follows:

$$E(t) = E_{\infty} + \sum_{i=1}^N E_i \exp\left(-\frac{t}{\tau_i}\right) \quad (4.9)$$

where  $E_i$  and  $\tau_i$  correspond to the rigidity and relaxation time of the  $i^{\text{th}}$  Maxwell element, respectively.  $E_{\infty}$  represents the long term modulus of the material. By substituting the deformation sinusoidal form (Eq. 4.1) into the hereditary integral expression (Eq. 4.8), the complex modulus can be expressed as follows:

$$E^*(\omega) = i\omega \int_0^{\infty} E(t) \exp(-i\omega t) dt \quad (4.10)$$

By expressing the time dependent modulus,  $E(t)$ , in its Prony series form (Eq. 4.9), the complex modulus can be expressed as follows:

$$E^* = E_{\infty} + \sum_{i=1}^N E_i \frac{(\omega\tau_i)^2}{1 + (\omega\tau_i)^2} + i \sum_{i=1}^N E_i \frac{\omega\tau_i}{1 + (\omega\tau_i)^2} \quad (4.11)$$

The storage and loss moduli are therefore expressed by:

$$E' = E_{\infty} + \sum_{i=1}^N E_i \frac{(\omega\tau_i)^2}{1 + (\omega\tau_i)^2} \quad (4.12a)$$

$$E'' = \sum_{i=1}^N E_i \frac{\omega\tau_i}{1 + (\omega\tau_i)^2} \quad (4.12b)$$

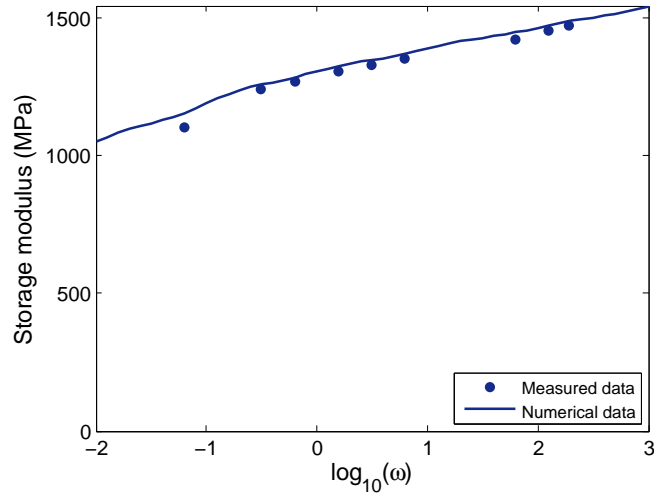
$N$  couples of  $E_i$  and  $\tau_i$  are found following a least square minimization scheme (Eq. 4.14).

$$\min_{E_i, \tau_i} \sum_{j=1}^M \left[ \left( \frac{E'(\omega_j)}{E'_{exp}(\omega_j)} - 1 \right)^2 + \left( \frac{E''(\omega_j)}{E''_{exp}(\omega_j)} - 1 \right)^2 \right] \quad (4.13)$$

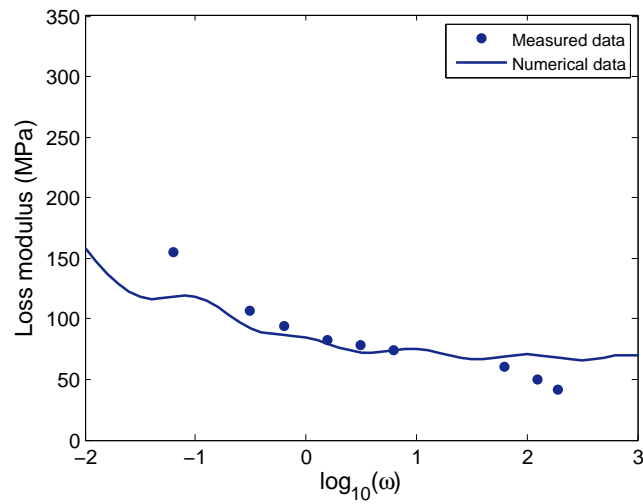
where  $E'_{exp}(\omega_j)$  and  $E''_{exp}(\omega_j)$  are obtained from measured data at pulsation  $\omega_j$ ,  $j \in \{1, \dots, M\}$ , with  $M$  the number of imposed frequencies. The identified viscoelastic parameters for a model composed of 7 Maxwell elements are listed in Table 4.2. Comparisons between the computed (from the Maxwell generalised model (Eq. 4.12)) and measured moduli are presented in Figure 4.4. It can be noted that the computed storage and loss moduli are in good agreement with the measured ones.

Table 4.2: Identified linear viscoelastic parameters of the PP matrix material

Rigidities $E_i$ (MPa)	Relaxation times $\tau_i$ (s)
620.7	$10^{+3}$
195.5	$10^{+2}$
146.6	10
124.6	1
89.59	$10^{-1}$
85.06	$10^{-2}$
79.12	$10^{-3}$
$E_\infty$ (MPa)	551.9



(a) Storage modulus



(b) Loss modulus

Figure 4.4: Comparison of measured and identified loss and storage moduli over a wide range of angular pulsation,  $\omega$

After the characterisation of the linear viscoelastic behaviour of the matrix material, next step is to characterise its non-linear plastic part (viscoplastic flow), based on monotonic tests, as described in the next paragraph.

## Monotonic tests

For the characterisation of the viscoplastic behaviour of unreinforced PP matrix, quasi-static and dynamic tests are performed at room temperature on specimens cut by water jet in the injection-moulded PP plates.

Quasi-static tensile tests are carried out using Instron E3000 electromagnetical device with a 3 kN cell force. The specimen geometry follows ISO527 norm with the shape and dimensions given in Figure 4.5(a).

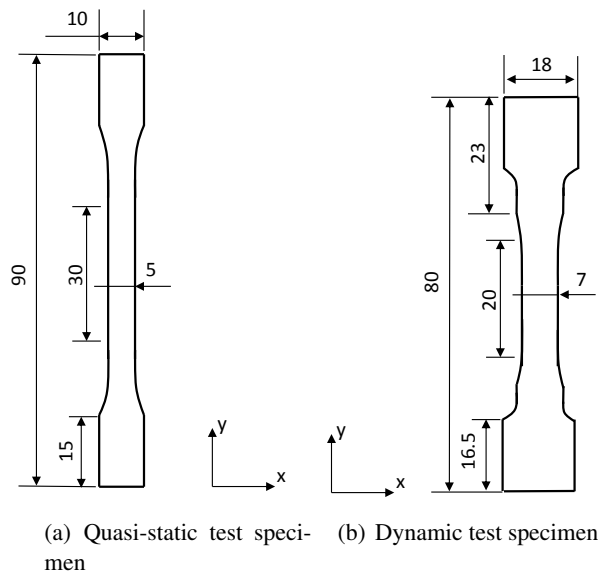


Figure 4.5: Geometry of tensile specimens (dimensions in mm)

Displacement rates of 1, 10 and 60  $\text{mm}\cdot\text{min}^{-1}$  are imposed, corresponding respectively to equivalent strain rates of  $5.55 \cdot 10^{-4} \text{ s}^{-1}$ ,  $5.55 \cdot 10^{-3} \text{ s}^{-1}$  and  $3.33 \cdot 10^{-2} \text{ s}^{-1}$  for a region of interest (ROI) of 30-mm-height. Dynamic tensile tests are carried out using Instron 65/20 hydraulic jack. A specific set-up for dynamic test, developed in LAMIH to prevent specimen loading as long as imposed test velocity is not reached, is used to clamp the specimen. The specimen geometry, shown in Figure 4.5(b), is specially designed for this set-up. The imposed displacement rates are of 10, 100 and 1000  $\text{mm}\cdot\text{s}^{-1}$ , corresponding to equivalent strain rates of  $0.5 \text{ s}^{-1}$ ,  $5 \text{ s}^{-1}$  and  $50 \text{ s}^{-1}$ , respectively. For both quasi-static and dynamic tensile tests, nominal axial stress,  $\sigma$ , is computed as the ratio

of load,  $F$ , measured by the cell force, by initial cross-section at the centre of the ROI,  $S_0$ , i.e.  $\sigma = F/S_0$ .

True displacement and true in-plane strain fields are determined using 2D Digital Image Correlation (DIC) technique [45]. A black and white random pattern is created on specimen surface. As shown in Figure 4.6, the ROI is divided into sub-pixel zones (called facets or Zone Of Interest (ZOI)), each of them being characterised by a unique signature in grey level.

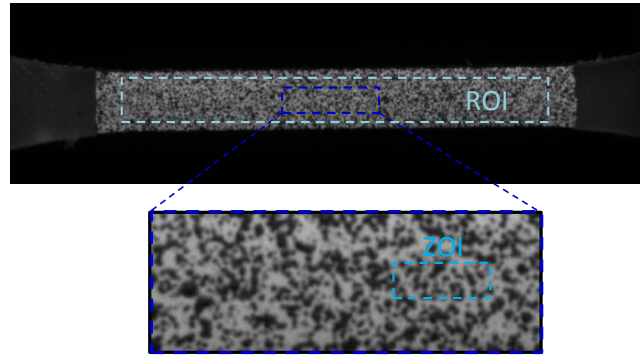


Figure 4.6: Definition of ROI and ZOI for the strain field measurement using DIC technique

The facets are tracked by DIC software (VIC 2D) with high speed cameras with different acquisition frequencies depending on the imposed strain rate (Table 4.3). In-plane displacement fields

Table 4.3: DIC acquisition rate

Strain rate	Camera frame rate (frs)
$5.55 \cdot 10^{-4} \text{ s}^{-1}$	2
$5.55 \cdot 10^{-3} \text{ s}^{-1}$	10
$3.33 \cdot 10^{-2} \text{ s}^{-1}$	100
$0.5 \text{ s}^{-1}$	600
$5 \text{ s}^{-1}$	6000
$50 \text{ s}^{-1}$	25000

of facet centres are determined with respect to a reference image, recorded at an unloaded stage. In-plane strain fields are computed at the center of all facets from displacement fields by spatial derivation.

The facet size influences displacement measurement, and so on computation of strain fields, because it has an impact on the noise/signal level recorded during the test. In order to find the best compromise between recorded noise level and spatial resolution, pre-tests with rigid body motion

are realised. Strain values are computed by DIC using different facet sizes. Strains are theoretically null during rigid body motion; the computed values are therefore representative of the noise level. Then, the facet size that allows noise minimisation together with high spatial resolution is selected. Based on the obtained results, shown in Figure 4.7, a facet size of  $21 \times 21 \text{ pix}^2$  is selected for the present case. It is to note that the same size of ZOI is used for all the tests.

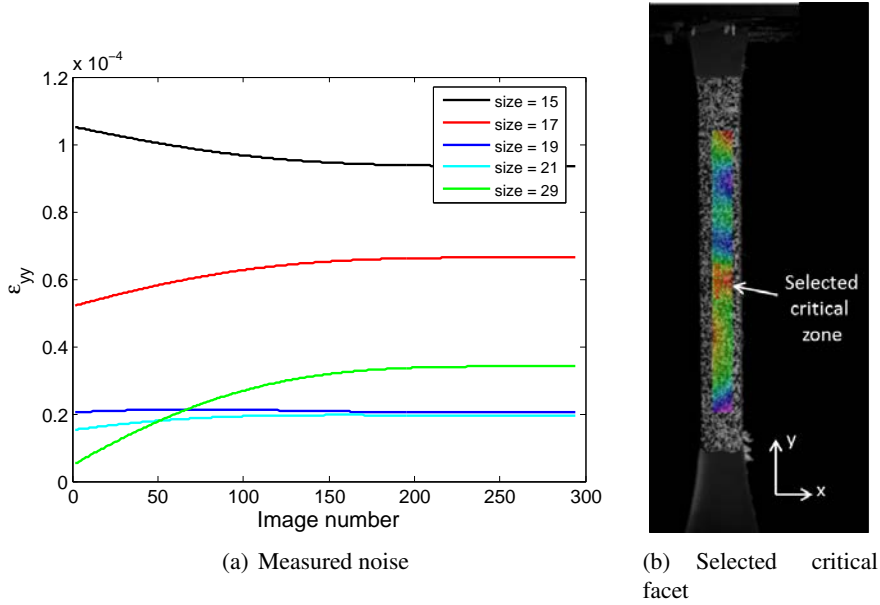


Figure 4.7: Influence of the facet size on the computation of “Axial strain” in a critical zone during a rigid body motion test

The use of the DIC technique allows to capture the heterogeneity of deformation fields in the ROI. Figure 4.8 shows the cartography of the measured strains corresponding to an imposed axial displacement of 4.5 mm of a test realised at 1 mm/min. In this figure, the evolution of the local longitudinal,  $\epsilon_{yy}$ , transversal,  $\epsilon_{xx}$ , and shear,  $\epsilon_{xy}$ , strains are also plotted for each ZOI. The heterogeneity of the strain fields is quantified by the standard deviation of the computed strain at the selected step as given in Table 4.4.

Table 4.4: Standard deviation of DIC strains (for an axial displacement of 4.5 mm at 1 mm/min)

	Standard deviation (%)
$\epsilon_{yy}$	16.53
$\epsilon_{xx}$	3.01
$\epsilon_{xy}$	19.05

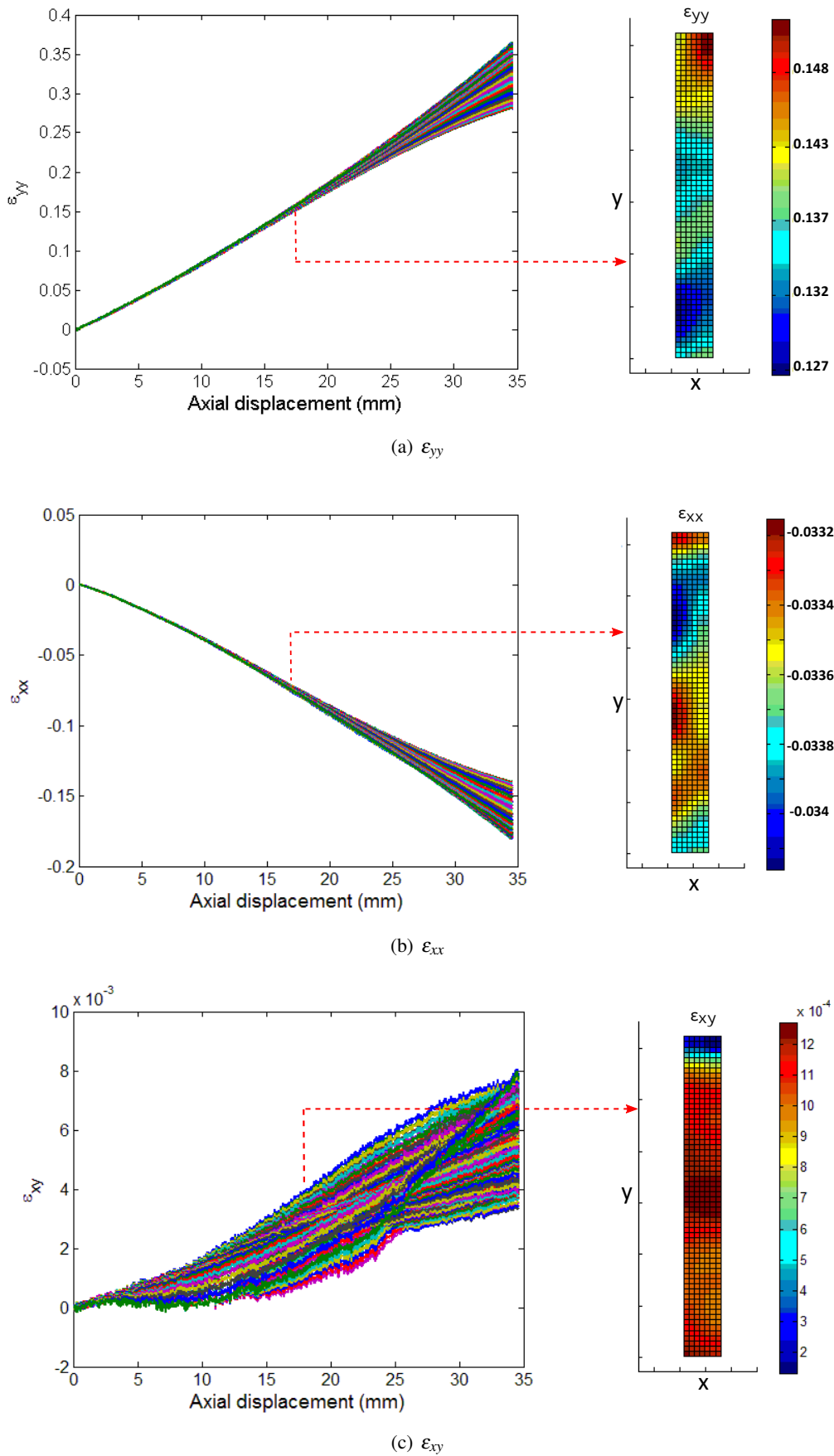
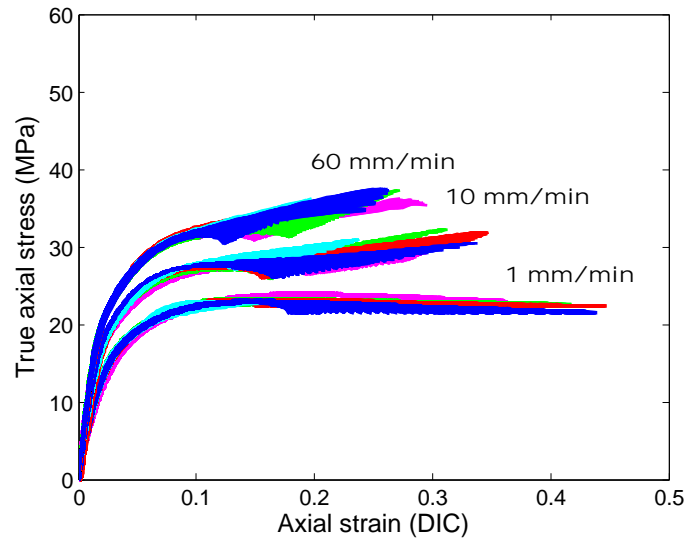
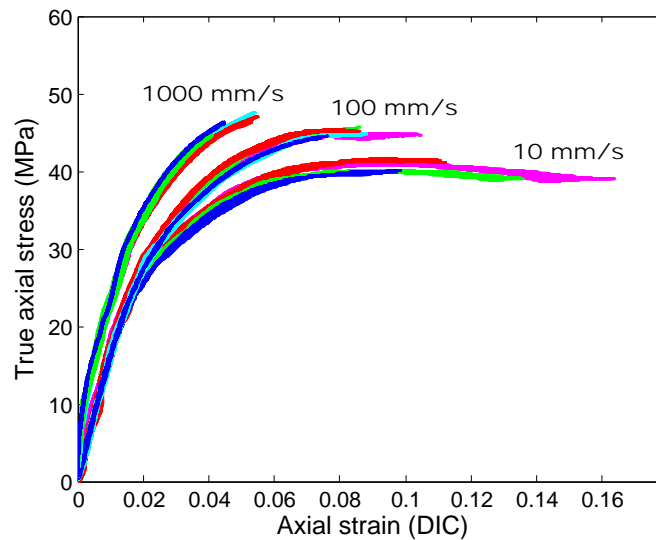


Figure 4.8: DIC strains computed during the test of PP at 1 mm/min

From results of quasi-static and dynamic tests, presented in Figure 4.9, strain-rate sensitivity of PP is obvious, with an increase of rigidity and strength with engineering strain rate simultaneously with a drop in axial strain at break.



(a) Quasi-static tests



(b) Dynamic tests

Figure 4.9: Quasi-static and dynamic tensile behaviour of PP, as measured by DIC

To further enrich the data that will be used for the characterisation of matrix behaviour, uni-axial compression tests are carried out on electromagnetic device INSTRON E3000 at crosshead speeds of  $0.08 \text{ mm}\cdot\text{min}^{-1}$  and  $0.8 \text{ mm}\cdot\text{min}^{-1}$  (Figure 4.10). Specimens are cylinders with a diameter of 5 mm and a height of 2.5 mm cut by water jet in the PP injected plates. The corresponding equivalent

strain rates are therefore of  $5 \cdot 10^{-4} s^{-1}$  and  $5 \cdot 10^{-3} s^{-1}$ , that is to say similar to those applied during quasi-static tensile tests.

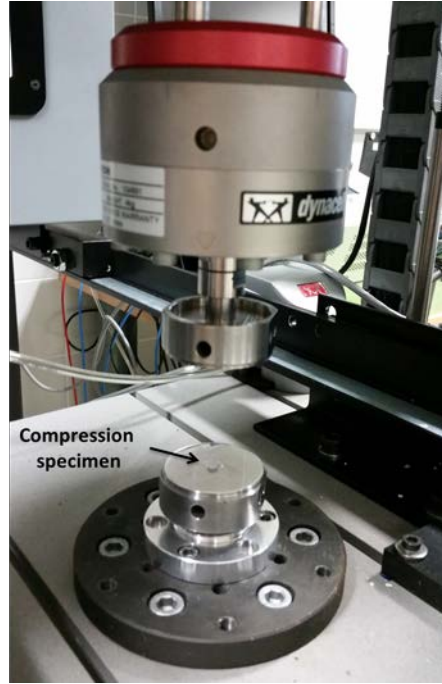


Figure 4.10: Compression test set-up

Results of compression tests are presented in Figure 4.11 where five specimens are tested for each loading speed.

Monotonic uniaxial tests are used to identify parameters of the matrix viscoplastic behaviour law. As presented in Section 3.2.1.3, the non-isochoric flow of the matrix material is modelled in the framework of non-associated viscoplasticity and a dissipation potential is introduced to capture the effect of volume change in the flow behaviour. In this modelling, an expansion,  $a^+$ , and compaction,  $a^-$ , parameters of the dissipation potential (Eq. 3.30) are associated, respectively, to tension and compression flow behaviour. The expansion can be characterised, using tensile tests, from the determination of the (visco)plastic Poisson coefficient,  $\nu_p$ , which is the ratio between the transverse,  $\epsilon_{xx}^{vp}$ , and longitudinal,  $\epsilon_{yy}^{vp}$ , viscoplastic strain components, such as:

$$\nu_p = -\frac{\epsilon_{xx}^{vp}}{\epsilon_{yy}^{vp}} \quad (4.14)$$

$\nu_p$  is calculated in all ZOI and for all loading speeds (i.e., quasi-static and dynamic) by neglecting



the elastic part of the total strain (i.e.  $\varepsilon_{ij}^{vp} \simeq \varepsilon_{ij} \quad \forall ij$ ).

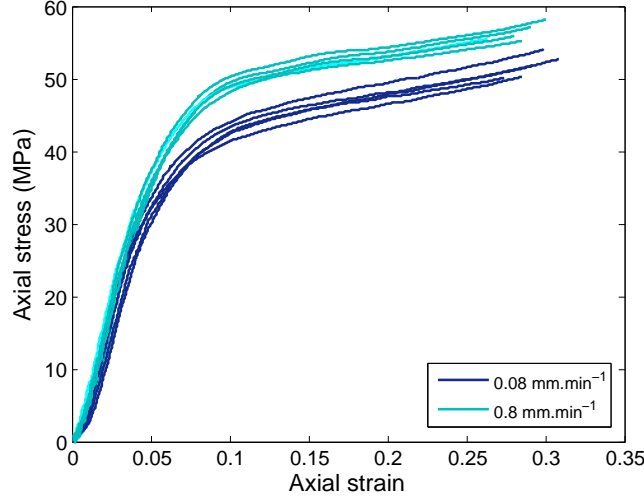


Figure 4.11: Compression behaviour of PP at two different strain rates

Figure 4.12 shows the evolution of the (visco)plastic Poisson ratio in function of true axial strain for all loading speeds and in all ZOI.

It can be seen that the evolution is scattered for the very low strain values and tends to be constant for higher ones (when  $\varepsilon^{ve}$  actually becomes neglectible compared to  $\varepsilon^{vp}$ ). The (visco)plastic Poisson ratio is therefore identified for axial strain level higher than 0.02. As for this strain values  $v_p$  is rather constant, it can be expressed in terms of incremental VP strain components:

$$v_p \simeq -\frac{\Delta \varepsilon_{xx}^{vp}}{\Delta \varepsilon_{yy}^{vp}} \quad (4.15)$$

Considering the incremental form of the VP strain tensor under tensile loading (i.e.  $\langle -I_1 \rangle = 0$  (Eq. 4.16)) the expression of  $v_p$  is given by Eq. 4.17.

$$\Delta \varepsilon^{vp} = \Delta \lambda \frac{\frac{3}{2} \sigma_{M,dev} + \frac{1}{9} (a^+ \langle I_1 \rangle + a^- \langle -I_1 \rangle) I}{\sqrt{3I_2 + \frac{1}{27} (a^+ \langle I_1 \rangle^2 + a^- \langle -I_1 \rangle^2)}} \quad (4.16)$$

$$v_p = -\frac{\frac{3}{2} \sigma_{M,dev,xx} + \frac{1}{9} a^+ I_1}{\frac{3}{2} \sigma_{M,dev,yy} + \frac{1}{9} a^+ I_1} \quad (4.17)$$

By definition of the deviatoric stress tensor,  $\sigma_{M,dev}$ , Eq. (4.17) becomes:

$$v_p = -\frac{\frac{3}{2} \left(-\frac{1}{3}I_1\right) + \frac{1}{9}a^+I_1}{\frac{3}{2} \left(\sigma_{yy} - \frac{1}{3}I_1\right) + \frac{1}{9}a^+I_1} \quad (4.18)$$

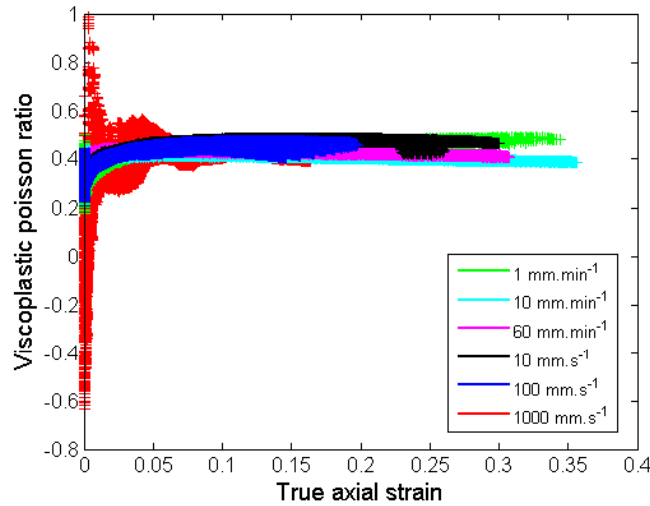


Figure 4.12: Evolution of the viscoplastic Poisson ratio versus true axial strain

The expression of the expansion parameter  $a^+$  is finally given by:

$$a^+ = \frac{9}{2} \left( \frac{1 - 2v_p}{1 + v_p} \right) \quad (4.19)$$

With an identified value of  $v_p$  equal to 0.43, the expansion parameter  $a^+$  is equal to 0.61. A similar analysis should be done under uniaxial compression loading in order to identify the compaction parameter  $a^-$ . Unfortunately the small size of the compression specimen did not allow the use of Digital Image Correlation technique and only axial displacements were measured by optical extensometry. Therefore, incompressibility will be assumed in the case of compression loading and  $a^-$  will be set to 0 in the following. It is worth noting that it will not biased the validation of the SFRC behaviour modelling as long as only tensile loadings are considered.

The use of Digital Image Correlation technique allows the determination of local strain but also local strain rate throughout the test. Then, using the assumption of transverse isotropy, the true tensile stress of each ZOI can be calculated as follows:

$$\sigma_{yy_i} = \frac{F}{S_0} \exp(-2\varepsilon_{xx_i}) \quad (4.20)$$

where  $\varepsilon_{xx_i}$  is the true transverse strain of the  $i^{th}$  ZOI. According to the  $SE\dot{E}$  method, developed by Lauro et al. [116], points of coordinates  $(\sigma_{yy_i}, e_i, \dot{e}_i)$  are plotted in the stress, strain and strain rate space to form the  $SE\dot{E}$  (“Sigma, Epsilon, Epsilon dot”) surface.  $e_i$  is the equivalent true strain expressed as follows:

$$e_i = \int_t \sqrt{\frac{2}{3} \dot{\varepsilon} : \dot{\varepsilon}} dt \quad (4.21)$$

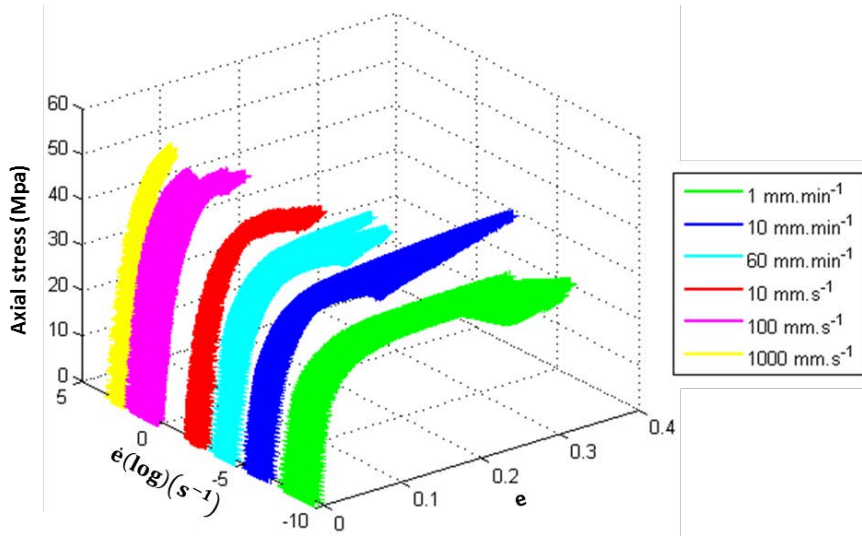


Figure 4.13: Experimentally obtained behaviour surface with the  $SE\dot{E}$  method

This surface represents material’s behaviour for a large strain rate range (Figure 4.13). The hardening and viscoplastic parameters ( $h_1, h_2, h_3, m$  and  $\dot{\kappa}_0$ ) are determined by fitting the expression (Eq. 3.34) with the behaviour surface (Figure 4.14). Note that the equivalent strain and equivalent strain rate are assumed here to be equal to the equivalent viscoplastic strain,  $h$ , and equivalent viscoplastic strain rate,  $\dot{h}$ , respectively. It is to note that in the constitutive model the yield stress,  $\sigma_f$ , is identified as the stress from which the true stress-strain curve becomes non-linear (7 MPa). This leads to a true equivalent viscoplastic threshold of about 0.5 % which justifies the later assumption.

The hydrostatic pressure dependency of the matrix viscoplastic flow is highlighted in Figure 4.15 where tensile and compression behaviour at the same strain rate of  $5.55 \cdot 10^{-4} s^{-1}$  are compared. From these results, it is deduced that the uniaxial compression response is stiffer than the uniaxial tensile stress response.

The pressure dependency parameter  $\eta$ , introduced in the Raghava yield surface (Eq. 3.27), is defined as the ratio of the compression and tension initial yield stresses. For its identification,

tensile and compression yield stresses must be measured from the tests realised at the same strain rate. The above tests are therefore considered, with yield stresses corresponding to the upper limits of the linear part of the behaviour law. Values of 23 MPa and 7 MPa are identified for the tensile and compression tests, respectively, corresponding to a value of 3.28 for  $\eta$ .

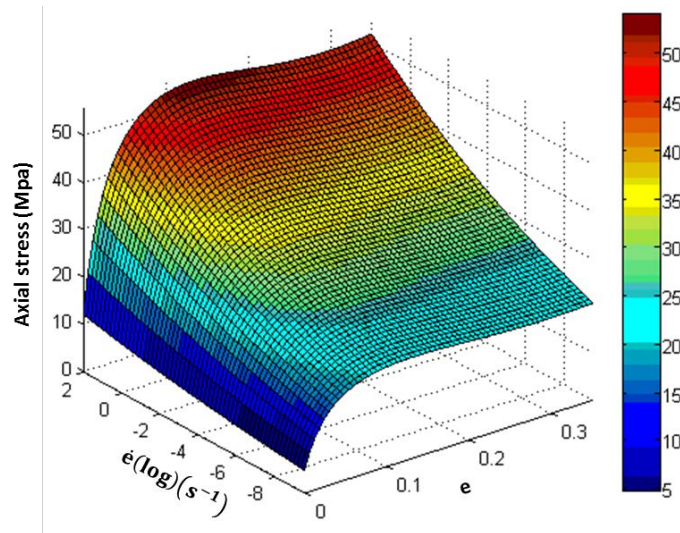


Figure 4.14: Behaviour laws obtained with the  $SE\dot{E}$  method

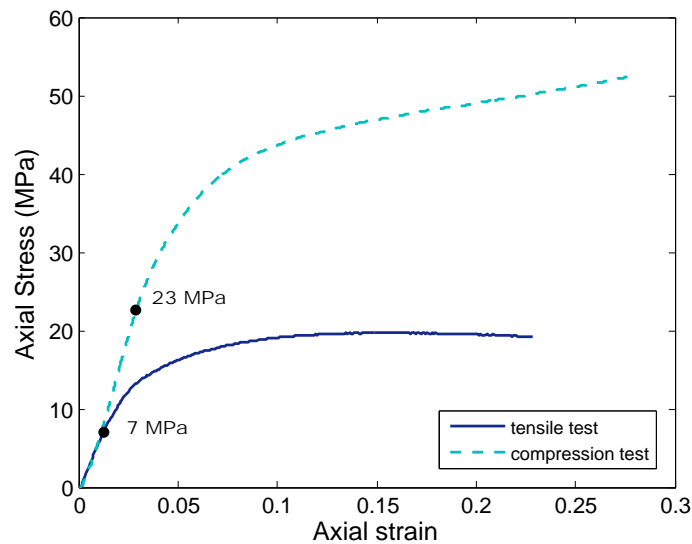


Figure 4.15: Tensile and compression behaviour of PP for the identification of the parameter of hydrostatic pressure dependency (at  $1 \text{ mm}\cdot\text{min}^{-1}$ )

Based on those tests, all parameters involved in the matrix constitutive model are finally identified.

Viscoplastic parameters are listed in Table 4.5 (it is reminded that viscoelastic parameters are listed in Table 4.2)

Table 4.5: Viscoplastic parameters of PP matrix material

Parameters	Value
$\sigma_t$ (3.27)	7 MPa
$h_1$ (3.28)	35.40 MPa
$h_2$ (3.28)	2.17
$h_3$ (3.28)	58.78
$\dot{\kappa}_0$ (3.34)	$10^{-5} s^{-1}$
$m$ (3.34)	0.035
$a^+$ (3.30)	0.61
$a^-$ (3.30)	0
$\eta$ (3.27)	3.28

#### 4.1.1.2 Validation of the implementation of matrix material model

Once all parameters of PP matrix VE-VP behaviour are identified, final step is to assess the relevance of the implemented constitutive model for the matrix material through its capacity to reproduce the experimental response of PP material over a relatively large range of strain rate. To this end, the constitutive equations presented in Section 2 are implemented in Abaqus 6.11 subroutine VUMAT (explicit temporal integration scheme). Uniaxial tensile tests of PP matrix are then simulated, using the parameters previously identified (Tables 4.2 and 4.5). Obviously, fibre volume fraction is null in the present numerical tests. Tensile tests are simulated at the same quasi-static (1, 10 and 60 mm/min) and dynamic (10, 100 and 1000 mm/s) loading speeds as during experiments. 8 nodes, full integration elements (C3D8) are used. All degrees of freedom are locked at the basis of the specimen and the loading consists on a prescribed monotonic velocity on nodes of the upper edge. Numerical results are compared to experimental data (averaged over the five tests realised for each loading speed) in Figure 4.16. In this figure, numerical and experimental data are averaged upon the ROI (height of 15 and 20 mm in quasi-static and dynamic tests, respectively). In fact, strain fields obtained both numerically and from DIC measurements were verified to be homogeneous enough in the ROI so that the comparison of averaged strains is reliable for the validation of the model. The presented results show that the numerical model is in agreement with experimental data at the different investigated loading rates. These results validate

the developed constitutive laws and their implementation for the prediction of VE-VP behaviour of thermoplastics over a wide range of strain rate (with a maximum standard deviation value of 11.2%).

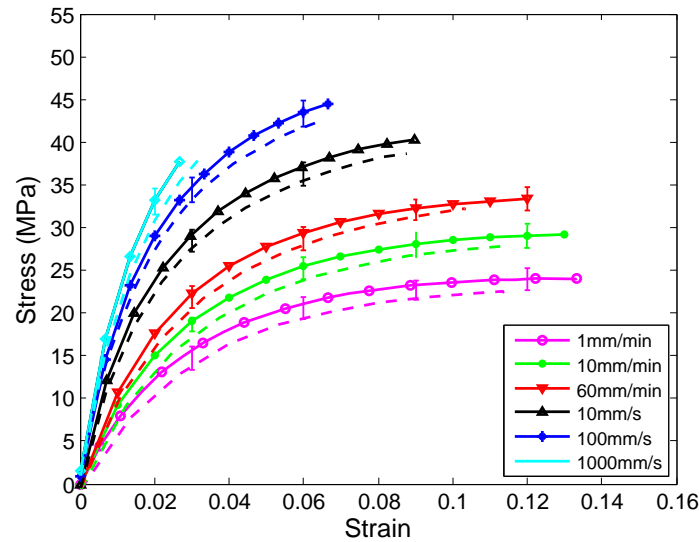


Figure 4.16: Comparison between modelled and experimental tensile behaviour of PP at different loading rates (Continuous lines = Experimental data, Dashed lines = Numerical data) with scattering bars

#### 4.1.2 Extension of the modelling to PP matrix reinforced with short glass fibres

The constitutive laws of the thermoplastic matrix behaviour model being characterised and their implementation validated, this section now focuses on the validation of the modelling of short-glass-fibre-reinforced PP composites. More precisely, the composites under investigation are made of a homopolymer polypropylene (PP) matrix reinforced with 30 wt.% or 40 wt.% of short-glass fibres with chemical coupling. Those composites will be called PP-30GF and PP-40GF, respectively, and are supplied by Albis. Technical information about the composite materials are given in Table 4.6.

Composite plates, 200 mm-edge-squares with a thickness of about 2.5 mm, are injection moulded

Table 4.6: Supplier specifications of the composites materials

	Commercial grade	MFR ( $\text{g} \cdot (10\text{min})^{-1}$ )	Density ( $\text{g} \cdot \text{cm}^{-3}$ )
PP-30GF	ALTECH PP-H A 2030/159 GF30 CP	2	1.12
PP-40GF	ALTECH PP-H A 2040/159 GF40 CP	3	1.22

following the process conditions prescribed by the supplier.

In order to model the behaviour of the composites using the constitutive laws developed in this work, their microstructure (in terms of fibre length, radius and distribution of orientation) and the fibre/matrix interfacial shear strength must be characterised. To this end, extensive campaigns of micro-computed microtomography (section 4.1.2.1) and tensile tests (section 4.1.2.2) are performed. Quasi-static and dynamic specimens of PP-30GF and PP-40GF, with geometries identical to the PP ones (Figure 4.5), are cut at different angles,  $\theta$ , with respect to the injection flow direction (IFD) ( $\theta = 0^\circ, 20^\circ, 45^\circ, 60^\circ$  and  $90^\circ$ , Figure 4.17) in order to enrich data with large range of distributions of fibre orientation.

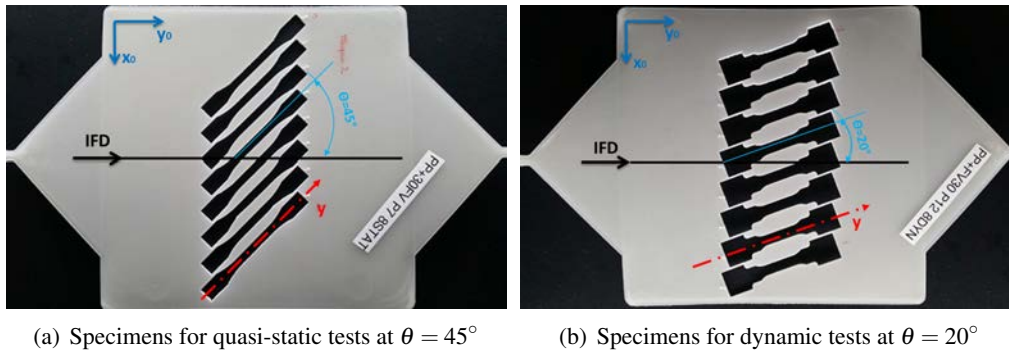


Figure 4.17: Orientation of tensile specimens in injection-moulded plates

#### 4.1.2.1 Microstructure characterisation using micro-computed microtomography

The microstructure of the SFRC is investigated aiming at the characterisation of fibres' geometrical properties and orientation. X-ray micro-computed tomography ( $\mu$ -CT) is used to scan central volume of some selected specimens. The micro-computed tomography is performed using high-resolution microtomograph Skyscan 1172 (Bruker Micro CT). A rotation step of  $0.4^\circ$ , voltage of 30 kV and current of  $40 \mu\text{A}$  are used, leading to a spatial resolution (voxel size) of  $3.87 \mu\text{m}$ . Some quasi-static specimens (ISO527-type), cut at different angles  $\theta$  with respect to the injection flow direction (IFD) ( $\theta = 0^\circ, 20^\circ, 45^\circ, 60^\circ$  and  $90^\circ$ ), are selected for micro-tomography analysis.

As shown in Figure 4.18, a volume centered on the specimen region of interest (ROI), with a height of about 5 mm and covering all specimen width and thickness, is scanned. An example of 3D representation of the PP-30GF microstructure, obtained using data acquired by  $\mu$ -CT, is shown in Figure 4.19. Reconstructed 3D microstructures show that the vast majority of fibres present a very low out-of-plane angle (i.e. with respect to the  $(x,y)$  plane, with  $y$  the specimen axis and  $z$  oriented along thickness). In all the following, fibres are therefore assumed to have in-plane



orientation. Sets of 2D greyscale images, in the  $(x,y)$  plane, are extracted from slices of the 3D view, at regular spaced positions in thickness direction.

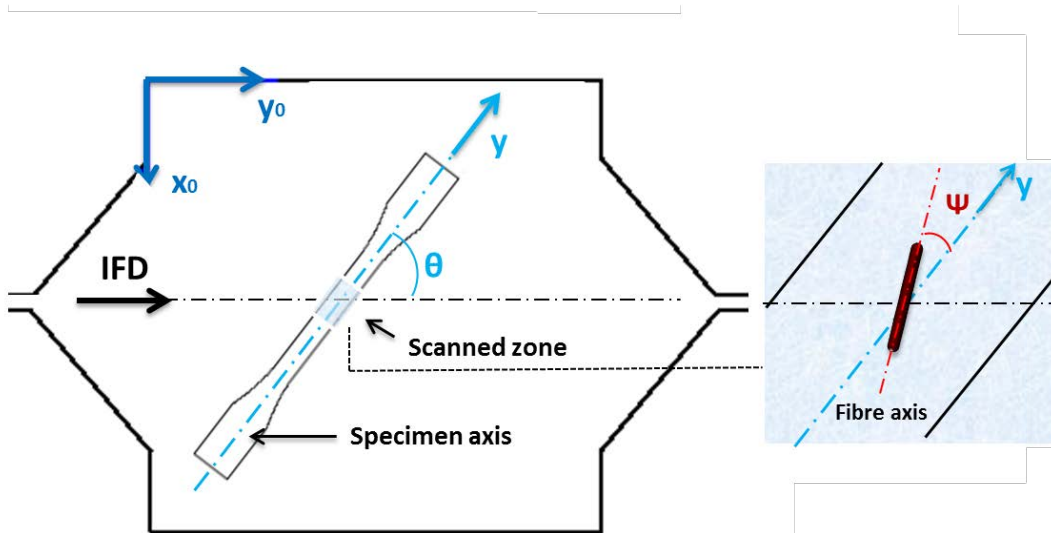


Figure 4.18: Scanned volume and definition of angles  $\theta$  and  $\psi$

As shown in Figure 4.20, fibres are first isolated from matrix material, using Fiji tools of Image J software [114], by applying a grey-level thresholding to the images (based on Otsu method [115]). Grey-scaled images are then filtered by removing outliers of a size equal to 2 pix.

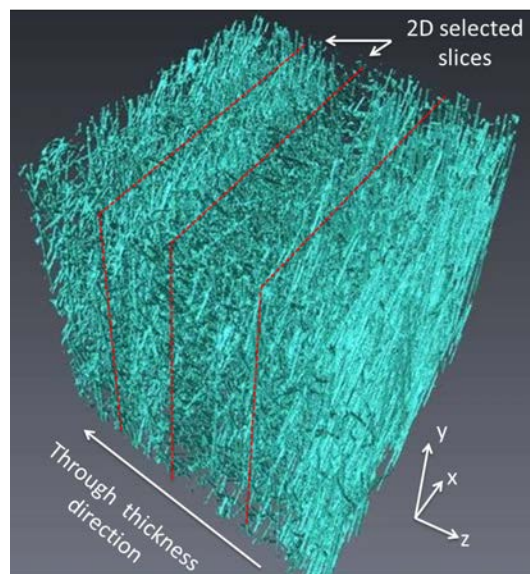


Figure 4.19: Reconstructed 3D microstructure of PP-30GF by micro-computed tomography



Fiji tools of structure detection and analysis are applied in order to identify and count fibres and determine their characteristics. Thus, average fibre length and diameter are determined and are respectively equal to  $750 \mu\text{m}$  and  $18 \mu\text{m}$ . Distributions of fibre orientation are obtained in the form of directionality histograms with density-angle data for each of the selected 2D greyscale images.

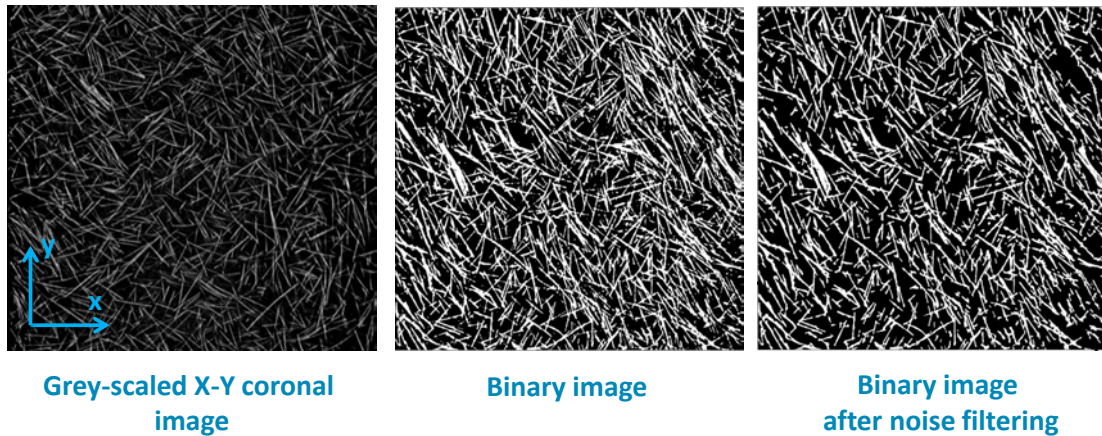


Figure 4.20: Treatment of 2D grey-scaled images obtained from  $\mu$ -CT scan of a PP-30GF specimen

In these diagrams, density of fibres characterised by an angle  $\psi$  with respect to specimen axis within the intervals  $[\alpha; \alpha + 2^\circ]$ , for  $\alpha$  varying from  $-90^\circ$  to  $86^\circ$ , are determined. Data obtained for a PP-30GF specimen cut at  $\theta = 0^\circ$ , i.e. along IFD, are shown in Figure 4.21, for all the analysed grey-scaled images.

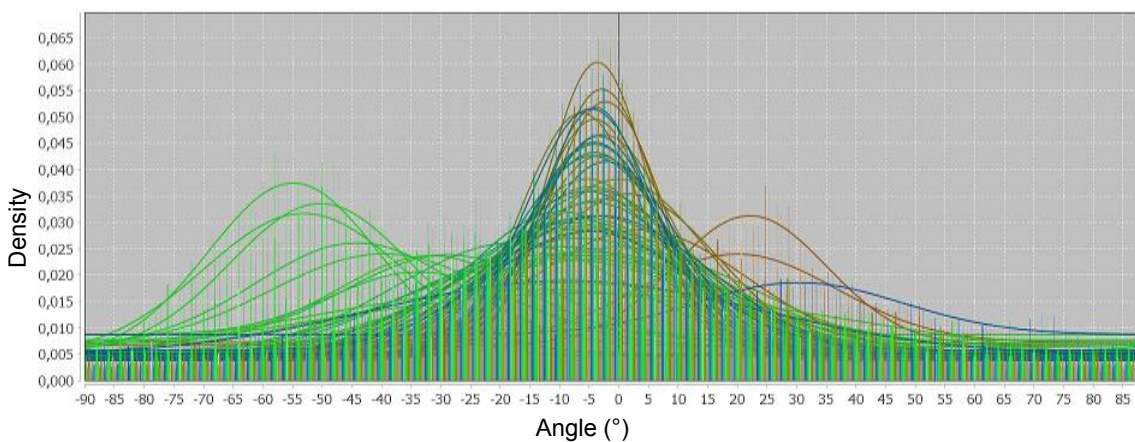


Figure 4.21: Example of directionality histogram obtained for a PP-30GF specimen cut at  $0^\circ$  with respect to the IFD

It can be seen that a preferential orientation equal to  $\psi = 0^\circ$  is detected. A variation of fibre orientation through specimen thickness is also noticed and is highlighted in Figure 4.22. Fibre orientation evolves in the thickness direction in accordance with the well-known skin-shell-core phenomenon [13]. In fact, average angle of fibre orientation increases (close to  $45^\circ$ ) in plate skins, i.e. at the vicinity of mould walls where fibres tend to orient randomly, then decreases in shell layers, where fibres are preferentially oriented along IFD, and increases again in core layer. This layered structure results, as explained in Chapter 2, from the combination of shear flow and fountain flow in injection moulded process [15].

Data obtained for scanned  $\theta$ -specimens (i.e. characterised by a cutting angle  $\theta$ ) are averaged through the whole specimen thickness for both composites, PP-30GF and PP-40GF, in order to obtain distributions of fibre orientation representative of the whole scanned volume.

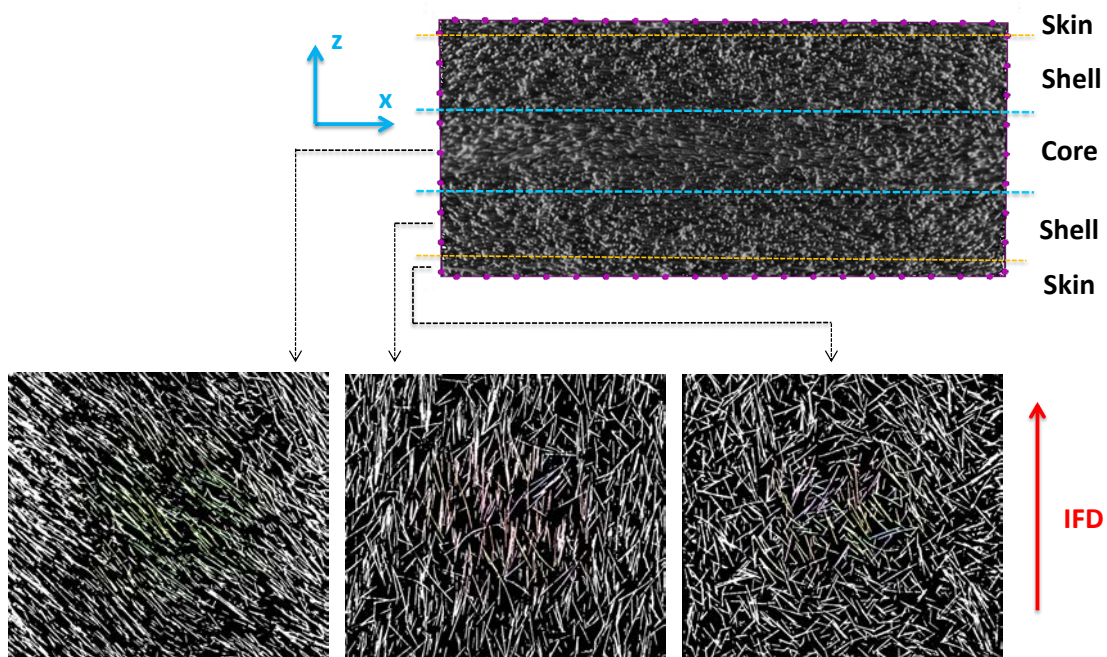


Figure 4.22: Variation of the fibre orientation through the specimen thickness (Skin-Shell-Core structure)

It is worth noting that to reduce the time cost of data treatment, the selection of the grey-scaled images in thickness direction is made with a step of 10 images (equivalent to  $41 \mu\text{m}$ ), thus allowing a reduction by a ratio of 7.25 of the computational cost. In order to validate this choice, a comparison between results obtained with a step equal to 1 (i.e. all images through the thickness are included in volume averaged distributions of fibre orientation) and a step of 10 (equivalent

to  $41\ \mu\text{m}$ ) is performed. Figure 4.23 shows that there is only a slight effect on the obtained data (with a maximum standard deviation value of 3%), which validates the choice of a step equal to 10. In those histograms, one can note that fibres are preferentially oriented to  $0^\circ$  with specimen axis, which is consistent with a cutting angle,  $\theta$ , equal to  $0^\circ$  with respect to IFD. The secondary peak observed at about  $50^\circ$  results from the core layer of the specimen where fibres are more “transversally” oriented.

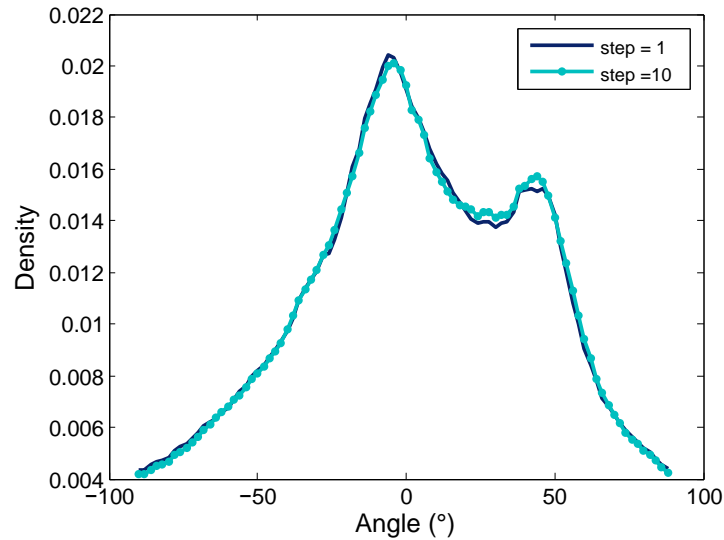
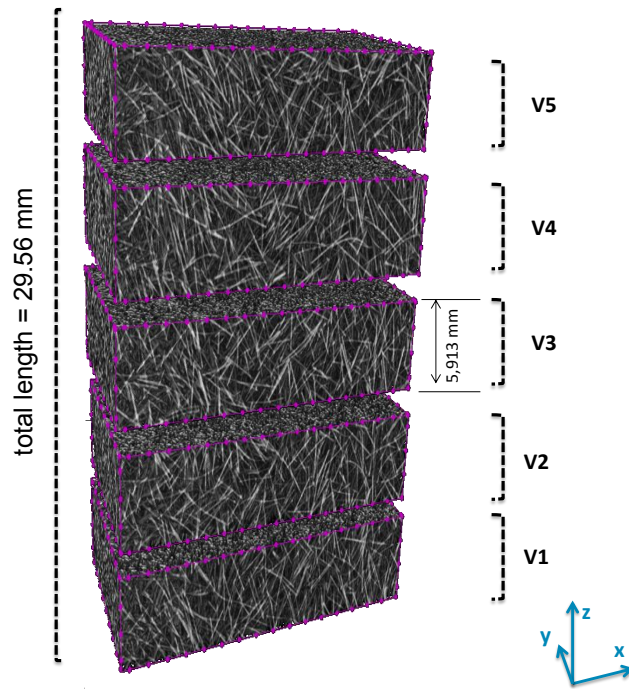
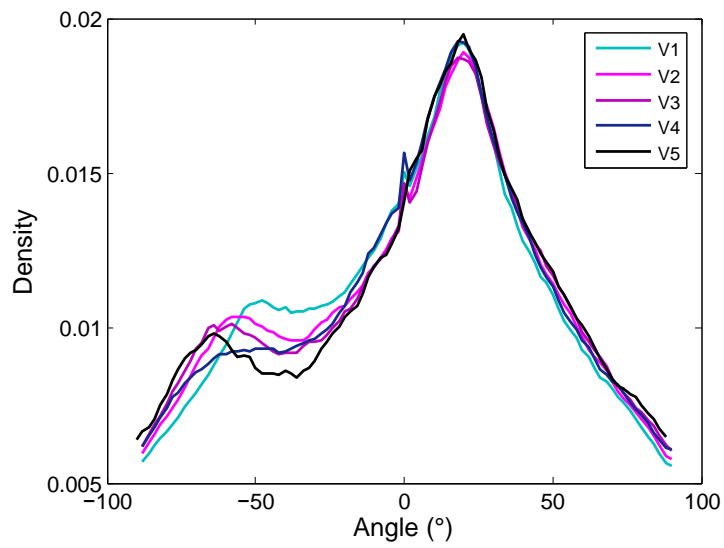


Figure 4.23: Comparison of results obtained with a “step” of 1 and 10 from a PP-30GF specimen at an angle  $\theta = 0^\circ$  for the selection of the 2D grey-scaled images through the thickness

As mentioned before, scanned volumes are centred on specimen ROI with a height of approximately 5 mm. To verify the repeatability of the distribution of fibre orientation on the whole specimen ROI, other volumes are scanned along specimen axis. The different scanned zones of the specimen ROI are shown in Figure 4.24(a). It can be seen in Figure 4.24(b) that distributions of orientation obtained in all scanned volumes of the ROI are similar to that obtained in the central volume (V3). That result is valuable from a modelling point a view since it validates the modelling of fibre distribution of orientation in the whole specimen’s ROI from  $\mu$ -CT scans performed over a reduced part of the ROI.



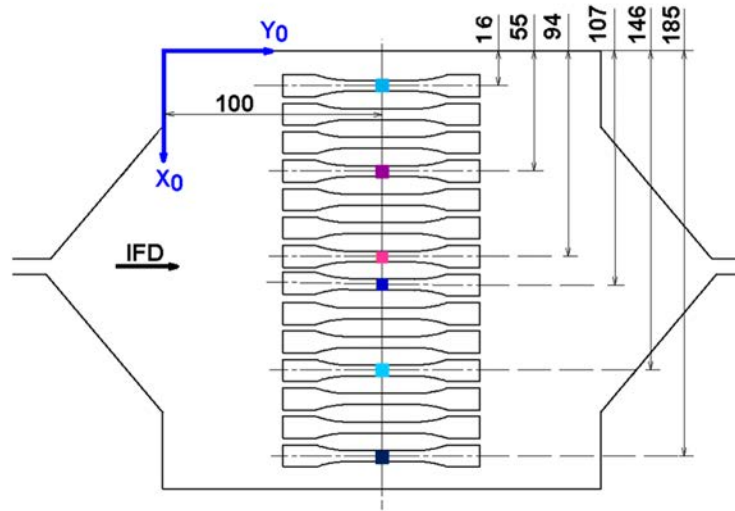
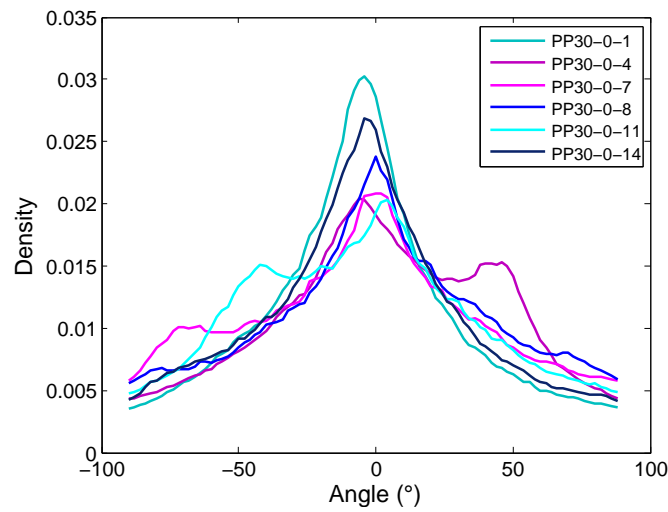
(a) Different scanned volumes over the specimen ROI



(b) Distributions of fibre orientation in the different scanned volumes

Figure 4.24: Comparison of scan results at different locations over the specimen ROI

Distribution of fibre orientation obtained in central scanned volumes (step of 10 images through thickness direction) for the composites PP-30GF and PP-40GF and for specimens with different cutting angles are presented in Figures 4.25 to 4.27.

(a) Location of  $0^\circ$ -specimens in the injection moulded plate(b) Distribution of fibre orientation in different specimens cut at  $\theta = 0^\circ$ Figure 4.25: Fibre orientation of specimens cut at different locations and  $0^\circ$  with respect to IFD for PP-30GF



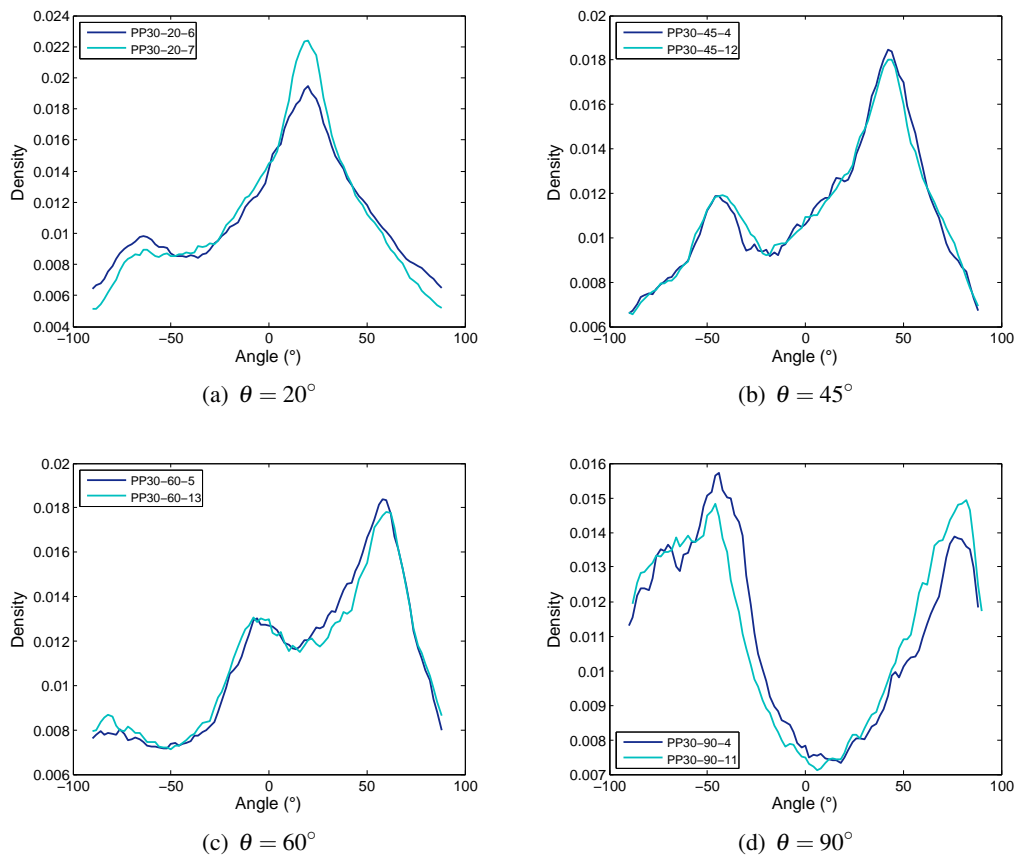


Figure 4.26: Fibre orientation of specimens cut at angles equal to  $20^\circ$ ,  $45^\circ$ ,  $60^\circ$  and  $90^\circ$  with respect to IFD for PP-30GF

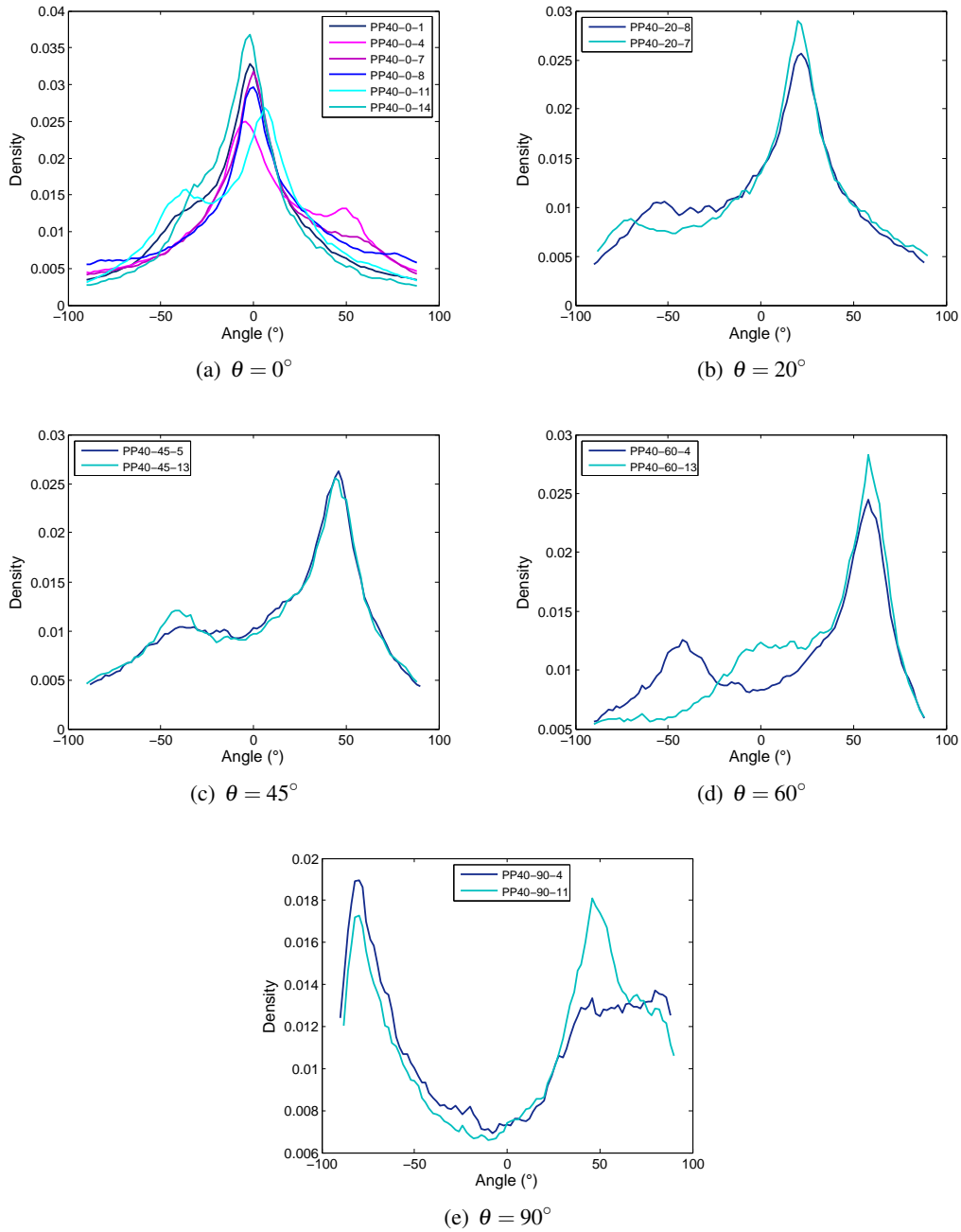


Figure 4.27: Fibre orientation histograms of specimens cut at angles equal to  $0^\circ$ ,  $20^\circ$ ,  $45^\circ$ ,  $60^\circ$  and  $90^\circ$  with respect to IFD for PP-40GF

In the case of PP-30GF, fibre orientations in  $0^\circ$ -specimens are distributed around the value  $0^\circ$  as a preferential orientation (Figure 4.25(b)). More generally, preferential orientation of fibres is IFD, i.e. equal to  $\pm\theta$  with respect to the specimen axis for all values of  $\theta$ , as expected (Figure 4.26).

This property is more pronounced in the case of PP-40GF (Figure 4.27), with a higher fraction of fibres oriented in IFD, as indicated by higher values of density for an angle equal to  $\theta$ . This may be due to the more pronounced shear flow and more fibre to fibre interactions at relatively high fibre content, i.e. fibres are more likely to inhibit rotation of surrounding fibres during the flow process. Moreover, histograms obtained for  $0^\circ$ -specimens show that fibres distribution of orientation depends on specimen location in the plate. For instance, as illustrated by specimen 0-1 of the PP-30GF (Figure 4.25), the distribution curve tends to be sharper around IFD direction near plate edge (i.e. fraction of fibres that are oriented in IFD increases).

This characterisation of the microstructure of some selected specimens can be taken into consideration as input data for the implementation of SFRC behaviour model. According to the concept of “fibre families” of the present approach, fibre distributions of orientations are modelled in the form of discrete histograms where all fibres characterised by an angle  $\psi$  within the interval  $[\alpha; \alpha + 10^\circ[$ , for  $\alpha$  varying from  $0^\circ$  to  $80^\circ$ , are grouped into the same family. This way, 9 fibre families are created to model fibre distribution of orientation. Discretised data, obtained for different  $\theta$ -specimens (i.e. characterised by a cutting angle  $\theta$ ) are presented in Figures 4.28 and 4.29 for the PP-30GF and PP-40GF composites, respectively. In those figures, the density calculated over the  $i^{th}$  interval (i.e.  $[10^\circ(i-1); 10^\circ i]$ ) is attributed to an angle of orientation equal to  $10^\circ(i-1) + 5^\circ$  for the  $i^{th}$  family, with  $i \in \{1, \dots, 9\}$ .



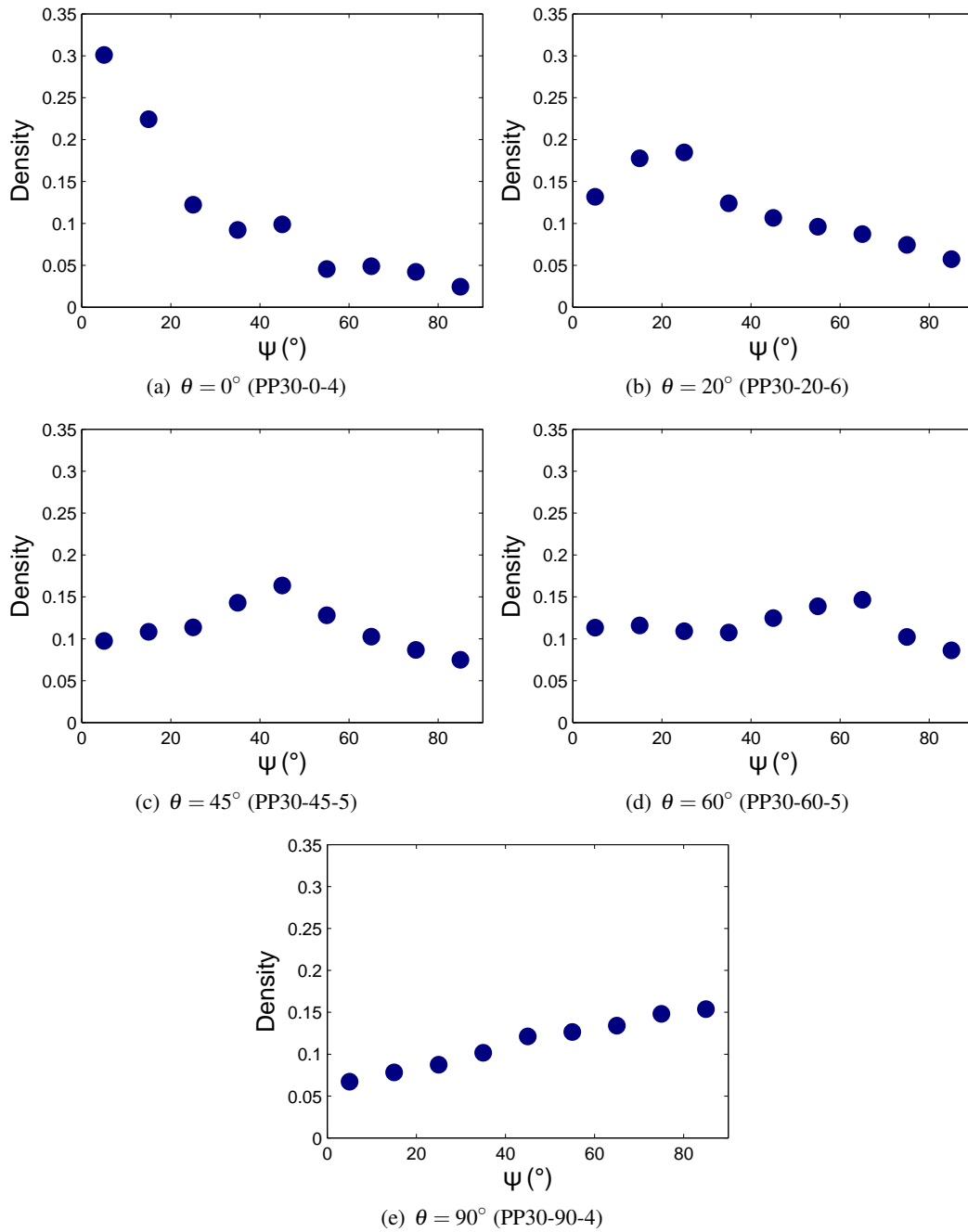


Figure 4.28: Fibre distribution of orientation of specimens cut at angles equal to  $0^\circ$ ,  $20^\circ$ ,  $45^\circ$ ,  $60^\circ$  and  $90^\circ$  with respect to IFD for PP-30GF

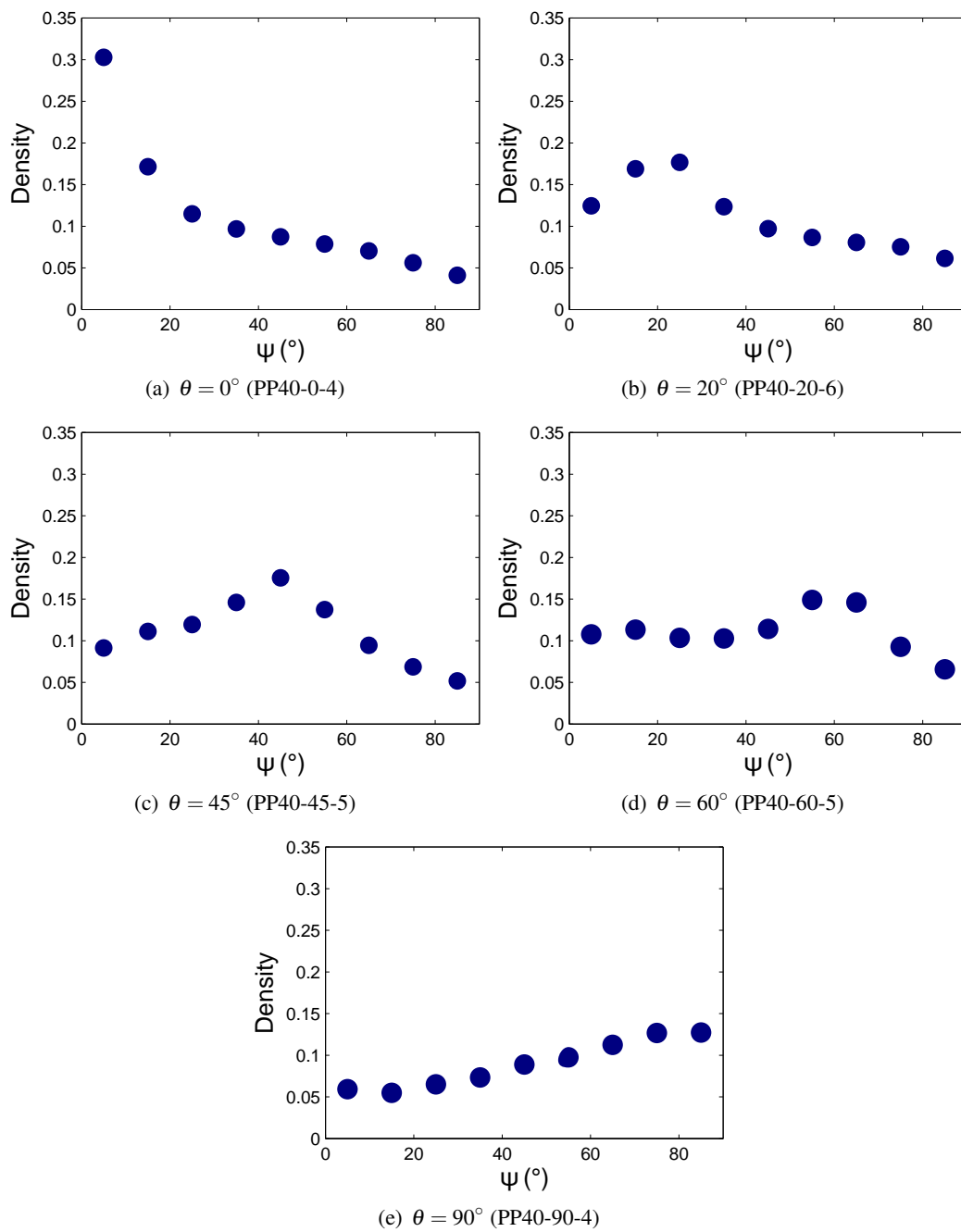


Figure 4.29: Fibre distribution of orientation of specimens cut at angles equal to  $0^\circ$ ,  $20^\circ$ ,  $45^\circ$ ,  $60^\circ$  and  $90^\circ$  with respect to IFD for PP-40GF

#### 4.1.2.2 Monotonic tensile tests of PP-30GF and PP-40GF and identification of the fibre-matrix interfacial shear strength

In order to fully characterise the behaviour model of the short-glass fibre reinforced polypropylene, only one parameter is actually missing, namely the fibre/matrix interfacial shear strength (IFSS,  $\tau$  - cf section 3.2.2). In fact, this parameter depends in particular on the nature of the matrix and fibres, process conditions and fibre volume fraction [118, 119, 120]. Yet, the experimental identification of the IFSS is not in the scope of this work. Therefore, it will be determined as the one leading to the best fit between numerically simulated and experimental results in the case of a PP-30GF and PP-40GF specimens tested at  $0^\circ$  and at the lowest loading rate (i.e.  $1 \text{ mm}\cdot\text{min}^{-1}$  - see hereafter). In practice, many other tensile tests were actually performed on composite materials with the aim to validate the implementation of SFRC behaviour model for different cutting angles and over a wide range of strain-rate. Although the validation of the model is not addressed in this section (but in the next one), all tensile tests are first presented and analysed in the following, for clarity.

Quasi-static and dynamic tensile tests are performed on composites PP-30GF and PP-40GF at various loading speeds and for all values of cutting angle  $\theta$ . Same testing devices and specimen geometries as for PP are used, as well as same imposed quasi-static and dynamic displacement rates (Section 4.1.1.1). As tensile behaviour of the composite materials is expected to be more brittle than that of unreinforced PP and therefore limited to low strain levels, DIC technique is not used for PP-30GF and PP-40GF. Instead, axial displacements are measured by optical extensometry, i.e. non-contact elongation measurement based on motion tracking of black-and-white transition lines. For quasi-static tests, optical extensometer ZS16D (CCD line scan sensor - Rudolf GmbH), with a precision of  $3 \mu\text{m}$  over 50 mm, is used. Elongation of a white-painted area of 15-mm-height, centred in the ROI, is followed (Figure 4.30(a)). Axial strain is computed as the ratio of measured axial elongation by the initial length of 15 mm. For dynamic tests, optical extensometer 200XR (Rudolf GmbH - precision of  $5 \mu\text{m}$  over 50 mm), which allows higher acquisition frequency, is used with a tracked zone covering all specimen's ROI (i.e. gauge length of 20 mm) (Figure 4.30(b)).

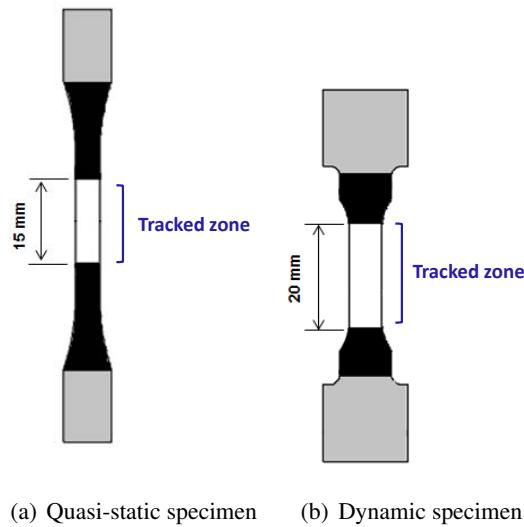


Figure 4.30: Tensile specimens for optical extensometry measurement

Results of the different tensile tests are presented in Figures 4.31 and 4.32 for both materials, where data is averaged over five tests for each configuration. Note that strain evolution is smoothed for dynamic behaviour using Matlab function “smooth”. As can be seen, composites PP-30GF and PP-40GF show quite brittle behaviour at all displacement rates and cutting angles.

Moreover, from comparison with the behaviour of unreinforced PP, presented in Figure 4.33, gain in tensile stress is observed in the composites for all values of  $\theta$ . This tendency is directly related to load transmission from PP matrix to high-rigidity glass fibres [117].

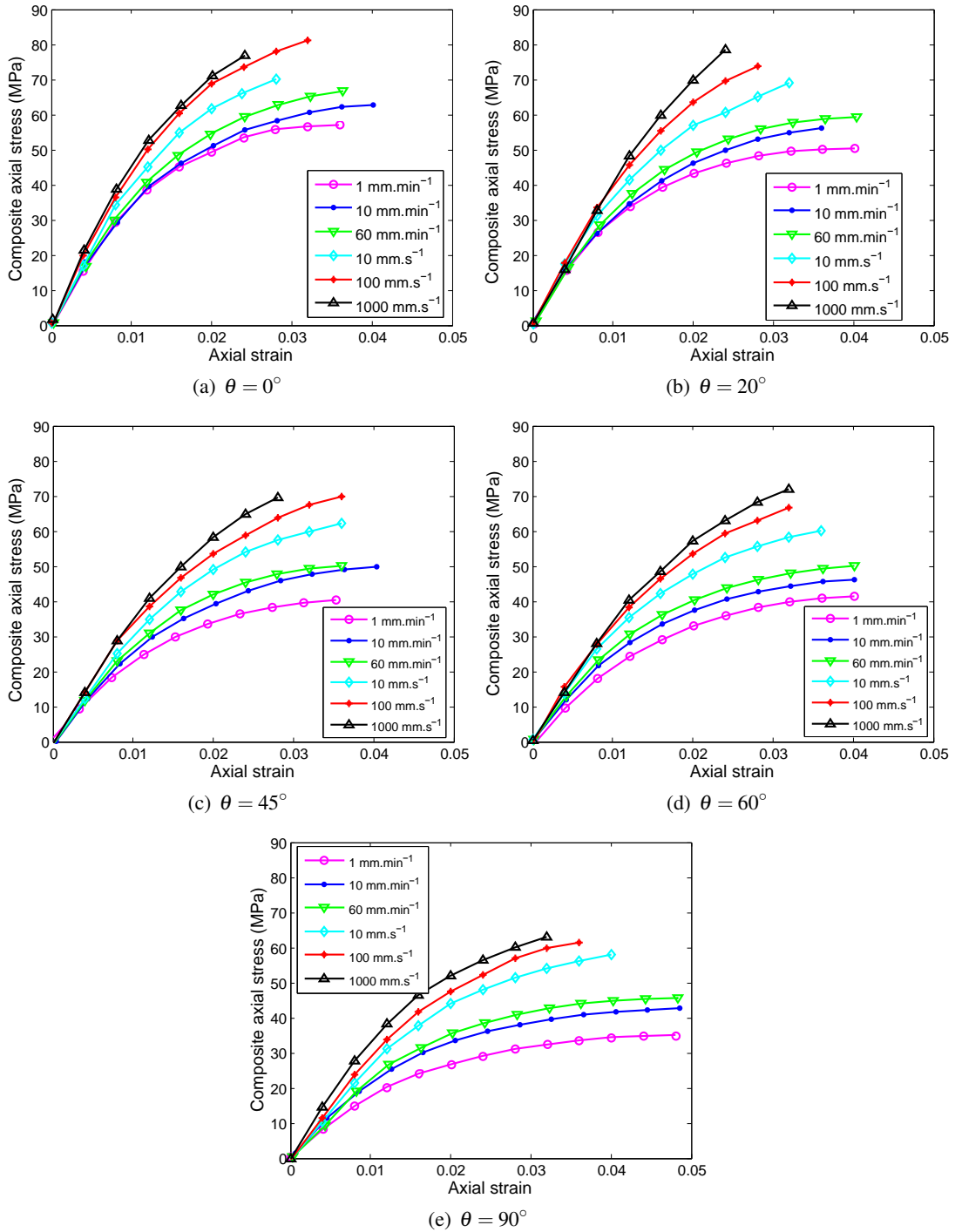


Figure 4.31: Tensile tests at different strain rates and loading angles for PP-30GF

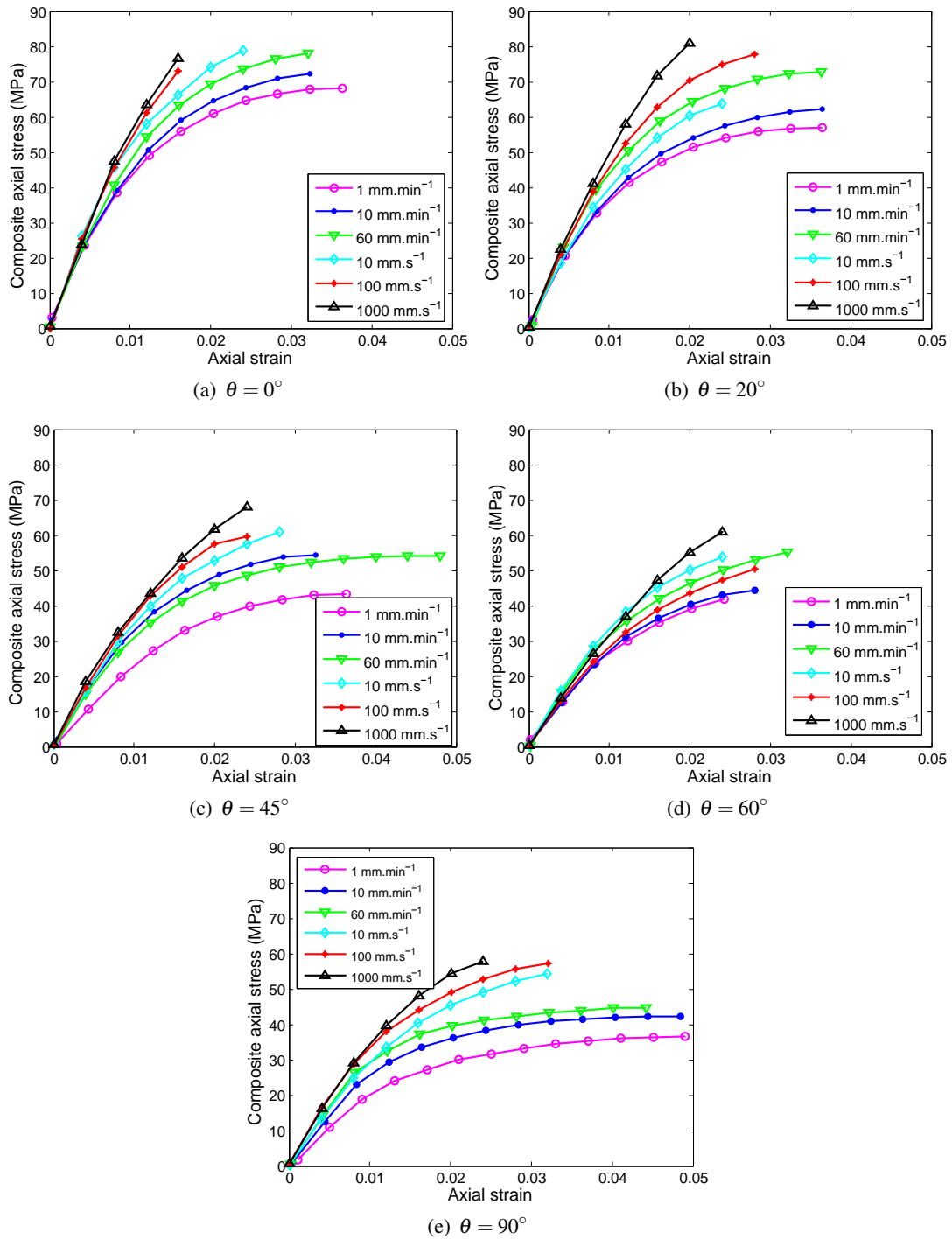


Figure 4.32: Tensile tests at different strain rates and loading angles for PP-40GF

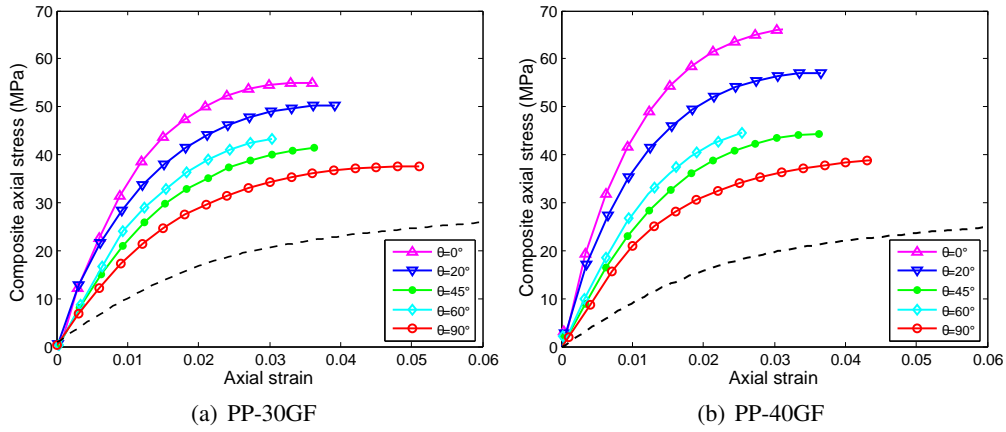


Figure 4.33: Observation of anisotropic behaviour by considering different loading directions from quasi-static tensile tests (at  $1 \text{ mm} \cdot \text{min}^{-1}$ ) for PP (dashed line) and the composite materials (PP-30GF and PP-40GF)

Table 4.7: Fibre average orientation with respect to specimen axis over the specimen central volume for the different  $\theta$  specimens of PPGF30

Angle $\theta$ between IFD and specimen axis	Specimen	Average value of $\psi$
$0^\circ$	PP30-0-1	$22.30^\circ$
	PP30-0-4	$25.88^\circ$
	PP30-0-7	$23.55^\circ$
	PP30-0-8	$25.45^\circ$
	PP30-0-11	$26.76^\circ$
$20^\circ$	PP30-20-6	$28.90^\circ$
	PP30-20-7	$29.35^\circ$
$45^\circ$	PP30-45-12	$35.58^\circ$
	PP30-45-4	$34.81^\circ$
$60^\circ$	PP30-60-5	$37.21^\circ$
	PP30-60-13	$37.83^\circ$
$90^\circ$	PP30-90-11	$43.96^\circ$
	PP30-90-4	$43.01^\circ$

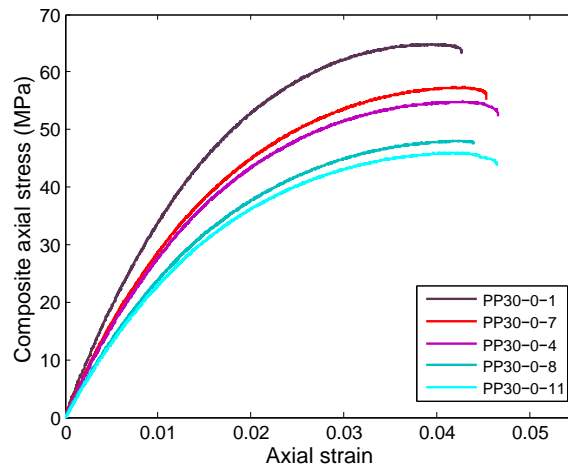


Figure 4.34: Tensile behaviour of  $0^\circ$ -specimens (at  $1 \text{ mm}\cdot\text{min}^{-1}$ ) with different average values of  $\psi$

As can be observed from the presented results and Table 4.7, load transmission, and therefore the “reinforcement efficiency”, is strongly dependent on fibre orientation  $\psi$  with respect to loading direction. Indeed, at a given strain, the closer is the average value of  $\psi$  to the loading direction the higher is the stress level in the fibres and so on in the composite. In the particular case of an angle  $\psi = 0^\circ$  between fibre axis and loading direction, the fraction of load that is transmitted to that fibre through PP/fibre interface is maximal. In addition to the strong anisotropy induced by complex distributions of fibre orientation, tensile behaviour of PP-30GF and PP-40GF composites was also verified to be strain-rate sensitive. This is highlighted in particular by the evolution of the apparent rigidity and axial stress at break with strain rate, presented respectively in Figures 4.35 and 4.36.

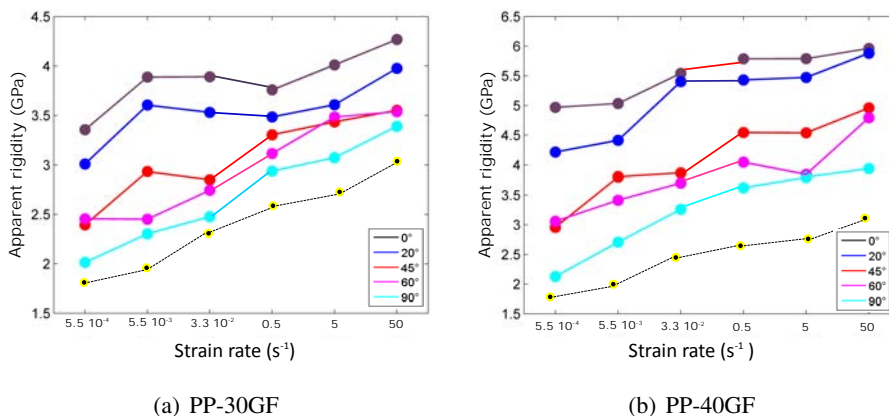


Figure 4.35: Apparent rigidity of PP-30GF and PP-40GF at different strain rates



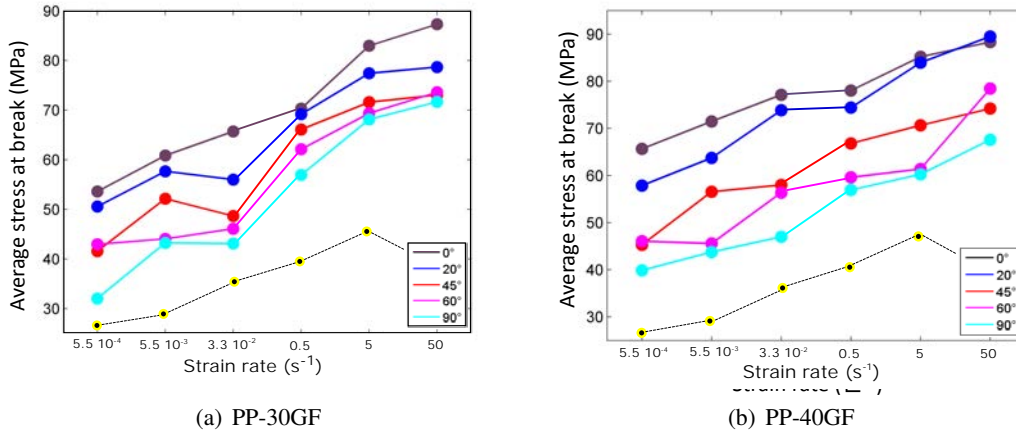


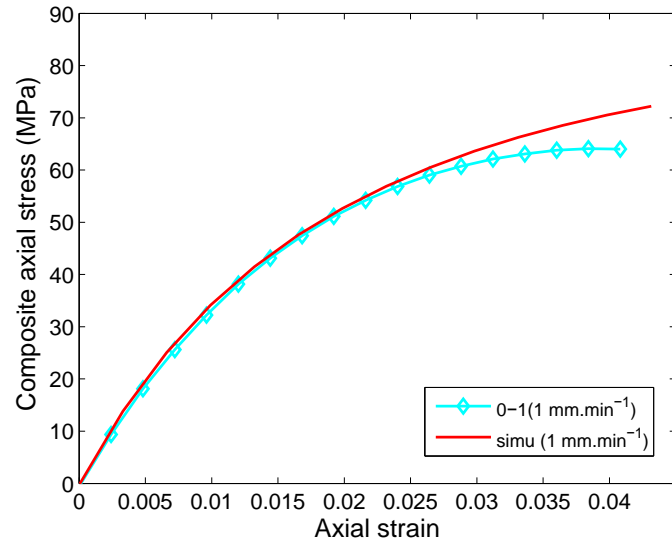
Figure 4.36: Average axial stress at break of PP-30GF and PP-40GF at different strain rates

It is deduced that the strain rate dependency of the composite response is dimmed down for decreasing  $\theta$ . In fact, weight of the rate independent behaviour of the fibres in the composite behaviour is of greater influence when  $\theta$  is small, as the majority of fibres are in that case loaded in their axis direction. On the contrary, composite mechanical response is rather dominated by strain rate dependent behaviour of matrix material at higher values of  $\theta$ .

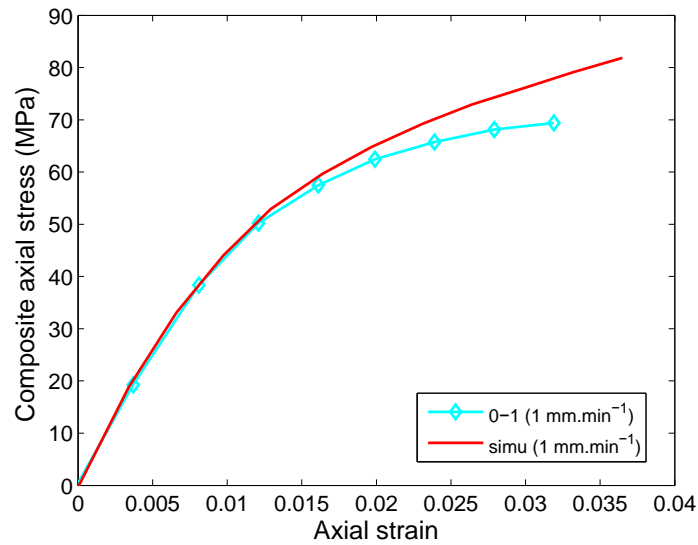
As stated in the beginning of this section, the IFSS,  $\tau$ , is determined as the one leading to the best fit between numerically simulated and experimental results in the case of a PP-30GF and PP-40GF specimens tested at 0° and at 1 mm.min<sup>-1</sup>. More precisely, the specimen 0-1 is considered for both materials because it is the one that presents the highest fraction of fibres oriented in tensile direction (Figures 4.25 and 4.27). For the simulation of mechanical behaviour of specimen 0-1, 9 families of fibres are considered with angles of orientation,  $\alpha$ , varying from 5° to 85° by step of 10° with the corresponding volume fractions identified based on  $\mu$ -CT scan (average orientations over the whole scanned volume). The same geometries and boundary conditions are used as in the case of simulation of PP specimens (Section 4.1.1.2). As presented in Section 3.2.2, fibres have a linear elastic behaviour and all fibres are assumed to have the same young modulus,  $E_F$ , equal to 76 GPa. Length,  $L$ , and radius,  $r$ , are respectively equal to 750  $\mu$ m and 18  $\mu$ m, as determined by microtomography. Matrix material parameters are those identified in section 4.1 (Tables 4.2 and 4.5). Finally, for the PP-30GF and PP-40GF, the values of,  $\tau = 23$  MPa and  $\tau = 26.5$  MPa, respectively, are the ones leading to the best fit between experimental and numerical responses (FigureS 4.37).

Once the IFSS is identified, all parameters of the behaviour model of short-glass-fibre reinforced polypropylene are known. In the next section, tensile tests are therefore used in order to validate

the implementation for both composites, i.e. with 30 and 40 wt.% of glass fibres, in the case of tensile tests in different loading directions with respect to the injection flow direction and over a wide range of strain-rate.



(a) PP-30GF



(b) PP40-GF

Figure 4.37: Comparison of experimental and numerically simulated tensile behaviour of specimens PP30-0-1 ( $\tau = 23$  MPa) and PP40-0-1 ( $\tau = 26.5$  MPa)

### 4.1.3 Validation of the composite model for tensile tests at different loading direction and strain-rate

As described in Section 3.2, the composite material is characterised by a distribution of fibre orientation having the injection flow direction (IFD) as preferential orientation. As already stated when dealing with the identification of the interfacial shear strength, 9 families of fibres are considered in the present model, with angles of orientation,  $\alpha$ , varying from  $5^\circ$  to  $85^\circ$  by step of  $10^\circ$ . Corresponding volume fractions are computed using density-angle diagrams from distributions of orientation averaged over the whole volume of  $\mu$ -CT scans. An example of input data for tensile tests simulation of PP-30GF and PP-40GF at  $0^\circ$  is presented in Table 4.8. Yet, as

Table 4.8: Angle-Volume fraction data at  $0^\circ$  for PP-30GF (PP30-0-1) and PP-40GF (PP40-0-1)

Angle ( $0^\circ$ )	Fibres volume Fraction	
	PP-30GF	PP-40GF
5	0,0391	0,0497
15	0,0291	0,0285
25	0,0158	0,0218
35	0,0119	0,0187
45	0,0128	0,0171
55	0,0059	0,0156
65	0,0063	0,0119
75	0,0054	0,0095
85	0,0031	0,0081

shown in section 4.1.2.1, a layered structure is identified with a distribution of fibre orientation varying through the thickness (Figure 4.22). One might therefore wonder whereas it is accurate to use orientations averaged through the specimen thickness in the modelling. The validity of this assumption is therefore assessed by comparison of results obtained with average and “non-average” data, i.e. by taking into account the layered structure of the fibre orientation. The specimen is meshed with three or five layers of elements having equal thickness with different distributions of fibre orientation attributed to the “exterior” and “interior” layers (Figure 4.38). In the three-layers configuration, distribution of the “exterior” layers corresponds to the identified skin-shell data, i.e. averaged over a thickness of 0.85 mm, while data associated to the “interior” layer corresponds to the identified core data for a thickness of 0.80 mm. For the five-layers configuration distributions are separately introduced with equal thickness. It is to note that the used distributions of orientation are that obtained from specimen PP30-0-4. Previously identified fibre and matrix parameters are used.

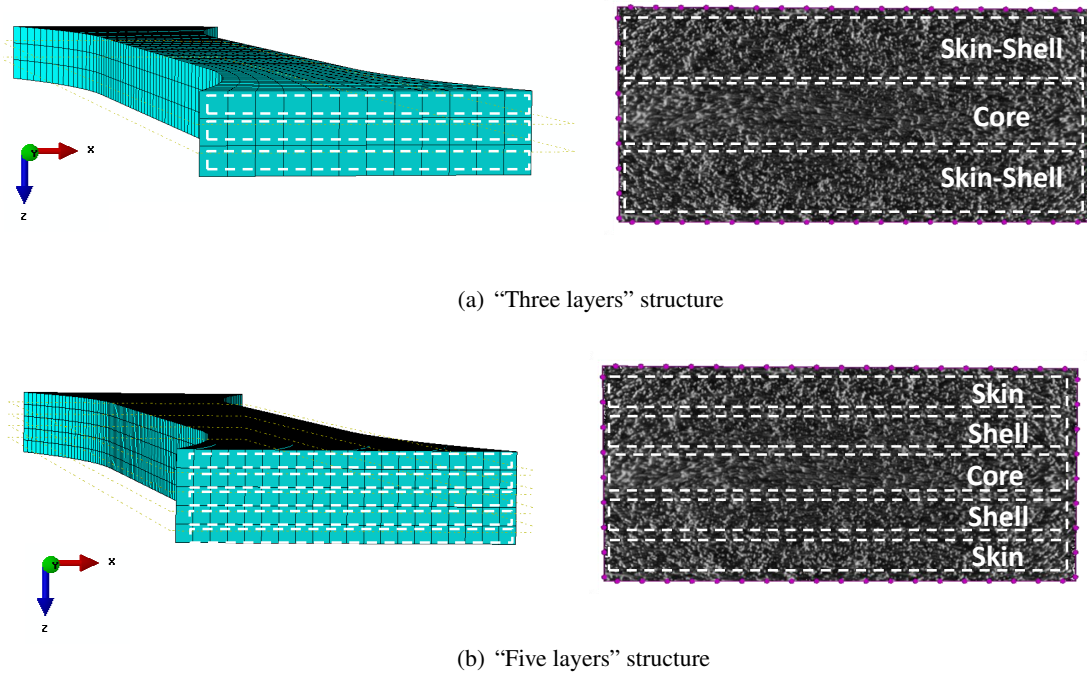


Figure 4.38: Representation of the layered structure of the fibre orientation for the computation of the tensile response of a PP30-0 specimen (at  $1 \text{ mm} \cdot \text{min}^{-1}$ )

Comparison of responses obtained for a simulated tensile test at  $1 \text{ mm}/\text{min}$ , is shown in Figure 4.39. It proves that the model accuracy is not improved by the consideration of different layers through specimen thickness in the finite element simulation and that these ones can be performed based on distributions of orientation averaged over the thickness. The tensile tests realised for PP-30GF and PP-40GF specimens with different cutting angles and at different loading rates (Section 4.1.2.2) are simulated taking into account actual fibre orientations, as far as possible. In fact, all PP-30GF and PP-40GF specimens were not analysed by  $\mu$ -CT. Then, distributions of fibre orientation in specimens, that were not scanned, are assumed to be identical to that of scanned specimens located at approximately the same position in the plate.

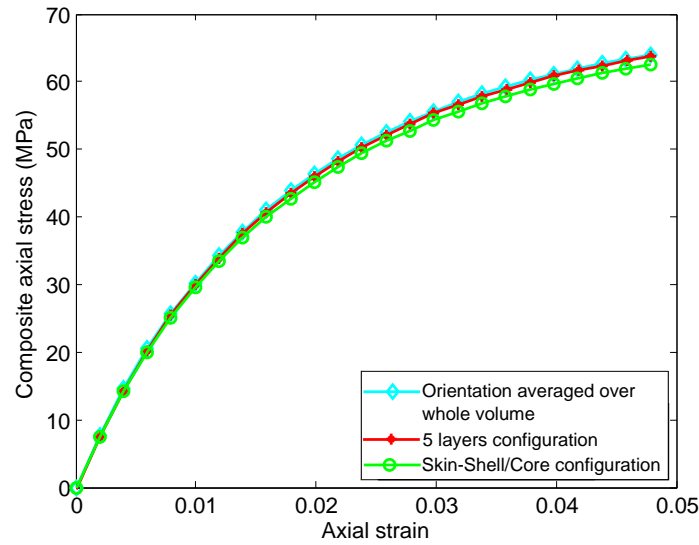


Figure 4.39: Results of simulated tensile test with layered distributions of fibre orientation of a PP30-0 specimen at  $1 \text{ mm} \cdot \text{min}^{-1}$

The conditions of simulations are the same as those used for the identification of the IFSS (previous section 4.1.2.2). The relevance of the developed constitutive model is then evaluated using the set of identified parameters and actual distributions of fibre orientation. Experimental results obtained for tensile tests at quasi-static and dynamic loading rates are compared with numerical responses for all cutting angles ( $0^\circ$ ,  $20^\circ$ ,  $45^\circ$ ,  $60^\circ$  and  $90^\circ$ ). Results presented in Figures 4.40 to 4.44 for PP-30GF and Figures 4.45 to 4.49 for PP-40GF demonstrate the accuracy of the implemented model for both composites, since the stress-strain response is well reproduced for the different cases.

A limitation was however noted with overestimated numerically computed stress levels when the tensile strain increases in quasi-static case. Actually a softening in the stress-strain curves is observed on the experimental results and is not predicted by the current constitutive model. An explanation is that this phenomenon is due to the development of damage mechanisms, mainly fibre-matrix decohesion and matrix ductile damage, in a lesser extent, which are not taken into account in the present model. It is also observed that this softening is more important at lower loading angles with respect to IFD ( $0^\circ$  and  $20^\circ$ ), which reveals the possible anisotropy of these damage mechanisms. The characterisation and the modelling of matrix ductile damage and debonding mechanisms are the object of following chapter.

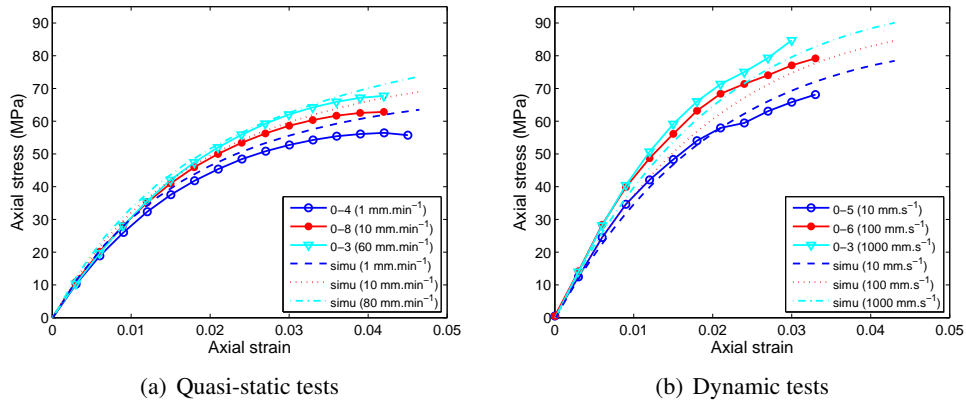


Figure 4.40: Comparison of experimental and numerical data for tests of 0° specimens of PP-30GF

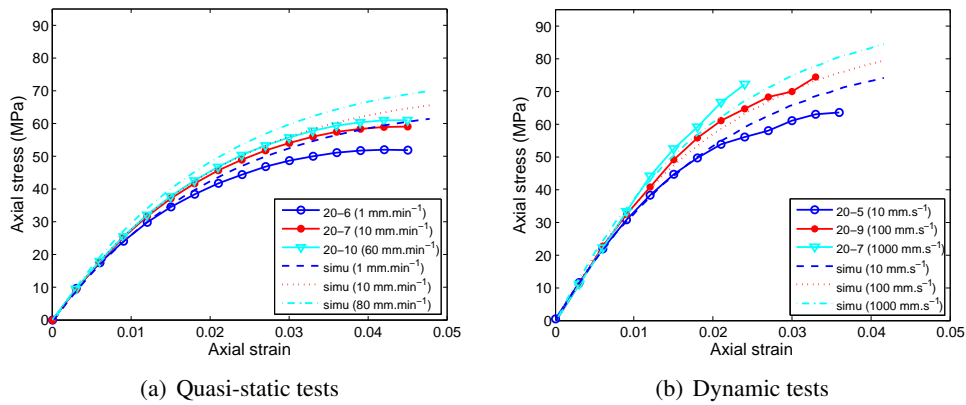


Figure 4.41: Comparison of experimental and numerical data for tests of 20° specimens of PP-30GF

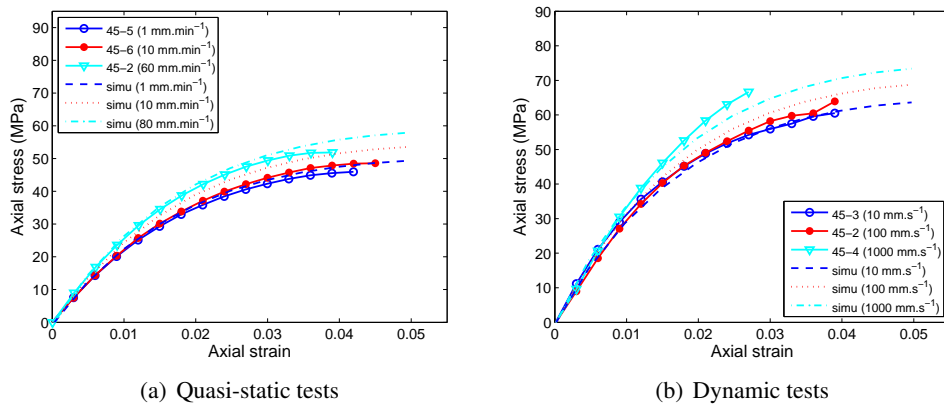


Figure 4.42: Comparison of experimental and numerical data for tests of 45° specimens of PP-30GF

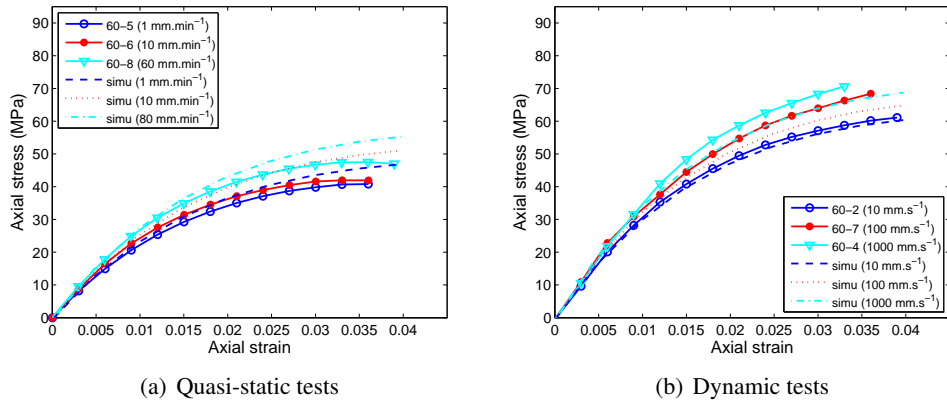


Figure 4.43: Comparison of experimental and numerical data for tests of 60° specimens of PP-30GF

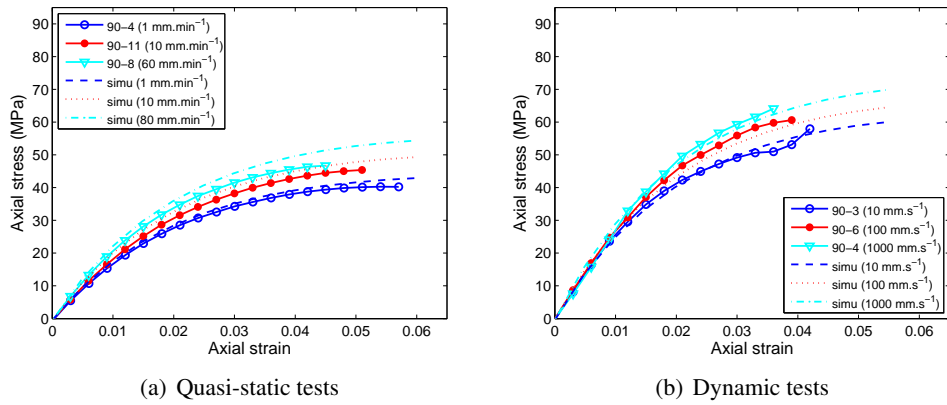


Figure 4.44: Comparison of experimental and numerical data for tests of 90° specimens of PP-30GF

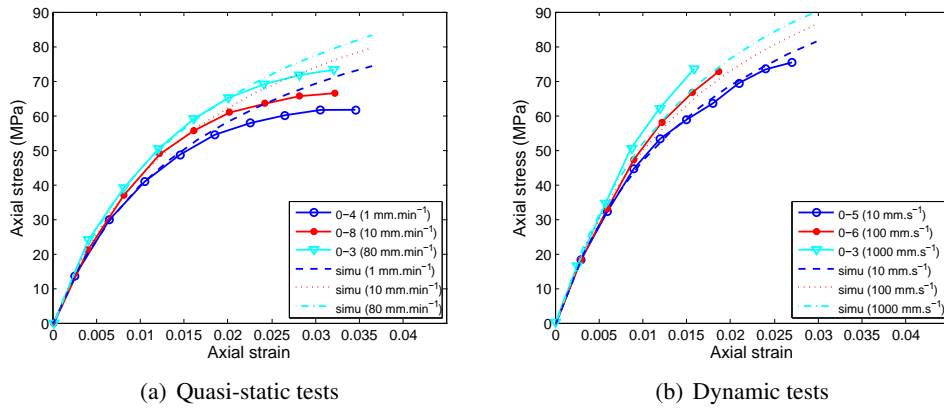


Figure 4.45: Comparison of experimental and numerical data for tests of  $0^\circ$  specimens of PP-40GF

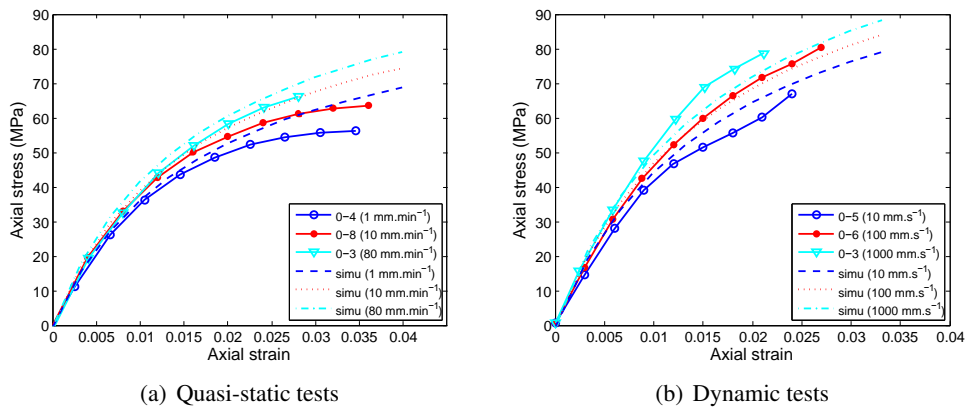


Figure 4.46: Comparison of experimental and numerical data for tests of  $20^\circ$  specimens of PP-40GF

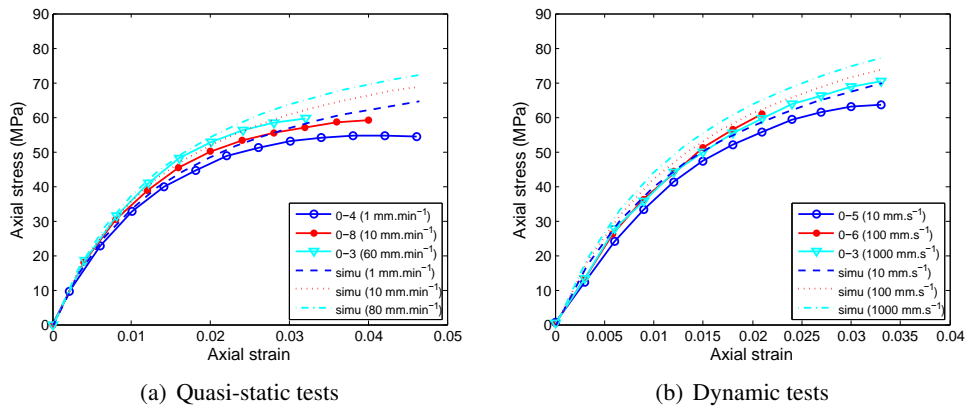


Figure 4.47: Comparison of experimental and numerical data for tests of  $45^\circ$  specimens of PP-40GF



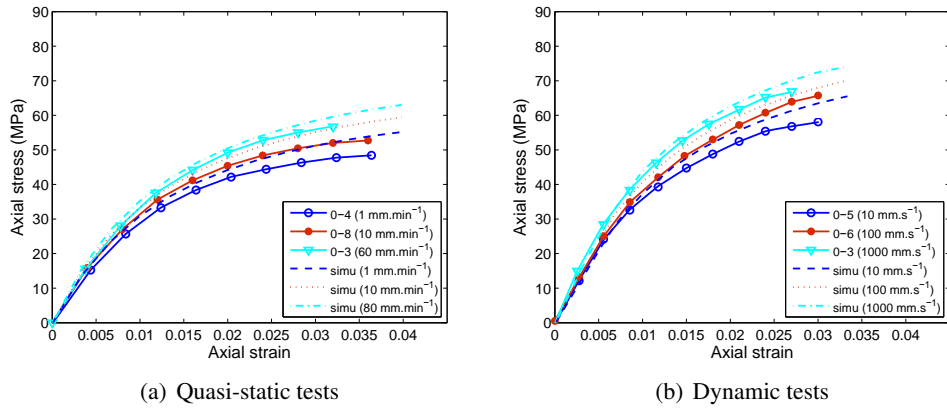


Figure 4.48: Comparison of experimental and numerical data for tests of 60° specimens of PP-40GF

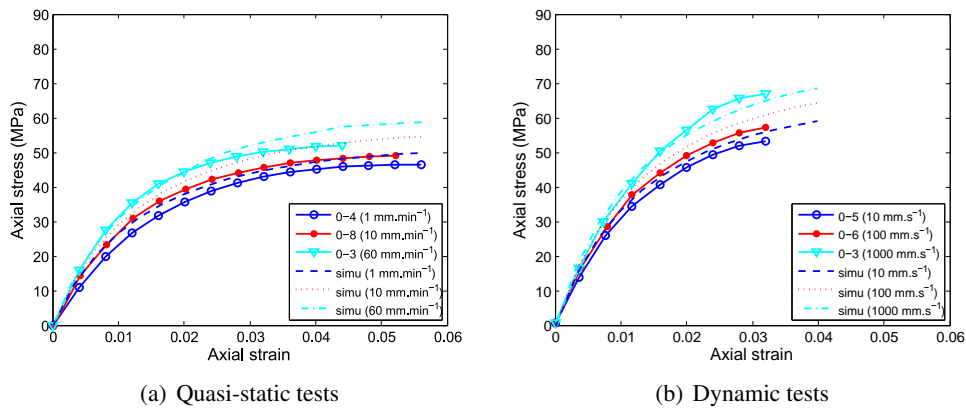


Figure 4.49: Comparison of experimental and numerical data for tests of 90° specimens of PP-40GF

## 4.2 Conclusion

This part of the work deals with the identification and validation of the developed constitutive model (presented in Chapter 3). To this end, a characterisation procedure was set-up for the determination of constitutive parameters used in the matrix, reinforcement and composite modelling. Parameters involved in the matrix behaviour law are identified based on dynamic mechanical analysis, compression and tensile tests under a wide range of strain rate realised on PP material. Then, dealing with the case of injection-moulded PP-short glass fibre composite, a first step is to characterise the actual distribution of fibre orientation using micro-computed tomography. Orientations thus identified were input of the behaviour model according to the “families of fibres” concept. In order to validate the implementation of both matrix and composite models,

comparisons of numerical and experimental results obtained for PP material and PP-GF were performed. Simulated quasi-static and dynamic tensile tests of PP-GF with different fibre content and distribution of fibre orientation proved the consistency of the implemented model.

To go further with the validation of the model, it would be interesting to extend the experimental campaign to other loading conditions, for instance, non-monotonic tests, triaxial loadings, ...etc . Finally, the advantageous adaptability of the present modelling offers the possibility to go further with the matrix material and interface behaviour modelling. Hence, the introduction of damage mechanisms in the behaviour prediction by the implementation of matrix ductile damage and fibre-matrix debonding models is dealt with in the following chapter.



---

## *Damage and fracture modelling*

---

The current chapter deals with the modelling of failure mechanisms of SFRC. The description of damage phenomena and the definition of a failure criteria are therefore addressed in the following sections. The chapter starts with a highlight on damage models proposed in the literature for SFRC. Then, the implementation and validation of laws aiming to describe the complex damage mechanisms in the composite material are presented. Experimental (cyclic loading/unloading and tensile tests) are realised on unreinforced and short-glass-fibre reinforced matrix (Chapter 4) in order to identify the involved parameters. Finally, the definition of a failure criteria, based on observations from the literature and the introduced damage laws, is investigated in the last part of the chapter.

### **5.1 State of art of damage characterisation and modelling for SFRC**

Damage mechanisms in short-fibre reinforced composites have been the object of many experimental and numerical investigations in the literature [121, 122, 123]. It was established that the microstructure of short-fibre reinforced composites, the complexity of damage mechanisms and the diversity of their scenarios significantly influence the composite properties. It has been extensively reported that damage in such materials occurs at the microscopic level according to different physical degradation mechanisms, namely: matrix microcracks, interfacial decohesion and fibre breakage [125]. Mouhmid et al. [134] used acoustic emission and scanning electron microscopy (SEM) techniques to investigate different types of damage in PA/GF composites. They reported that the damage mechanisms in PA/GF composites are characterised by matrix plasticization and microcracks, fibre fracture and pull-out. More recently, the development of X-ray micro-computed tomography  $\mu$ CT-technique has been used to investigate damage mechanisms in various composite materials [135, 136] and has pushed forward the quantitative analysis of its evolution [137]. Arif et al. [121] have studied the specific case of damage evolution, using  $\mu$ CT-tomography, in PA66-GF30 composite through the measurement of main features of defects, such

as volume, orientation and shape, at several levels of overall damage. Following the analysis of Horst and Spoomaker [138], they have proposed a damage progression scenario in which the damage starts at the fibre ends, area where local stress concentration is the highest, and propagates along the fibre in the form of fibre/matrix interfacial debonding. Then, matrix microcracks develop and propagate in a ductile way accompanied with high matrix deformation bands [121]. For the particular case of short glass fibre reinforced polyamide-66, in-situ damage mechanisms characterisation under quasi-static monotonic loading were investigated by Sato et al. [122], Horst et al. [123] and Bernasconi et al. [133]. These authors also reported that in most cases, interfacial damage starts at the fibre ends and further propagates along the fibre-matrix interface.

Based on the different reported observations, damage mechanisms can be classified in two principal types. The first class are mechanisms relative to the degradation of the matrix, which includes initiation, coalescence and propagation of microcracks. The second type of damage mechanisms are those linked to interfacial decohesion and to any other related process, such as fibre/matrix friction and fibre pull-out processes.

The development of microcracks and ductile damage in the matrix material (void growth and coalescence), is strongly influenced by the reinforcement characteristics [124]. For the modelling of such a phenomena, some interesting approaches combine micromechanical and continuum damage mechanics (CDM) descriptions. For instance, Nguyen and Khaleel [126] have evaluated the effective and damaged stiffness tensors of composites reinforced by randomly oriented fibres using self-consistent and Mori-Tanaka schemes, applied to a reference aligned fibre composite and a distribution over all possible orientations. The evolution of the cracks in an elastic matrix material was then modelled in the Continuum Damage Mechanics framework [126]. The case of elastoplastic matrix material was similarly treated by Lee and Simunovic [127]. More recently, a strongly anisotropic ductile damage of the matrix material was modelled in the framework of continuum damage mechanics by Notta-Cuvier et al. [54], using a 4<sup>th</sup>-order damage tensor for matrix material built based on the characteristics of the reinforcement.

Modelling of the interface degradation in composite materials has received a lot of interest in the past two decades. One of the developed modelling methods consists in the consideration of a dedicated fibre coating, also called an interphase, as a third phase of the material [125]. The main drawback is that such a three-phase model implies the knowledge of coating properties, which are rarely available. Hashin introduced the imperfect interface approach which accounts for the displacement and stress jump at the fibre/matrix interface [128, 129]. Zhong and Meguid [132] developed a new solution for the eigenstrain problem, as defined by Eshelby, of a spherical

inclusion with an imperfect interface. In addition, the Shear Lag Model (SLM) has been developed to model the load transmission degradation in the load transmission at fibre/matrix interface [89]. The symbiosis of microscopic observations constitutes an indispensable data-base for the statement of accurate assumptions for the modelling of complex damage phenomena. In particular, and due to complex fibre configurations in SFRC, all damage phenomena (more precisely matrix damage and interfacial decohesion) are likely to coexist and may also interact. Obviously, the nature of dominant damage phenomenon also depends on the kind of loading.

In the following sections, the implemented constitutive model (Chapter 3) is extended to the case of damageable short-fibre reinforced thermoplastics by taking into account the matrix anisotropic ductile damage and the progressive fibre/matrix interfacial decohesion mechanisms.

## 5.2 Modelling of matrix ductile damage

In this part of the chapter, the first damage class, i.e. mechanisms relative to the matrix degradation is addressed. Bearing in mind the anisotropy induced by the complex orientation of the reinforcing short fibres, an anisotropic ductile damage is coupled to the matrix constitutive model. The damage laws are developed in the framework of continuum damage mechanics and identified, consistently with the previous investigations (Chapter 3), for a PP matrix material, using cyclic tensile tests as described hereafter.

### 5.2.1 Anisotropic damage model for the matrix material

As presented by Lemaitre [38], ductile damage mechanism can be interpreted at the microscale as the creation of microsurfaces of discontinuities (i.e. enlargement of microcavities). At the mesoscale, the pattern of microcavities may be approximated by the area of the intersections of all the cavities with a given plane. This area is scaled by the size of a representative element. For a given plane in a Representative Volume Element (RVE) of a damaged body, damage variable is therefore defined by a scalar value  $D$  bounded between 0 and 1, as follows:

$$D = \frac{A_D}{A} \quad (5.1)$$

where  $A$  and  $A_D$  are the areas of intersections of, respectively, the RVE and the microdefects within a given plane. In the framework of Continuum Damage Mechanics, the effective stress is introduced as the stress related to the elementary surface of the material that effectively withstands

the load, namely  $(A - A_D)$ . In the case of isotropic damage, the effective stress is expressed as follows [38]:

$$\tilde{\sigma} = \frac{\sigma}{1 - D} \quad (5.2)$$

where  $\tilde{\sigma}$  and  $\sigma$  are respectively the effective and true Cauchy stress tensors (Figure 5.1).

Consistently with earlier formulation of the constitutive laws (section 3.2.1.1), damage description is performed within the framework of thermodynamics of irreversible processes. In the case of homogeneous material and if the ratio of surface defects is identical in all directions, the damage can be modelled as isotropic. In that case, it can be entirely characterised by the scalar variable,  $D$ .

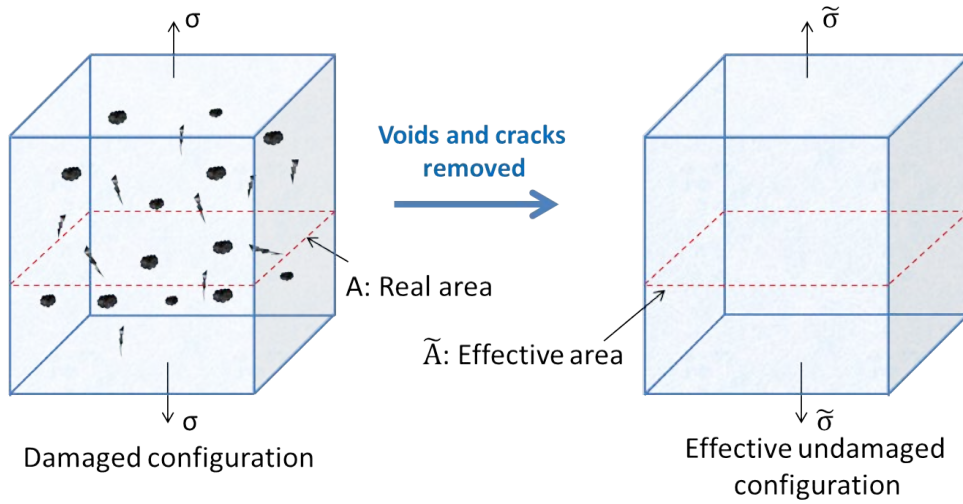


Figure 5.1: Definition of the damaged and effective configurations in Continuum Damage Mechanics

When dealing with anisotropic materials, for instance fibre reinforced matrices, the whole behaviour, including damage development, is governed by the reinforcement properties (Figure 5.2). Anisotropy has, therefore, to be taken into account for the modelling of damage development. In this case, the scalar variable can no longer be representative of the damage development and a 4th-order damage tensor,  $\mathcal{D}$ , is introduced in order to link the real,  $\sigma_M$ , and effective,  $\tilde{\sigma}_M$ , Cauchy stress tensors [54] (Equation 5.3).

$$\sigma_M = \mathcal{D} \tilde{\sigma}_M \quad (5.3)$$

Indeed, damage development in the matrix material is directly dependent on the orientation and the volume fraction of fibres.

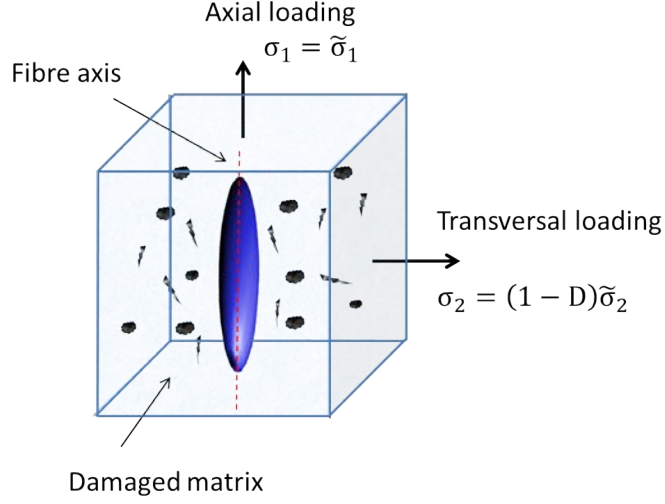


Figure 5.2: Damage anisotropy of the reinforced matrix material

In the model, each family of fibres  $\alpha$  is assumed to govern the characteristics of damage over the volume  $V_F^\alpha$  of the matrix material, which is assumed to be equal to the volume of fibre medium  $\alpha$ , i.e.  $V_F^\alpha = v_F^\alpha V$  where  $V$  is the volume of the composite material. Matrix damage is therefore governed by each fibre family over a corresponding volume fraction of the matrix material equal to  $v_F^\alpha / v_M$  with  $\alpha \in \{1, \dots, N_{fam}\}$ . Intermediate damage tensors,  $\mathcal{D}^\alpha$ , and corresponding inverse tensors,  $\mathcal{M}^\alpha$ , are introduced (Equation 5.4).

$$\begin{aligned}\sigma_M^{\alpha_0} &= \mathcal{D}^\alpha \tilde{\sigma}_M^{\alpha_0} \\ \tilde{\sigma}_M^{\alpha_0} &= \mathcal{M}^\alpha \sigma_M^{\alpha_0}\end{aligned}\tag{5.4}$$

where  $\tilde{\sigma}_M^{\alpha_0}$  and  $\sigma_M^{\alpha_0}$  currently stand for, respectively, the effective and real stress tensors that would be computed for the matrix of a fictitious composite material constituted of one family of fibres  $\alpha$  (with the superscript “0” indicating that mechanical tensors are expressed in the coordinates system related to the family of fibres  $\alpha$ ). Note that  $\tilde{\sigma}_M^{\alpha_0}$  and  $\sigma_M^{\alpha_0}$  have actually no physical sense. Anisotropy of the damage mechanism is mainly due to the fact that for a given fibre family, short fibres prevent the damage in their direction of orientation, so that:

$$\begin{aligned}\sigma_{Mii}^{\alpha_0} &= \tilde{\sigma}_{Mii}^{\alpha_0} \quad \text{if } i = j = 1 \\ \sigma_{Mij}^{\alpha_0} &= (1 - D) \tilde{\sigma}_{Mij}^{\alpha_0} \quad \text{else } (i, j \in \{1, 2, 3\} \text{ and } (i, j) \neq (1, 1))\end{aligned}\tag{5.5}$$



It leads then to the following expression of the tensor  $\mathcal{D}^\alpha$ :

$$\mathcal{D}_{ijkl}^\alpha = \delta_{ik}\delta_{jl} [1 - D\delta_{ij}(1 - \delta_{11}) - D(1 - \delta_{ij})], \quad \forall \alpha \quad (5.6)$$

where  $\delta_{ij}$  is the Kronecker symbol defined by  $\delta_{ij} = 1$  if  $i = j$  and  $\delta_{ij} = 0$  if  $i \neq j$ . For the computation of the real Cauchy stress tensor in the global coordinates system, the transition matrix,  $T^\alpha$ , is used to express the effective stresses in fibres' coordinates system, with  $\sigma_M^{\alpha 0} = T^{\alpha^{-1}} \sigma_M^\alpha T^\alpha$ . The tensor  $\mathcal{D}^\alpha$  is then applied to  $\sigma_M^{\alpha 0}$ , before the real stress tensor is re-expressed in the global coordinates system. The global damage state of the matrix is described by assembling all the contributions, i.e. damage effect of all the fibre families, over the volume fractions of the matrix medium. Finally, the volume fraction of the matrix material,  $v_M'$ , which is not affected by the presence of the fibres damages isotropically. Note that  $v_M'$  is equal to  $1 - \sum_{\alpha} v_F^\alpha / v_M$  or equivalently to  $2 - 1/v_M$ . This model is therefore valid for matrix volume fraction higher than 0.5, which is generally the case in injection moulded short-fibre composites. Taking into account all these considerations, the tensor  $\mathcal{D}$  is finally expressed as follows:

$$\mathcal{D}_{ijkl} = v_M' (1 - D) \delta_{ik} \delta_{jl} + \sum_{\alpha=1}^{n_{fam}} \frac{v_M^\alpha}{v_M} \sum_{p,q=1}^3 T_{ip}^\alpha \left( T^{\alpha^{-1}} \right)_{qj} \left( T^{\alpha^{-1}} \right)_{pk} T_{lq}^\alpha \mathcal{D}_{pqpq}^\alpha \quad (5.7)$$

### 5.2.2 Thermodynamic formulation of damage evolution laws

As already stated, the framework of thermodynamics of irreversible processes, where the Helmholtz free energy function is decomposed into a viscoelastic part and a viscoplastic part, is considered. Damageable materials are dealt with, within this formalism, by coupling damage with the viscoelastic part of the free energy. The Helmholtz free energy of the “damageable” matrix therefore becomes:

$$\phi_M = \phi_M^{ve,D} + \phi_M^{vp} \quad (5.8)$$

where  $\phi_M^{ve,D}$  is the viscoelastic free energy coupled to damage and, according to Lemaitre [38], is defined by:

$$\rho_M \phi_M^{ve,D} = \frac{1}{2} \int_{-\infty}^t \int_{-\infty}^t \frac{\partial \epsilon^{ve}}{\partial \tau} (\tau) : R_{dam}^{ve} (2t - \tau - \xi) : \frac{\partial \epsilon^{ve}}{\partial \xi} (\xi) d\tau d\xi \quad (5.9)$$

$R_{dam}^{ve}$  is the “damaged” fourth-order relaxation tensor of the matrix material and is defined in case of anisotropic damage by:

$$R_{dam}^{ve} = \mathcal{D} R^{ve} \quad (5.10)$$

with 4<sup>th</sup> order tensor  $\mathcal{D}$  defined in previous section (5.2.2) and  $\rho_M$  the matrix density. For the determination of damage fourth-order tensor,  $\mathcal{D}$ , evolution law of damage scalar variable  $D$  has to be defined. The damage thermodynamic force  $Y$ , also defined as the strain energy density release rate, and its conjugate variable  $D$  are related by the state law given as follows [38]:

$$Y = -\frac{\partial \rho_M \phi_M^{ve,D}}{\partial D} \quad (5.11)$$

Given the expression of  $\phi_M^{ve,D}$  (5.9),  $Y$  is obtained by:

$$Y(t) = \frac{1}{2} \int_{-\infty}^t \int_{-\infty}^t \frac{\partial \varepsilon^{ve}}{\partial \tau}(\tau) : \mathcal{D}' R^{ve}(2t - \tau - \xi) : \frac{\partial \varepsilon^{ve}}{\partial \xi}(\xi) d\tau d\xi \quad (5.12)$$

where  $\mathcal{D}' = \frac{\partial \mathcal{D}}{\partial D}$ , i.e. ∴

$$\mathcal{D}'_{ijkl} = -v'_M \delta_{ik} \delta_{jl} + \sum_{\alpha=1}^{n_{fam}} \frac{v'_M \alpha}{v_M} \sum_{p,q=1}^3 T_{ip}^\alpha (T^{\alpha-1})_{qj} (T^{\alpha-1})_{pk} T_{lq}^\alpha \mathcal{D}'_{pqpq} \quad (5.13)$$

where  $\mathcal{D}'^\alpha$  is defined as follows:

$$\mathcal{D}'^\alpha_{ijkl} = \delta_{ik} \delta_{jl} (\delta_{ij} \delta_{i1} - 1), \quad \forall \alpha \quad (5.14)$$

with straightforward manipulations:

$$\mathcal{D}'_{ijkl} = -v'_M \delta_{ik} \delta_{jl} + \sum_{\alpha=1}^{n_{fam}} \frac{v'_M \alpha}{v_M} \sum_{p,q=1}^3 T_{ip}^\alpha (T^{\alpha-1})_{qj} (T^{\alpha-1})_{pk} T_{lq}^\alpha (\delta_{pq} \delta_{p1} - 1) \quad (5.15)$$

The damage thermodynamic force can be written as the sum of a deviatoric,  $Y_{dev}$ , and hydrostatic,  $Y_H$ , parts [105, 109]:

$$Y(t) = Y_{dev}(t) + Y_H(t) \quad (5.16)$$

with

$$\begin{cases} Y_{dev}(t) = \int_{-\infty}^t \int_{-\infty}^t G^{ve}(2t - \tau - \xi) \mathcal{D}' \frac{\partial \varepsilon_{dev}^{ve}}{\partial \tau}(\tau) : \frac{\partial \varepsilon_{dev}^{ve}}{\partial \xi}(\xi) d\tau d\xi \\ Y_H(t) = \frac{9}{2} \int_{-\infty}^t \int_{-\infty}^t K^{ve}(2t - \tau - \xi) \mathcal{D}' \frac{\partial \varepsilon_H^{ve}}{\partial \tau}(\tau) I : \frac{\partial \varepsilon_H^{ve}}{\partial \xi}(\xi) I d\tau d\xi \end{cases} \quad (5.17)$$

The use of Prony series leads then to:

$$Y_{dev}(t) = G_{\infty} \mathcal{D}' \boldsymbol{\varepsilon}_{dev}^{ve}(t) : \boldsymbol{\varepsilon}_{dev}^{ve}(t) + \sum_{i=1}^N G_i \int_{-\infty}^t \int_{-\infty}^t \exp\left(\frac{\tau-t}{\tau_i^d}\right) \exp\left(\frac{\xi-t}{\tau_i^d}\right) \mathcal{D}' \frac{\partial \boldsymbol{\varepsilon}_{dev}^{ve}}{\partial \tau}(\tau) : \frac{\partial \boldsymbol{\varepsilon}_{dev}^{ve}}{\partial \xi}(\xi) d\tau d\xi \quad (5.18)$$

$$Y_H(t) = \frac{9}{2} K_{\infty} \mathcal{D}' \boldsymbol{\varepsilon}_H^{ve}(t) \mathbf{1} : \boldsymbol{\varepsilon}_H^{ve}(t) \mathbf{1} + \frac{9}{2} \sum_{i=1}^N K_i \int_{-\infty}^t \int_{-\infty}^t \exp\left(\frac{\tau-t}{\tau_i^v}\right) \exp\left(\frac{\xi-t}{\tau_i^v}\right) \mathcal{D}' \frac{\partial \boldsymbol{\varepsilon}_H^{ve}}{\partial \tau}(\tau) \mathbf{1} : \frac{\partial \boldsymbol{\varepsilon}_H^{ve}}{\partial \xi}(\xi) \mathbf{1} d\tau d\xi \quad (5.19)$$

By considering the expressions of the deviatoric and hydrostatic stresses (previously defined in section 3.2.1.2) and introduced here as effective quantities,  $\tilde{\boldsymbol{\sigma}}_{M,dev}$  and  $\tilde{\boldsymbol{\sigma}}_{M,H}$ , we obtain:

$$Y(t) = \frac{\mathcal{D}' \tilde{\boldsymbol{\sigma}}_{M_{\infty},dev} : \tilde{\boldsymbol{\sigma}}_{M_{\infty},dev}}{4G_{\infty}} + \frac{\mathcal{D}' \tilde{\boldsymbol{\sigma}}_{M_{\infty},H} : \tilde{\boldsymbol{\sigma}}_{M_{\infty},H}}{2K_{\infty}} + \sum_{i=1}^N \frac{\mathcal{D}' \tilde{\boldsymbol{\sigma}}_{M_i,dev}(t) : \tilde{\boldsymbol{\sigma}}_{M_i,dev}(t)}{4G_i} + \sum_{i=1}^N \frac{\mathcal{D}' \tilde{\boldsymbol{\sigma}}_{M_i,H}(t) : \tilde{\boldsymbol{\sigma}}_{M_i,H}(t)}{2K_i} \quad (5.20)$$

The developed damage model of the matrix material is implemented, as described above, for the case of short-fibre reinforced matrix, i.e. where the damage anisotropy is taken into account. The presented damage laws are, in fact, fully identified when the evolution law of the scalar damage variable  $D$  is identified. This parameter can be determined based on tests on unreinforced matrix material, for which damage is isotropic. In the following the constitutive equations are therefore simplified considering an isotropic damage for the identification of  $D$ .

### 5.2.3 Characterisation and validation of the matrix damage model

For the particular case of unreinforced materials, damage is assumed to develop isotropically. Consequently, terms corresponding to the fibre families effect in the expression of  $Y$  vanish and it leads to:

$$Y(t) = \frac{\tilde{\boldsymbol{\sigma}}_{M_{\infty},dev} : \tilde{\boldsymbol{\sigma}}_{M_{\infty},dev}}{4G_{\infty}} + \frac{\tilde{\boldsymbol{\sigma}}_{M_{\infty},H} : \tilde{\boldsymbol{\sigma}}_{M_{\infty},H}}{2K_{\infty}} + \sum_{i=1}^N \frac{\tilde{\boldsymbol{\sigma}}_{M_i,dev}(t) : \tilde{\boldsymbol{\sigma}}_{M_i,dev}(t)}{4G_i} + \sum_{i=1}^N \frac{\tilde{\boldsymbol{\sigma}}_{M_i,H}(t) : \tilde{\boldsymbol{\sigma}}_{M_i,H}(t)}{2K_i} \quad (5.21)$$

The damage variable  $D$  is a state thermodynamic variable and derives from the dissipation potential of the matrix material using the normality rule. In the present case, i.e. when damage is taken into account as a dissipation phenomena in the matrix material, the expression of its dissipation potential becomes:

$$\psi_M^{vp,D} = \psi_M^{vp} + \psi_M^D \quad (5.22)$$

where  $\psi_M^{vp}$  is the viscoplastic dissipation potential defined in section 3.2.1.3 and  $\psi_M^D = \psi_M^D(D)$  is the damage dissipation potential associated to the state variable  $D$ . Using the viscoplastic multiplier,  $\dot{\lambda}$ , the normality rule for the damage variable evolution is expressed as follows:

$$\dot{D} = \dot{\lambda} \frac{\partial \psi_M^{vp,D}}{\partial Y} = \dot{\lambda} \frac{\partial \psi_M^D}{\partial Y} \quad (5.23)$$

According to the fact that the damage variable stands for deterioration of a material and not for recovery of strength, i.e.  $Y\dot{D} \geq 0$ , Lemaitre [38] demonstrates that it is correlated to the viscoplastic strain level and that  $\psi_M^D$  can be expressed as a function of  $Y^2/(1-D)$ . A damage threshold,  $\kappa_D$ , which corresponds to the equivalent viscoplastic strain from which damage begins, is therefore introduced and the evolution law for the scalar damage variable is given by:

$$\begin{cases} \dot{D} = \dot{\kappa} \frac{Y}{S} & , \text{ if } \kappa \geq \kappa_D, \\ \dot{D} = 0 & , \text{ else} \end{cases} \quad (5.24)$$

where  $\kappa$  is the equivalent viscoplastic strain defined in section 3.2.1.3. The damage evolution laws are coupled to the constitutive laws of the matrix material and the predicted responses are now expressed in terms of effective and “damaged” ( i.e. real) stress tensors. In order to verify the current implementation, the extended constitutive law of the matrix material, i.e damage-coupled viscoelastic-visoplastic law, is tested for several values of damage parameter,  $S$  (Equation 5.24). A unique 3D cubic element (C3D8) is considered for these tests, with an edge size of 1 mm. All degrees of freedom of nodes at the element basis are constrained to 0, while the upper ones are subjected to an imposed velocity. Results for the variation of  $D$  and the stress-strain response with different values of the parameter  $S$  are given in Figures 5.3 and 5.4.

Several methods exist for the characterisation of damage development in different materials. In the case of polymers, among methods to characterise ductile damage, one can cite techniques based on direct measurement, which consist on a mesoscale evaluation of the total crack areas lying on a surface. This is however a tedious method to perform. Non-direct measurement methods have also been developed and are judged more straightforward.

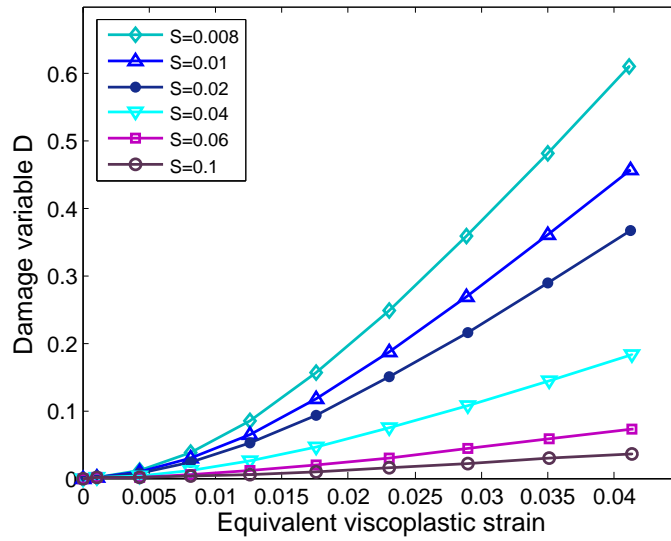


Figure 5.3: Influence of parameter  $S$  on the evolution of the damage variable  $D$  ( $1 \text{ mm}\cdot\text{min}^{-1}$ )

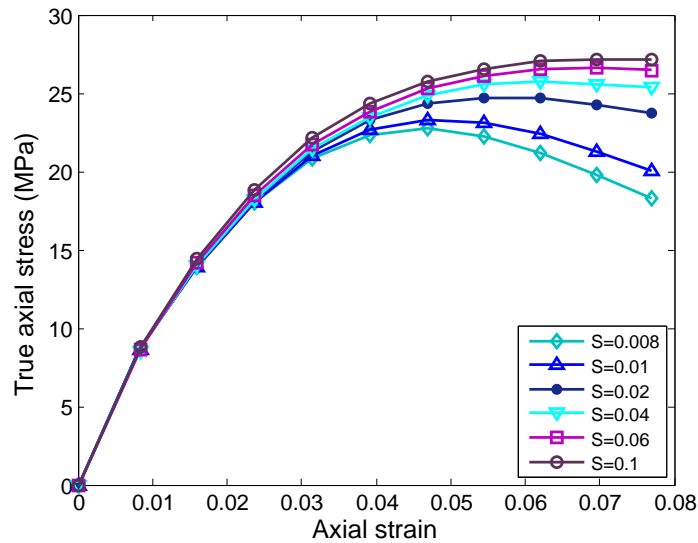


Figure 5.4: Influence of parameter  $S$  on the damaged matrix response at tension ( $1 \text{ mm}\cdot\text{min}^{-1}$ )

In this work, the variation of the elastic modulus is used as a non-direct measurement method of damage. This method is based on the influence of damage on elasticity through the state coupling defined in the framework of Continuum Damage Mechanics (Section 5.2.2). In case of isotropic damage, an effective elastic modulus of the damaged material is defined by:  $\tilde{E} = E(1 - D)$ , where  $E$  is the non-damaged elastic modulus. The value of the damage variable,  $D$ , can then be derived

from measurement of  $\tilde{E}$ , provided that  $E$  is known, as follows:

$$D = 1 - \frac{\tilde{E}}{E} \quad (5.25)$$

In practice, cyclic loading/unloading tensile tests are performed to assess the evolution of  $D$  by measurement of  $\tilde{E}$  during unloadings (Figure 5.5).

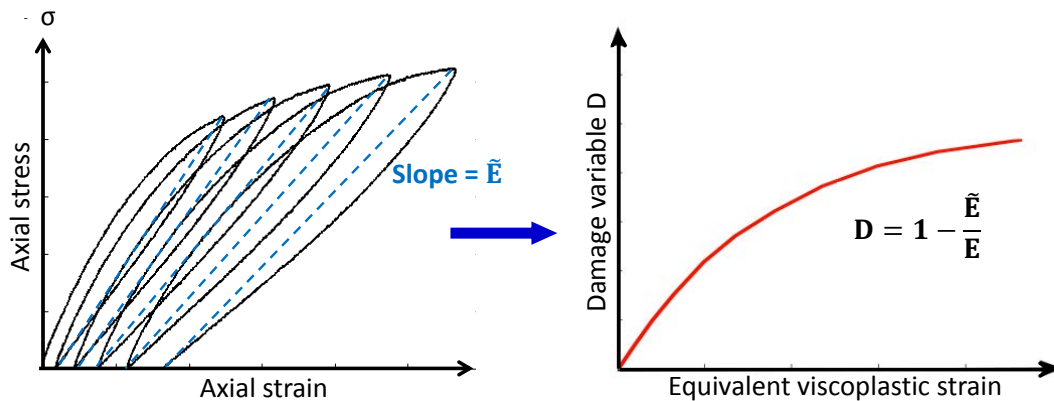


Figure 5.5: Damage variable determination from cyclic tests using the stiffness-loss method [38]

In this work, this technique is applied to PP with the same specimen geometry and testing set-up (Instron E3000 electromagnetic device with a 3 kN cell force) as for quasi-static monotonic tests (see section 4.1.1.1). Cyclic loading is applied with a prescribed displacement at  $1 \text{ mm} \cdot \text{min}^{-1}$ . During unloading, the imposed strain rate is the same as during loading. It is to note that this method remains reliable as long as the damage is uniformly distributed in the volume on which the strain is measured. To assess the validity of this hypothesis, strain values are tracked by Digital Image Correlation technique so that the homogeneous area of the ROI can be delimited, as shown in Figure 5.6.

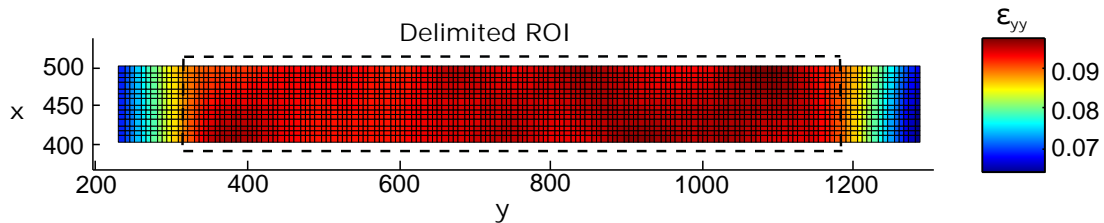


Figure 5.6: Cartography corresponding to an engineering strain of 0.087 and determination of the ROI of homogeneous strain

The evolution stress-strain response is shown in Figure 5.7, where axial strains are averaged over the homogeneous area of the tracked ROI. It is to note that these data correspond to an average of three tests, which showed a good repeatability.

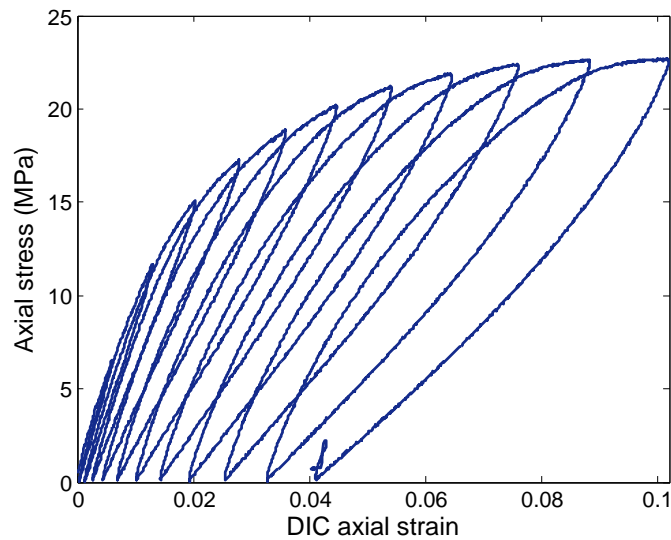


Figure 5.7: Stress-true strain response for cyclic uniaxial tensile test on PP

From these results one can observe the expected hysteresis effect characterising the viscoelastic behaviour. As shown in Figure 5.7, the loading and unloading phases are not linear. Therefore, an equivalent stiffness, different from the Young modulus but considered as an indicator of the damaged material rigidity, is taken between the lower and upper points of each hysteresis. Note that the “non-damaged” modulus is calculated from the first loading path. The damage variable is then calculated for each damaged (or equivalent stiffness) modulus,  $\tilde{E}$ , using Equation 5.25. The obtained values of  $D$  are presented in Figure 5.8.

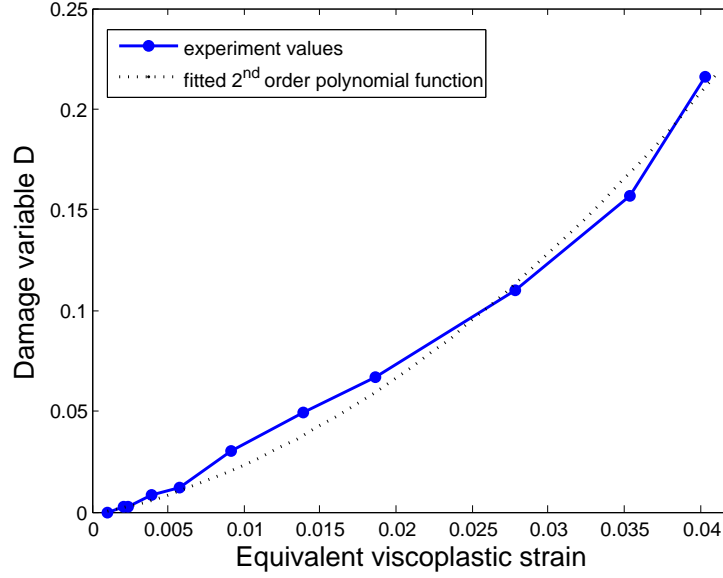


Figure 5.8: Damage evolution law calculated using the stiffness-loss method

### Identification of the damage law

The evolution law of the damage variable (Equation 5.24) can now be identified. The determination of the parameters  $S$  and  $\kappa_D$  is performed based on the elasticity change method, described above. Cyclic tensile tests, described hereabove, were realised at a loading speed ( $1 \text{ mm} \cdot \text{min}^{-1}$ ) assessed to be sufficiently low so that the time-dependent terms in the expression of the strain energy density release rate,  $Y$ , can be neglected. The Equation 5.21 then becomes:

$$Y(t) \simeq \frac{\tilde{\sigma}_{M_\infty,dev} : \tilde{\sigma}_{M_\infty,dev}}{4G_\infty} + \frac{\tilde{\sigma}_{M_\infty,H} : \tilde{\sigma}_{M_\infty,H}}{2K_\infty} \quad (5.26)$$

Expressing  $Y$  (in the case of isotropic damage) in terms of real stress tensors leads to:

$$Y(t) \simeq \frac{\sigma_{M_\infty,dev} : \sigma_{M_\infty,dev}}{4G_\infty (1-D)^2} + \frac{\sigma_{M_\infty,H} : \sigma_{M_\infty,H}}{2K_\infty (1-D)^2} \quad (5.27)$$

With the performed uniaxial tensile tests, the stress state is unidimensional and is defined as follows:

$$\sigma = \begin{bmatrix} 0 & 0 & 0 \\ 0 & \sigma_{yy} & 0 \\ 0 & 0 & 0 \end{bmatrix} \quad (5.28)$$



where  $\sigma_{yy}$  is the axial stress component. Based on definitions given in section 3.2.1.2, the corresponding deviatoric,  $\sigma_{M_{\infty},dev}$ , and hydrostatic,  $\sigma_{M_{\infty},H}$ , stresses are determined as follows:

$$\sigma_{M_{\infty},dev} = \begin{bmatrix} -\frac{1}{3}\sigma_{yy} & 0 & 0 \\ 0 & \frac{2}{3}\sigma_{yy} & 0 \\ 0 & 0 & -\frac{1}{3}\sigma_{yy} \end{bmatrix} \quad \text{and} \quad \sigma_{M_{\infty},H} = \frac{1}{3}\sigma_{yy} \quad (5.29)$$

Using the later expressions in Equation 5.27,  $Y$  can be written as follows:

$$Y(t) = \frac{\frac{2}{3}\sigma_{yy}^2}{4G_{\infty}(1-D)^2} + \frac{\frac{1}{3}\sigma_{yy}^2}{2K_{\infty}(1-D)^2} = \frac{\sigma_{yy}^2}{6(1-D)^2} \left( \frac{1}{G_{\infty}} + \frac{1}{K_{\infty}} \right) \quad (5.30)$$

where  $G_{\infty}$  and  $K_{\infty}$  are obtained from previous identification (Section 4.1).

The expression of the damage evolution law, can then be written in a ‘‘discretised’’ form as follows:

$$\frac{dD}{d\kappa} = \frac{Y}{S} \quad (5.31)$$

At each instant of the loading-unloading cycles when the axial viscoplastic strain is available,  $\kappa_i$ ,  $D_i$  and  $\sigma_{yy,i}$  are known. For the calculation of  $\left(\frac{dD}{d\kappa}\right)_i$  a second order polynomial function,  $p(\kappa)$  (Equation 5.32), is fitted to the experimental data  $D(\kappa)$ , as shown in Figure 5.8.

$$p(\kappa) = -0.0017 + 2\kappa + 142\kappa^2 \quad (5.32)$$

Using this expression, its derivative,  $p'$ , is calculated at each  $\kappa_i$  so that  $\left(\frac{dD}{d\kappa}\right)_i = p'(\kappa)$ . The parameter  $S$  can therefore be calculated as follows:

$$S_i = \frac{Y_i}{p'(\kappa_i)} \quad (5.33)$$

The computed values of  $S$  for the different instants are presented in Figure 5.9, where the final value is determined as its ‘‘average’’. A value of 0.05 MPa is obtained for sufficiently high values of  $\kappa$  (higher than 0.006).

The validation of the implemented model is performed using the determined damage law coupled with the matrix constitutive parameters previously identified. Comparisons are performed with tensile results of PP matrix where the experimental axial stress is determined with the compressibility

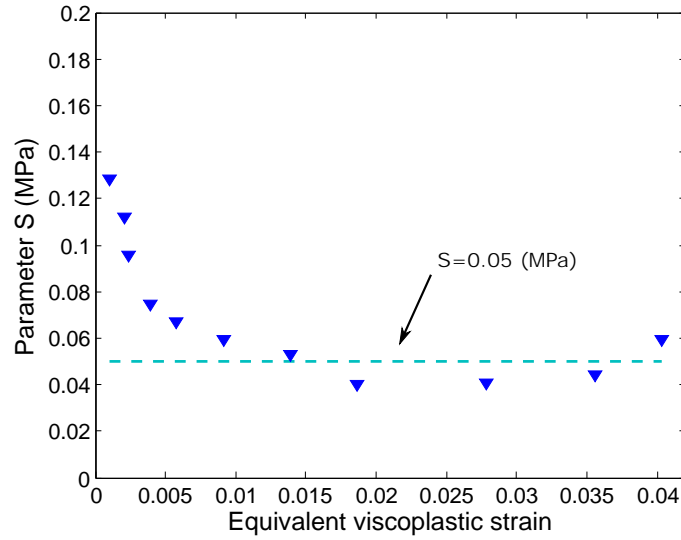


Figure 5.9: Identification of the parameter S

and transverse isotropy assumptions (Figure 5.10). That leads to express the true axial stress as:

$$\sigma = \frac{F}{S} \exp(-2\varepsilon_{xx}) \quad (5.34)$$

where  $\varepsilon_{xx}$  is the true transverse strain, measured by DIC. It is demonstrated from the presented comparisons that a better fit with experimental results is obtained. Indeed, a stress softening that occurs at a given strain range is well reproduced with the implemented damage law. As it can be seen in Figure 5.10, this is more valuable for quasi-static tests (i.e. for strain rates of  $5.55 \cdot 10^{-4} \text{ s}^{-1}$ ,  $5.55 \cdot 10^{-3} \text{ s}^{-1}$  and  $6.67 \cdot 10^{-2} \text{ s}^{-1}$ ). For higher strain rates, stress softening does not ameliorate the numerical-experimental fit. This is presumably due to a strain-rate dependency of damage development in the polymeric material that should be introduced.

### Anisotropy of the matrix damage model

The described damage law is implemented in its anisotropic form, i.e. with the fourth-order damage tensor,  $\mathcal{D}$ , taking the effect of the different fibre families into account (Equation 5.7). The effect of fibre orientation, and therefore the damage anisotropy, are highlighted in Figure 5.11, for two different distributions of fibre orientation (around  $0^\circ$  and  $90^\circ$  as preferential direction of orientation). A difference between the axial effective and real stress components,  $\delta\sigma_{yy}$ , is

computed for both distributions of fibre orientation in order to quantify this anisotropy (5.11(b)). It is to note that the used distributions of fibre orientation are those identified by micro-computed tomography, as presented in Chapter 4.

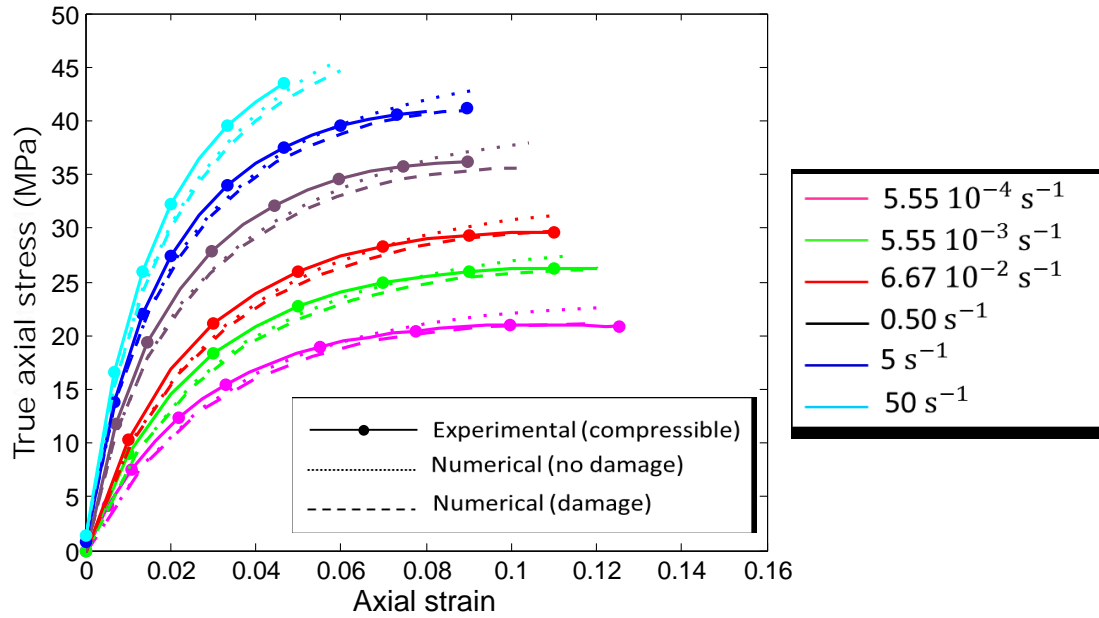
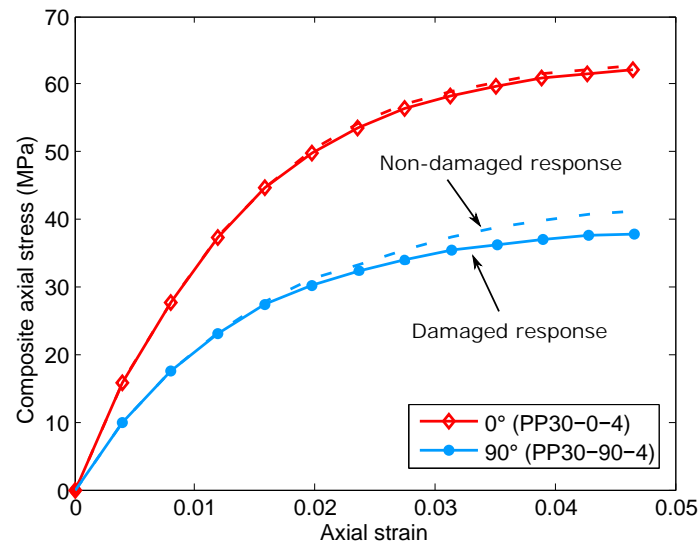
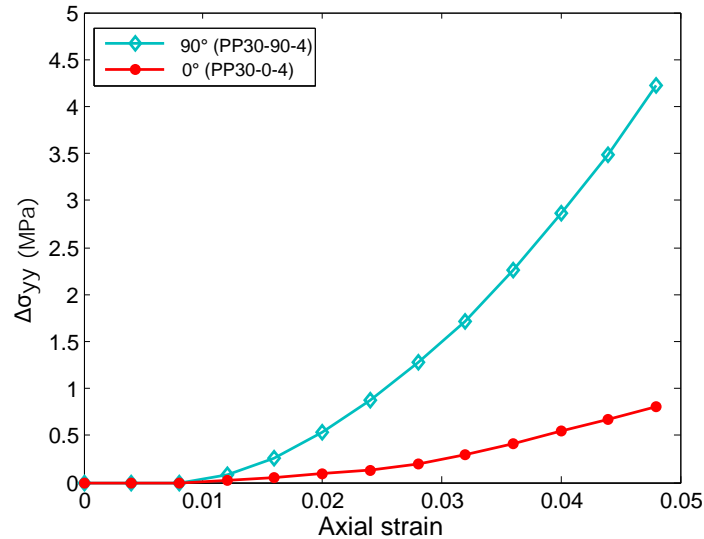


Figure 5.10: Influence of damage on computation of PP matrix tensile behaviour, for a wide range of strain rate



(a) Stress strain response of “non-damaged” (dashed lines) and “damaged” (continuous lines) matrix for different fibre orientations



(b) Computed difference between the effective and real axial stress with different fibre orientations

Figure 5.11: Anisotropy of the matrix damage for the PP-30GF composite (data computed using distributions of fibre orientation of specimens PP30-0-4 and PP30-90-4)

### 5.3 Fibre-Matrix interfacial damage

As explained in the first part of this chapter, the development of damage phenomena in short-fibre reinforced materials is governed by the properties of the reinforcement. More precisely, and in addition to the anisotropy of matrix damage (dealt with in the first part of the chapter), the effect of fibres intervenes in the progressive failure mechanism through alteration of load transmission at fibre-matrix interface or fibre breakage. Fibre breakage is not addressed in this work since it

is assumed that fibre length is sufficiently low with respect to the critical length so that fibre breakage is unlikely to happen. On the contrary, degradation of fibre/matrix bonds at the interface is generally considered as a major damage phenomenon of SFRC. It is addressed in this part of the work based on microscopic observations reported in the literature. In particular, a highlight is done on the interface degradation process described by Sato et al. [55] for a polyamid reinforced by short glass fibres. These authors established a scenario of successive steps leading to composite failure under tension, which constitutes the basis of current developments. Thanks to direct in-situ SEM observations, Sato et al. [55] have postulated that mechanism of composite progressive failure initiates at fibre tips and can be described by the following steps:

1. Initiation of interfacial microfailure at fibre tips due to high tensile stress concentration around fibre tips (from about 50% of ultimate composite stress).
2. Separation at the interface, formation of microvoids in the matrix material at the vicinity of the fibre tips.
3. Propagation of interfacial microfailures along fibre sides due to critical shear stress concentration: from about 75 % of ultimate composite stress.
4. Occurrence of plastic deformation bands in the matrix and ductile crack propagation through plastic deformation bands.
5. Ultimate failure by brittle crack propagation: failure is governed by a critical value of crack size propagating through the matrix material.

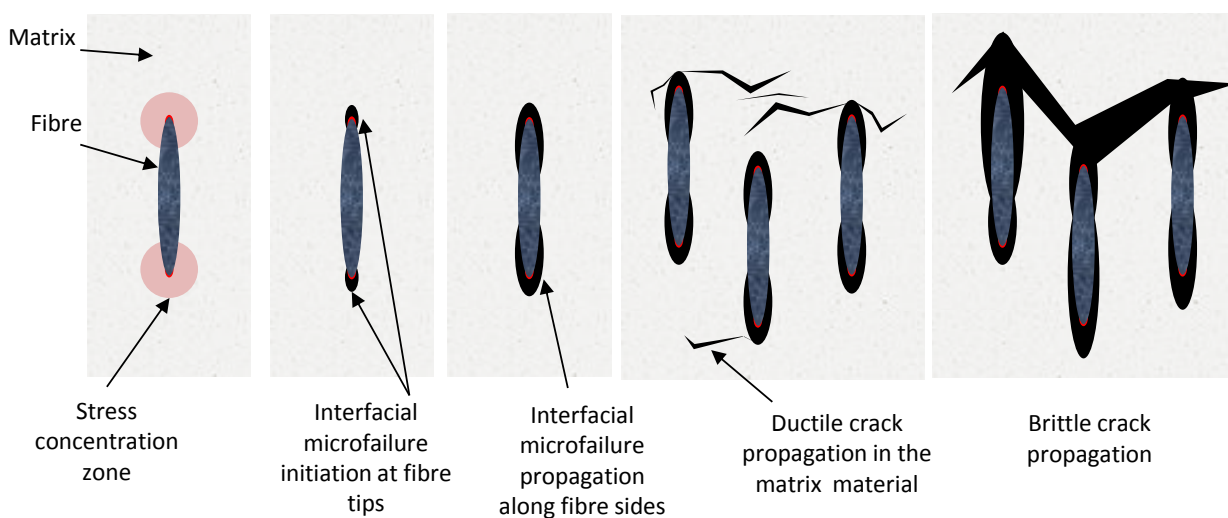


Figure 5.12: A schematic representation of failure scenario in SFRC subjected to an axial loading (in the direction of the fibre axis)

### Modelling strategy

In this part, the degradation of the fibre-matrix interface is addressed based on the later observations of Sato et al. [55] and first modelling presented by Notta-Cuvier et al. [139]. The load transmission, which is governed by shear transfer process, remains unaffected as long as no micro-defects are initiated on the fibre-matrix interface. Yet, this transmission is degraded as soon as microcracks start to propagate along fibre tips and sides. For a given fibre medium  $\alpha$ , interfacial microfailures, or voids, are assumed to develop when the fibre axial strain reaches a threshold value called  $\varepsilon_{th}$ . Then, the voids area extends from each fibre tip to a length equal to  $L^{\alpha D}$  and prevents load transmission over a fibre length equal to  $\delta^\alpha \leq L^{\alpha D}$  (Figure 5.13).

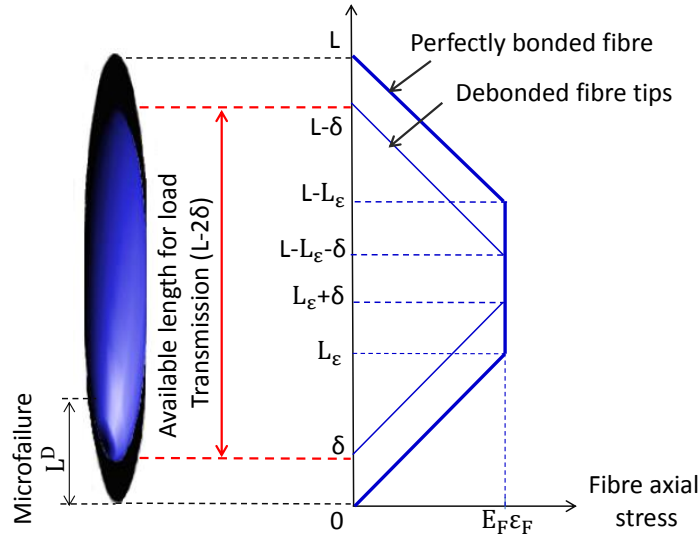


Figure 5.13: Effect of fibre/matrix debonding on load transmission

The actual fibre 1D stress state is therefore computed by replacing  $L^\alpha$  by  $L^\alpha - 2\delta^\alpha$  in the fibre stress expression (given in Section 3.2.2), so that (for all values of  $\alpha$ ):

$$\left\{ \begin{array}{ll} \sigma_F^{0,\alpha} = \varepsilon_F^{0,\alpha} \left( 1 - \frac{E_F^\alpha r^\alpha}{2(L^\alpha - 2\delta^\alpha) \tau^\alpha} \left| \varepsilon_F^{0,\alpha} \right| \right) E_F^\alpha & \text{if } \left| \varepsilon_F^{0,\alpha} \right| \leq \frac{(L^\alpha - 2\delta^\alpha) \tau^\alpha}{E_F^\alpha r^\alpha} \\ \sigma_F^{0,\alpha} = \text{sign}(\varepsilon_F^{0,\alpha}) \frac{(L^\alpha - 2\delta^\alpha) \tau^\alpha}{2r^\alpha} & \text{otherwise} \end{array} \right. \quad (5.35)$$

$\delta^\alpha$  is assumed to increase with fibre 1D strain, as soon as it becomes higher than the threshold  $\varepsilon_{th}$ ,

as follows:

$$\begin{cases} \delta^\alpha = a \left( \frac{\varepsilon_F^{\alpha 1D} - \varepsilon_{th}}{\varepsilon_{th}} \right)^b \frac{L^\alpha}{2} & \text{if } \varepsilon_F^{\alpha 1D} \geq \varepsilon_{th}, \\ \delta^\alpha = 0 & \text{otherwise} \end{cases} \quad (5.36)$$

where  $a$  and  $b$  are constant parameters to be identified. The loss in load transmission is responsible for the development of shear stress concentration in matrix material and, consequently, of the growth and coalescence of voids within the matrix. The volume of nucleated voids around each fibre is given by  $2\pi (r_v^\alpha r^\alpha)^2 L^{\alpha D}$ , where  $r_v^\alpha$  is the average ratio of nucleated voids diameter by fibre radius. The corresponding volume fraction (i.e. of nucleated voids),  $v_v^{nucl}$ , with respect to the composite volume is therefore given by:

$$v_v^{nucl} = \sum_\alpha \left( \frac{2L^{\alpha D}}{L^\alpha} \right) r_v^{\alpha 2} v_F^\alpha \quad (5.37)$$

In the following, it is assumed that values of  $r_v^\alpha$  and  $L^{\alpha D}/\delta^\alpha$  are the same for all the fibre media, so that  $r_v^\alpha = r_v$  and  $L^{\alpha D}/\delta^\alpha = L^D/\delta$ ,  $\forall \alpha$ . Finally, the volume fraction of nucleated voids is given by:

$$v_v^{nucl} = C^{nucl} \sum_\alpha \left( \frac{2\delta^\alpha}{L^\alpha} \right) v_F^\alpha \quad (5.38)$$

where the parameter  $C^{nucl}$  is introduced as  $C^{nucl} = r_v^2 L^D/\delta$ . Using the expression of the nucleated voids fraction, the evolution of the total voids volume fraction,  $\dot{v}_v^{tot}$ , is computed as follows:

$$\dot{v}_v^{tot} = \Pi \left[ \dot{v}_v^{nucl} + C^{growth} v_v^{nucl} \dot{\sigma}_H \right] \quad (5.39)$$

where  $\dot{v}_v^{nucl}$  is the rate of volume fraction of nucleated voids and  $C^{growth}$  is a constant parameter defining the void growth dependency to macroscopic composite hydrostatic stress,  $\sigma_H$ , [96]. According to Zairi et al. [96], the parameter  $C^{growth}$  is of an order of magnitude close to  $1/G$ , with  $G$  the shear modulus of the composite. In the expression (5.39) the influence of the surrounding area of debonded fibre is taken into account using the parameter  $\Pi$ . Indeed, at fibre vicinity, voids nucleation, growth and coalescence and then crack propagation, is strongly influenced by the fibre environment and its local mechanical state. Void nucleation growth and propagation may be accelerated when the fibre is surrounded by area of shear stress concentration, a stress state conducive to debonding, occurring due to the presence of close fibres. On the contrary, if neighbouring fibres have higher angles of orientation with respect to loading direction than the debonded fibre, the development of shear bands is delayed as well as debonding development.

Moreover, when neighbouring fibres are transversally oriented to the crack path, they may act as obstacles to its propagation [139]. Based on these observations, parameter  $\Pi$  is introduced according to a probabilistic approach as follows:

$$\Pi = \frac{1}{v_F^{tot}} \sum_{\alpha} v_F^{\alpha} \frac{L^{\alpha D}}{L_{max}^D} = \Pi \frac{1}{v_F^{tot}} \sum_{\alpha} v_F^{\alpha} \frac{\delta^{\alpha}}{\delta_{max}} \quad (5.40)$$

where  $\alpha$  designates family of fibres with debonded tips, i.e.  $\alpha \in \{1, \dots, N_{fam}\}$  and  $\epsilon_F^{\alpha 1D} \geq \epsilon_{th}$ .

Note that the probability of void nucleation and then growth increases with the number of partially debonded fibres in the neighbourhood of the debonded fibre. In order to prevent jumps in the values of  $\Pi$ , the factor  $L^{\alpha D}/L_{max}^D = \delta^D/\delta_{max}$  is introduced. where  $L_{max}^D = \max_{\alpha} (L^{\alpha D})$  and  $\Delta_{max} = \max_{\alpha} (\Delta^{\alpha})$ . Finally, the parameter  $C^{nucl}$  has to be determined. Its value is experimentally identified as described in Annexe (A).

Once the described laws are implemented and coupled to the developed constitutive model of SFRC behaviour, first verifications are made to show the effect of each parameter. In particular the effect of parameters a and b on the evolution of  $\delta^{\alpha}$  is highlighted in Figures 5.14 and 5.15. As these two parameters have a coupled effect on the evolution of  $\delta^{\alpha}$ , they have to be simultaneously determined. From observations on experimental tensile results of composite material (PP-30GF), it is found that debonding evolution can not be linear. Therefore the value of the parameter b is different from 1, and is taken equal to 2. The effect of the parameter a is shown in Figures 5.16 and 5.17 on the fibre and composite axial responses, respectively. Value of a is then identified by fitting the computed composite axial response to the experimental data obtained for PP-30GF at  $1 \text{ mm} \cdot \text{min}^{-1}$  (Figure 5.18). For this comparison, the specimen PP30-0-1 is chosen as the one having the highest density of fibres oriented in loading direction (see section 4.1.2.1). A value of  $a = 0.15$  is obtained.



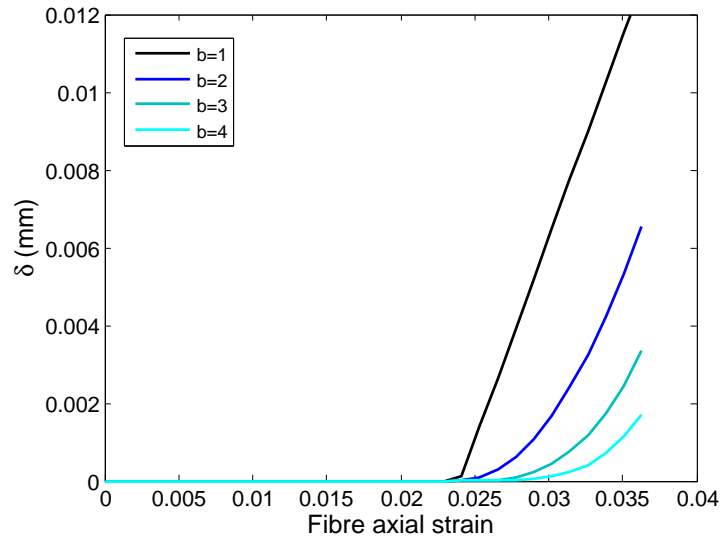


Figure 5.14: Influence of parameter  $b$  on the fibre length unavailable for load transmission ( $a$  fixed at 0.2)

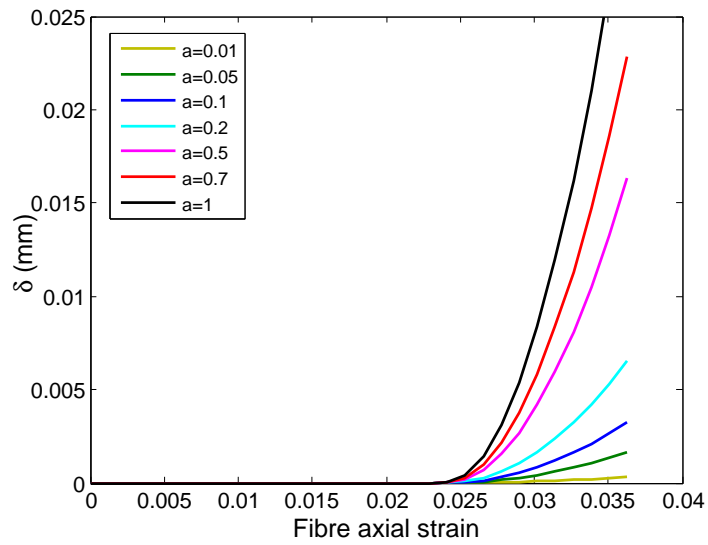


Figure 5.15: Influence of parameter  $a$  on the fibre length unavailable for load transmission ( $b$  fixed at 2)

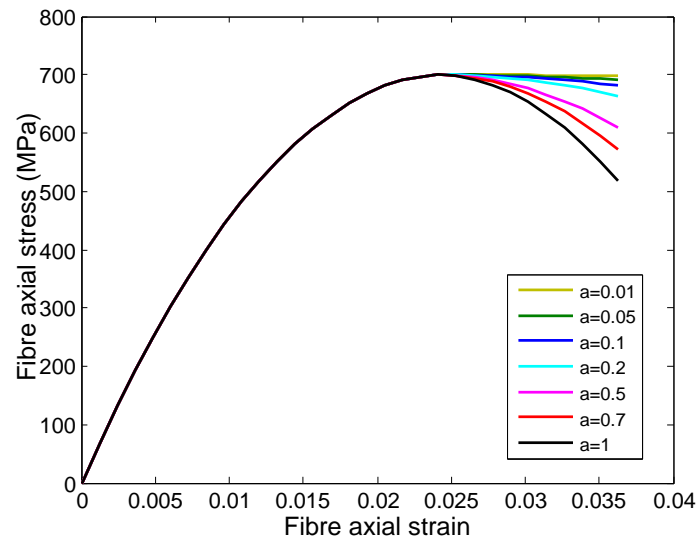


Figure 5.16: Influence of parameter  $a$  on the fibre axial stress ( $b$  fixed at 2)

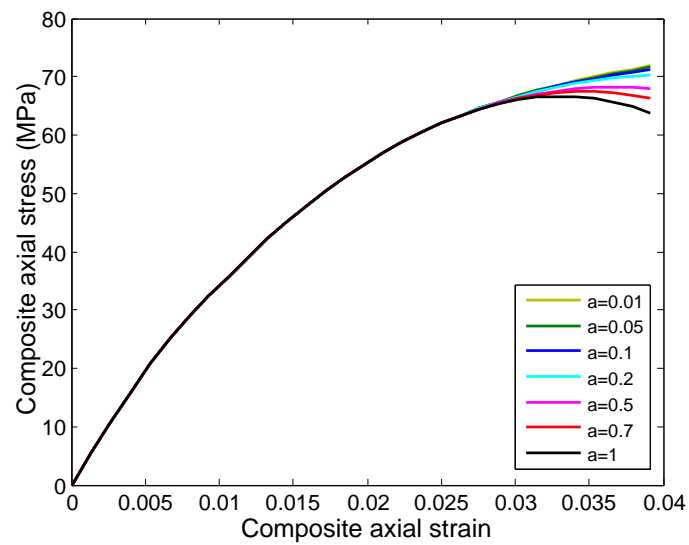


Figure 5.17: Influence of parameter  $a$  on the composite PP-GF30 axial stress ( $b$  fixed at 2), in the case of specimen PP30-0-1 tested at  $1 \text{ mm} \cdot \text{min}^{-1}$

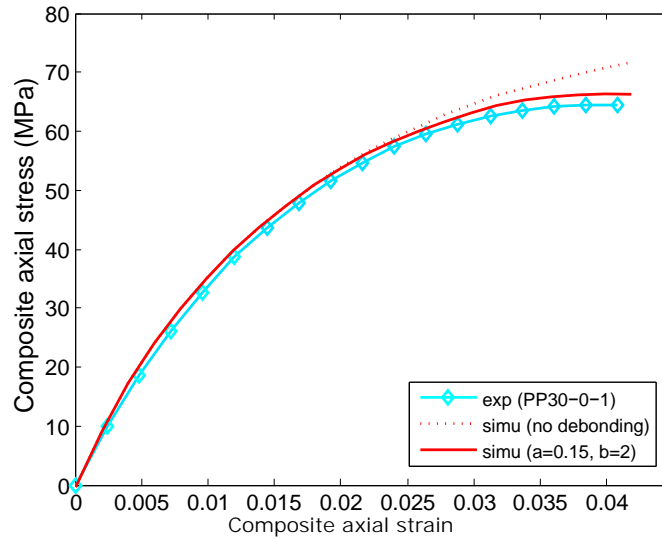


Figure 5.18: Comparison of experimental and numerical results for the identified parameters  $a$  and  $b$  (specimen PP30-0-1 tested at  $1 \text{ mm}\cdot\text{min}^{-1}$ )

## 5.4 Validation of the damage model

The described laws of debonding evolution are coupled to the previously described constitutive laws of the composite material (with damageable viscoelastic-viscoplastic matrix).

A flowchart summarising the implementation of the behaviour model, including laws of the matrix ductile damage and fibre-matrix debonding, is presented in Figure 5.19.

The validation of the complete model is performed by comparison with experimental tensile data obtained for the PP-30GF with the different loading angles (realised at  $1 \text{ mm}\cdot\text{min}^{-1}$ ). Note that the effect of strain rate on the development of damage mechanisms is not addressed in this work. Results presented in Figure 5.20 show that the predicted response of the implemented model is in a better agreement with the experimental results for the presented cases compared with previous results, obtained without the consideration of damage phenomena. So, these comparisons prove the ability of the present model to reproduce the damage phenomena occurring in the composite material.

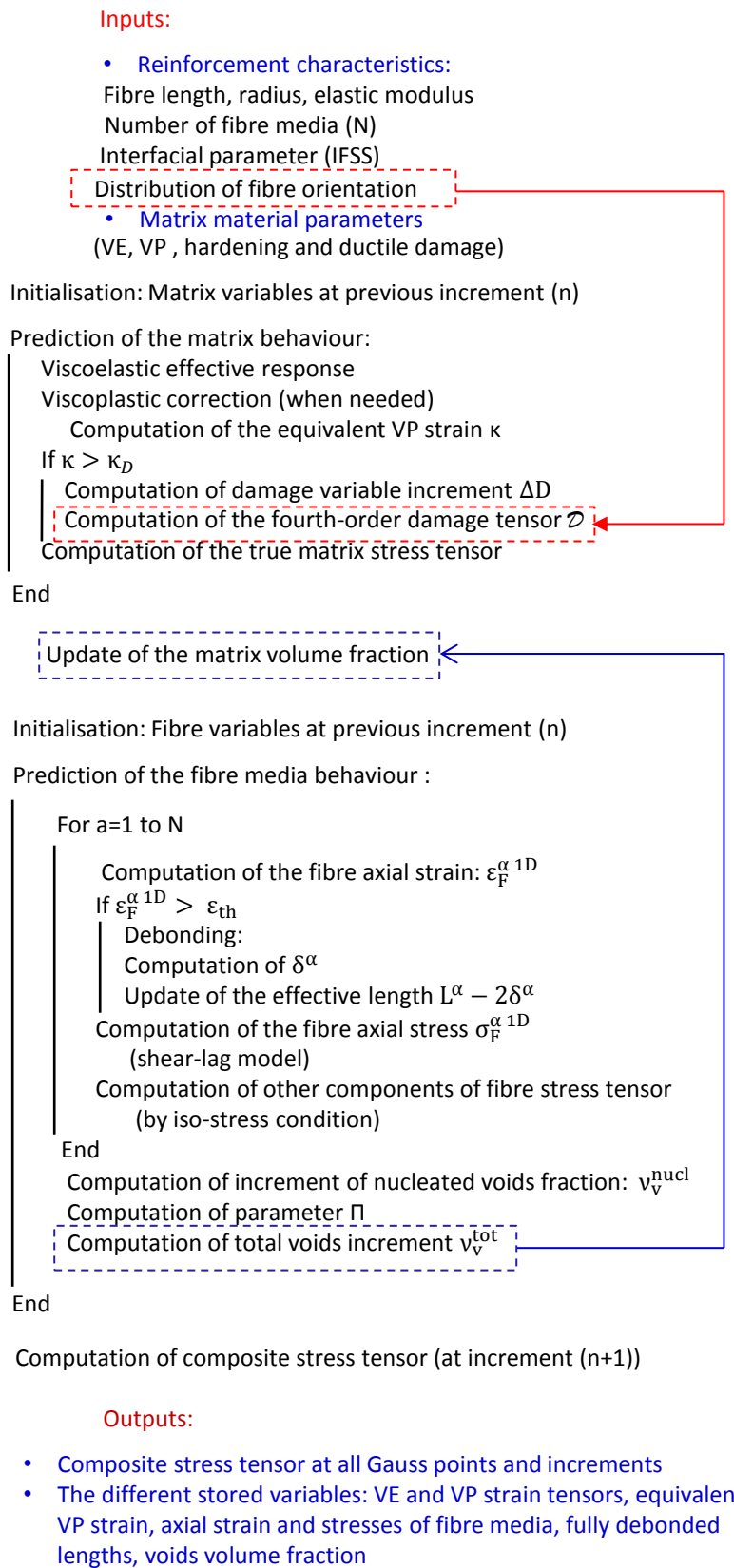


Figure 5.19: Implementation scheme

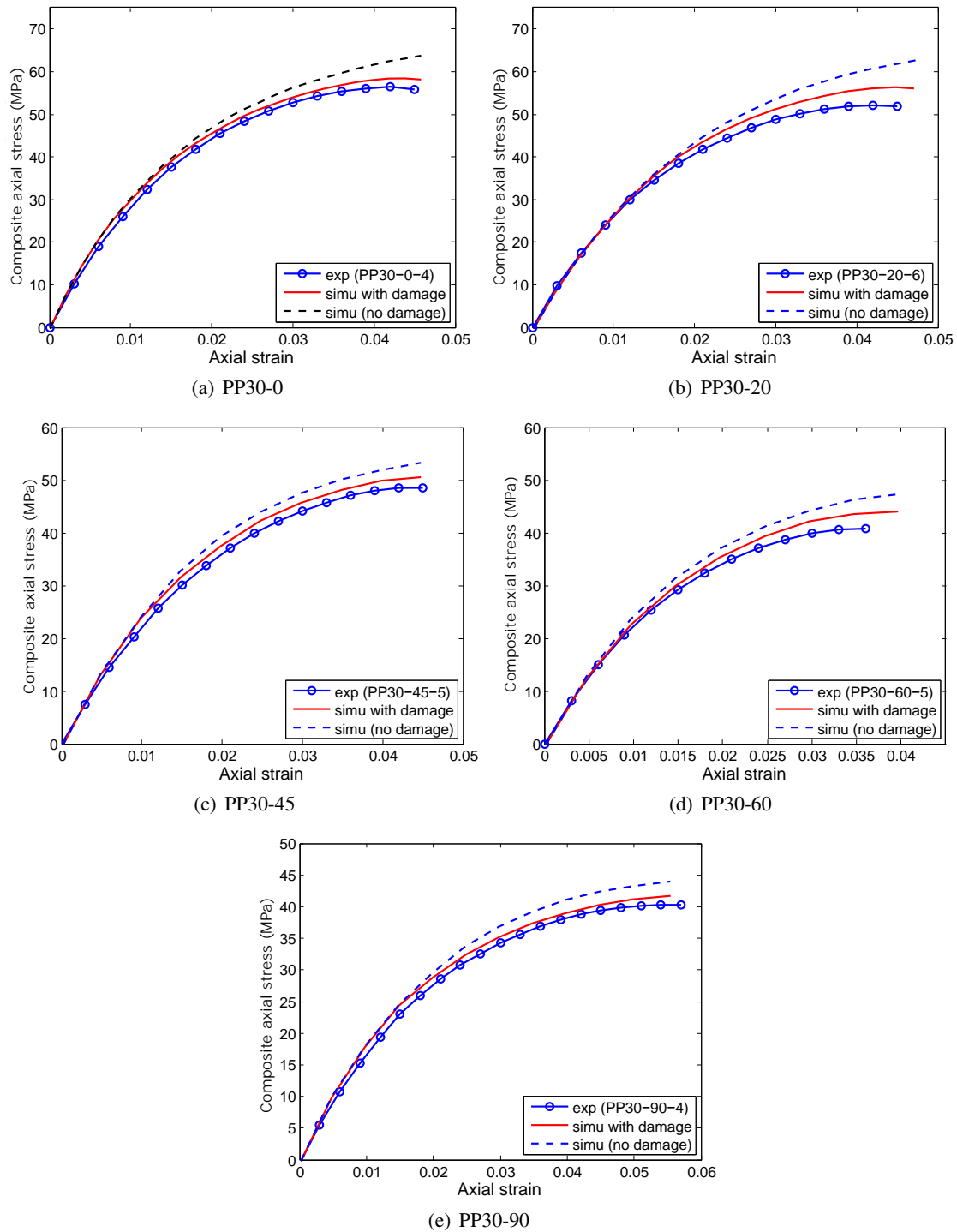


Figure 5.20: Verification of the model with the implemented matrix and interfacial damage models by comparison with experimental results in the case of PP-30GF

## 5.5 Fracture modelling

Failure of short fibre reinforced composites have been the object of some experimental and numerical investigations in the literature. Most of the research work on fracture modelling were performed in the framework of fracture mechanics, where the concept of dissipation energy is investigated [140, 141, 142]. Among this, Lauke and Pompe [143] have treated failure of SFRC as a combination of different energy dissipation mechanisms (fibre debonding and sliding, brittle and ductile matrix fracture,...) acting within a zone ahead of a notch tip. They proposed then a fracture criterion based on the basis of an energy principle. This approach is however limited by the difficulty to identify the distinct dissipation energies in case of complex microstructure. Very few works have been proposed for the prediction of SFRC ultimate failure on the basis of damage mechanisms accumulation. In this part of the work, a failure criterion is introduced in order to predict SFRC macroscopic mechanical state at break. The implemented criterion is based on the assumption that SFRC failure is governed by the developpement of damage mechanisms [139], in particular, fibre/matrix interfacial debonding and matrix ductile damage (Sections 5.2 and 5.3). The objective is to identify this failure criterion for a SFRC with known reinforcement characteristics, including reinforcement distribution of orientation, and then to use it to predict failure of a similar composite, i.e. made of the same constituents but with other reinforcement characteristics (i.e. orientations) and/or kinds of loading. This study is applied to the PP-30GF subjected to quasi-static uniaxial tensile loadings in two different directions with respect to the injection flow direction. Identification and validation of the implemented fracture criterion are therefore performed based on results of these experimental tests.

### 5.5.1 Damage development based criteria

A failure criterion is defined here based on a critical void content reached in the composite material as a consequence of the developpement of damage “quantities”. As stated above, several damage mechanisms can simultaneously develop depending on the microstructure/reinforcement properties of the composite material. Among them, fibre/matrix interfacial debonding is undoubtedly a predominant damage phenomena, as indicated by the presence of debonded fibres on the fracture surface of PP-30GF (Figure 5.21).

It is assumed here that ultimate failure is function of the voids induced by interfacial debonding that develops at fibre tips. It is therefore defined by the critical fraction of the cumulated voids, with void fraction evolving according to equations of section 5.3.

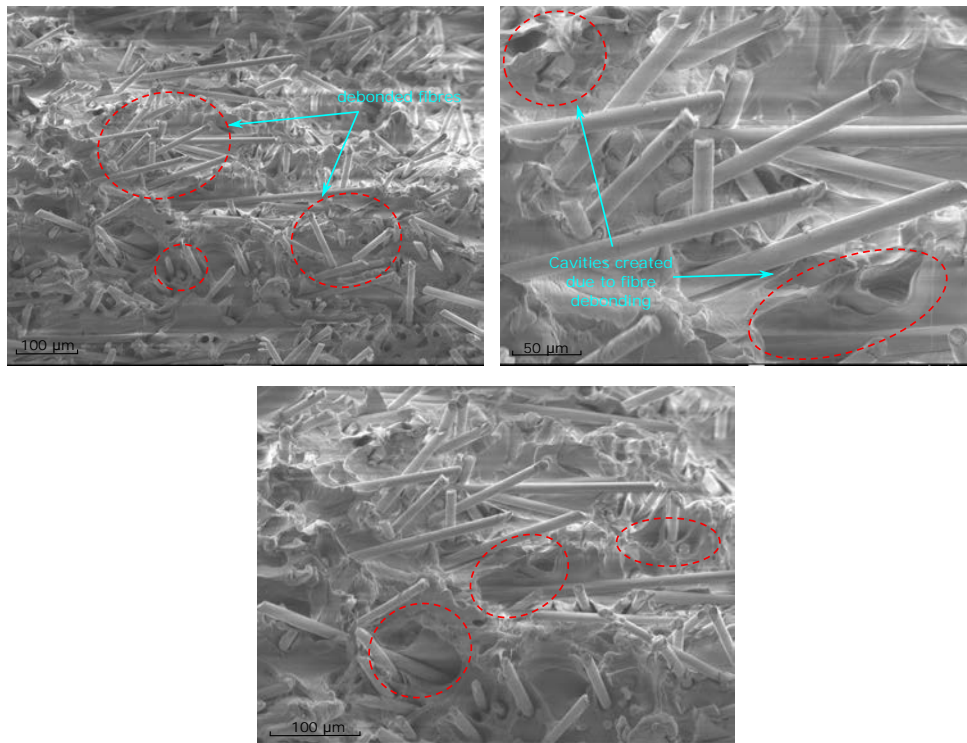


Figure 5.21: Fibre debonding in a fracture surface of PP-30GF tested at  $1\text{mm}\cdot\text{min}^{-1}$  (visualised by MEB)

Critical void fraction,  $v_v^{crit}$ , is identified for a reference composite with “perfectly” known reinforcement characteristics, by noting the value of  $v_v^{tot}$  that is reached at composite break. Then,  $v_v^{crit}$  is a failure criterion that can be used to predict the strain at break of all composites made from the same constituents in nature than the reference composite, whatever reinforcement characteristics, particularly in terms of fibre orientation. This failure description is consistent with the experimental observations stating that composite strain at break increases with fibre angle of orientation with respect to loading direction [133]. Indeed, the nucleated void fraction,  $v_v^{nucl}$  (Equation 5.37), and therefore the total void fraction,  $v_v^{tot}$  (Equation 5.39), decreases when fibre angle of orientation increases, at identical composite strain rate, and higher values of loading have

therefore to be reached to fulfill the failure criterion.

$$v_v^{tot} = v_v^{crit} \quad (5.41)$$

The evolution of the cumulated void fraction in PP-30GF is computed for different distributions of fibre orientation, as presented in Figure 5.22. The considered orientations correspond to those established by  $\mu$ -computed tomography for specimens cut at different angles,  $\theta$ , with respect to the injection flow direction (see Section 4.1.2.1). It can be reminded that in those cases,  $\theta$  is the preferential (but not unique) orientation of fibres with respect to loading direction.

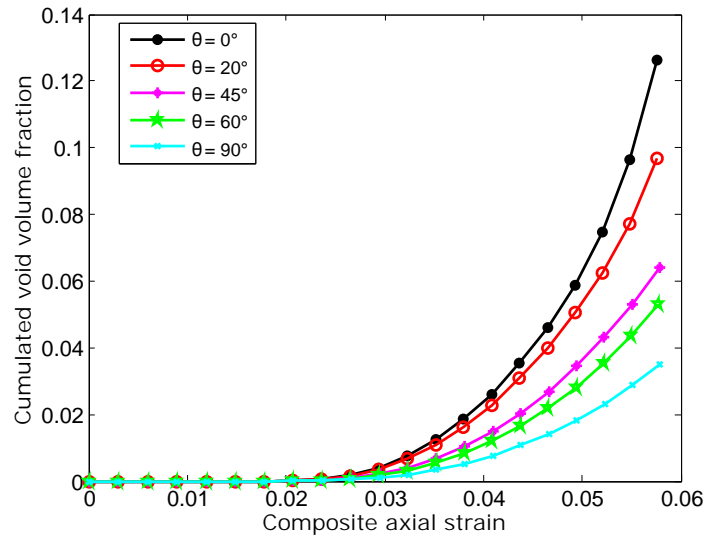


Figure 5.22: Evolution of cumulated void volume fraction with different distributions of fibre orientation resulting from different cutting angles  $\theta$

As expected, the volume fraction of voids induced by interfacial debonding is higher and increases faster as fibre orientation becomes closer to loading direction.

### 5.5.2 Tensile tests with notched specimens

In order to characterise the failure criterion, uniaxial tensile tests are performed with notched specimens of the composite PP-30GF (Figure 5.23). Notched specimens are characterised by a weakened section resulting in a strain concentration zone that leads to damage localisation (notch zone). The uniaxial tensile tests are performed on the electromagnetical device with a cell force of 3KN (INSTRON E3000). Load is applied with a prescribed displacement of  $1 \text{ mm} \cdot \text{min}^{-1}$  and with



specimens cut at angle  $\theta$  equal to  $0^\circ$  and  $90^\circ$  with respect to the injection flow direction (IFD). True in-plane strain fields are determined using 2D Digital Image Correlation (DIC) technique for a local measurement within the area of strain concentration (Figure 5.23). The facets are tracked by DIC software (VIC 2D) at an acquisition rate of 2 im/s. The influence of facet size and step size on the measured strains is studied. They are chosen as a compromise between a good level of accuracy of the measured strains (in terms of captation of strain localisation in particular) and the avoidance of loss of data at the step preceeding failure. As shown in Figure 5.24, a loss of data occurs at step 150 (corresponding to an engineering strain of 0.04) for relatively small sizes of facet and step. Based on this observation a facet size of  $31 \times 31 \text{ pix}^2$  and step size equal to 15 pix are chosen.

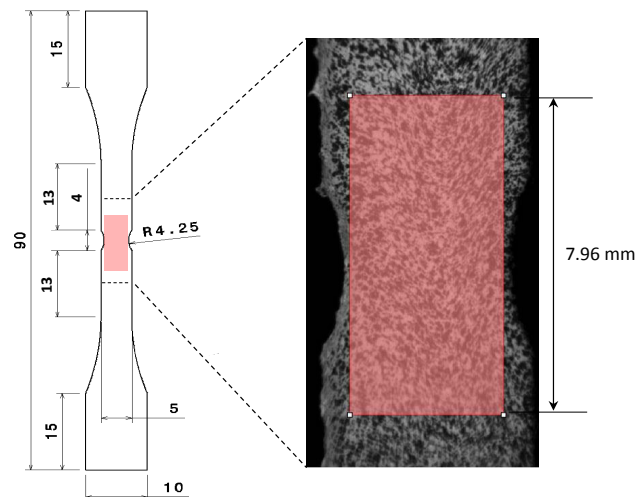


Figure 5.23: Notched specimen geometry and definition of the ROI

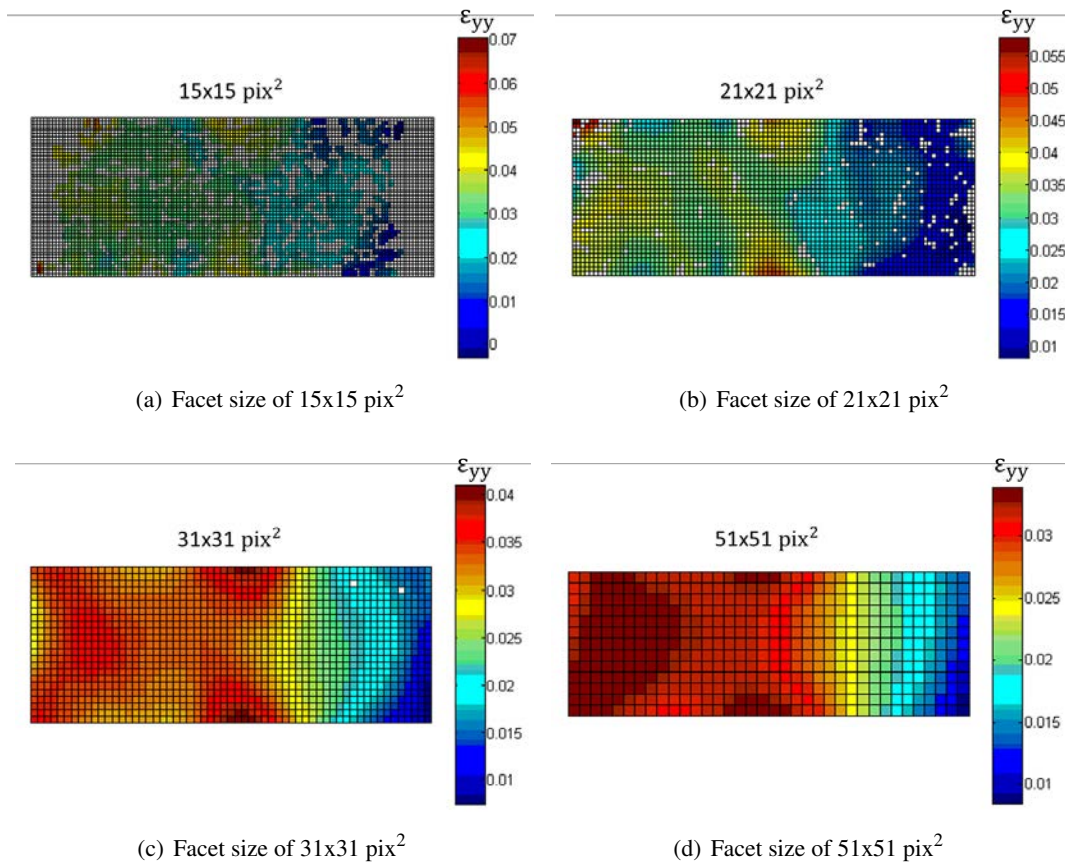


Figure 5.24: Influence of the facet size on the measured axial strain at the step 150 (corresponding to an engineering strain of 0.04)

### 5.5.3 Identification and verification of the fracture criteria

For the determination of failure axial strain, the computed local axial strains at the pre-failure step, i.e. final step before failure, in notched specimens cut at 0° with respect to loading direction are presented. To verify the consistency of the measurement, three specimens are tested and results are presented in Figure 5.25. It can be observed that failure occurs when a high level of strain is locally reached. This is of great importance for the following concerns, as this indicates that the failure occurs when a critical strain value is reached and is not the consequence of a material local defect (e.g. created during the manufacturing process).

Failure strain is determined as the maximum value reached in the strain localisation zone of a reference specimen, the PP30-0-4. Its value is determined as the average of local strain values over a diameter of 1.68 mm (Figure 5.26) and is equal to 0.048.

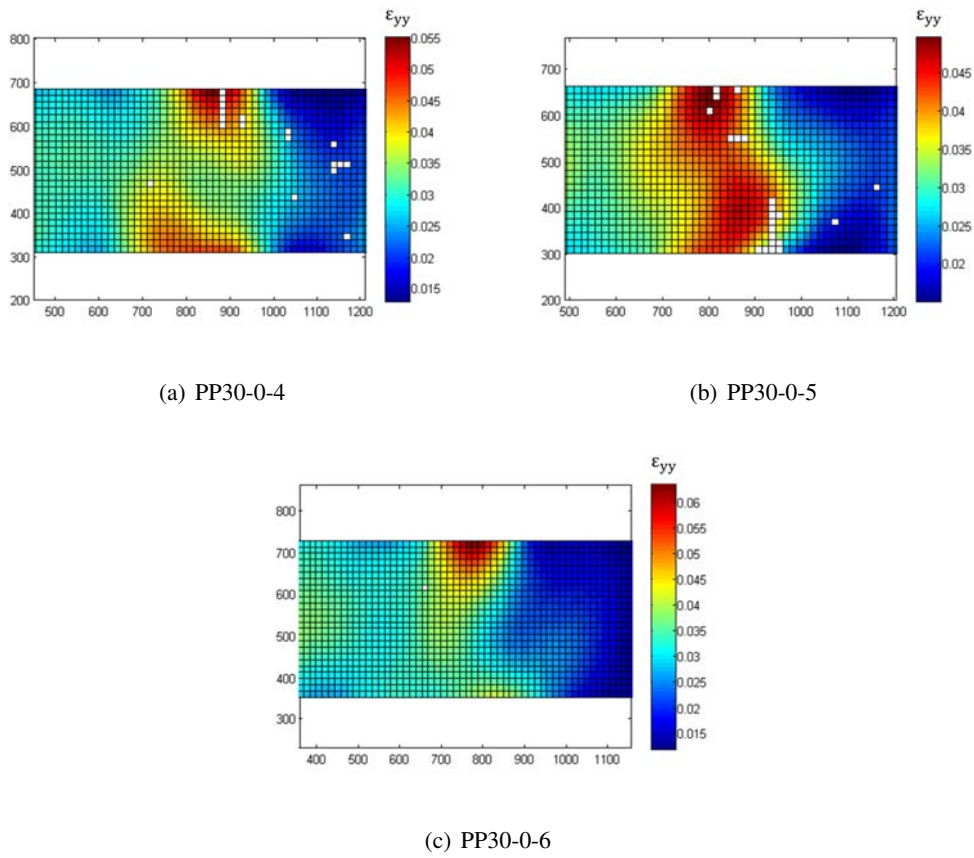


Figure 5.25: Cartography of axial strains at the pre-failure step (last step) for  $0^\circ$ -specimens with a facet size of  $31 \times 31 \text{ pix}^2$

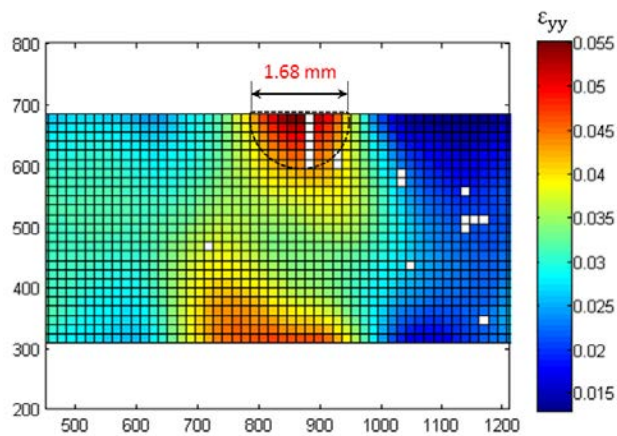


Figure 5.26: Local strain measurement at the pre-failure step of the specimen PP30-0-4

It is to note that the choice of this specimen (PP30-0-4) for the failure strain identification is made based on the fact that its distribution of fibre orientation is known. Knowing the actual fibre orientation will be of great importance when identifying the critical cumulated void fraction as presented later.

The notched specimen tests are simulated using the developed constitutive model with all the identified parameters. Geometry of notched specimens presented in Figure 5.23 is used. Tests are simulated with the same boundary conditions and applied velocity as those described in section 4.1.3. Attention is paid to element size for the computation of local axial strain values at the notched zone. As presented in Figure 5.27, three sizes are considered and no significant effect is observed on the strain localisation in the critical zone (i.e. notched zone). Computation is therefore realised with a mesh size of 0.5 mm. Similarly to experimental tests, results are averaged over a critical zone with a diameter of 2 mm (Figure 5.28).

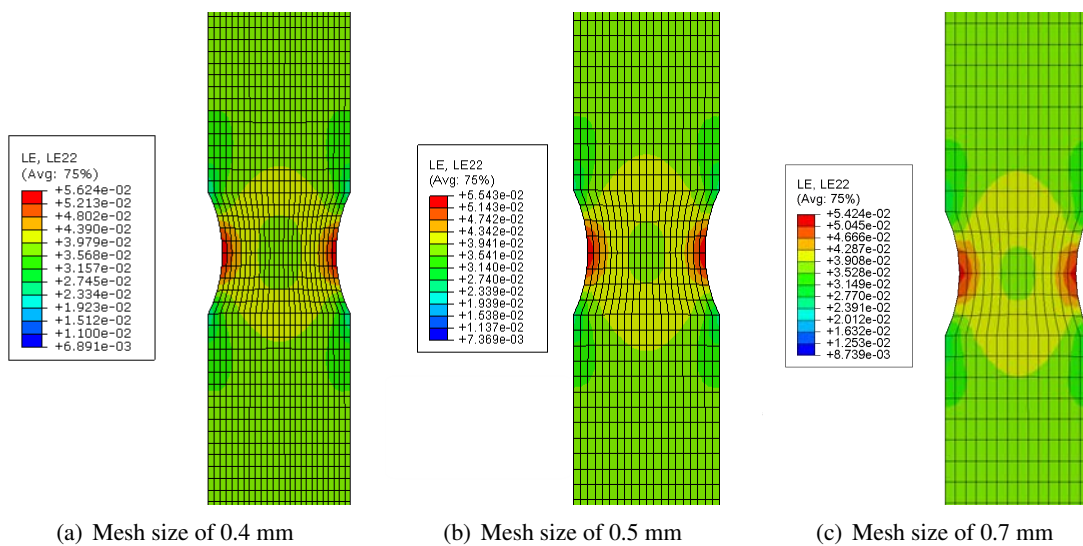


Figure 5.27: Influence of the mesh size on the strain localisation at the notch zone

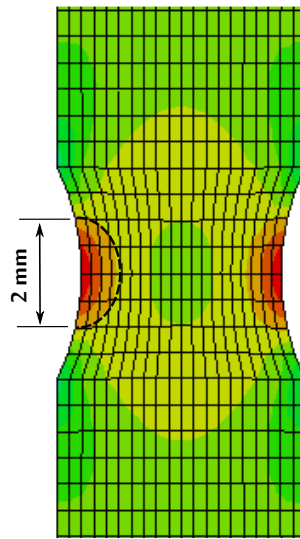


Figure 5.28: simulated zone of failure initiation

The critical cumulated void fraction is then determined as the one corresponding to the measured failure strain in the case of a  $0^\circ$ -specimen. More precisely, the considered distribution of fibre orientation is that of the specimen PP30-0-4. As shown in Figure 5.29, a critical void fraction of 0.057 is found.

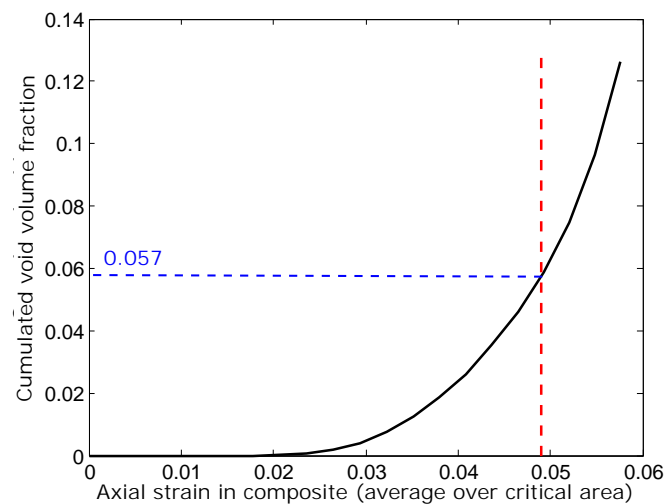


Figure 5.29: Identification of the critical cumulated void fraction with results obtained for the specimen PP30-0-4

In order to highlight the sensitivity of the computed total void fraction on the fibre orientation,  $v_v^{tot}$  is computed for different distributions of fibre orientation of  $0^\circ$ -specimens (Figure 5.30).

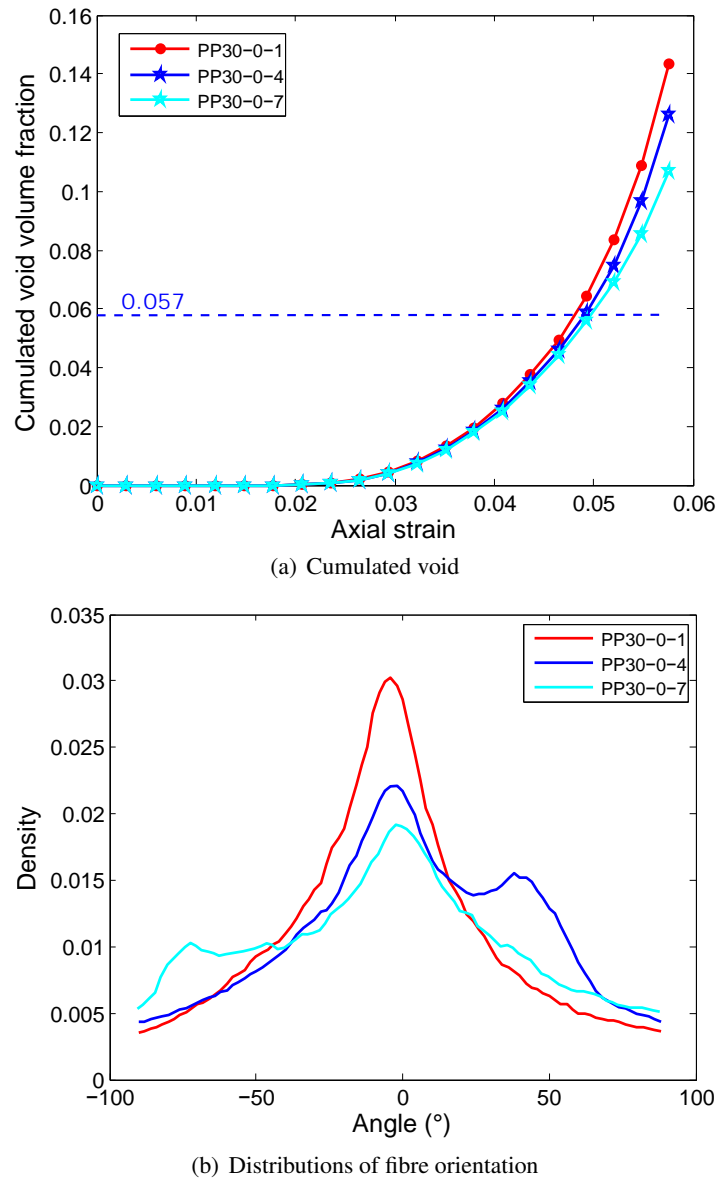


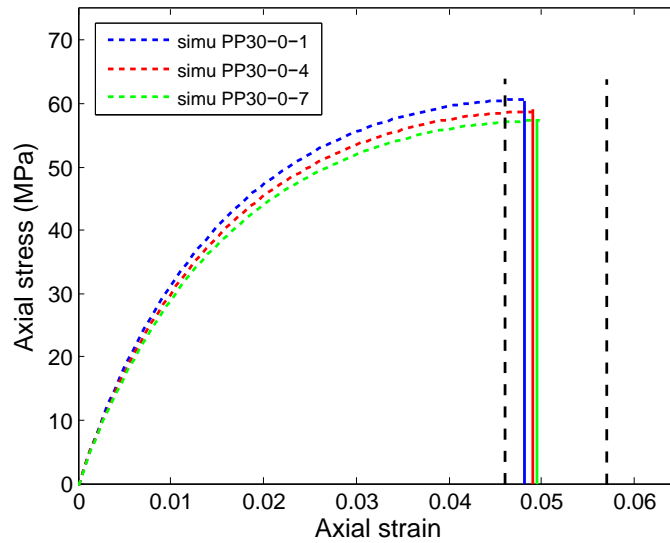
Figure 5.30: Evolution of the cumulated void (a) with different distributions of fibre orientation obtained from specimens cut at  $\theta = 0^\circ$  (b)

The corresponding failure strains are then computed (Table 5.1). It can be noted that for the same loading angle,  $\theta = 0^\circ$ , a variation in the computed critical strain values exists, which is due to the fact that different distributions of fibre orientation (corresponding to  $0^\circ$ -specimens scanned at different positions) are present.

Failure strains computed with simulated  $0^\circ$ -notched tensile tests are presented in Figure 5.31 and are within the experimental values range.

Table 5.1: Values of critical axial strain for different distributions of fibre orientation of  $0^\circ$ -specimens

Specimen	Critical axial strain
PP30-0-1	0.046
PP30-0-4	0.048
PP30-0-7	0.05

Figure 5.31: Failure criteria at  $0^\circ$  with respect to IFD (dashed vertical lines correspond to the experimental minimum (PP30-0-5) and maximum (PP30-0-6) failure strains obtained with notched specimens

As shown in this figure, experimental minimum and maximum failure strains measured from notched specimens are of the values of 0.046 (PP30-0-5) and 0.057 (PP30-0-6), respectively.

From comparison of these results, it is observed that predicted failure strain values are rather close to the inferior limit of the experimental range. The relatively important variation of experimental values of the failure strain, i.e. the large experimental range, is not reproduced by the simulated one (respective relative deviations are of 23.9 % and 8.7 %). This is presumably due to the fact that local variation of fibre orientation within the fracture zone, which is not taken into account with the current distributions of orientation (averaged over the scanned volume), has its effect on the failure strain level.

The same procedure is adopted for the computation and verification of the failure strain for specimens cut at  $90^\circ$  with respect to the injection flow direction. It is observed from cartography of axial strain at the pre-failure step (Figure 5.32) that area of high strain values at break is more

extended than that of  $0^\circ$ -specimens. In other words, axial strain is less localised in the case of  $90^\circ$ -specimens. This may be an indicator of a more ductile fracture behaviour for specimens with higher preferential fibre orientation with respect to loading direction.

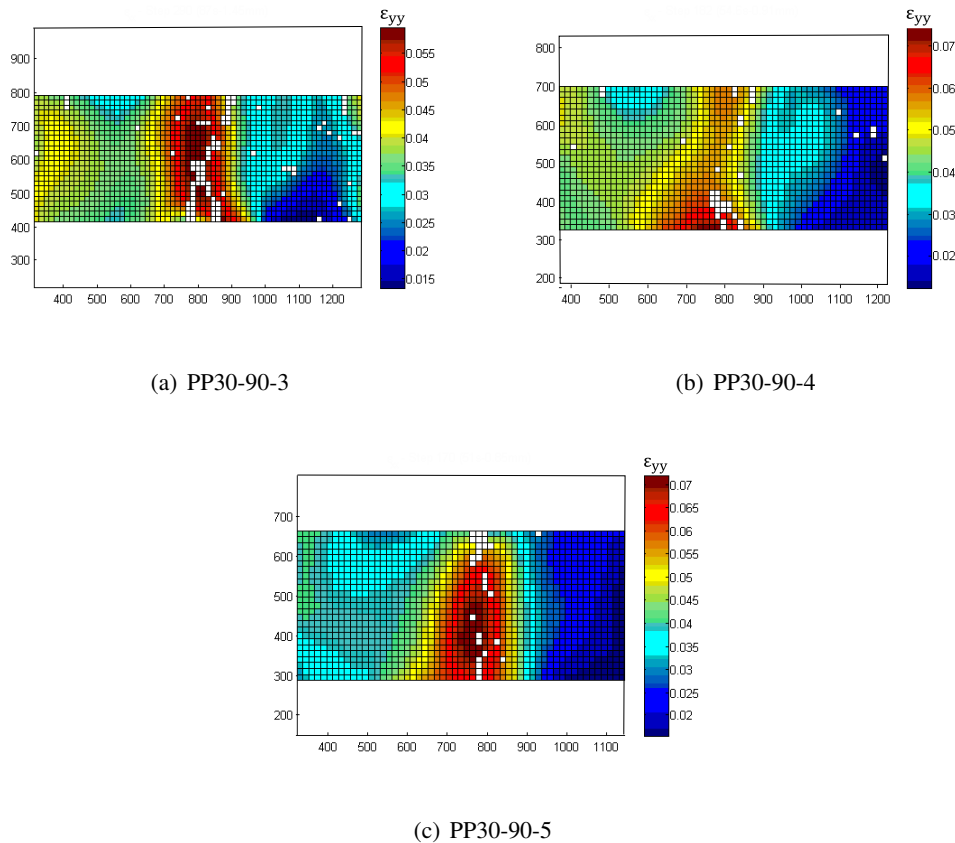


Figure 5.32: Cartography of axial strains at the pre-failure step (last step) for  $90^\circ$ -specimens with a facet size of  $31 \times 31 \text{ pix}^2$

Tensile test is simulated with the distribution of fibre orientation of the PP30-90-4 specimen. Note that one distribution of fibre orientation is used for the tensile test simulation (PP30-90-4) as no significant difference between available orientations of the scanned specimens is noticed in the case of  $90^\circ$ -specimens (see section 4.1.2.1). Using this data, the critical cumulated void is reached at a composite axial strain of 0.067 (Figure 5.33) and a fairly good correlation with experimental data is obtained (Figure 5.34).

It is worth mentioning that a higher value of failure strain would be predicted by the implemented model if fibres were more oriented in transverse direction than in specimen PP30-90-4, which is characterised by an important proportion of fibres with low angle with respect to loading direction



(Figure 5.33(b)). This is highlighted in Figure 5.35, where theoretical extreme cases of aligned fibres are treated for the computation of total cumulated void fraction. The case of fibre families with intermediate orientation angles is highlighted in Table 5.2, where  $v_v^{tot}$  computed at an axial strain of 0.05 is presented for different angles of aligned fibres. Note that the selected orientation angles correspond to highly oriented fibres (higher than  $45^\circ$ ) so that the significant decrease of the computed void fraction can be quantified for such angles. As shown in Table 5.2, the computed total void fraction can be neglected from an angle of  $75^\circ$ .

Table 5.2: Total void computed at a composite axial strain of 0.05 for different angles of fibre orientation

Orientation angle	$v_v^{tot}$
$45^\circ$	0.041
$55^\circ$	0.031
$65^\circ$	0.019
$75^\circ$	0.009
$85^\circ$	0.002

Extreme orientations, similar to the ones considered in Figure 5.35, are unlikely to be reached in real composites with injection moulding process because of the layered structure of the composite, i.e. the contribution of the different orientations. It can however be barely approximated with high volume fraction of reinforcement, where fibres are more preferentially oriented in the injection flow direction.

In those cases, debonding initiated at fibre tips becomes negligible when the vast majority of fibres is highly angled with respect to the loading direction. In those cases of SFRC with high proportion of highly angled fibres with respect to loading direction, composite failure is more likely to be governed by debonding initiated at fibre sides whatever, in case of complex loading, all phenomena are likely to coexist. In order to accurately predict the void development, and therefore the failure state, for composites with all kind of orientation and subjected to more complex loadings, transverse interfacial decohesion should be introduced in the current debonding model.

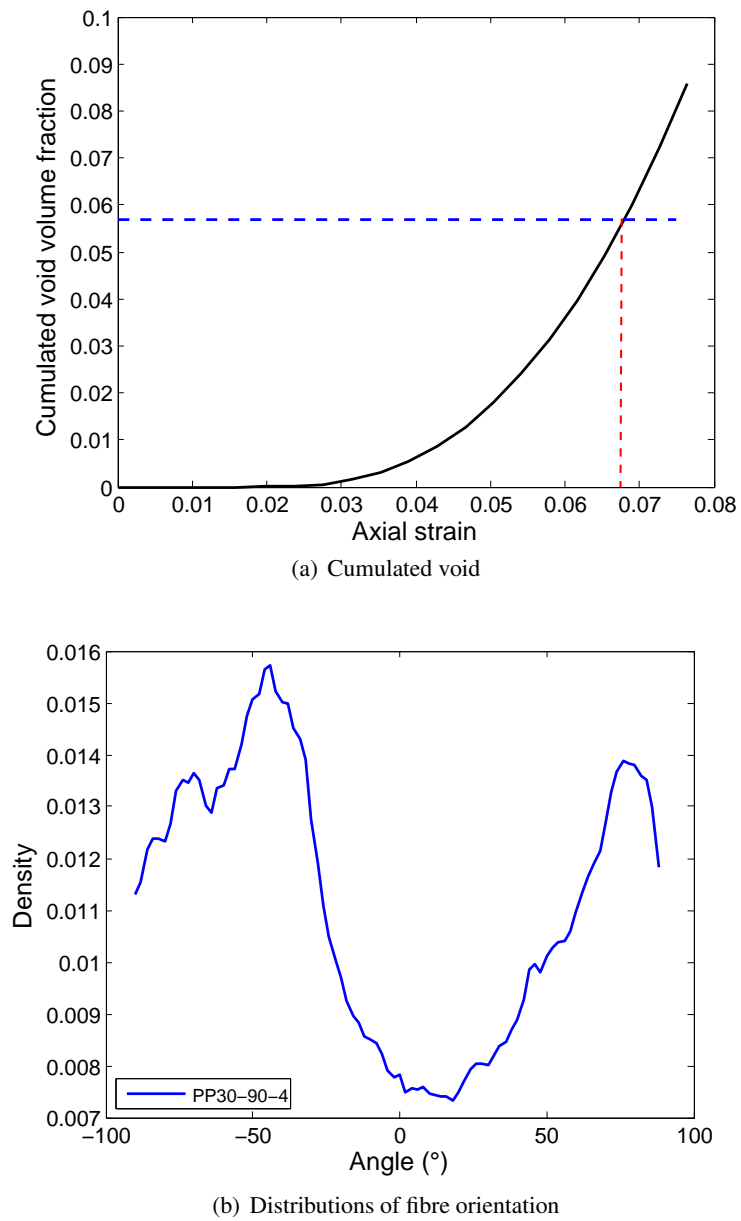


Figure 5.33: Identification of the failure strain with notched specimen PP30-90-4

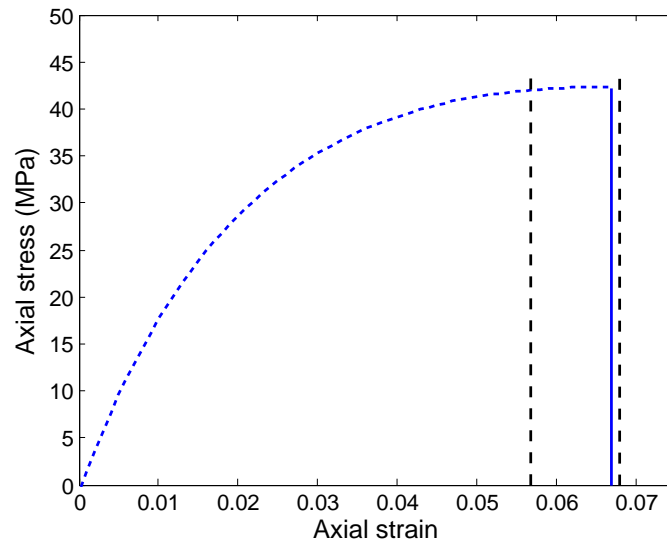


Figure 5.34: Failure criteria at  $90^\circ$  with respect to IFD (dashed vertical lines correspond to the experimental minimum (PP30-90-3) and maximum (PP30-90-5) failure strains obtained with notched specimens)

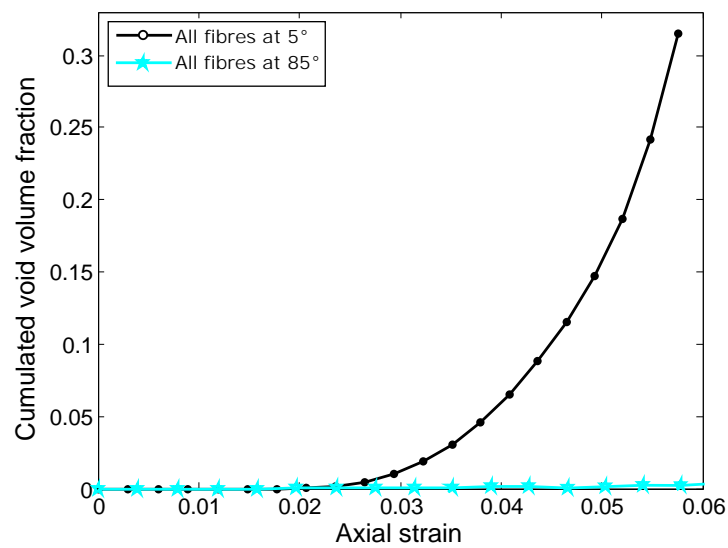


Figure 5.35: Cumulated void evolution for theoretical composites with aligned fibres ( $0^\circ$  and  $90^\circ$ )

## 5.6 Conclusion

Damage phenomena leading to failure of short fibre reinforced composites are the object of the modelling presented in this chapter. Earlier developments, presented in Chapter 3, for the modelling of SFRC behaviour over a wide range of strain rate, are therefore extended in the present

chapter to deal with damage/failure mechanisms. The representation of the composite reinforcement as an assembly of fibre families has enabled the modelling of damage mechanisms in an independent way. The matrix degradation has been introduced using an anisotropic ductile damage model, so that the effect of fibre orientation on its evolution is taken into account. The identification of the matrix damage model is based on cyclic tensile tests, where the stiffness loss method is used. Fibre/matrix interfacial decohesion is described by a tip-debonding model. Void creation at fibre tips, zone of stress concentration is modelled, followed by defect nucleation and growth at fibre side. Both damage models are verified by comparison with experimental results under different loading conditions. A failure criterion is defined in terms of the critical content of created voids at fibre/matrix interface. Its identification is then based on strain at break of a composite with known characteristics. Extending the current tip-debonding model to take into account debonding initiated at fibre side is in the scope of a further work.



---

# *Conclusion*

---

## **5.7 General conclusion**

The principle objective of this thesis is to propose an efficient modelling for the prediction of the mechanical behaviour of short-fibre reinforced thermoplastics. The main guidelines of this approach is to take SFRC's behaviour specificities into account, in particular for the case of extreme loading conditions, for instance high strain-rate loading. The originality of this contribution is to propose constitutive laws for SFRC behaviour modelling that include strain rate dependency and damage mechanisms while taking into account the real properties of the reinforcement in terms of complex fibre orientations. The composite is thus constituted of a damageable viscoelastic-viscoplastic matrix reinforced by short fibres with distributed orientations. In addition, load transmission from matrix to fibre through the interface can be affected by progressive fibre/matrix debonding.

After a bibliographic review in Chapter 2, first part of the present work (Chapter 3) aimed to describe the constitutive laws of the model for an undamaged state of the material. A linear viscoelastic model is coupled to overstress based viscoplastic model in order to predict the viscoelastic-viscoplastic (VE-VP) behaviour of the matrix material. Viscoplasticity is implemented in the framework of non-associated plasticity so that the dependency to hydrostatic pressure can be taken into account. The coupled VE-VP laws are described in the framework of thermodynamics of irreversible processes with a return mapping algorithm based on two steps, a VE predictor followed by a VP corrector. The prediction of the SFRC response is based on its assimilation to an assembly of several fibre media (or families) embedded in the polymeric matrix medium. Each of the fibre medium is modelled as linear elastic and is characterised by its own geometrical and mechanical properties. The composite response is then computed based on an additive decomposition of the state potential. One of the main assets of this approach, apart from the possibility to introduce complex behaviour laws for the matrix material, is that complex reinforcement properties can be dealt with. In this work we focus on the complex orientations of short fibres. A distribution

of orientation is thus associated to a finite number of fibre families. The developed model is implemented in the explicit finite element code ABAQUS as a user-material subroutine (VUMAT).

In the second part of the work (Chapter 4), an experimental procedure is conducted aiming at characterising the material behaviour and identifying the parameters involved in the developed constitutive model. We propose here to verify the model validity for the case of a Polypropylene (PP) matrix reinforced by short glass fibres (PP-GF; weight fraction of 30 or 40 %). Different kinds of tests (DMA, tensile and compression) have been realised on PP material for the identification of the viscoelastic and viscoplastic parameters of the matrix behaviour laws. Digital Image Correlation technique has been used in order to represent, according to the SEÉ method, a behaviour surface of the material over a wide range of strain rate. Then, the characterisation of the reinforcement properties is performed using micro-computed tomography. Identified orientations are input of the behaviour model according to the “families of fibres” concept. In order to validate the implementation of both matrix and composite behaviour models, comparisons of numerical and experimental results obtained for PP material and PP-GF were performed. Simulated quasi-static and dynamic tensile tests of PP-GF at different loading angles with respect to injection flow direction (i.e. preferential orientation of fibres in the composite) and with different fibre content proved the consistency of the implemented model.

As the advantageous adaptability of the present modelling offers the possibility to go further with the developed laws, the third part of the work (Chapter 5) aimed to introduce damage mechanisms in the behaviour prediction. First an anisotropic ductile damage, whose evolution is governed by fibre orientation, has been introduced. Then, fibre/matrix interfacial decohesion was described by a tip-debonding model. Void creation is described as being initiated at fibre tips, zone of stress concentration and therefore of defect nucleation and growth. Both damage models are identified and validated using experiments (cyclic loading/unloading tests for the matrix damage model and tensile tests with notched specimens for the fibre/matrix debonding model). Finally, a failure criterion is defined in terms of a critical content of voids.

## 5.8 Future works

Among future improvements of the current work, some issues that deserve further investigations are proposed in the following paragraphs.

The current modelling of the matrix material viscoelasticity is performed using a linear viscoelastic law. It is however established in the literature that polymers can exhibit nonlinear viscoelastic responses. Going further with the matrix material modelling by introducing non-linearities in the modelling of matrix viscoelasticity should be addressed in a future work. It can be noted that the influence of a modification in the matrix viscoelastic response modelling will be more pronounced as fibre volume fraction decreases in the composite. Indeed, behaviour of composites with low fibre content is more sensible to the non-linearities of matrix behaviour.

The implemented viscoplastic correction scheme for the thermoplastic matrix material enables to reproduce the sensitivity to hydrostatic pressure of viscoplastic flow behaviour. Therefore, it might be of great interest to go beyond the case of uniaxial loading and investigate the triaxiality effect in order to fully address this feature. Future experimental work should therefore concern non-uniaxial loadings with various triaxiality ratios in order to validate the matrix behaviour model under such loading conditions.

In the modelling of the composite damage mechanisms, fibre-matrix interfacial decohesion is currently assumed to initiate at fibre tips and then develop along fibre sides. This formulation is motivated by the existing microscopic observations stating that fibre tip is an area of stress concentration which favours void nucleation and growth. The initiation of decohesion in SFRC may however not be restricted to fibre tips and may happen at fibre sides.

This limitation can be highlighted by considering highly angled fibres with respect to the loading direction, where transverse fibre-matrix interface is the most sollicitated and may become the area of defect creation. Further development of the debonding model should take the different decohesion mechanisms by introducing the debonding initiation at fibre sides. Moreover, a direct characterisation of damage mechanisms, i.e. direct measurement of the tip and transverse interfacial defects (e.g. by in-situ tests), is to be investigated, so that an accurate identification of the involved initiation and evolution parameters as well as the failure state should be performed.

Finally, in the current investigations, the strain rate dependency of damage phenomena is not addressed. This, however, might be an important feature of the material behaviour, especially when



large strain rate range applications are targeted. For instance, strain rate effect on the dominant damage mechanisms, i.e. matrix ductile damage and/or fibre/matrix interfacial debonding, might be a key point in the prediction of ultimate failure at high strain rate. This idea is motivated by an observation of fracture surface of SFRC (PP-30GF) loaded at low and high strain rates (Figure 5.36), where a different surface state of fibres may be indicator of strain rate dependency. Indeed, it can be observed that fibre/matrix debonding is more pronounced on the fracture surface of the SFRC subjected to low speed loading (Figure 5.36a) and fibre surface appear clean, i.e. without residue of matrix. At the contrary, at high speed loading (Figure 5.36b), a better adhesion between matrix and fibres is observed on the fracture surface, which may be an indicator of the predominance of matrix damage in the mechanisms leading to composite failure.

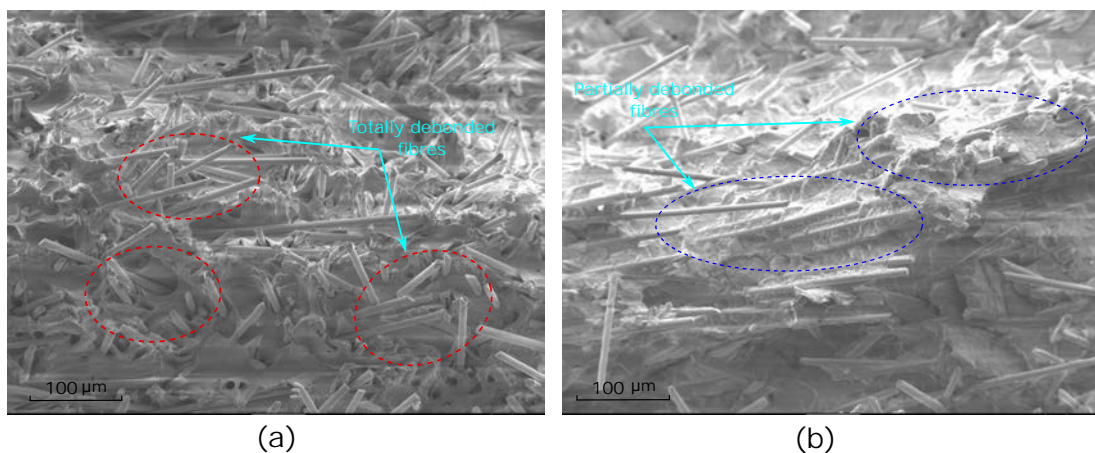


Figure 5.36: Fracture surface of PP-30GF tested at (a) 1 mm.min<sup>-1</sup> and (b) 1000 mm.min<sup>-1</sup> obtained by SEM observations.

At longer term, composites with more complex reinforcement properties could be investigated. For instance, the current modelling could be extended to the case of natural fibres, which are characterised by a large variability of physical, geometrical and mechanical properties.

---

# *Bibliography*

---

- [1] White JR, De SK. Survey of short fibre-polymer composites. Woodhead Publishing Limited, Cambridge England, 1996.
- [2] Rosato DV, Rosato MG. Injection molding handbook: Springer Science, Business Media, 2000.
- [3] Vu-Khanh T, Denault J, Habib P, Low A. The effects of injection molding on the mechanical behavior of long-fiber reinforced PBT/PET blends. *Composites science and technology*;1991;4:423-435.
- [4] Kamal MR, Song L, Singh P. Measurement of fibre and matrix orientations in fibre reinforced composites. *Polymer Composites* 1986;7:323-329.
- [5] Ramani K, Bank D, Kraemer N. Effect of screw design on fiber damage in extrusion compounding and composite properties. *Polymer composites* 1995;16:258-266.
- [6] Milewski JV. A study of the packing of milled fiberglass and glass beads, 1974.
- [7] Fu SY, Lauke B, Mai YW. Science and engineering of short fibre reinforced polymer composites. Woodhead Publishing, 2009.
- [8] Zhou Y, Mallick PK. A non-linear damage model for the tensile behavior of an injection molded short E-glass fiber reinforced polyamide-6,6. *Mater. Sc. and Eng. A* 2005;393:303-209.
- [9] Bay RS, Tucker III CL. Fiber Orientation in Simple Injection Moldings. Part I: Theory and Numerical Methods. *Polymer Composites* 1992;13:317-331.
- [10] Advani SG, Tucker III CL. Closure approximations for three-dimensional structure tensors. *Polymer Composites* 1990;11:367-382.
- [11] Goettler LA. Mechanical property enhancement in short-fiber composites through the control of fiber orientation during fabrication. *Polymer Composites* 1984;5:60-71.
- [12] Akay M, Barkley D. Fibre orientation and mechanical behaviour in reinforced thermoplastic injection mouldings. *Journal of Materials Science* 1991;26:2731-2742.
- [13] Thin TBN, Morioka M, Yokoyama A, Hamanaka S, Yamashita K, Noromura C. Measurement of fibre orientation distribution in injection-molded short-glass-fiber composites using X-ray computed tomography. *Journal of Material Processing Technology* 2015;216:1-9. series.
- [14] Tadmor Z. Molecular Orientation in Injection Molding. *Journal of Applied Polymer Science* 1974;18:1753-1772.
- [15] Hull D, Clyne TW. An introduction to composite materials. 2nd ed. Cambridge solid state science series. 1996.
- [16] Sirkis JS, Cheng A, Dasgupta A, Pandelidis I. Image processing based method of predicting stiffness characteristics of short fibre reinforced injection molded parts. *Journal of Composite Materials* 1994;28:784-799.
- [17] Vincent M, Agassant JF. Experimental study and calculations of short glass fibre orientation in a center gated molded disc. *Polymer Composites* 1986;7:76-83.
- [18] Ranganathan S, Advani SG. Characterization of orientation clustering in short-fibre composites. *Journal of Polymer Science: Part B-Polymer Physics* 1990;28:2651-2672.

- [19] Fischer G, Eyerer P. Measuring spatial orientation of short fibre reinforced thermoplastics by image analysis. *Polymer Composites* 1988;44:297-304.
- [20] Bay RS, Tucker III CL. Stereological measurement and error estimates for three-dimensional fibre orientation. *Polymer Engineering and Science* 1992;4:240-253.
- [21] Zhu YT, Blumenthal WR, Lowe TC. Determination of non-symmetric 3-D fibre-orientation distribution and average fibre length in short-fibre composites. *Journal of Composite Materials* 1997;31:1287-1301.
- [22] Hine PJ, Duckett RA, Davidson N, Clarke AR. Modelling of the elastic properties of fibre/reinforced composites. I: Orientation measurement. *Composites Science and Technology* 1993;47:65-73.
- [23] Zak G, Park CB, Banhabib B. Estimation of Three-Dimensional Fibre-Orientation Distribution in Short-Fibre Composites by a Two-Section Method. *Journal of Composite Materials* 2001;35:316-399.
- [24] Eberhardt C, Clarke A. Fibre-orientation measurements in short-glass-fibre composites. Part I: automated, high-angular-resolution measurement by confocal microscopy. *Composites Science and Technology* 2001;61:1389-1400.
- [25] Clarke AR, Davidson NC, Archenhold G. Measurements of fibre direction in reinforced polymer composites. *Journal of Microscopy* 1993;171:69-79.
- [26] Clarke AR, Archenhold G, Davidson NC. A novel technique for determining the 3D spatial distribution of Glass fibres in polymer composites. *Composites Science and Technology* 1995;55:75-91.
- [27] Bernasconi A, Cosmi F, Hine PJ. Analysis of fibre orientation distribution in short fibre reinforced polymers: a comparison between optical and tomographic methods. *Compos. Sci. Technol.* 2012;72:2002-2008.
- [28] Bracewell RN. Strip integration in radio astronomy. *Aust. J. Phys.* 1956;9:198.
- [29] Hounsfield GN. Computerized transverse axial scanning (Tomography): Part I Description of system. *British Journal of Radiology* 1973;46:1016-1022.
- [30] Shen H, Nutt S, Hull D. Direct observation and measurement of fibre in short fibre-polymer composite foam through Micro-CT imaging. *Compos. Sci. Technol.* 2004;64:2113-2120.
- [31] Nguyen Thi TB, Yokoyama A, Ota K, Kodama K, Yamashita K, Isogai Y, Furuichi K, Nonomura C. Numerical approach of the injection molding process of fibre-reinforced composite with considering fibre orientation. *AIP Conf. Proc.* 2014:571-577.
- [32] Olabisi O, Adewale K. *Handbook of thermoplastics*. CRC press 1997.
- [33] Zhang C, Moore ID. Nonlinear mechanical response of high density polyethylene. Part I: Experimental investigation and model evaluation. *Polym. Eng. Sci.* 1997;37:404-413.
- [34] Christensen RM. *Theory of Viscoelasticity*. Academic Press: New York. 1971.
- [35] Findley WN, Lay JS, Onaran K. *Creep and Relaxation of nonlinear viscoelastic materials*. Dover Publication: New York. 1976.
- [36] Salençon J. *Viscoélasticité*. Presses de l'École Nationale des Ponts et Chaussées: Paris. 1983.
- [37] Perzyna P. Fundamental problems in viscoplasticity. *Advances in Applied Mechanics* 1966;9:234-377.
- [38] Lemaitre J, Chaboche JL. *Mechanics of Solid Materials*. Cambridge University Press: England. 1996.
- [39] Nikolov S, Doghri I, Pierard O, Zealouk L, Goldberg A. Multi-scale constitutive modeling of the small deformations of semi-crystalline polymers. *J Mech Phys Solids* 2002;50:2275-2302.
- [40] Chaboche JL. Thermodynamic formulation of constitutive equations and application to the viscoelasticity and viscoplasticity of metals and polymers. *Int. J. Solids Structures* 1966;34:2239-2254.

- [41] Karger-Kocsis J, Friedrech K. Temperature and strain-rate effects on the fracture toughness of poly(ether ether ketone) and its short glass-fibre reinforced composite. *Polymer* 1986;27:1753-1760.
- [42] GSELL C, Hiver JM, Dahoun A. Experimental characterization of deformation damage in solid polymers under tension and its interrelation with necking. *International Journal of Solids and Structures* 2002;3:3857-3872.
- [43] GSELL C, Bai SL, Hiver JM. Polypropylene/polyamide 6/polyethyleneoctene elastomer blends. Part II: volume dilatation during plastic deformation under uniaxial tension. *Polymer* 2004;45:5785-5792.
- [44] Jerabek M, Major Z, Renner K, Moczo J, Pukánszky B, Lang RW. Filler/matrix-debonding and micro-mechanisms of deformation in particulate filled polypropylene composites under tension. *Polymer* 2010;51:2040-2048
- [45] Wang DA, Pan J. A non-quadratic yield function for polymeric foams. *International Journal of Plasticity* 2006;22:434-458.
- [46] Khan AS, Farrokh B. Thermo-mechanical response of nylon 101 under uniaxial and multi-axial loadings: Part I, experimental results over wide ranges of temperatures and strain rates. *International Journal of Plasticity* 2006;22:1506-1529.
- [47] Sauer JA, Pae KD. The ow of solid polymers under high pressure. *Colloid and Polymer Science* 1974;252:680-695.
- [48] Thomason JL, Vlug MA. Influence of fibre length and concentration on the properties of glass fibre-reinforced polypropylene: 1. Tensile and flexural modulus. *Composites Part A: Applied science and manufacturing* 1996;27:477-484.
- [49] Mouhmid B, Imad A, Benseddiq N, Benmedakhene S, Maazouz A. A study of the mechanical behaviour of a glass fibre reinforced polyamide 6,6: Experimental investigation. *Polymer Testing* 2006;25:544-552.
- [50] Reis JML, Chaves FL, da Costa Mattos HS (2013) Tensile behaviour of glass fibre reinforced polyurethane at different strain rates. *Materials and Design* 49:192-196.
- [51] SchoSSig M, Bierögel C, Grellmann W, Mecklenburg T. Mechanical behavior of glass-fiber reinforced thermoplastic materials under high strain rates. *Polymer Testing* 2008;27:893-900.
- [52] Fitoussi J, Bocquet M, Meraghni F. Effect of matrix behavior on the damage of ethylene-propylene glass fiber reinforced composite subjected to high strain rate tension. *Composites: Part B* 2013;45:1181-1191.
- [53] Krivachy R, Riedel K, Weyer S, Thoma K. Characterisation and modelling of short fibre reinforced polymers for numerical simulation of a crash. *International Journal of Crashworthiness* 2008;13:559-566.
- [54] Notta-Cuvier D, Lauro F, Bennani B, Balieu R. Damage of short-fibre reinforced materials with anisotropy induced by complex fibres orientations. *Mechanics of Materials* 2014;68:193-206.
- [55] Sato N, Kurauchi T, Sato S, Kamigaito. Microfailure behaviour of randomly dispersed short fibre reinforced thermoplastic composites obtained by direct SEM observation. *Journal of Materials Science* 1991;26:3891-3898.
- [56] Charles LT III, Liang E. Stiffness prediction for unidirectional short-fiber composites: Review and evaluation. *Composites Science and Technology* 1999;59:655-671.
- [57] Smit RJM, Brekelmans WAM, Meijer HEH. Prediction of the mechanical behavior of nonlinear heterogeneous systems by multi-level element modeling. *Comput Methods Appl Mech Engrg* 1998;155:181-192.
- [58] Ghosh S, LeeK K, Moorthy S. Two scale analysis of heterogeneous elastic-plastic materials with asymptotic homogenization and Voronoi cell finite element model. *Comput Methods Appl Mech Engrg* 1996;132:63-116.
- [59] Cox HL. The elasticity and strength of paper and other fibrous materials. *British Journal of Applied Physics* 1952;3:72.
- [60] Hill R. Elastic properties of reinforced solids: some theoretical principles. *Journal of Mechanics and Physics of Solids* 1963;11:357-372.

- [61] Hill R. A self-consistent mechanics of composite materials. *Journal of Mechanics and Physics of Solids* 1965;13:213-222.
- [62] Eshelby JD. The determination of the elastic field of an ellipsoidal inclusion, and related problems. *Mathematical and Physical Sciences, Proceedings of the Royal Society of London* 1957;241:376-396.
- [63] Mori T, Tanaka K. Average stress in matrix and average elastic energy of materials with misfitting inclusions. *Acta Metall* 1973;21:571-574.
- [64] Fiebel C, Doghri I, Legat V. General mean-field homogenization schemes for viscoelastic composites containing multiple phases of coated inclusions. *Int J Solids Struct* 2006;43:2513-2541
- [65] Hashin Z. Viscoelastic behavior of heterogeneous media. *J Appl Mech, ASME* 1965;32E:630-636.
- [66] Berveiller M, Zaoui A. An extension of the self-consistent scheme to plastically-owing polycrystals. *Journal of the Mechanics and Physics of Solids* 1979;26:325-344.
- [67] Tandon GP, Weng GJ. A theory of particle-reinforced plasticity. *Journal of Applied Mechanics* 1988;55:126-135.
- [68] Hill R. A self-consistent mechanics of composite materials. *Journal of the Mechanics and Physics of Solids* 1965;13:213-222.
- [69] Masson R, Zaoui A. Self-consistent estimates for the rate-dependent elastoplastic behavior of polycrystalline materials. *J Mech Phys Solids* 1999;47:1543-1568.
- [70] Pierard O, Doghri I. An enhanced affine formulation and the corresponding numerical algorithms for the mean-field homogenization of elasto-viscoplastic composites. *Int J Plast* 2006a;22:131-157.
- [71] Ju J. Consistent tangent moduli for a class of viscoplasticity. *J. Engrg. Mech. ASCE* 116. 1990;8:1764-1779.
- [72] Doghri I. *Mechanics of deformable solids. Linear, nonlinear, analytical and computational aspects.* Springer, Berlin 2000.
- [73] Molinari A, Canova GR, Ahzi S. A self consistent approach at the large deformation polycrystal viscoplasticity. *Acta Metall.* 1987;35:2983-2994.
- [74] Masson R, Zaoui A. Self-consistent estimates for the rate-dependent elasto-plastic behavior of polycrystalline materials. *J. Mech. Phys. Solids* 1999;47:1543-1568.
- [75] Masson R, Bornert M, Suquet P, Zaoui A. An affine formulation for the prediction of the effective properties of nonlinear composites and polycrystals. *J. Mech. Phys. Solids* 2000;48:1203-1227.
- [76] Pierard O, Doghri I. An enhanced affine formulation and the corresponding numerical algorithms for the mean-field homogenization of elasto-viscoplastic composites. *Int. J. Plasticity* 2006;22:131-157.
- [77] Doghri I, Adam L, Bilger N. Mean-field homogenization of elasto-viscoplastic composites based on a general incrementally affine linearization method. *Int. J. Plasticity* 2010;26:219-238.
- [78] Kim JS, Muliana AH. A time-integration method for the viscoelastic viscoplastic analyses of polymers and finite element implementation. *Int. J. Numer. Meth. Engng* 2009;79:550-575.
- [79] Aboudi J. Micromechanically established constitutive equations for multiphase materials with viscoelastic-viscoplastic phases. *Mech. Time-Depend. Mater.* 2005;9:121-145.
- [80] Lusti HR, Hine PJ, Gusev A. Direct numerical predictions for the elastic and thermoelastic properties of short fibre composites. *Composites science and technology* 2002;62:1927-1934.
- [81] Pan Y, Iorga L, Pelegri A. A Analysis of 3D random chopped fiber reinforced composites using FEM and random sequential adsorption. *Computational Materials Science* 2008;43:450-461.
- [82] Ionita A, Weitsman YJ. On the mechanical response of randomly reinforced chopped-fibers composites: Data and model. *Composites science and technology* 2006;66:2566-2579.

- [83] Berger H, Kurukuri S, Kari S, Gabbert U, Rodriguez-Ramos R, Bravo-Castillero J, Guinovart-Diaz R. Numerical and analytical approaches for calculating the effective thermomechanical properties of three-phase composites. *Journal of Thermal Stresses* 2007;30:801-817.
- [84] Kari S, Berger H, Gabbert U. Numerical evaluation of effective material properties of randomly distributed short cylindrical fibre composites. *Computational materials science* 2007;39:198-204
- [85] Doghri I, Tinel L. Micromechanics of inelastic composites with misaligned inclusions: numerical treatment of orientation. *Computer Methods in Applied Mechanics and Engineering* 2005;195:1387-1406.
- [86] Notta-Cuvier D, Lauro F, Bennani B, Balieu R. An efficient modelling of inelastic composites with misaligned short fibres. *International Journal of Solids and Structures* 2013;50:2857-2871.
- [87] Nedjar B. An anisotropic viscoelastic fibre-matrix model at finite strains: continuum formulation and computational aspects. *Comput Methods Appl Mech Eng* 2007;196:1745-1759.
- [88] Klinkel S, Gavazzi C, Nigam H. Elastoplastic fibre-matrix material model at finite elastic-plastic strains. *Comput Mech* 2005;35:409-417.
- [89] Bowyer WH, Bader MG. On the re-inforcement of thermoplastics by imperfectly aligned discontinuous fibres. *Journal of Materials Science* 1972;7:1315-1321.
- [90] Nikolov S, Doghri I. A micro/macro constitutive model for the small-deformation behavior of polyethylene. *Polymer* 2000;41:1883-1891
- [91] Drozdov AD, Gupta RK. Non-linear viscoelasticity and viscoplasticity of isotactic polypropylene. *International Journal of Engineering Science* 2003;41:2335-2361
- [92] Drozdov A, Christiansen J. Cyclic viscoplasticity of high-density polyethylene: experiments and modeling. *Computational Materials Science* 2007;39:465-480
- [93] Khan AS, Farrokh B. Thermo-mechanical response of nylon 101 under uniaxial and multi-axial loadings: Part I, experimental results over wide ranges of temperatures and strain rates. *International Journal of Plasticity* 2006;22:1506-1529
- [94] haboche JL. Thermodynamic formulation of constitutive equations and application to the viscoplasticity and viscoelasticity of metals and polymers. *International Journal of Solids and Structures* 1997;34:2239-2254
- [95] Ayoub G, Zari F. Effects of crystal content on mechanical behaviour of polyethylene. *International Journal of Plasticity* 2011;27:409-417.
- [96] Zairi F. Effects of crystal content on mechanical behaviour of polyethylene. *International Journal of Plasticity* 2011;27:409-417.
- [97] Regrain C, Toillon S. Multi-mechanism model for semi-crystalline polymers. *International Journal of Plasticity* 2009;25:1253-1279.
- [98] Drozdov A, Klitkou R, Christiansen J. Cyclic viscoplasticity of semicrystalline polymers with finite deformations. *Mechanics of Materials* 2013;56:53-64.
- [99] Balieu R, Lauro F, Bennani B, Delille R, Matsumoto T, Mottola E. A full coupled elastoviscoplastic damage model at finite strains for mineral filled semi-crystalline polymer. *International Journal of plasticity* 2013;51:241-271.
- [100] Krempl E, Khan F. Rate (time)-dependent deformation behavior: an overview of some properties of metals and solid polymers. *International Journal of Plasticity* 2005;19:1069-1095
- [101] Khan F, Yeakle C. Experimental investigation and modeling of non-monotonic creep behavior in polymers. *International Journal of Plasticity* 2011;27:512-521
- [102] Colak OU. Modeling deformation behavior of polymers with viscoplasticity theory based on overstress. *International Journal of Plasticity* 2005;21:145-160

- [103] Ayoub G, Zari F, Nat-Abdelaziz, M, Gloaguen J. Modelling large deformation behaviour under loading-unloading of semicrystalline polymers: Application to a high density polyethylene. *International Journal of Plasticity* 2010;26:329-347.
- [104] Khan A, Zhang H. Finite deformation of a polymer: experiments and modeling. *International Journal of Plasticity* 2001;17:1167-1188
- [105] Miled B, Doghri I, Delannay L. Coupled viscoelasticviscoplastic modeling of homogeneous and isotropic polymers: Numerical algorithm and analytical solutions. *Comput. Methods Appl. Mech. Engrg.* 2011;3381-3394.
- [106] Christensen RM, Naghdi PM. Linear non-isothermal viscoelastic solids. *Acta Mechanica* 1967;3:1-12.
- [107] Voyiadjis GZ, Abu Al-Rub RK. Thermodynamic based model for the evolution equation of the backstress in cyclic plasticity. *International Journal of Plasticity* 2003;19:2121-2147.
- [108] Krairi A, Doghri I. A thermodynamically-based constitutive model for thermoplastic polymers coupling viscoelasticity, viscoplasticity and ductile damage. *International Journal of Plasticity* 2014;60:163-181.
- [109] Haouala S, Doghri I. Modeling and algorithms for two-scale time homogenization of viscoelastic-viscoplastic solids under large numbers of cycles. *International Journal of Plasticity* 2015;70:98-125.
- [110] Ohkani M, Ichikawa P. Linear non-isothermal viscoelastic solids. *Acta Mechanica* 1967;3:1-12.
- [111] Raghava R, Caddell RM, Yeh GSY. The macroscopic yield behaviour of polymers. *Journal of Materials Sciences* 1973;8:225-232.
- [112] Simo JC, Hughes R. *Computational Inelasticity . Interdisciplinary Applied Mechanics*, second ed., 1998, vol. 7. Springer, Berlin.
- [113] Bernasconi A, Cosmi F. Analysis of the dependence of the tensile behaviour of a short fibre reinforced polyamide upon fibre volume fraction, length and orientation. *Procedia Eng.* 2011;10: 2129-2134.
- [114] Schindelin J, Arganda-Carreras I, Frise E. Fiji: an open-source platform for biological-image analysis. *Nature methods* 9 2012;7:676-682.
- [115] Otsu N. A Threshold Selection Method from Gray-Level Histograms. *IEEE Transactions on Systems, Man, and Cybernetics* 1979;9;62-66.
- [116] Lauro F, Bennani B, Morin D, Epee AF. The SEË method for determination of behaviour laws for strain rate dependent material: Application to polymer material. *International Journal of Impact Engineering* 2010;37:715-722.
- [117] Notta-Cuvier D, Nciri M, Lauro F, Chaari F, Robache F, Haugou G, Maalej Y. Coupled influence of strain rate and heterogeneous fibre orientation on the mechanical behaviour of short-glass-fibre reinforced polypropylene. *Mechanics of Materials* 2016;100:186-197.
- [118] Thomason JL. Structure-Property relationships in glass-reinforced polyamide, part 1: the effects of fiber content. *Polymer Composites* 2006;27:552-562.
- [119] Thomason JL. Structure-Property relationships in glass-reinforced polyamide, part 2: the effects of average fiber diameter and diameter distribution. *Polymer Composites* 2007;28:331-343.
- [120] Thomason JL. The influence of fibre length, diameter and concentration on the strength and strain to failure of glass fibre-reinforced polyamide 6,6. *Composites: Part A* 2008;39:1618-1624.
- [121] Arif M, Saintier N, Meraghni F, Fitoussi J, Chemisky Y, Robert G. Multiscale fatigue damage characterization in short glass fiber reinforced polyamide-66. *Composites Part B* 2014;61:55-65.
- [122] Sato N, Kurauchi T, Sato S, Kamigaito O. Microfailure behaviour of randomly dispersed short fibre reinforced thermoplastic composites obtained by direct SEM observation. *J Mater Sci* 1991;26:3891-3898.

- [123] Horst JJ, Spoomaker JL. Fatigue fracture mechanisms and fractography of short-glass fibre-reinforced polyamide 6. *J Mater Sci* 1997;32:3641-3651.
- [124] Meraghni F, Benzeggagh M.L. Micromechanical modelling of matrix degradation in randomly oriented discontinuous-fibre composites. *Composites Science and Technology* 1955;55:171-186.
- [125] Christensen R, Lo K. Solutions for effective shear properties in three phase sphere and cylinder models. *J Mech Phys Solids* 1979;27:315-330.
- [126] Nguyen BN, Khaleel MA. A mechanistic approach to damage in short-fiber composites based on micromechanical and continuum damage mechanics descriptions. *Composites Science and Technology*. 2004;64:607-617.
- [127] Lee HK, Simunovic S. Modeling of progressive damage in aligned and randomly oriented discontinuous fiber polymer matrix composites. *Composites: Part B*. 2000;31:77-86
- [128] Hashin Z. Thermoelastic properties of fiber composites with imperfect interface. *Mech Mater* 1990;8:333-348.
- [129] Hashin Z. Thin interphase/imperfect interface in elasticity with application to coated fiber composites. *J Mech Phys Solids* 2002;50:2509-2537.
- [130] Benveniste Y, Miloh T. Imperfect soft and stiff interfaces in two-dimensional elasticity. *Mech Mater* 2001;33:309-323.
- [131] Hazanov S. On micromechanics of imperfect interfaces in heterogeneous bodies smaller than the representative volume. *Int J Eng Sci* 1999;37:847-861.
- [132] Zhong Z, Meguid SA. On the elastic field of a spherical inhomogeneity with an imperfectly bonded interface. *J Elast* 1997;46:91-113.
- [133] Bernasconi A, Davoli P, Basile A, Filippi A. Effect of fibre orientation on the fatigue behaviour of a short glass fibre reinforced polyamide-6. *Int J Fatigue* 2007;29:199-208.
- [134] Mouhmid B, Imad A, Benseddiq S, Benmedkhène S, Maazouz A. A study of the mechanical behaviour of a glass fibre reinforced polyamide 6,6: Experimental investigation? *Polymer Testing* 2006;25:544-552.
- [135] Bayraktar E, Antolonovich S, Bathias C. Multiscale study of fatigue behaviour of composite materials by X-rays computed tomography. *Int J Fatigue* 2006;28:1322-1333.
- [136] Withers PJ, Preuss M. Fatigue and damage in structural materials studied by X-ray tomography. *Annu Rev Mater Res* 2012;42:81103.
- [137] Cosmi F, Bernasconi A. Micro-ct investigation on fatigue damage evolution in short fibre reinforced polymers. *Compos. Sci. Technol.* 2013;79:7076.
- [138] Horst JJ, Spoomaker JL. Fatigue fracture mechanisms and fractography of short-glass fibre-reinforced polyamide 6. *J. Mater. Sci.* 1997;32:3651.
- [139] Notta-Cuvier D, Lauro F, Bennani B. Modelling of progressive fibre/matrix debonding in short-fibre reinforced composites up to failure. *International Journal of Solid and Structures*. 2015;66:140-150.
- [140] Gaggar SK, Broutman LJ. Strength and fracture properties of random fibre polyester composites. *Fibre Sci. Tech.* 1976;9:205-224.
- [141] Agarwal BD, Giare GS. Fracture toughness of short fibre composites in Modes II and III. *Engng. Fracture Mech.* 1981;15:219-230.
- [142] Agarwal BD, Giare GS. Effect of matrix properties on fracture toughness of short fibre composites. *Mat. Sci. Engng.* 1982;5:139-145.
- [143] Lauke B, Pompe B. Fracture toughness of short-fibre reinforced thermoplastics. *Composites Science and Technology*. 1986;26:37-57.





## *Identification of the parameter $C^{nucl}$*

---

As stated in Section 5.3 the parameter  $C^{nucl}$  (Equation 5.38) is experimentally identified. It is to note that experimental data used here are obtained from tensile tests realised on notched specimens of composite material (PP-30GF) and described in section 5.5.1. The parameter  $C^{nucl}$  is identified by measuring the relative variation of the composite volume,  $\Delta V$ , using measurements of axial,  $\epsilon_{yy}$ , and transversal,  $\epsilon_{xx}$ , strain fields (by DIC), and by assuming transverse isotropy. The relative variation of the composite volume,  $\Delta V$ , is in that case expressed as follows:

$$\Delta V = \exp(\text{tr}(\boldsymbol{\epsilon})) - 1 = \exp(\epsilon_{yy} + 2\epsilon_{xx}) - 1 \quad (\text{A.1})$$

$\Delta V$  can be split into a damage volume fraction,  $\Delta V^d$ , equal to  $v_v^{tot}$ , and into a relative variation of strain volume due to Poisson effect. According to G'Sell et al. [?], the relative variation of strain volume is the sum of a linear,  $\Delta V^{\epsilon,L}$ , and a non-linear,  $\Delta V^{\epsilon,NL}$ , parts. In the linear elastic range, the variation of strain volume is defined by:  $\Delta V^{\epsilon,L} = (1 - 2\nu) \epsilon_{yy}$ , where  $\nu$  is the composite Poisson ratio. Similarly, in the non-linear range, the ‘‘tangent Poisson ratio’’,  $\nu_T = -d\epsilon_{xx}/d\epsilon_{yy}$ , is introduced so that:

$$\Delta V^{\epsilon,NL} = (1 - 2\nu_T) \epsilon_{yy} \quad (\text{A.2})$$

As non-linearity of behaviour begins at a relatively low level of axial strain, the  $\Delta V^{\epsilon,L}$  is neglected in the following, i.e.  $\Delta V \simeq \Delta V^{ed} + \Delta V^{\epsilon,NL}$ . Evolution of fractions of volume change,  $\Delta V$  and  $\Delta V^{\epsilon,NL}$ , is presented in Figure A.1 for the notched specimen PP30-0-4 (as the corresponding distribution of fibre orientation is known and will be used for the parameter identification). It is now possible to plot the evolution of  $v_v^{tot}$  and to identify the value of  $C^{nucl}$  as the one leading to the best fit with experimental data. This way, a value of 12 is found for the parameter  $C^{nucl}$ . Figure A.2 allows to compare the experimental evolution of damage in the composite to the evolution of void volume fraction computed with this value of  $C^{nucl}$  and thus demonstrates the accuracy of the identification.

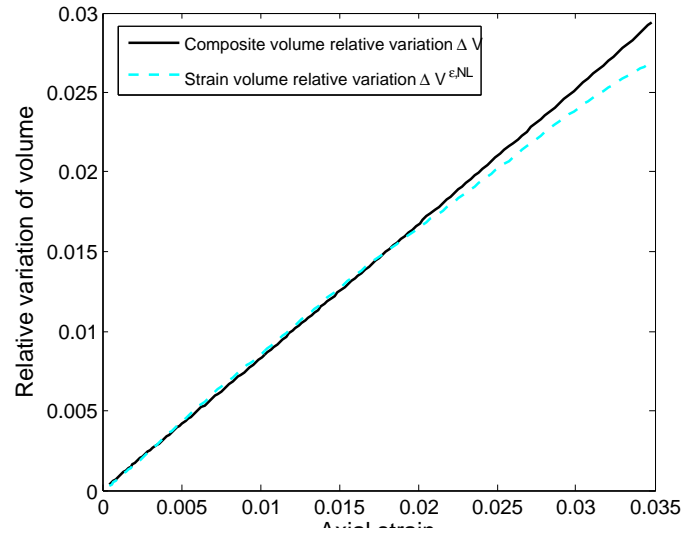


Figure A.1: Total volume variation and strain volume variation fraction of the composite material (PP-30GF)

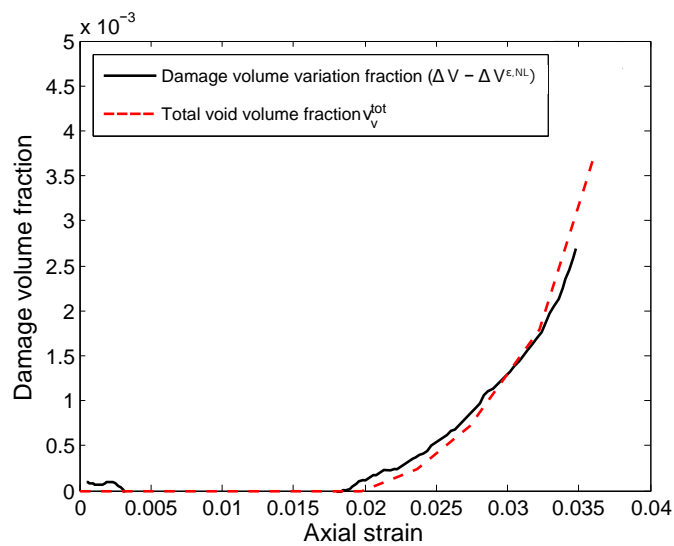


Figure A.2: Comparison between experimental and computed void volume fraction with the identified value of  $C^{nucl}$  (with data corresponding to the notch specimen PP30-0-4)

---

## *Abstract*

---

Short fibre-reinforced composites are commonly used in a variety of engineering applications, including automotive and aerospace industry. Today, their use is progressively extended to parts possibly subjected to severe loading conditions (e.g. crash...), characterised by high strain rates. Therefore, an efficient modelling that takes into account material's specificities at a large strain rate range is needed. A constitutive model of viscous behaviour of short-fibre reinforced composites (SFRC) where complex distributions of fibre orientations are taken into account is proposed in this work. The approach considered for the computation of composite macroscopic behaviour is based on an additive decomposition of the state potential. The SFRC is assimilated to an assembly of several fibre media embedded in a polymeric matrix medium. One of the main assets of this approach is the possibility to model reinforcement with complex distributions of fibre orientations. Moreover, this decomposition allows the implementation of complex behaviour laws coupled with damage models. The polymeric matrix behaviour is typically strain-rate sensitive, i.e. viscoelastic-viscoplastic. This property has to be taken into account when the modelling of the composite behaviour over a large range of strain rate is intended. Therefore, a viscoelastic constitutive model, based on generalised Maxwell model, and a viscoplastic correction scheme, based on an overstress approach, are implemented for matrix material. The developed constitutive model is then coupled to two damage laws. The first one is introduced in the framework of Continuum Damage Mechanics in order to model the anisotropic ductile damage behaviour of the matrix material. The second one deals with fibre/matrix interfacial degradation through an interfacial debonding law. In order to identify the parameters involved in the present model, experimental tests are performed (case of polypropylene reinforced with short glass fibres). Micro-computed tomography is used for the characterisation of the fibres distribution of orientation. The efficiency of the proposed model is demonstrated by comparisons between numerical and experimental responses in different loading conditions, including dynamic loadings.



---

## *Résumé*

---

L'utilisation de composites à matrice thermoplastique renforcée par fibres courtes (TRFC) connaît une forte croissance pour une large gamme d'applications industrielles pour des conditions de chargement extrêmes (e.g. pare-chocs d'automobiles). Il est donc indispensable de développer des modèles de comportement des TRFC tenant compte des spécificités du matériau pour une large gamme de vitesse de déformation. Toutefois, le comportement de ces composites est complexe. Cette complexité est due, en premier lieu, au comportement viscolastique (VE)-viscoplastique (VP) de la matrice avec une sensibilité à la pression. A cela s'ajoute les caractéristiques complexes du renfort en termes de distributions d'orientation des fibres courtes. De plus, le comportement de ces composites est affecté par des phénomènes d'endommagement coexistants (e.g. endommagement de la matrice et décohésion à l'interface fibre/matrice). Dans ce travail, un modèle permettant la prise en compte de l'ensemble de ces phénomènes est proposé. Sa formulation est basée sur la décomposition du matériau en un milieu matriciel et plusieurs milieux de fibres, sur la base d'une décomposition additive du potentiel thermodynamique. Cette approche permet une implémentation simplifiée avec une résolution successive (mais non indépendante) du comportement de chaque milieu. Un avantage immédiat est la possibilité de prendre en compte tout type de comportement matriciel et tout type d'orientation. L'interface fibre/matrice, siège de la transmission de l'effort est modélisée par un transfert par cisaillement, avec sur une hypothèse locale d'iso-déformation dans la direction de la fibre. L'endommagement ductile de la matrice est pris en compte par un modèle d'endommagement anisotrope. La dégradation de l'interface fibre/matrice est décrite par un modèle de décohésion initiée en pointe de fibres. Un critère de rupture se basant sur le taux maximal de vide créé par décohésion est enfin introduit. La caractérisation du modèle est basée sur des campagnes d'essais quasi-statiques et dynamiques pour le cas de polypropylène pur et renforcé par fibres courtes de verre, à différents angles de chargement par rapport à la direction d'injection. Ces essais sont complétés par des observations au microtomographe permettant la caractérisation des distributions d'orientation locale des fibres. Des observations au MEB ont enfin permis de constater une éventuelle influence de la vitesse de sollicitation sur les mécanismes d'endommagement.

**Title :**

**Abstract:**

**Keyword :**

**Titre :**

**Rsum :**

**Mots-clis :**

---

# Modélisation du comportement des composites à fibres courtes en dynamique

Les thermoplastiques renforcés par des fibres courtes (TRFC) étant de plus en plus utilisés dans des applications industrielles, y compris pour des pièces subissant des sollicitations extrême (pare-chocs d'automobiles par exemple), il est nécessaire de développer des modèles de comportement de ces composites valables pour une large gamme de déformation. Pour permettre une prédiction la plus précise possible, ces modèles doivent prendre en compte l'ensemble des spécificités des TRFC. En premier lieu, le comportement mécanique de la matrice thermoplastique est très généralement sensible à la vitesse de déformation (viscoélastique et viscoplastique), avec un écoulement plastique sensible à la pression hydrostatique (comportement différent en traction et en compression notamment) et non isochore. Aux spécificités de la matrice thermoplastique s'ajoutent les caractéristiques complexes du renfort, notamment en termes de distributions d'orientation des fibres dans le cas de pièces moulées par injection. Dans le cas de renfort par fibres végétales (non abordé ici), il faut aussi tenir compte de la forte variabilité des propriétés constitutives, géométriques et mécaniques des fibres. Enfin, le comportement des TRFC est affecté par différents phénomènes d'endommagement, comme l'endommagement ductile de la matrice, la décohésion à l'interface fibre/matrice (et entre fibrilles dans le cas de fibres végétales) et la rupture des fibres (dans une moindre mesure de par leur faible longueur initiale). On peut noter que l'évolution de ces phénomènes dépend directement des états de contrainte et de déformation locaux, et donc de l'orientation locale des fibres.

Le modèle développé vise à prendre en compte l'ensemble de ces spécificités du comportement mécanique des TRFC. Dans un contexte de sollicitation sous haute vitesse de déformation, le temps de calcul des simulations numériques peut vite devenir très important. Ainsi, l'approche proposée vise à atteindre le meilleur compromis possible entre précision des comportements simulés et temps de calcul (schéma d'intégration temporel explicite), sur la base de deux hypothèses simplificatrices majeures par rapport aux méthodes d'homogénéisation plus classiques.

Le principe du modèle ainsi que les équations constitutives sont décrits en détail dans ce qui suit.

L'approche repose sur la division du composite en plusieurs milieux : un milieu matriciel et  $N$  milieux élastiques linéaires de fibres dispersés dans la matrice. Les milieux de fibres sont définis en «regroupant» les fibres en fonction de leurs propriétés géométriques (longueur et rayon), mécaniques (module d'Young) et leur orientation dans le repère global. La division des fibres en plusieurs milieux, chacun ayant sa propre fraction volumique, permet donc en particulier une modélisation aisée des distributions d'orientation et/ou de longueur des fibres dans le composite. Le comportement de chaque milieu est résolu successivement. Ceci permet notamment l'adaptabilité du modèle à tous types de comportement de la matrice.

Les fibres ont un comportement supposé unidimensionnel et élastique linéaire. Ceci est justifié par un important ratio d'aspect de ces fibres. Le comportement de la matrice thermoplastique est modélisé en viscoélasticité (VE)-viscoplasticité (VP) pour la prise en compte la dépendance à la vitesse de déformation. Enfin, le comportement macroscopique du composite est calculé en supposant une partition additive du potentiel thermodynamique du matériau composite.

## Comportement viscoélastique-viscoplastique de la matrice thermoplastique :

On se place dans le cadre de l'hypothèse des petites déformations. La modélisation du comportement viscoélastique de la matrice repose sur un modèle de Maxwell généralisé. Le tenseur contrainte de Cauchy de la matrice,  $\sigma_M(t)$  est linéairement lié à la déformation VE,  $\varepsilon^{ve}$ ,  
Via l'intégrale de Boltzmann :



$$\sigma_M(t) = \int_{-\infty}^t R^{ve}(t-\zeta) : \frac{\partial \varepsilon^{ve}(\zeta)}{\partial \zeta} d\zeta \quad (\text{Eq. 1})$$

$R^{ve}$  est le tenseur d'ordre quatre de relaxation de Maxwell.

$$R^{ve}(t) = 2G(t)I^{dev} + 3K(t)I^{vol} \quad (\text{Eq. 2})$$

Avec  $G(t)$  et  $K(t)$  sont respectivement les modules de cisaillement et de dilatation de la matrice, définis comme suit:

$$\begin{aligned} G(t) &= G_\infty + \sum_{i=1}^N G_i \exp\left(-\frac{t}{\tau_i^{dev}}\right) \\ K(t) &= K_\infty + \sum_{i=1}^N K_i \exp\left(-\frac{t}{\tau_i^{vol}}\right) \end{aligned} \quad (\text{Eq. 3})$$

avec:

$$\begin{aligned} G_\infty &= \frac{E_\infty}{2(1+\nu)}, \quad G_i = \frac{E_i}{2(1+\nu)} \\ K_\infty &= \frac{E_\infty}{3(1-2\nu)}, \quad K_i = \frac{E_i}{3(1-2\nu)} \end{aligned} \quad (\text{Eq. 4})$$

Où  $G_\infty$  et  $K_\infty$  sont les modules indépendants du temps.  $G_i$  et  $K_i$  sont les modules de relaxation correspondants aux  $N$  éléments Maxwell.

La partie non-linéaire du comportement de la matrice est décrite par une surface de charge de type Raghava, sensible à la pression hydrostatique, est définie pour marquer la transition (visco)elasto-plastique (1).

$$f(I_1, I_2, p) = \frac{(\eta-1)I_1 + \sqrt{(\eta-1)^2 I_1^2 + 12\eta I_2}}{2\eta} - \sigma_t - R(p) \quad (\text{Eq. 5})$$

Où  $I_1 = \text{tr}(\sigma_M(t))$ ,  $I_2 = \frac{1}{2} S_M(t) : S_M(t)$ , avec  $S_M$  le déviateur de la contrainte de Cauchy de la matrice;  $\sigma_t$  est la limite d'élasticité en traction du matériau et  $p$  la déformation plastique cumulée.  $\eta$  est le paramètre de sensibilité à la pression hydrostatique, défini comme le rapport entre la limite d'élasticité en compression et en traction. Enfin,  $R$  est la loi d'écrouissage isotrope, à adapter au matériau considéré. La viscoplasticité est modélisée par le principe d'une sur-contrainte visqueuse.

La surface de charge  $f$  (Eq. 5) est alors étendue à une surface de charge dynamique:

$$F = f - \sigma_{vp} \quad (\text{Eq. 6})$$

avec  $\sigma_{vp}$  la sur-contrainte visqueuse. Son expression est par exemple donnée par le modèle de Perzyna, à savoir :

$$\sigma_{vp} = (\sigma_t + R(p)) \left( \frac{\dot{p}}{\dot{p}_0} \right)^m \quad (\text{Eq. 7})$$

Où  $\dot{p}_0$  et  $m$  sont des paramètres matériau.

Enfin, on se place dans le cadre de la viscoplasticité non associée, avec la définition d'un potentiel viscoplastique de dissipation hyperbolique permettant la modélisation de la non-symétrie et de la non-isochorie de l'écoulement (visco)plastique:

$$\psi_M^{vp} = \sqrt{3I_2 + \frac{1}{3}(a^+ \langle I_1 \rangle^2 + a^- \langle -I_1 \rangle^2)} \quad (\text{Eq. 8})$$

Avec  $a^+$  et  $a^-$  des paramètres matériau et  $\langle x \rangle = \frac{x+|x|}{2}$ .

L'ensemble des équations constitutives sont implémentées en suivant un schéma du type état test viscoélastique suivi, si besoin, d'une correction viscoplastique.

### Comportement élastique linéaire des milieux de fibres

Comme précisé avant, les fibres sont divisées en différents milieux à comportement élastique linéaire. Chaque milieu de fibres est ainsi caractérisé par une longueur,  $L$ , et un rayon,  $r$ , de fibre, un module d'Young,  $E_F$ , et un vecteur d'orientation,  $\vec{a}$ , dans le repère global (lié à la matrice). On définit également la matrice d'orientation,  $A = \vec{a} \otimes \vec{a}$ .

La première hypothèse fondamentale du modèle est que le tenseur gradient de déformation appliqué à chaque milieu de fibre  $i$ ,  $F_F^i$ , est la projection du tenseur gradient de déformation appliqué au composite,  $F$ , selon la direction d'orientation des fibres, i.e.  $F_F^i = FA^i, \forall i$ . On peut d'ores et déjà noter que la seconde hypothèse forte est que le tenseur  $F$  est transmis en l'état au milieu matriciel. La relation  $F_F^i = FA^i, \forall i$  permet d'exprimer les tenseurs de Cauchy-Green des familles de fibres,  $C_F^i$ , comme suit :  $C_F^i = F_F^{iT} F_F^i = A^i F^T F A^i = A^i C A^i, \forall i$ , avec  $C$  le tenseur de Cauchy-Green du composite. On peut noter que, par construction, les tenseurs  $C_F^i$  admettent une unique valeur propre non-nulle, notée  $c^i$ , associée au vecteur propre  $\vec{a}^i$ , ce qui sous-entend un comportement unidimensionnel des fibres. Ce point est cohérent avec le haut ratio d'aspect, longueur sur rayon, des fibres courtes, qui permet de négliger les déformations dans les directions transverses à l'axe de la fibre. A partir des tenseurs  $C_F^i$ , on peut exprimer la déformation 1D de Hencky de chaque milieu de fibre, ainsi :

$$\varepsilon_F^{0i} = \frac{1}{2} \ln(c^i), \forall i \quad (\text{Eq. 9})$$

La contrainte axiale moyenne dans la fibre est ensuite calculée en utilisant un modèle de transfert par cisaillement (Eq. 10), basé sur les travaux originels de Bowyer and Bader [6] et étendu à des cas d'orientations complexes [3].

$$\begin{cases} \sigma_F^{0i} = \varepsilon_F^{0i} E_F^i \left( 1 - \frac{E_F^i r^i}{2L^i \tau^i} |\varepsilon_F^{0i}| \right) \text{ si } |\varepsilon_F^{0i}| \leq \frac{L^i \tau^i}{E_F^i r^i} \\ \sigma_F^{0i} = \text{signe}(\varepsilon_F^{0i}) \frac{L^i \tau^i}{2r^i} \text{ sinon} \end{cases} \quad \forall i \quad (\text{Eq. 10})$$

Dans l'expression précédente, les  $\tau^i$  sont les résistances en cisaillement de l'interface matrice/fibres du milieu  $n^\circ i$ . Finalement, le tenseur des contraintes des fibres,  $\sigma_F^i$ , est exprimé dans le repère global en utilisant les matrices de passage,  $T$ , du repère lié à un milieu de fibre dans le repère global. Les contraintes transverses à l'axe de la fibre sont calculées en utilisant des conditions d'iso-contrainte avec celles d'un matériau du type matriciel mais dont le comportement serait purement viscoélastique (i.e., pas de plasticité). On obtient alors :

$$\sigma_F^i = T^i \begin{bmatrix} \sigma_F^{0i} & \sigma_{Mve}^{0i} 12 & \sigma_{Mve}^{0i} 13 \\ \sigma_{Mve}^{0i} 12 & \sigma_{Mve}^{0i} 22 & \sigma_{Mve}^{0i} 23 \\ \sigma_{Mve}^{0i} 13 & \sigma_{Mve}^{0i} 23 & \sigma_{Mve}^{0i} 33 \end{bmatrix} \forall i \quad (\text{Eq. 11})$$

L'exposant "0 i" signifie une expression dans le repère local lié au milieu de fibres  $n^\circ i$ .

---

## Comportement du composite

Le comportement macroscopique du composite est obtenu en considérant une décomposition additive de son potentiel thermodynamique,  $\Phi_C$ :

$$\rho_C \Phi_C = v_M \rho_M \Phi_M + \sum_{i=1}^N v_F^i \rho_F^i \Phi_F^i \quad (\text{Eq. 12})$$

Où les  $\rho$  sont les masses volumiques, les  $\Phi$  les potentiels thermodynamiques et les  $v$  les fractions volumiques. Les indices C, M et F renvoient respectivement au composite, à la matrice et à un milieu de fibre, caractérisé par un exposant  $i$ .

Finalement, la résolution de l'inégalité de Clausius-Duhem (Eq. 13) permet d'exprimer le tenseur des contraintes de Cauchy du matériau composite (Eq. 14).

$$\sigma_C : \dot{\varepsilon} - [v_M \rho_M \dot{\Phi}_M + \sum_{i=1}^{N_{\text{fam}}} v_F^i \rho_F^i \dot{\Phi}_F^i] \geq 0 \quad (\text{Eq. 13})$$

$$\sigma_C = v_M \sigma_M + \sum_{i=1}^N v_F^i A^i \sigma_F^i A^i \quad (\text{Eq. 14})$$

## Validation du modèle : exemple d'un composite polypropylène + 30% de fibres courtes de verre (PP-GF) moulé par injection

Les équations constitutives présentées ci-avant sont implémentées sous Abaqus Explicit (sous forme d'une "VUMAT"). La validation du modèle repose sur des comparaisons entre des données expérimentales et la simulation numérique de ces essais utilisant le modèle développé. Pour cela, il est d'abord nécessaire d'identifier les paramètres du modèle.

### Identification des paramètres de comportement de la matrice polypropylène (PP)

Les paramètres viscoélastiques de la matrice thermoplastique sont identifiés par des DMA (dynamic mechanical analyses) réalisé à des fréquences de 0.01 Hz à 30 Hz (Figure 1).

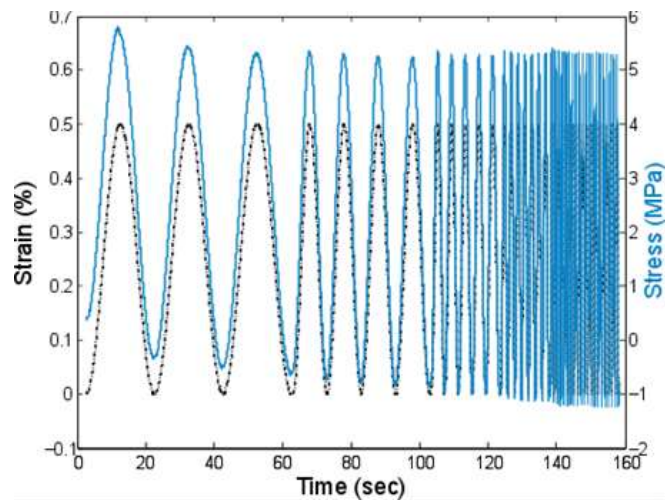


Fig. 1. Réponse en contrainte et déformation à un chargement en déplacement sinusoïdal

Des modules de gain et de perte sont donc déterminés par la méthodes des moindres carrés avec les mesures faites moyennant les essais à chargement sinusoïdal (Figure 2).

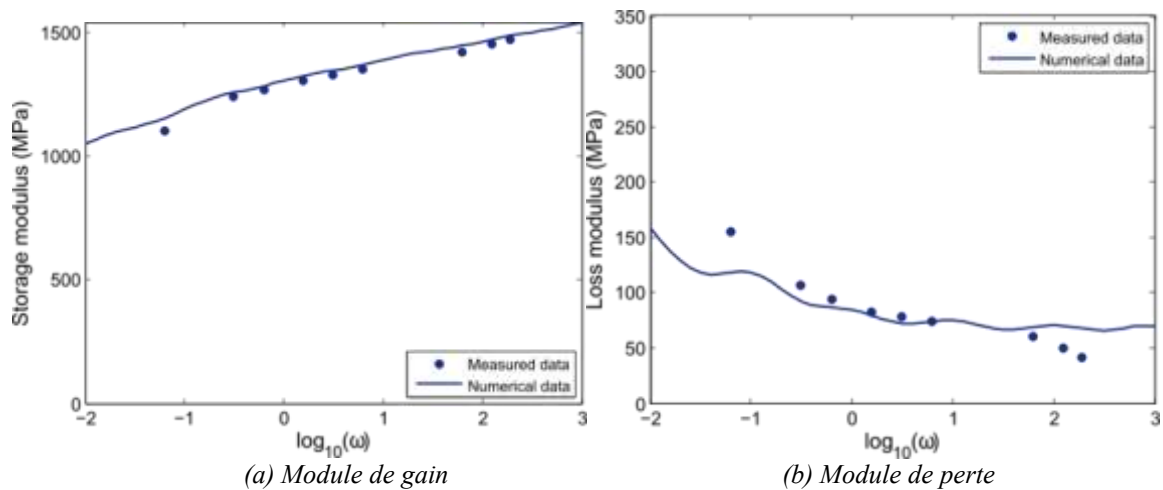
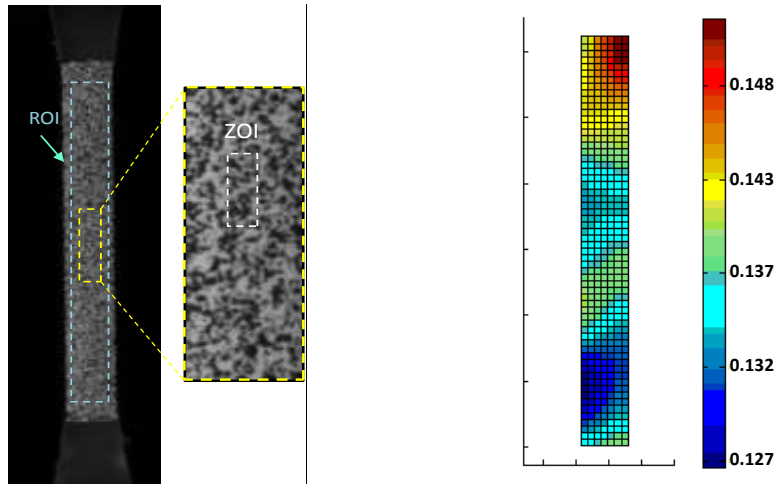


Fig. 2. Identification des modules de perte et de gain

Les paramètres de l'écoulement viscoplastiques sont identifiés en utilisant la méthode SEE grâce à une série d'essais de traction uniaxiale, à différentes vitesses de sollicitation quasi-statiques et dynamiques, associé à des mesures de champ par corrélation d'images numériques (DIC) (Figure 3).



(a) Définition de la région et des zones d'intérêt (ROI et ZOI) (b) Cartographie des déformations axiales

Fig. 3. Caractérisation en traction du composite par corrélation d'image

Les résultats des essais réalisés à plusieurs vitesses de déformation sont présentés dans la Figure 4.

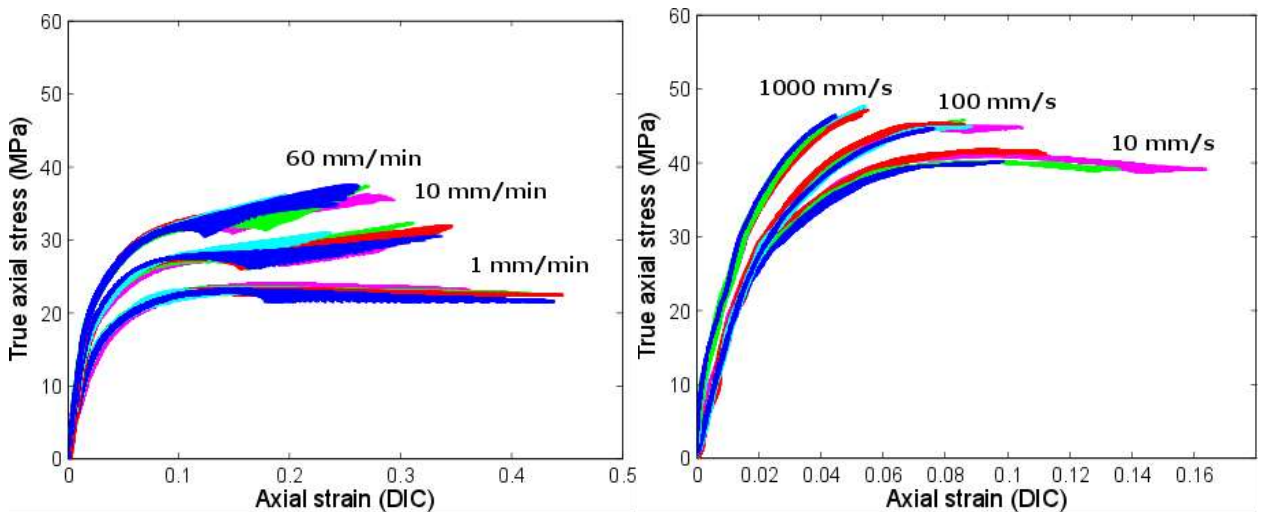


Fig. 4. Comportement axial à différentes vitesses de chargement du PP caractérisé par corrélation d'image

La loi d'écoulement isotrope donnée par l'Eq. 16 est considéré

$$R(p) = h_1 \exp(h_2 p^2) (1 - \exp(-h_3 p)) \quad (\text{Eq. 16})$$

Avec  $h_1$ ,  $h_2$  et  $h_3$  sont des paramètres matériau. Les paramètres d'écoulement ainsi que les paramètres de viscosité sont déterminés moyennant la méthode SEE. La méthode consiste à identifier les paramètres d'écoulement viscoplastique par corrélation avec la surface de comportement dans l'espace contrainte-déformation-vitesse de déformation (Figure 5).

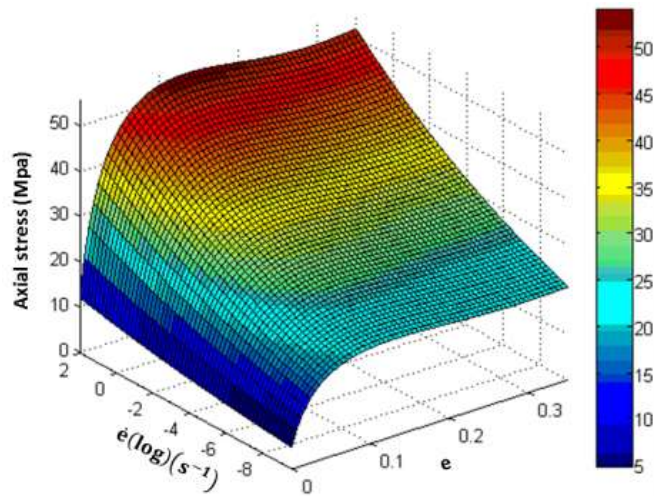


Fig. 5. Surface de comportement obtenue par la méthode SEÈ

Des essais de compression sur plots permettent l'identification du paramètre  $\eta$ . Le paramètre  $a^+$  est identifié à partir du coefficient de Poisson plastique mesuré en traction. Malheureusement, il n'a pas été possible d'utiliser des mesures par DIC sur les plots de compression, le paramètre  $a^-$  est donc fixé arbitrairement à 0.

Une comparaison des résultats expérimentaux et numériques est illustrée par la Figure 6 pour le PP. Pour information, les vitesses de déformation « ingénieur » correspondantes sont, par ordre croissant, de  $5.55 \cdot 10^{-4}$ ,  $5.55 \cdot 10^{-3}$ ,  $3.33 \cdot 10^{-2}$ , 0.5, 5 et  $50 \text{ s}^{-1}$ .

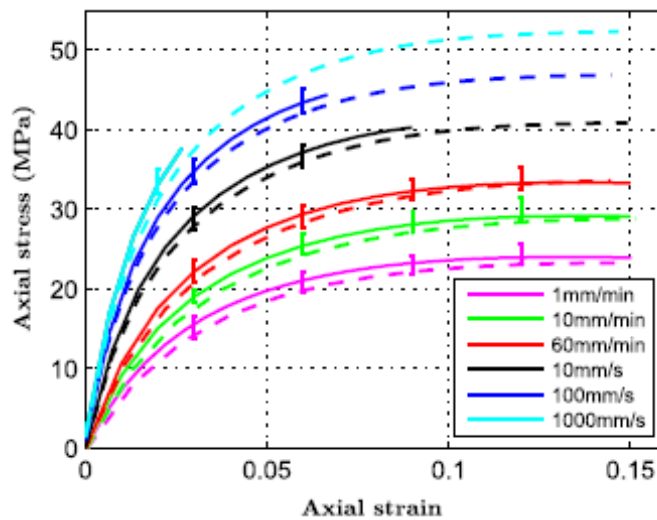
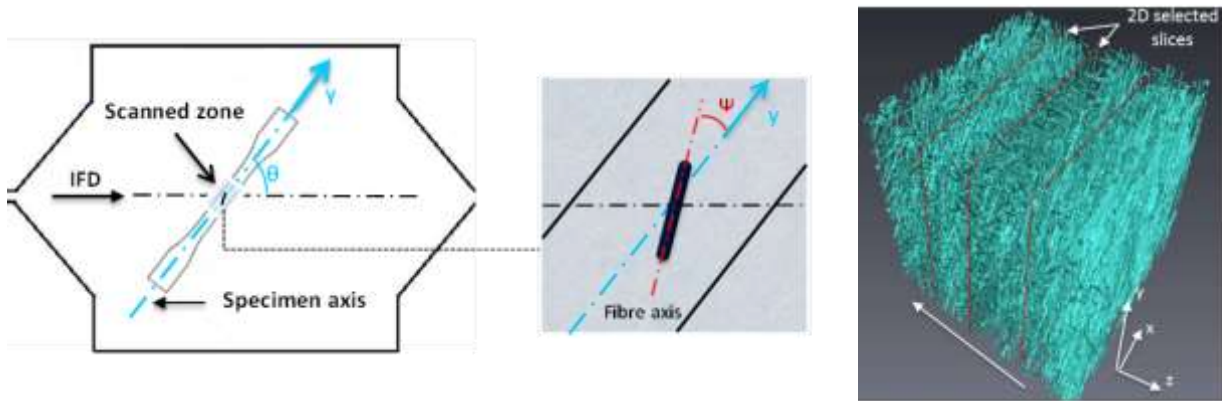


Fig. 6. Comportement en traction uniaxial du PP (traits continus : données expérimentales, pointillés = simulation numériques).

### Identification des distributions d'orientation locale des fibres par microtomographie et de la résistance interfaciale en cisaillement, $\tau$

La microstructure du composite PP-GF est analysée par microtomographie aux rayons X (microtomographe Skyscan 1172 de Bruker Micro CT, pas de rotation de  $0.4^\circ$ , 30 kV, 40  $\mu\text{A}$  pour une résolution de spatiale (taille de voxel) de  $3.87 \mu\text{m}$  – scans à  $360^\circ$ ). Plus précisément, les volumes centraux d'éprouvettes de traction de type ISO527, découpées à différents angles  $\theta$  (0, 20,

45, 60 et 90°) par rapport à la direction d'injection sont scannés (Figure 7a). Les images extraites sont ensuite analysées pour détecter toutes les structures (fibres) présentes et déterminer leurs caractéristiques (longueur, rayon et orientation dans l'image). Une pré-analyse a montré que les fibres étaient quasi-exclusivement orientées dans le plan de la plaque. Leur orientation peut donc être déterminée par la connaissance de l'angle  $\psi$  uniquement (Figure 7a).



(a) Définition de l'angle de découpe,  $\theta$ , et de l'angle d'orientation d'une fibre par rapport à la direction de chargement,  $\psi$

(b) Reconstitution 3D de la microstructure

Fig. 7. Principe de la détermination des orientations locales des fibres par micro-tomographie.

La détermination de l'ensemble des fibres présentes dans le volume scanné et de leur orientation permet d'établir les distributions d'orientations réelles dans le matériau. Une sélection d'image 2D (Figure 8) suivant l'épaisseur du volume scanné et leur traitement moyennant l'outil FiJi permet ensuite la détermination d'histogrammes de densité d'orientation.

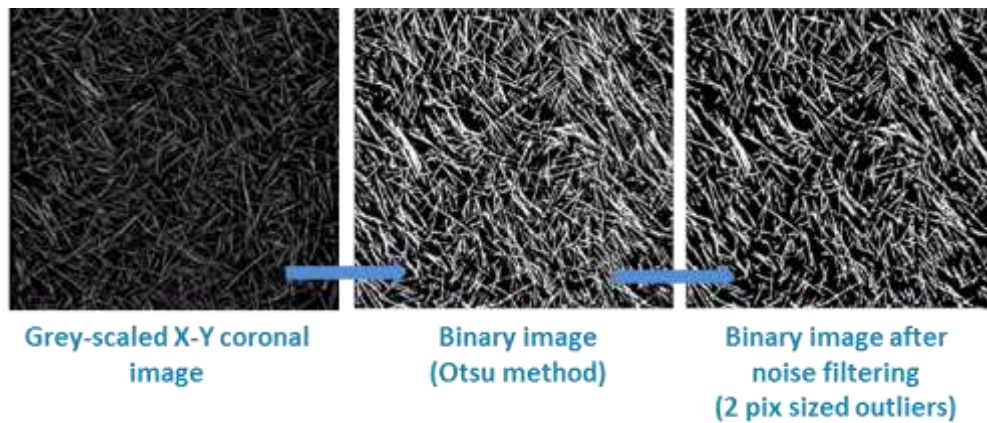
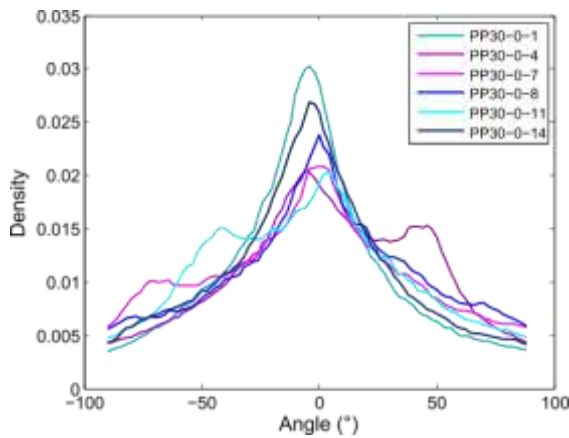


Fig. 8. Traitement des images 2D obtenue par micro-tomographie.

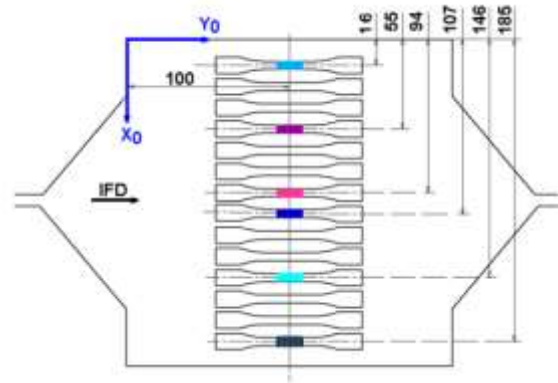
La Figure 9a donne ainsi des exemples de distributions d'orientations moyennées dans le volume scanné pour des éprouvettes découpées à  $\theta=0^\circ$ , c'est-à-dire selon la direction d'injection. On peut noter que pour tous les angles de découpe, la direction d'orientation préférentielle est toujours égale à  $\pm \theta$ , ce qui signifie que les fibres s'orientent préférentiellement dans la direction d'injection dans le volume du matériau. Toutefois, la Figure 5a montre que, pour un même angle de découpe (ici  $\theta=0^\circ$ ), les distributions d'orientation locale des fibres varient. Dans le cas présent, cette variation est liée à une position différente des éprouvettes dans la plaque injectée (Figure 9b - plus on se rapproche des bords, plus la proportion de fibres orientées dans la direction d'injection augmente). Ces différences sur les caractéristiques du renfort ont un impact non négligeable sur le



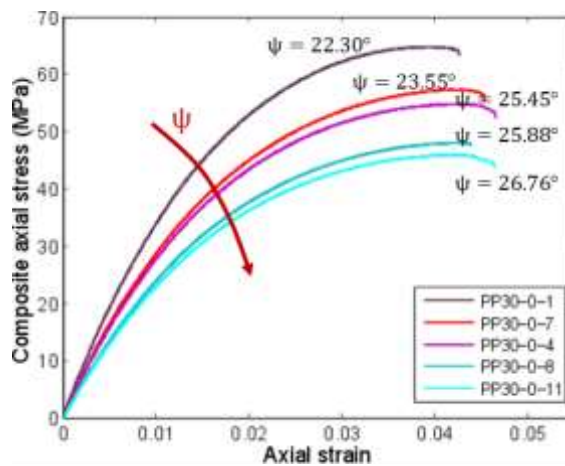
comportement mécanique du composite, par exemple en traction (Figure 9c). Il est donc évident qu'une prédiction correcte du comportement du matériau doit reposer sur un modèle prenant en compte les caractéristiques locales du renfort et non pas simplement l'angle de découpe des éprouvettes, par exemple.



(a) Distributions d'orientation des fibres dans les éprouvettes découpées selon la direction d'injection



(b) Positionnement des éprouvettes scannées dans la plaque de PP-GF



(c) Comportement en traction uniaxiale à 1mm/min des éprouvettes découpées dans la direction d'injection

Fig. 9. Exemples de distributions d'orientation des fibres dans le composite PP-GF et influence sur le comportement en traction.

L'identification de la résistance interfaciale en cisaillement,  $\tau$ , repose sur le recalage du comportement en traction de l'éprouvette 0-1 (i.e. présentant la proportion la plus élevée de fibres orientées dans la direction de chargement) avec la simulation numérique par EF de cet essai, utilisant le modèle de comportement développé (Figure 10). On utilise bien sûr les paramètres de la matrice PP identifiés et la distribution d'orientation des fibres déterminée par micro-tomographie pour l'éprouvette 0-1. Dans cet exemple d'application, on considère que toutes les fibres ont la même longueur, le même rayon et le même module d'Young. Les paramètres géométriques des fibres sont issus de l'analyse micro-tomographique et leur module d'Young est issu de la littérature.



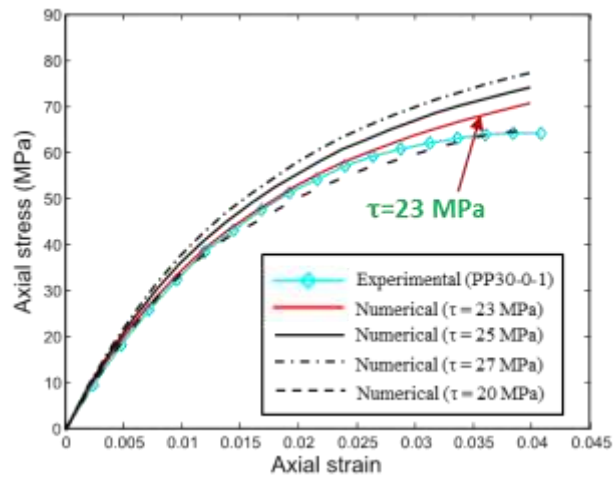
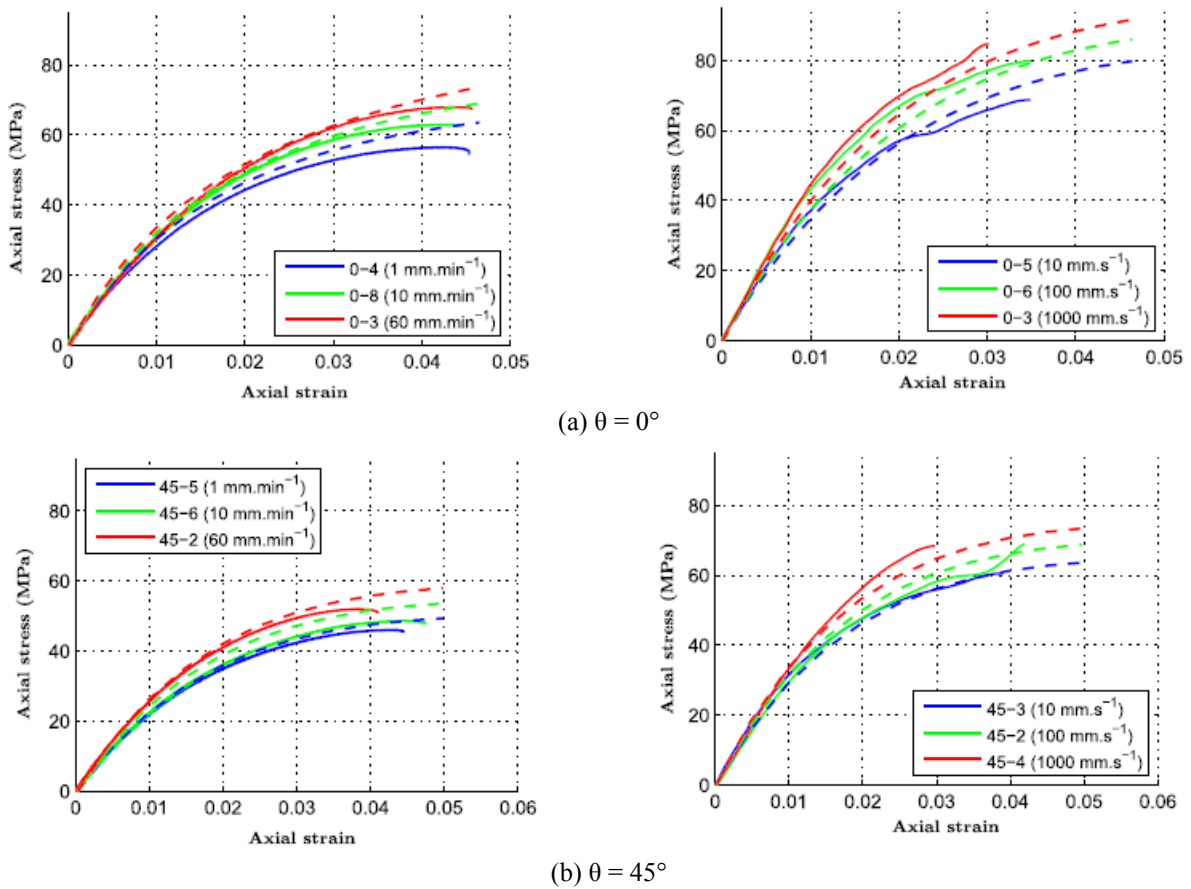
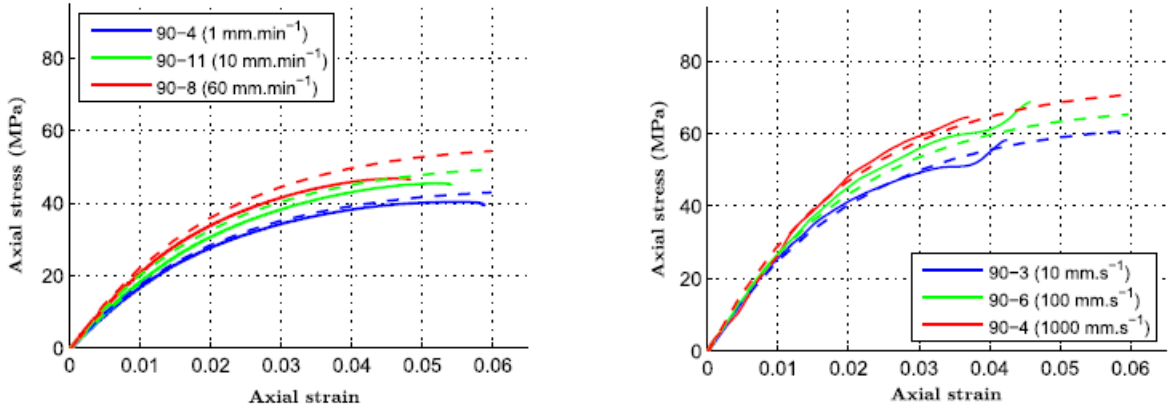


Fig. 10. Identification du paramètre de résistance interfaciale en cisaillement.

### Validation du modèle de comportement pour le composite PP-GF

La Figure 11 donne des exemples de comparaison de comportements en traction du PP-GF, avec différents angles de découpe  $\theta$  des éprouvettes, expérimentaux et simulés numériquement avec le modèle développé. Ces résultats permettent de valider les équations constitutives et leur implémentation pour la gamme de vitesse de déformation considérée ( $5.55 \cdot 10^{-4}$  à  $50 \text{ s}^{-1}$ ).





(c)  $\theta = 90^\circ$

Fig. 11. Exemples de comparaisons données expérimentales/numériques pour le comportement en traction du PP-GF.

Des essais de caractérisation ont été aussi réalisés pour des composites à des taux massiques de renfort différents (15% et 40% de fibres de verre). L'identification des distributions d'orientation par micro-tomographie a ainsi permis la validation du modèle pour des taux de renforts différents.

### Extensions du modèle de comportement

Les extensions du modèle de comportement est le sujet de la partie suivante.

Les premières évolutions concernent la prise en compte des phénomènes d'endommagement. Leur effet est observable sur les derniers niveaux de chargement du composite avec un adoucissement qui n'est pas pris en compte par le modèle non-endommageable (Figure 11). L'extension du modèle porte sur la prise en compte de l'endommagement ductile anisotrope de la matrice et de la dégradation de l'interface entre fibres et matrice.

### Endommagement ductile anisotrope de la matrice

Le comportement de la matrice thermoplastique non renforcée peut être affecté par un endommagement ductile, généralement isotrope. Toutefois, l'endommagement de la matrice dans le composite peut devenir complètement anisotrope, en raison des distributions d'orientation complexes des fibres qui vont modifier les états mécaniques locaux.

Ce phénomène peut être modélisé par l'utilisation d'un tenseur d'endommagement du 4<sup>ème</sup> ordre. Celui-ci est construit en considérant l'assemblage des contributions de chaque milieu de fibres au pilotage de l'endommagement de la matrice (Eq. 17). Pour cela, des tenseurs d'endommagement intermédiaires sont construits en considérant notamment que les fibres empêchent l'endommagement matriciel dans leur direction d'orientation (Eq. 18).

$$D_{ijkl} = v'_M(1 - d)\delta_{ik}\delta_{jl} + \sum_{a=1}^N \frac{v_F^i}{v_M} \sum_{p,q=1}^3 T_{ip}^a (T^a)^{-1}_{qj} (T^a)^{-1}_{pk} T_{lq}^a D_{ppqq}^a \quad (\text{Eq. 17})$$

$$D_{ijkl}^a = \delta_{ik}\delta_{jl} [1 - d(\delta_{ij}(1 - \delta_{i1}) - (1 - \delta_{ij}))] \quad \forall a \quad (\text{Eq. 18})$$

Avec  $d$  la variable d'endommagement scalaire;  $v'_M = 1 - \sum_{a=1}^N v_F^a / v_M$  est la fraction volumique de la matrice dont l'endommagement n'est pas affecté par la présence des fibres.

Dans l'implémentation, cet endommagement est pris en compte en définissant une contrainte matricielle effective et en utilisant le principe d'équivalence en déformation. Le schéma d'implémentation est semi-couplé.

L'évolution de la variable scalaire d'endommagement,  $d$ , est définie suivant la mécanique de l'endommagement continu par la loi de Lemaitre (Eq. 19).

$$\begin{cases} \dot{D} = \dot{\kappa} \frac{Y}{S} & , \text{if } \kappa \geq \kappa_D \\ \dot{D} = 0 & \text{else} \end{cases} \quad (\text{Eq. 19})$$

L'identification de cette loi (détermination des paramètres  $S$  et  $\kappa_D$ ) est réalisée moyennant des essais cycliques sur la matrice PP non-renforcée. Le paramètre  $S$  est identifié suivant la méthode de la dégradation de la rigidité équivalente (Figure 12).

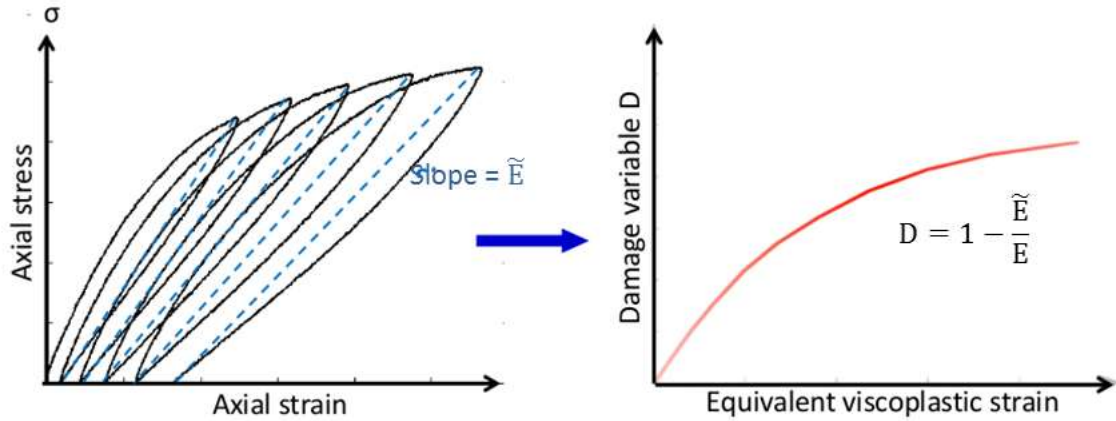


Fig. 12. Identification de la loi d'endommagement matriciel par la dégradation de la rigidité apparente.

Cette méthode a permis la détermination de l'évolution de  $d$  en fonction de la déformation viscoplastique équivalente,  $\kappa$  (Figure 13).

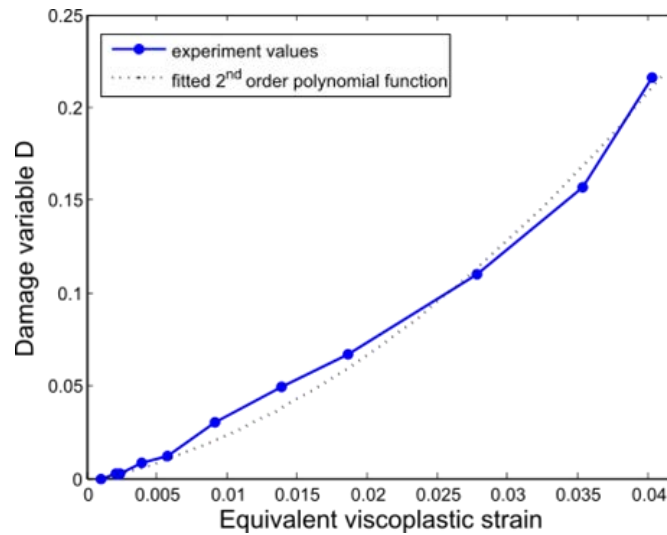


Fig. 13. Evolution de  $d$  déterminée par la méthode de dégradation de la rigidité apparente.

Une évaluation de la loi de comportement de la matrice avec la prise en compte de l'endommagement matriciel est faite pour un état d'endommagement isotrope par comparaison avec les résultats des essais en traction. Cette comparaison a permis la validation de la loi d'endommagement pour plusieurs vitesses de déformation, comme présenté dans la Figure 13. L'anisotropie de la loi d'endommagement dans le cas d'une matrice renforcée par 30% de fibres de verre est vérifiée par la prise en compte de deux distributions d'orientations de fibres différentes (avec des orientations préférentielles proches de  $0^\circ$  et  $90^\circ$ ) comme montré dans la Figure 14. La

comparaison des deux réponses en traction montre que l'endommagement matriciel est prépondérant pour le cas des fibres fortement orientées par rapport à la direction du chargement.

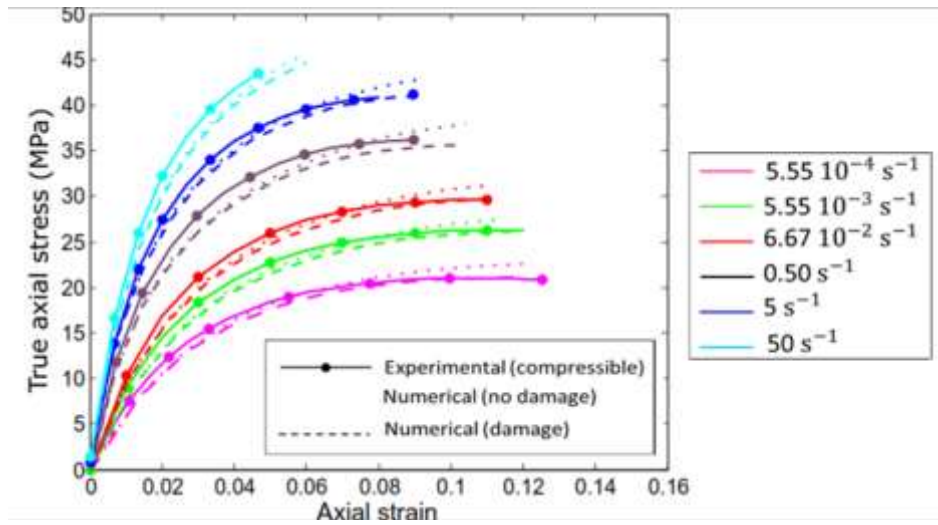
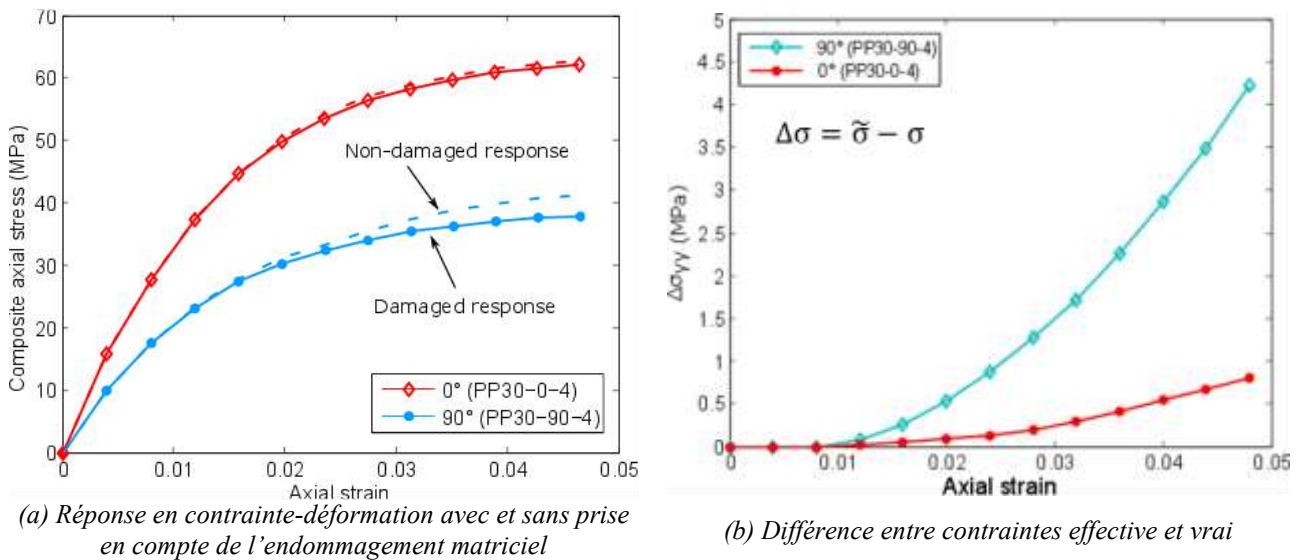


Fig. 14. Validation de la loi de comportement matricielle avec la prise en compte de l'endommagement



(a) Réponse en contrainte-déformation avec et sans prise en compte de l'endommagement matriciel

(b) Différence entre contraintes effective et vrai

Fig. 15. Vérification de l'anisotropie de la loi d'endommagement matriciel avec prise en compte de deux distributions d'orientation des fibres.

### Décohésion à l'interface fibre-matrice

La décohésion interfaciale est un phénomène d'endommagement majeur des TRFC. En effet, la décohésion entraîne une diminution de l'effort transmis à la fibre via la matrice, ce qui se traduit par un adoucissement du comportement du composite. De plus, ceci entraîne une augmentation de la concentration de contrainte dans la matrice, à proximité des fibres, en raison de la quantité d'effort non transmise, ce qui peut favoriser la localisation de la déformation plastique, l'apparition de microfissure etc... jusqu'à rupture du composite. D'après les travaux de Sato et al. [11], lorsque les fibres sont sollicitées en traction avec un angle proche de  $0^\circ$ , la décohésion s'initie en pointe de

fibres, puis, avec l'augmentation du niveau de chargement, des micro-vides se propagent le long de la fibre, à l'interface (Figure 15).

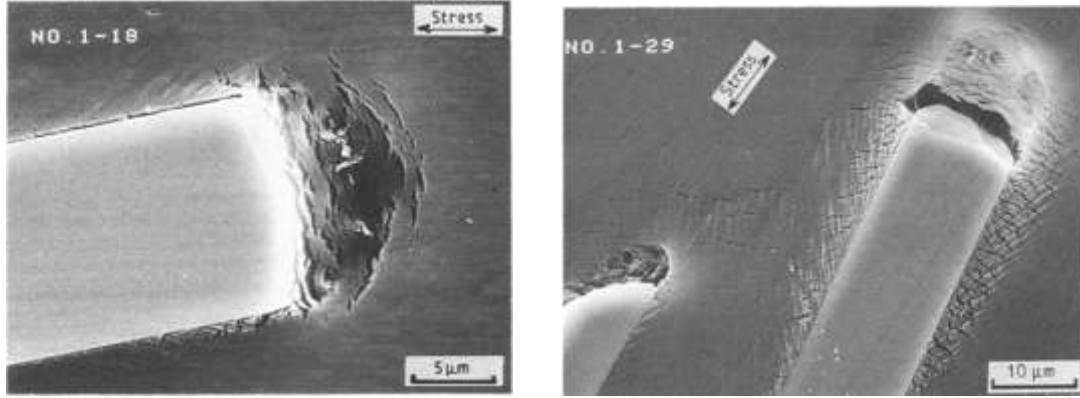


Fig. 16. Décohésion en pointe de fibre et propagation des micro-vides latéralement (images extraites de Sato et al. [10]).

Basé sur ces observations, le modèle développé prend en compte la décohésion progressive à l'interface fibre/matrice [12]. Ainsi, la propagation latérale des micro-vides est modélisée par une réduction progressive de la longueur de la fibre disponible pour la transmission de l'effort, à partir d'un seuil en déformation axiale de la fibre,  $\varepsilon_{th}$ . Dans l'équation (6), permettant le calcul de la contrainte axiale moyenne dans la fibre, la longueur  $L^i$  est alors remplacée par  $L^i - 2\delta^i$ , pour tout milieu de fibre  $i$  :

$$\begin{cases} \sigma_F^{0i} = \varepsilon_F^{0i} E_F^i \left( 1 - \frac{E_F^i r^i}{2(L^i - \delta^i) \tau^i} |\varepsilon_F^{0i}| \right) & \text{si } |\varepsilon_F^{0i}| \leq \frac{(L^i - \delta^i) \tau^i}{E_F^i r^i} \\ \sigma_F^{0i} = \text{signe}(\varepsilon_F^{0i}) \frac{(L^i - \delta^i) \tau^i}{2r^i} & \text{sinon} \end{cases} \quad \forall i \quad (\text{Eq. 20})$$

avec :

$$\begin{cases} \delta^i = a \left( \frac{\varepsilon_F^{0i} - \varepsilon_{th}}{\varepsilon_{th}} \right)^b \frac{L^i}{2} & \text{si } \varepsilon_F^{0i} \geq \varepsilon_{th} \\ \delta^i = 0 & \text{sinon} \end{cases} \quad \forall i \quad (\text{Eq. 21})$$

Où  $a$  et  $b$  sont des paramètres à identifier.

L'identification de ces paramètres a été faite en se basant sur des résultats d'essai de traction réalisé sur une éprouvette de référence (avec une distribution de fibres les plus orientées suivant la direction du chargement). Les paramètres  $a$  et  $b$  sont simultanément identifiés par la méthode inverse, en assurant la meilleure corrélation avec la réponse expérimentale du composite et en utilisant la distribution d'orientation réelle de l'éprouvette (Figure 17).

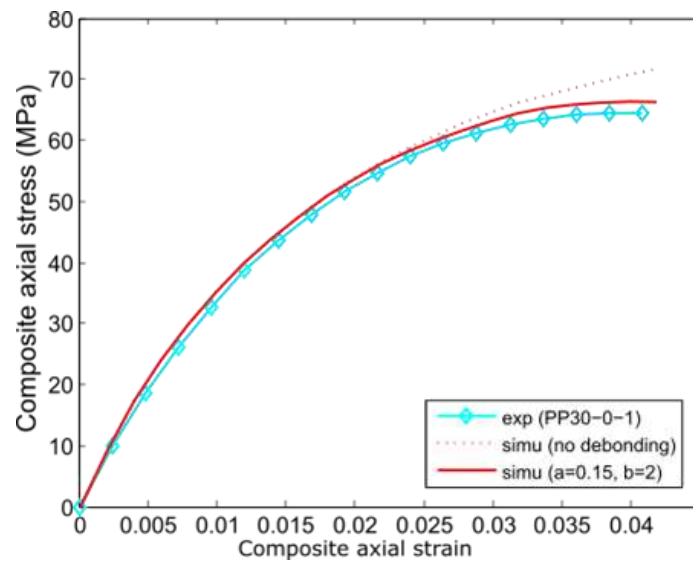
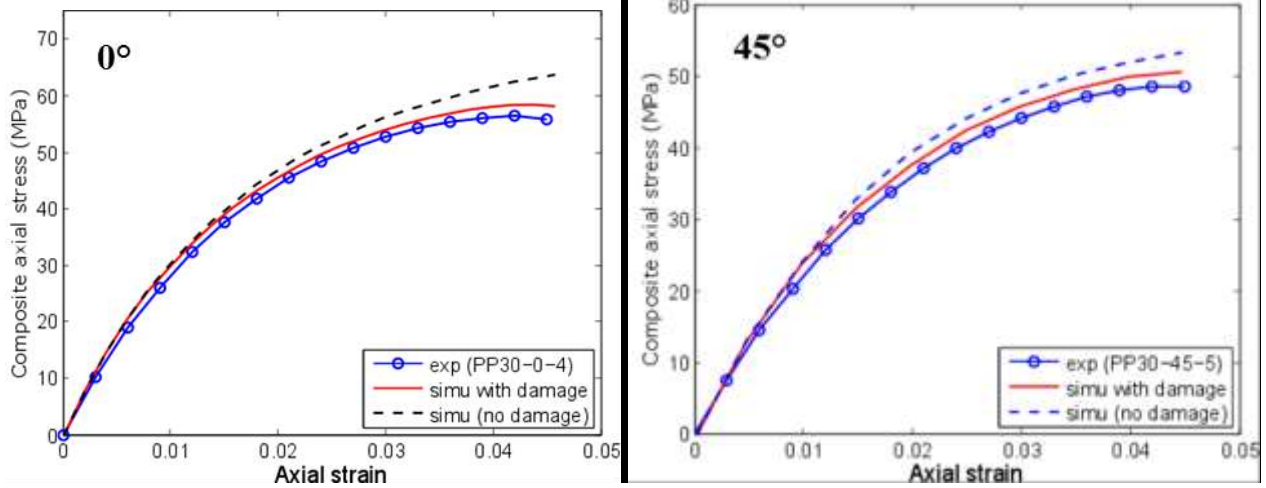


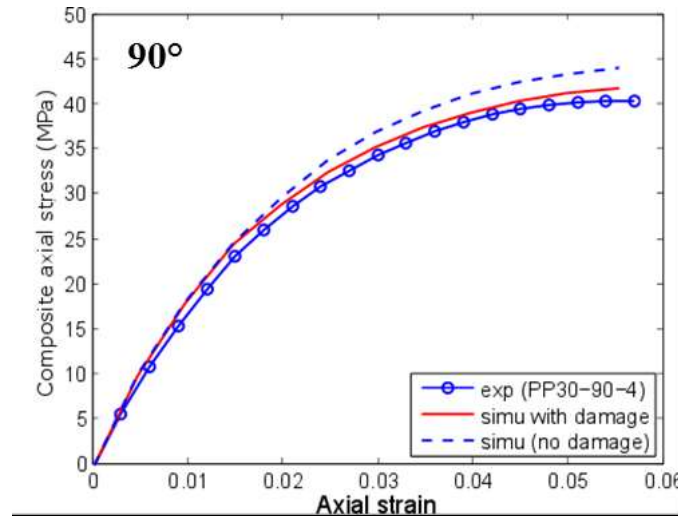
Fig. 17. Identification des paramètres de la loi de décohésion  $a$  et  $b$

L'évaluation du modèle ainsi couplé aux deux lois d'endommagement, matriciel et interfacial, a été par comparaison avec les résultats des essais de traction réalisés sur le composite avec différentes distribution d'orientation des fibres. Les cas des distributions à  $0^\circ$  et  $90^\circ$  sont présentés dans la Figure 18.



(a) Essai réalisé à 0° par rapport à l'orientation préférentielle des fibres

(b) Essai réalisé à 45° par rapport à l'orientation préférentielle des fibres



(c) Essai réalisé à 90° par rapport à l'orientation préférentielle des fibres

Fig. 18. Validation du modèle avec implémentation des deux d'endommagement en traction avec différentes distributions d'orientation des fibres

On peut noter qu'à partir de l'expression (21), il est possible d'exprimer la fraction volumique totale de vides causés par la décohésion (nucléation et coalescence). L'évolution de la fraction volumique du vide est définie par l'Equation 22.

$$\dot{v}_v^{\text{tot}} = \Pi[\dot{v}_v^{\text{nucl}} + C^{\text{growth}} v_v^{\text{nucl}} \dot{\sigma}_H] \quad (\text{Eq. 22})$$

L'évolution de volume de vide créée est donnée par l'Equation 13.

$$v_v^{\text{nucl}} = C^{\text{nucl}} \sum_i \left( \frac{2\delta^i}{L^i} \right) v_f^i \quad (\text{Eq. 23})$$

Un critère est défini comme étant le taux critique de vide créé par décohésion en s'appuyant sur des résultats de la littérature et des observations faites sur des faciès de rupture du composite, présentés dans la Figure 18. Ce critère est donc défini suivant l'équation suivante :

$$v_v^{\text{tot}} = v_v^{\text{crit}} \quad (\text{Eq. 24})$$



Des premiers tests [12] ont permis de montrer qu'il est alors possible d'identifier le taux de vide à rupture pour un composite dans une configuration donnée (en termes d'angle de chargement) et d'utiliser ce taux critique comme critère de rupture pour le même composite, mais chargé avec un angle différent.

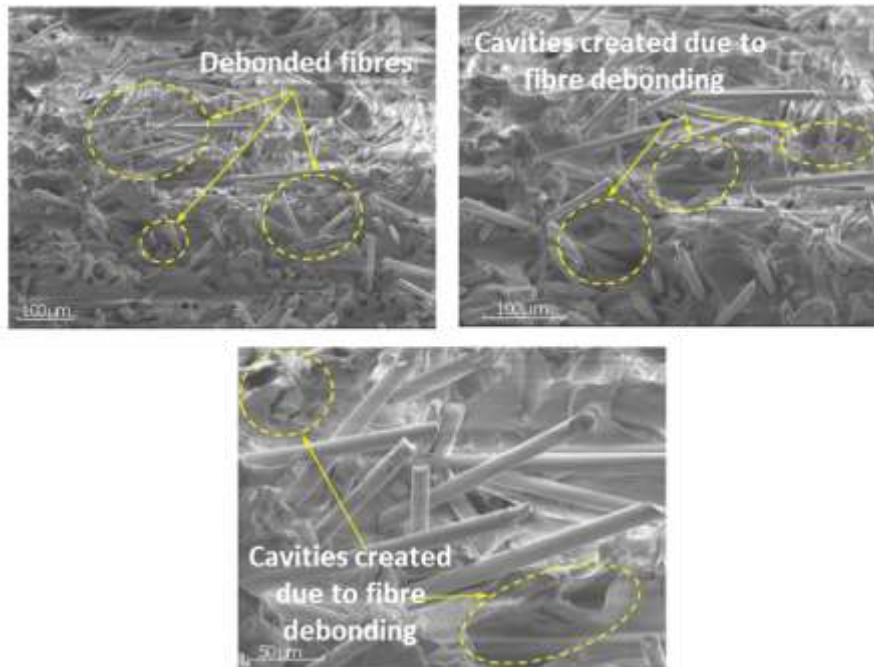


Fig. 19. Observation des défauts créés par décohésion sur des faciès de rupture du composite testé en traction

L'identification du taux critique de vide est réalisée en se basant sur des essais de traction sur un composite chargé à 30% en fibres de verre. A partir de ces essais, suivit par corrélation d'image, la déformation maximale atteinte est moyennée sur la zone d'initiation de la rupture (Figure 19). Le taux de vide critique correspondant à cette déformation est donc déterminé en simulant ces essais, comme montré dans la Figure 20.

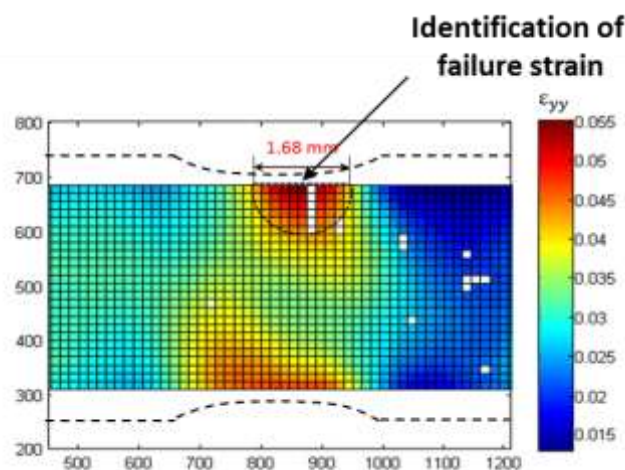


Fig. 20. Identification de la déformation à la rupture du composite



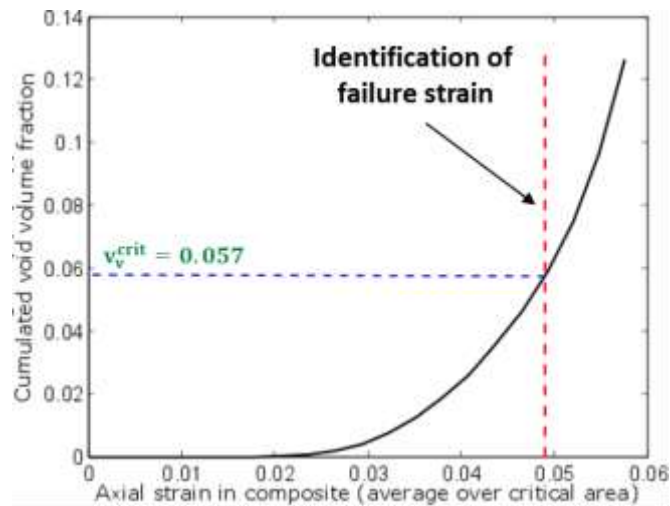


Fig. 21. Identification du taux de vide critique du composite

La validation du critère de rupture est réalisée par comparaison entre les déformations à rupture simulées avec différentes orientations des fibres par rapport à la direction du chargement et les déformations de rupture mesurée expérimentalement. Les exemples des essais à  $0^\circ$  et  $90^\circ$  sont présentés dans la Figure 22.

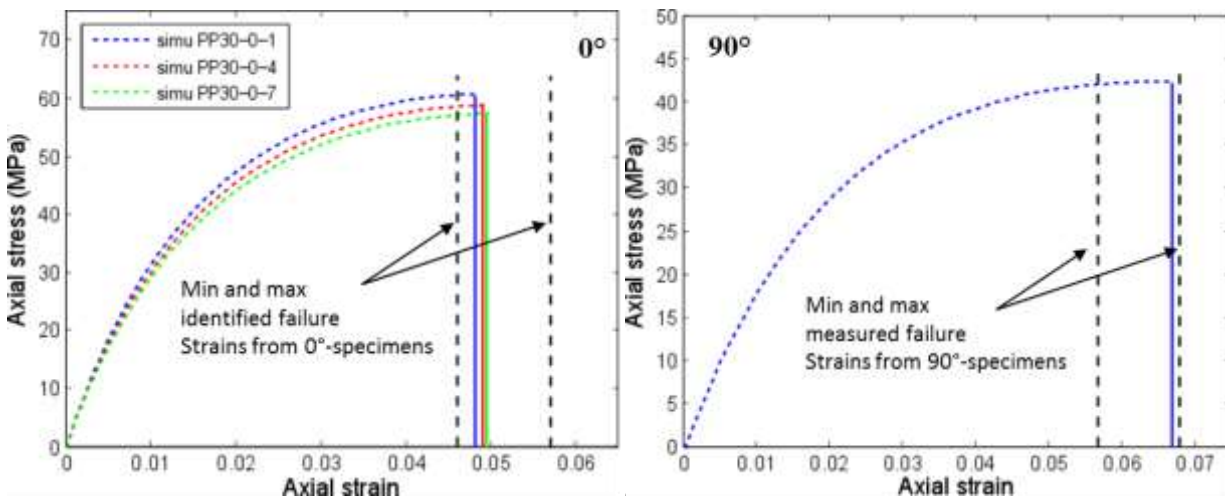


Fig. 22. Prédiction de la déformation à la rupture pour des composites testés à  $0^\circ$  et  $90^\circ$  par rapport à l'orientation préférentielle des fibres

Les résultats sont très satisfaisant jusqu'à des angles de l'ordre de  $45^\circ$  entre la direction de chargement et la direction d'orientation préférentielle des fibres (ici, direction d'injection), mais moins pour des angles plus élevés. Ceci s'explique très probablement par le fait que, lorsque les fibres sont chargées quasi-transversalement, l'endommagement initié en pointe de fibre, tel qu'il a été observé par Sato et al. [11] et modélisé [12], n'est plus le phénomène d'endommagement prépondérant. La rupture du composite est alors effective avant que le taux de vide critique identifié en utilisant ce modèle ne soit atteint.

## Conclusion

Cette thèse porte sur la proposition d'une loi qui permet la modélisation du comportement de thermoplastiques renforcés par fibres courtes en prenant en compte la sensibilité à la vitesse de déformation couplée aux caractéristiques complexes du renfort. La caractérisation du comportement du composite a fait l'objet d'une campagne expérimentale portant sur la réalisation des essais à plusieurs conditions de chargement. L'identification de la loi de comportement viscoélastique linéaire de la matrice a été faite par des essais à excitation fréquentielle permettant la détermination des modules et temps de relaxations. L'identification des paramètres viscoplastique a été faite moyennant des essais de compression et de traction réalisés à plusieurs vitesses de déformation. La détermination des paramètres viscoplastiques est faite en se basant sur la méthode SEE. Le modèle viscoélastique-visoplastique de la matrice est ensuite validé par comparaison avec les essais de traction réalisés sur la matrice pure à plusieurs vitesses de déformation. La caractérisation de la microstructure du composite avec des taux de renfort de 30% et 40% en masse de fibre de verre a été faite par des analyses micro-tomographiques. La géométrie des fibres est identifiée moyennant ces analyses. L'orientation des fibres est caractérisée sous forme d'histogramme de densité d'orientation. Ces orientations sont ensuite exprimées par des distributions d'orientation et utilisées pour alimenter le modèle de comportement du composite.

Le modèle est validé sur une large gamme de vitesse de déformation pour le cas d'un composite polypropylène – fibres courtes de verre, moulé par injection, caractérisé par une matrice viscoélastique, viscoplastique et à écoulement plastique sensible à la pression et non-isochore, et par des distributions d'orientation des fibres complexes. Celles-ci sont notamment responsables de l'anisotropie du comportement, ainsi que de disparités, même à angle de chargement fixé.

Deux types d'endommagement sont implémentés : l'endommagement ductile de la matrice renforcé, fortement anisotrope, et la décohésion progressive à l'interface fibre/matrice. Ces extensions du modèle ont été validées par comparaison avec des résultats expérimentaux. Un critère de rupture du composite a été défini en se basant sur le taux de vide critique créé par décohésion. Son identification et sa validation a été faite par comparaisons avec les déformations à rupture du composite avec plusieurs angles du chargement par rapport à la direction préférentielle des fibres.

Des extensions de ce travail porteront sur la prise en compte de l'initiation de la décohésion entre fibres et matrice sur les côtés des fibres afin de traiter d'une manière plus précise le cas des fibres transversalement orientées par rapport à la direction de chargement. Ces perspectives s'intéressent aussi à la prise en compte de l'effet de vitesse de déformation sur l'évolution et la prépondérance des mécanismes d'endommagement et sur rupture du composite. Cela est motivé par des observations sur des faciès de rupture des éprouvettes testées en traction à différentes vitesses de déformation comme montré dans la Figure 23.

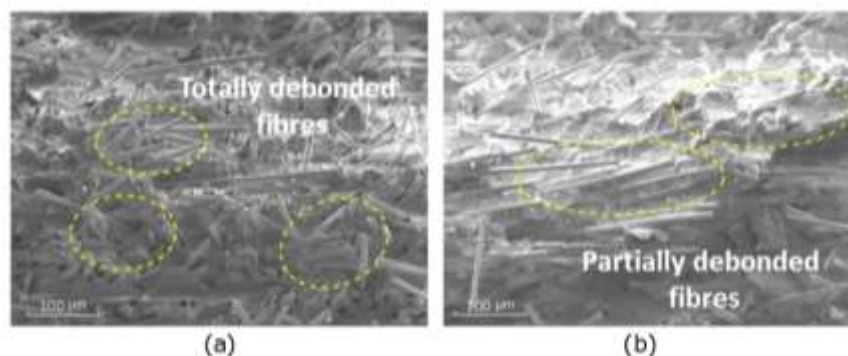


Fig. 23. Observation au MEB des faciès de rupture des éprouvettes testées à (a) 1mm/min et (b) 1000 mm/s.

---

## Références

- [1] A. Bernasconi, F. Cosmi, D. Dreossi, “Local anisotropy analysis of injection moulded fibre reinforced polymer composites ». *Composite Science and Technology*, Vol. 68, pp. 2574-2581, 2008.
- [2] A. Krairi, I. Doghri, G. Robert, “Multiscale high cycle fatigue models for neat and short fiber reinforced thermoplastic polymers ». *International Journal of Fatigue*, Vol. 92, pp. 179-192, 2016.
- [3] D. Notta-Cuvier, F. Lauro, B. Bennani, R. Balieu, « An efficient modelling of inelastic composites with misaligned short fibres ». *International Journal of Solids and Structures*, Vol. 50, pp. 2857-2871, 2013.
- [4] M. Nciri, D. Notta-Cuvier, F. Lauro, F. Chaari, Y. Maalej, B. Zouari, « Modelling and characterisation of dynamic behaviour of short-fibre-reinforced composites ». *Composite Structures*, Vol. 160, pp. 516-528, 2017.
- [5] R. Raghava, R.M. Caddell, G.S.Y. Yeh, “The macroscopic yield behaviour of polymers”. *Journal of Materials Sciences*, Vol. 8, pp. 225-232, 1973.
- [6] W.H. Bowyer, M.G. Bader, “On the reinforcement of thermoplastics by imperfectly aligned discontinuous fibres”. *Journal of Materials Science*, Vol. 7, pp. 1315-1321, 1972.
- [7] F. Lauro, B. Bennani, D. Morin, A.F. Epee, “The SEE method for determination of behaviour laws for strain rate dependent material: application to polymer material”. *International Journal of Impact Engineering*, Vol. 37, pp. 715-722, 2010.
- [8] S. Kammoun, I. Doghri, L. Adam, G. Robert, L. Delannay, “First pseudo-grain failure model for inelastic composites with misaligned short fibers”. *Composites: Part A*, Vol. 42, pp. 1892-1902, 2011.
- [9] D. Notta-Cuvier, F. Lauro, B. Bennani, M. Nciri, « Impact of natural variability of flax fibres properties on mechanical behaviour of short-flax-fibre-reinforced polypropylene ». *Journal of Materials Science*, Vol. 51, pp. 2911-2925, 2016.
- [10] D. Notta-Cuvier, F. Lauro, B. Bennani, R. Balieu, « Damage of short-fibre reinforced materials with anisotropy induced by complex fibres orientations”, *Mechanics of Materials*, Vol. 68, pp. 193-206, 2014.
- [11] N. Sato, T. Kurauchi, S. Sato, O. Kamigaito, “Microfailure behaviour of randomly dispersed short fibre reinforced thermoplastic composites obtained by direct SEM observation”. *Journal of Materials Science*, Vol. 26, pp. 3891-3898, 1991.
- [12] D. Notta-Cuvier, F. Lauro, B. Bennani, “Modelling of progressive fibre/matrix debonding in short-fibre reinforced composites up to failure”. *International Journal of Solids and Structures*, Vol. 66, pp. 140-150, 2015.